INTERPRETATION OF TEMPERATURE SIGNALS FROM ICE CORES

DISSERTATION

THOMAS MÜNCH

ALFRED-WEGENER-INSTITUT
HELMHOLTZ-ZENTRUM FÜR POLAR-
UND MEERESFORSCHUNG

Universität Potsdam

INTERPRETATION OF TEMPERATURE SIGNALS FROM ICE CORES

Insights into the spatial and temporal variability of water isotopes in Antarctica

Publikationsbasierte Dissertation
zur Erlangung des akademischen Grades
"doctor rerum naturalium"
(Dr. rer. nat.)

in der Wissenschaftsdisziplin
KLIMAPHYSIK

eingereicht an der
Mathematisch-Naturwissenschaftlichen Fakultät
der Universität Potsdam

angefertigt am
Alfred-Wegener-Institut
Helmholtz-Zentrum für Polar- und Meeresforschung

vorgelegt von
THOMAS MÜNCH

Potsdam

Eingereicht: 30. November 2017
Verteidigt: 01. Juni 2018

GUTACHTER

DR. THOMAS LAEPPLE
Alfred-Wegener-Institut
Helmholtz-Zentrum für Polar- und Meeresforschung, Potsdam
und
Mathematisch-Naturwissenschaftliche Fakultät
Universität Potsdam

PROF. DR. DR. H.C. MULT. JÜRGEN KURTHS
Potsdam-Institut für Klimafolgenforschung
und
Mathematisch-Naturwissenschaftliche Fakultät
Humboldt-Universität zu Berlin

PROF. DR. PETER DITLEVSEN
Niels Bohr Institute
University of Copenhagen

Thomas Münch:
Interpretation of Temperature Signals from Ice Cores: Insights into the spatial and temporal variability of water isotopes in Antarctica,
November 2017 & August 2018.

Document typeset using the LaTeX template `classicthesis` developed by André Miede with style inspired by Robert Bringhurst: "*The Elements of Typographic Style*". `classicthesis` is available at `https://bitbucket.org/amiede/classicthesis/`.

I have my mother’s dreams
I have my father’s eyes

— Tim McIllrath, Rise Against

für meine Eltern

ABSTRACT

Earth's climate varies continuously across space and time, but humankind has witnessed only a small snapshot of its entire history, and instrumentally documented it for a mere 200 years. Our knowledge of past climate changes is therefore almost exclusively based on indirect proxy data, i.e. on indicators which are sensitive to changes in climatic variables and stored in environmental archives. Extracting the data from these archives allows retrieval of the information from earlier times. Obtaining accurate proxy information is a key means to test model predictions of the past climate, and only after such validation can the models be used to reliably forecast future changes in our warming world. The polar ice sheets of Greenland and Antarctica are one major climate archive, which record information about local air temperatures by means of the isotopic composition of the water molecules embedded in the ice. However, this temperature proxy is, as any indirect climate data, not a perfect recorder of past climatic variations. Apart from local air temperatures, a multitude of other processes affect the mean and variability of the isotopic data, which hinders their direct interpretation in terms of climate variations. This applies especially to regions with little annual accumulation of snow, such as the Antarctic Plateau. While these areas in principle allow for the extraction of isotope records reaching far back in time, a strong corruption of the temperature signal originally encoded in the isotopic data of the snow is expected. This dissertation uses observational isotope data from Antarctica, focussing especially on the East Antarctic low-accumulation area around the Kohnen Station ice-core drilling site, together with statistical and physical methods, to improve our understanding of the spatial and temporal isotope variability across different scales, and thus to enhance the applicability of the proxy for estimating past temperature variability. The presented results lead to a quantitative explanation of the local-scale ($1 - 500\,\mathrm{m}$) spatial variability in the form of a statistical noise model, and reveal the main source of the temporal variability to be the mixture of a climatic seasonal cycle in temperature and the effect of diffusional smoothing acting on temporally uncorrelated noise. These findings put significant limits on the representativity of single isotope records in terms of local air temperature, and impact the interpretation of apparent cyclicalities in the records. Furthermore, to extend the analyses to larger scales, the timescale-dependency of observed Holocene isotope variability is studied. This offers a deeper understanding of the nature of the variations, and is crucial for unravelling the embedded true temperature variability over a wide range of timescales.

KURZFASSUNG

Das Klima der Erde verändert sich stetig sowohl im Raum als auch in der Zeit, jedoch hat die Menschheit nur einen Bruchteil dieser Entwicklung direkt verfolgen können und erst seit 200 Jahren mit instrumentellen Beobachtungen aufgezeichnet. Unser Wissen bezüglich früherer Klimaveränderungen beruht daher fast ausschließlich auf indirekten Proxydaten, also Stellvertreterdaten, welche sensitiv auf Veränderungen in bestimmten Klimavariablen reagieren und in Klimaarchiven abgespeichert werden. Essentiell ist eine hohe Genauigkeit der erhaltenen Proxydaten. Sie erlaubt, Modellvorhersagen früherer Klimazustände quantitativ zu überprüfen und damit die Modelle zu validieren. Erst dann können mit Hilfe der Modelle verlässliche Aussagen über die anthropogen bedingten zukünftigen Klimaveränderungen getroffen werden. Die polaren Eisschilde von Grönland und Antarktika sind eines der wichtigsten Klimaarchive. Über die isotopische Zusammensetzung der im Eis eingelagerten Wassermoleküle zeichnen sie Veränderungen der lokalen Lufttemperatur auf. Jedoch stellen die Daten dieses Temperaturproxys keine perfekte Aufzeichnung früherer Klimaschwankungen dar – was im Übrigen für alle Proxydaten gilt –, da neben der Temperatur eine Fülle anderer Effekte Mittelwert und Varianz der Proxyschwankungen beeinflussen und damit die direkte Interpretation der Daten in Bezug auf klimatische Veränderungen beeinträchtigen. Insbesondere trifft dies auf Gebiete mit geringen jährlichen Schneefallmengen zu, wie z.B. das Polarplateau des antarktischen Kontinents. Diese Gebiete erlauben zwar prinzipiell die Gewinnung von Proxydatensätzen, die weit in die Vergangenheit zurückreichen, allerdings erwartet man im Allgemeinen auch eine starke Beeinträchtigung des ursprünglichen, in der isotopischen Zusammensetzung des Schnees eingeprägten Temperatursignals. Unter Verwendung von Beobachtungsdaten aus der Antarktis – hauptsächlich aus dem Niedrigakkumulationsgebiet von Dronning Maud Land in Ostantarktika, in dem auch die Kohnen-Station liegt –, sowie durch Anwendung statistischer und physikalischer Methoden, trägt diese Dissertation zu einem besseren Verständnis der räumlichen und zeitlichen Variabilität der Isotopendaten über einen weiten Skalenbereich bei. Damit verbessert die vorliegende Arbeit die Anwendbarkeit dieses Temperaturproxys in Bezug auf die Rekonstruktion natürlicher Klimavariabilität. Im Speziellen wird aus den Beobachtungsdaten ein statistisches Modell abgeleitet, welches quantitativ die lokale räumliche ($1 - 500$ m-Skala) Variabilität erklärt; des Weiteren wird gezeigt, dass die zeitliche Variabilität hauptsächlich bedingt wird durch die Kombination zweier Effekte: einen klimatischen Jahreszyklus angetrieben durch den Jahresgang der Temperatur, und die Wirkung des Diffusionsprozesses auf einen zeitlich unkorrelierten Rauschterm. Diese Resultate führen zum einen zu einer wesentlich eingegrenzten Abschätzung der Repräsentativität einzelner, isotopenbasierter Proxyzeitreihen in Bezug auf lokale Temperaturveränderungen. Zum anderen beeinflussen sie erheblich die Interpretation scheinbarer Periodizitäten im Isotopensignal. Es wird darüber hinaus vermutet, dass die Gesamtstärke des Rauschens im Isotopensignal nicht nur durch die örtliche Akkumulationsrate bestimmt wird, sondern auch durch andere Parameter wie die lokale mittlere Windstärke und die räumliche und zeitliche Kohärenz der Niederschlagswichtung. Schließlich erlaubt die Erweiterung der Analyse auf größere räumliche und zeitliche Skalen die Untersuchung, inwieweit die Variabilität isotopenbasierter Proxyzeitreihen aus dem Holozän von der Zeitskala abhängt. Dadurch wird ein tieferes Verständnis der Proxyvariabilität erzielt, welches grundlegend dafür ist, die tatsächliche, in den Daten einzelner Zeitreihen verdeckt vorhandene Temperaturvariabilität, über einen weiten Zeitskalenbereich zu entschlüsseln.

PUBLICATIONS OF THE AUTHOR

ISI peer-reviewed

Münch, T., Kipfstuhl, S., Freitag, J., Meyer, H. and Laepple, T.: Regional climate signal vs. local noise: a two-dimensional view of water isotopes in Antarctic firn at Kohnen Station, Dronning Maud Land, Clim. Past, **12** (7), 1565–1581, DOI: `10.5194/cp-12-1565-2016`, 2016.

Münch, T., Kipfstuhl, S., Freitag, J., Meyer, H. and Laepple, T.: Constraints on post-depositional isotope modifications in East Antarctic firn from analysing temporal changes of isotope profiles, The Cryosphere, **11** (5), 2175–2188, DOI: `10.5194/tc-11-2175-2017`, 2017.

Laepple, T., Hörhold, M., **Münch, T.**, Freitag, J., Wegner, A. and Kipfstuhl, S.: Layering of surface snow and firn at Kohnen Station, Antarctica: Noise or seasonal signal?, J. Geophys. Res. Earth Surf., **121** (10), 1849–1860, DOI: `10.1002/2016JF003919`, 2016.

Laepple, T., **Münch, T.**, Casado, M., Hoerhold, M., Landais, A. and Kipfstuhl, S.: On the similarity and apparent cycles of isotopic variations in East Antarctic snow pits, The Cryosphere, **12** (1), 169–187, DOI: `10.5194/tc-12-169-2018`, 2018.

Rehfeld, K., **Münch, T.**, Ho, S. L. and Laepple, T.: Global patterns of declining temperature variability from the Last Glacial Maximum to the Holocene, Nature, **554** (7692), 356–359, DOI: `10.1038/nature25454`, 2018.

Casado, M., Landais, A., Picard, G., **Münch, T.**, Laepple, T., Stenni, B., Dreossi, G., Ekaykin, A., Arnaud, L., Genthon, C., Touzeau, A., Masson-Delmotte, V. and Jouzel, J.: Archival processes of the water stable isotope signal in East Antarctic ice cores, The Cryosphere, **12** (5), 1745–1766, DOI: `10.5194/tc-12-1745-2018`, 2018.

Non peer-reviewed

Laepple, T., **Münch, T.** and Dolman, A. M.: Inferring past climate variations from proxies: Separating climate and non-climate variability, Past Global Changes Magazine, **25** (3), 140–141, DOI: `10.22498/pages.25.3.140`, 2017.

CONTENTS

LIST OF FIGURES

LIST OF TABLES

1

GENERAL INTRODUCTION

Earth's climate is of highly complex and non-linear nature. As an abstract concept, it is the state, including a statistical description, of the climate system, including the atmosphere, oceans, cryosphere, biosphere and the lithosphere. From an empirical point of view, the climate can be characterised by the mean and variability of a set of climatic variables, such as temperature. The components of the climate system are coupled, and interact with each other on different timescales arising from the different associated response times to changes in boundary conditions[1]. Individual climate components, e.g., the atmosphere and the ocean, show diffusive dynamics, due to which the temporal and spatial scale variations are intricately linked. Therefore, the variations on a local, a regional and the global scale are a function of the studied timescale. As a result of the coupling of the climate components, observations of the average state of one component may, at least partly, include indirect information on the entire system; and thus, the climate is in a narrower sense also often described by the average atmospheric conditions, or, the average weather[2].

The global mean state of the system is controlled by the energy balance between the incoming solar and outgoing thermal radiation, making it to a first approximation a deterministic system driven by the variations of these two quantities. However, due to the complex and non-linear interactions of the individual components, the climate is in general a stochastic system, characterised by continuous internal variations in space and time around a certain mean state.

The amplitudes of the changes are typically larger when looking at longer periods of time (e.g., Shackleton and Imbrie, 1990; Peltier, 1998; Zachos et al., 2001). For example, large changes occurred on tectonic timescales ($\gtrsim 10^6$ years), driven by the global carbon cycle (Ruddiman, 2008), with transitions from possibly completely ice-covered (Hoffman et al., 1998) to ice-free worlds (Zachos et al., 2001). By contrast, the entire last ~ 3 million years show a partly ice-covered planet, where the quasi-periodic solar forcing variations due to changes in Earth's orbit around the Sun (Milanković, 1941; Imbrie and Imbrie, 1980) cause climate variations on multi-millennial timescales between stronger glacial (up to 30 % of landmasses covered with

---

[1] The troposphere typically reacts within days, while the ocean mixed layer reacts on monthly to annual scales; by contrast, the response times of the deep ocean and the ice sheets are typically of the order of 10^2–10^3 years, and longer (Ruddiman, 2008).

[2] The typical temporal averaging scale for this is 30 years, according to the definition of the World Meteorological Organization (`http://www.wmo.int/pages/prog/wcp/ccl/faqs.php`, last access: 17th August 2018).

ice; Latif, 2009) and weaker interglacial periods (Lisiecki and Raymo, 2005; EPICA community members, 2004). Finally, when investigating only the time periods of the Holocene, global mean temperatures vary even less (Marcott et al., 2013) with approximately half of the variability being due to internal variations (Crowley, 2000).

Since direct instrumental observations of climatic variables are only possible since ~ 200 years, which represents only a short snapshot ($< 10^{-5}\,\%$) of the entire climate history, most of this knowledge has been inferred from indirect climate proxy data, i.e. from indicators which are sensitive to changes in climatic variables and stored in environmental archives. Extracting the proxy data from these archives then allows retrieval of the information from earlier times.

One of the major climate archives are the polar ice sheets of Greenland and Antarctica, storing information on past temperatures in the form of the isotopic composition of the water. Accessing these information by drilling ice cores thus allows in principle the retrieval of climate information over a large range of timescales, from subannual to glacial–interglacial variations. However, as any climate proxy, the isotopic temperature proxy is not a perfect recorder of the climate variations, since a multitude of processes affect the isotopic composition of the deposited ice, leading to strong isotope variations that do not reflect actual changes in temperature.

Still, proxy data are, due to the short instrumental observations, the most important means to study past climates in order to gain an understanding of the climate system, and to test this against predictions from conceptual and numerical climate models. This is essential to unravel the mechanisms behind climate and its variability changes, and thus to make realistic projections of the future changes in mean and variability under the ongoing anthropogenic (IPCC, 2013) climate change. An improved quantitative understanding of proxy variability is hence not only driven by scientific curiosity, but also key for improving both proxy- and model-based inferences on the climate system, and thus to disentangle the effects of natural and anthropogenic forcings. This is vital since the welfare of humankind, and of all living beings, is linked to the spatial and temporal modes of climate variability, and thus depends on our knowledge concerning the changes in climate in the future ahead of us.

This thesis makes a contribution to a better understanding of the mechanisms that drive the spatial and temporal variations of the isotopic composition recorded in Antarctic ice. This is achieved by applying the following methods and strategies: (1) analysis of surface snow data of isotopic composition and other proxies to study and model the spatial variability; (2) investigation of the depositional processes by studying the temporal changes and the spectral properties of firn isotope profiles to establish a process-based understanding of the proxy signal formation; and (3) studies to infer the timescale dependencies of temperature- and non-temperature-related variations. The following two sections describe in more detail the challenges related to temperature reconstructions inferred from isotope variations, and highlight how this thesis improves our current understanding of their recording system.

1.1 ISOTOPE-INFERRED RECONSTRUCTION OF POLAR TEMPERATURES, AND THE RELATED CHALLENGES

The polar ice sheets of Greenland and Antarctica play a major role in the climate system. They significantly affect the global surface albedo (Laine, 2008), controlling the amount of incoming solar radiation which is directly reflected off the surface to the atmosphere, and influence atmospheric circulation owing to their elevation by affecting storm tracks (e.g., Dethloff et al., 2004) and due to creating typical wind and large-scale pressure systems (Parish and Cassano, 2003). Interactions of the corresponding ice shelves with the ocean influence ocean circulation and deep-water formation (Nicholls et al., 1991). Finally, they store more than 99 % of the global freshwater in form of snow and ice, which thus has a strong potential to affect global sea level under climate change (IPCC, 2013). The reconstruction of past polar temperatures from the isotopic composition measured on ice cores is thus important to obtain crucial information on the climate system. However, many challenges are connected with the interpretation of isotope in terms of temperature variations.

The use of ice-core isotope data as a temperature proxy builds on the relationship between the isotopic composition of precipitation and the local temperature at the point of precipitation formation (Dansgaard, 1964; Jouzel and Merlivat, 1984). This arises from the temperature-dependent fractionation of the individual isotope species in water during phase changes, together with the successive distillation of air masses on their pathway from temperate to polar regions (Dansgaard, 1964; Craig and Gordon, 1965; Jouzel and Merlivat, 1984; and Sect. 2.1). Consequently, transfer functions have been established relating the spatial variations in isotopic composition of surface snow to the corresponding spatial gradients in local annual mean temperature (e.g., Johnsen et al., 1989; Masson-Delmotte et al., 2008). These empirical relationships can then be applied to past changes assuming that the present-day spatial covariance between the variables also holds in time at a single site. However, in detail the processes influencing the isotopic composition of precipitation are complex (Jouzel et al., 1997), and using the spatial relationship as a surrogate for the temporal relationship has been critically questioned (Jouzel et al., 1997, 2003), with severe implications for the interpretation of Greenlandic ice-core records (Jouzel et al., 1997; Masson-Delmotte et al., 2005). Nowadays, state-of-the-art isotopeenabled global climate models are able to help developing a physical understanding of the relevant processes from the source to the precipitation site (Werner et al., 2000, 2011; Sjolte et al., 2011).

However, adding another level of complexity, the variability of the isotopic composition of the near-surface snow is not a one-to-one image of that in the precipitating snow, but additionally influenced by a number of processes not directly linked to temperature. The seasonal and interannual distribution of precipitation and accumulation can bias the original atmospheric isotope signal and/or induce temporal variability (Persson et al., 2011). Seasonal intermittency of accumulation has been shown to have a strong impact on the mean isotopic composition of Antarctic snow (Sime et al., 2009; Laepple et al., 2011). Additionally, strong spatial variability arises from the uneven deposition of the surface snow (Fisher et al., 1985), commonly termed *stratigraphic noise*, possibly enhanced further by the wind-driven erosion, redistribution and vertical mixing of the snow in low-accumulation areas. Indicative of this are the observed low intercore correlations on the Antarctic Plateau for Holocene timescales (Graf et al., 2002; Karlöf et al., 2006; Altnau et al., 2015). Furthermore, changes in near-surface isotopic composition of the snow (often referred to as *post-depositional changes*) are proposed to arise from diffusive or wind-driven exchange of water vapour between the firn and the overlying atmosphere (Waddington et al., 2002; Neumann and Waddington, 2004; Town et al., 2008); isotopic exchanges have been observed on daily (Steen-Larsen et al., 2014) and diurnal scales (Ritter et al., 2016). Moreover, observations (Moser and Stichler, 1974; Stichler et al., 2001) as well as lab experiments (Hachikubo et al., 2000; Sokratov and Golubev, 2009) showed isotopic fractionation associated with sublimation, condensation and recrystallisation processes. However, despite these findings, the general significance and implication of the effects for the interpretation of ice-core data are still unclear. In the deposited snow, prior to its transformation to solid ice, the molecular diffusion of vapour through connecting air channels (Johnsen, 1977; Whillans and Grootes, 1985; Johnsen et al., 2000; and Sect. 2.2.4) smoothes the isotope variations, affecting the temporal variability and hence the spectral shape of a record (van der Wel et al., 2015b). The effect of diffusion can be understood from a physical point of view (Sect. 2.2.4), but the validity of the current model (Johnsen et al., 2000) has been questioned recently (van der Wel et al., 2015a). Finally, the temporal amount of information that can be retrieved strongly varies with the depth of the ice core. The possible total time span at a given location is controlled by the thickness of the ice and the annual amount of snowfall. The latter also regulates the maximum resolution at the top of the ice sheet. However, the effective resolution quickly decreases with depth due to the smoothing effect of diffusion, the compression of the layers by the densification from snow to ice (Herron and Langway, 1980; Hörhold et al., 2011; and Sect. 2.2.2), and ultimately due to the further thinning caused by the horizontally diverging flow of ice in an ice sheet (Dansgaard and Johnsen, 1969; Alley and Joughin, 2012).

Many of these processes are, or are assumed to be, a function of the annual accumulation rate at the ice-core site. In general, the mass balance of ice sheets is a function of elevation, and it typically decreases with elevation for the Antarctic ice sheet (Oerlemans, 2011). Therefore, a stronger impact of the processes is expected for the dry Antarctic Plateau where the major ice-core sites are situated (Petit et al., 1999; EPICA community members, 2004, 2006; Uemura et al., 2012). However, a comprehensive physical understanding of the variability in Antarctic ice-core data depending on the isotopic composition of precipitation and the environmental and climatic parameters is still missing. While an empirical model for stratigraphic noise has been developed for Greenland (Fisher et al., 1985), its applicability for the low-accumulation areas of Antarctica is unclear. Forward models have been applied to simulate artificial isotope profiles (Helsen et al., 2006; Sime et al., 2011; van der Wel et al., 2011; Dee et al., 2015), but none of the models accounts for both the potentially high spatial and temporal variability unrelated to local temperatures.

Such an understanding is ultimately needed to improve the interpretation of isotope records. For instance, large spatial variability questions the representativity of single cores, affecting attempts to study the true climatic relationship between spatial and temporal variations. Whether the non-temperature-related variability is strong enough to mask the actual temperature variability will depend on the actual strength of the climatic signal. This raises the question of how the signal-to-noise ratio depends on the spatial and temporal scales.

Figures (1.1) and (1.2) provide a visual illustration of these issues. While for glacial–interglacial timescales temperature proxy records show a consistent picture between different regions of the world, here shown for deep ocean versus atmospheric temperatures in Antarctica[3] (Fig. 1.1a), the picture is less clear for variations within the last glacial period (Fig. 1.1b) and especially within the Holocene (Fig. 1.1c). For the last glacial period, Antarctic millennial-scale variations in oxygen isotopic composition (δ^{18}O) are highly correlated (Pearson correlation coefficient $r > 0.9$) and also well correlated with Greenland ($r \sim 0.8$). However, much higher variability is observed in Greenland for the last glacial period which is not seen in Antarctica (Fig. 1.1b). By contrast, Holocene decadal δ^{18}O variations at the drilling site of the European Project for Ice Coring in Antarctica (EPICA) in Dronning Maud Land at Kohnen Station (EDML) are

---

[3] Note however that the benthic δ^{18}O data of the LR04 stack (Lisiecki and Raymo, 2005) are a proxy for both deep ocean temperatures and global ice volume, thus are expected to co-vary with Antarctic temperatures.

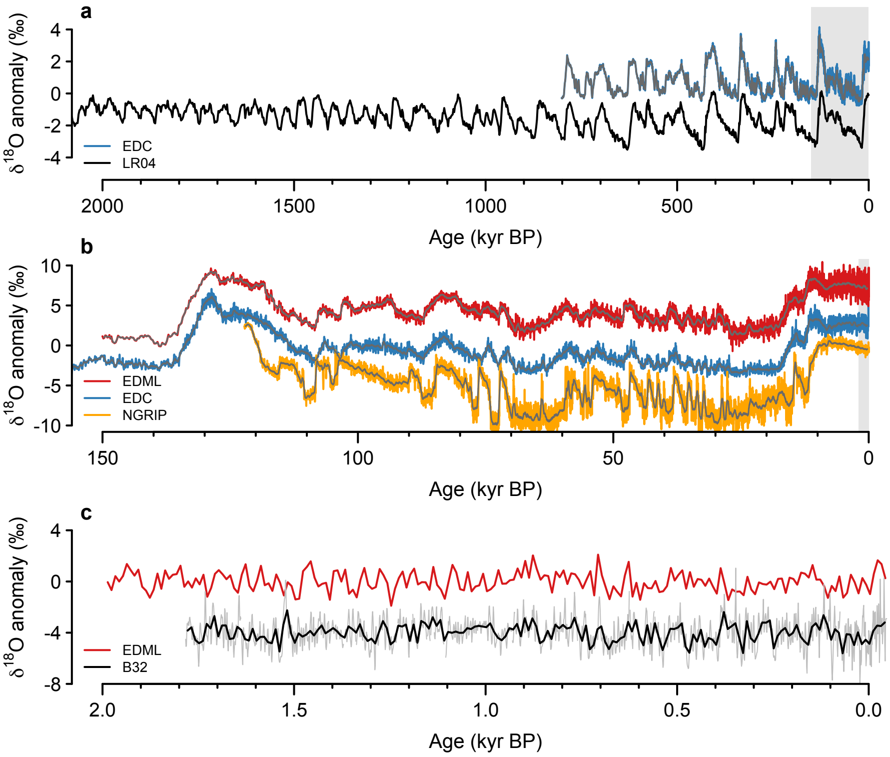

FIGURE 1.1. Temperature proxy time series (δ^{18}O) for different time periods (horizontal axis, in kyr before 1950 CE) and regions. (**a**) δ^{18}O anomalies from the LR04 benthic stack (Lisiecki and Raymo, 2005; black) and the Antarctic EPICA Dome C (EDC) ice core (EPICA community members, 2004; blue: original resolution, grey: 1000-yr running mean). The y-axis orientations are aligned and both records normalised to unit variance. (**b**) δ^{18}O anomalies from the EDC (blue), the EPICA DML (EPICA community members, 2006; red) and the Greenlandic NGRIP (NGRIP members, 2004; orange) ice cores. Coloured lines show the original resolution, grey lines the 500-year running means. (**c**) Decadal δ^{18}O anomalies from EPICA DML (red) and the nearby B32 firn core (Graf et al., 2002; black, original annual resolution in grey). All records have been slightly offset vertically to improve visibility. Shaded areas denote the time period displayed in the subsequent figure.

poorly correlated ($r = 0.27$), even on short spatial scales ($\sim 1\,\text{km}$). A complementary picture is obtained from the spectral shape of the variations (Fig. 1.2). For the Holocene, Antarctic and Greenlandic ice cores show a strong influence by diffusion on shorter scales and a nearly white spectrum above decadal timescales. The latter is unexpected for climatic variations (see Sect. 2.3). This either suggests that the Holocene temperature variability in polar regions can be described mainly by white noise, or that we observe proxy-specific variability here.

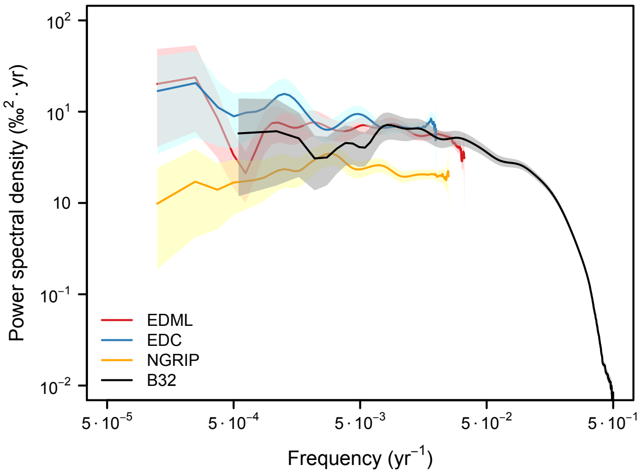

FIGURE 1.2. Holocene ice-core-based temperature proxy spectra. Shown are the power spectral densities of the δ^{18}O variations over the last 8000 years from the EDML (red), EDC (blue) and NGRIP (orange) ice cores, and over the last 2000 years from the firn core B32 (black). Prior to spectral analysis, the longer records have been block-averaged to an even resolution of 20 (NGRIP), 15 (EDML) and 25 (EDC) years. B32 is annually resolved. Shadings denote the 90 % confidence intervals of the spectral estimates.

1.2 THESIS OVERVIEW: AIMS AND STRUCTURE

Based on the challenges presented in the previous section, this dissertation aims at answering the following questions:

- What is the representativity of single isotope records as a function of different spatial and temporal scales in the low-accumulation region of Dronning Maud Land in East Antarctica?
- What is the source of the spatial variability, how does it influence the temporal variability, and what is the relationship between signal-to-noise ratio and timescale?
- What implications arise for the reconstruction of Holocene Antarctic temperature variabilities?

The dissertation is organised as a cumulative thesis that consists, besides the general introduction, of seven main chapters and two appendices, which cover (1) the theoretical background, (2) several individual research articles, and (3) an overall discussion.

Chapter 2 provides the theoretical background for the thesis and the individual articles. It is an integral part of this work, because it firstly provides the necessary knowledge for a self-contained understanding of the manuscript chapters and secondly highlights thereby the challenges common to all of the presented studies.

In the overall discussion and conclusion (Chap. 8), the main findings of the individual publications are discussed and put into context with respect to the general aims of this thesis.

The main part (Chaps. 3–7) presents individual and independent research articles for international ISI-listed and peer reviewed scientific journals. Chapters 3–5 and 7 are published, Chap. 6 is a manuscript in preparation. In addition, Appendix B presents a published manuscript included for completeness.

Chapter 3 analyses a large set of observational near-surface isotope data obtained at the EDML site at Kohnen Station on the Antarctic Plateau. The applied two-dimensional sampling of the isotopic composition in elongated snow trenches allows us to study the representativity and the signal and noise content of oxygen isotope profiles from seasonal to interannual timescales. A statistical model for stratigraphic noise is developed which provides the first quantitative model for the short-scale spatial variability at an Antarctic low-accumulation region. By applying the model with estimated parameters to deeper firn cores, implications for Holocene climate reconstructions are derived. Throughout the thesis, this chapter is cited as Münch et al. (2016b).

Chapter 4 presents a second trench study from Kohnen Station and is an extension of Münch et al. (2016b). It focuses on post-depositional changes of the isotopic composition, such as firn diffusion and densification as well as other possible processes debated in the literature, by comparing the trench records over the course of two years. The study thereby provides constraints on the isotopic signal formation in the near-surface firn. Throughout the thesis, this chapter is cited as Münch et al. (2017a).

Chapter 5 investigates the statistical nature of firn isotope profiles from the Antarctic Plateau by analysing their spectral characteristics such as the typical spacing of the isotope variations. This is compared to a minimalistic forward model simulating isotope profiles. By this, we gain additional insights into the signal formation that are valid for large parts of the Antarctic Plateau, as well as obtain further constraints on the signal-to-noise ratio of the isotope variations. Throughout the thesis, this chapter is cited as Laepple et al. (2018).

Chapter 6 presents a model to separate the climate signal from the noise in isotope records based on analyses in the spectral domain. The model is applied to two Antarctic core arrays, one from Dronning Maud Land and a second one from the West Antarctic Ice Sheet, to estimate the timescale-dependency of the signal variability and of the signal-to-noise ratio. The study provides a first link between the hitherto obtained results on short timescales to the interpretation of deep ice-core records. Although the manuscript is not yet published, the chapter has been included in the thesis due to its linking character with the following work.

Chapter 7 investigates the change in temperature variability from the Last Glacial Maximum to the Holocene from a global collection of temperature proxy records. The study presents the first quantitative estimate of a change in variability linked to a change in mean climate. It further sheds light on the mechanisms behind the generation of climate variability, and discusses the potentially different recording of climate variability by ice cores in Greenland and Antarctica. The methods to this study are compiled in Appendix A for the sake of clarity. Throughout the thesis, this chapter is cited as Rehfeld et al. (2018).

Finally, Appendix B presents a third and complimentary trench study analysing firn density and ion data from the same trenches as used in Münch et al. (2016b). Since the study is not directly linked to the interpretation of isotope data it is included in the appendix. Nevertheless, the work gives additional insights into the layering of snow and firn and into the interrelationship of the different proxies. Throughout the thesis, this chapter is cited as Laepple et al. (2016).

1.3 AUTHOR CONTRIBUTIONS TO PUBLISHED MANUSCRIPTS AND TECHNICAL COMMENTS

This section lists the detailed author contributions to the included individual research articles and gives a few technical comments.

Chapter 3: *Regional climate signal vs. local noise: a two-dimensional view of water isotopes in Antarctic firn at Kohnen Station, Dronning Maud Land (Münch et al., 2016b)*: T. Laepple, S. Kipfstuhl and J. Freitag organised and conducted the field works. T. Münch and T. Laepple designed the study. T. Münch led the isotope measurements and conducted part of it. H. Meyer co-supervised the measurements in Potsdam. T. Münch reviewed relevant literature, performed all analyses, developed the statistical noise model and wrote and coordinated the manuscript. All authors contributed to the discussion of the results and the revision of the manuscript.

Chapter 4: *Constraints on post-depositional isotope modifications in East Antarctic firn from analysing temporal changes of isotope profiles (Münch et al., 2017a)*: T. Münch, T. Laepple, S. Kipfstuhl and J. Freitag designed and organised the trench field campaign, S. Kipfstuhl and T. Münch conducted the field work. T. Münch and T. Laepple designed the study. T. Münch and H. Meyer co-supervised the isotope measurements. T. Münch reviewed relevant literature, performed all analyses and wrote and coordinated the manuscript. All authors contributed to the discussion of the results and the refinement of the manuscript.

Chapter 5: *On the similarity and apparent cycles of isotopic variations in East Antarctic snow pits (Laepple et al., 2018)*: M. Casado motivated the study, T. Laepple designed the study and conducted the main analyses. M. Casado, T. Münch and M. Hörhold provided data. T. Laepple and T. Münch implemented the numerical analyses. All authors contributed to the discussion of the results. T. Laepple wrote and coordinated the manuscript with contributions from all co-authors.

Chapter 6: *What climate signal is contained in decadal to centennial scale Antarctic isotope variations? (manuscript in preparation)*: T. Münch and T. Laepple designed the research. T. Münch reviewed relevant literature, established the database, performed all analyses, and wrote the manuscript with contributions from T. Laepple.

Chapter 7: *Global patterns of declining temperature variability from the Last Glacial Maximum to the Holocene (Rehfeld et al., 2018)*: K. Rehfeld and T. Laepple designed the research; T. Münch established the ice database and signal-to-noise ratio correction. S. L. Ho established the marine database. K. Rehfeld and T. Laepple developed the methodology. K. Rehfeld performed the data analysis and wrote the first draft of the manuscript. All authors contributed to the interpretation and the preparation of the final manuscript.

Appendix B: *Layering of surface snow and firn at Kohnen Station, Antarctica: Noise or seasonal signal? (Laepple et al., 2016)*: T. Laepple, S. Kipfstuhl and J. Freitag organised and conducted the field works. T. Laepple conducted the DEP measurements, A. Wegner the impurity measurements. T. Laepple and M. Hörhold designed the research, T. Laepple performed the main analyses. T. Münch performed additional analyses and investigated the relationship between the DEP density, oxygen isotope and impurity data. All authors contributed to the discussion of the results and the writing of the manuscript.

In the manuscript chapters, obvious typing errors in the original publications have been corrected. Instances where wording has been slightly modified to achieve consistency throughout the thesis, or to correct the language, are marked by the symbol * at their first occurrence. Obviously missing words have been inserted and marked by the symbol $^\vee$. Larger changes are explained in footnotes. Correlations have been denoted throughout the thesis by the symbol r to avoid confusion with ratios marked by capital R or similar. In Chap. 7 and Appendix B, the spelling has been changed from American to British English for consistency. The layout of some figures and tables has been adjusted for overall consistency, but in none of the cases the original content was changed. The trench terminology changed between different works: Trenches *T1* and *T2* in Chap. 3 and Appendix B refer to trenches *T13–1* and *T13–2* in the other works.

2

THEORETICAL BACKGROUND

This chapter discusses the relationship between the isotopic composition of precipitation and local air temperature, relevant prerequisites for the modelling of the temporal evolution of firn isotope profiles, and theoretical models for the internal variability of the climate system. The first part is essential to understand the background of this dissertation. The second part provides information required for the studies in Chaps. 3–5, and the third part presents theoretical background for the studies in Chaps. 6 and 7.

2.1 THE ISOTOPIC COMPOSITION OF FIRN AND ICE AND ITS RELATIONSHIP WITH TEMPERATURE

2.1.1 *Fractionation of stable water isotopologues*

Chemical elements naturally occur in different isotopes, i.e. vary in their neutron number, which can be stable or decay in radioactive processes. In consequence, two molecules of the same species can differ in their isotopic composition; such molecules are called isotopologues. On a global scale, the relative abundance ratios of the stable isotopes of the same element are constant which hence also applies to the corresponding isotopologues of a molecule.[1]

Water naturally occurs in several different stable isotopologues of which the four most abundant ones ($H_2{}^{16}O$, $H_2{}^{18}O$, $H_2{}^{17}O$, $HD^{16}O$) are important for climate research. In the corresponding literature it is common to refer to these simply as stable water isotopes, although the term is not correct in the strict sense presented above. Nevertheless, for consistency we have adopted this terminology in the publications contributing to this thesis.

Isotopologues differ slightly in their chemical and physical properties. Important for climatology is the fractionation of the isotopic composition, i.e. the enrichment or depletion in abundance of one isotopologue species relative to another, during phase changes. Fractionation can originate both from equilibrium as well as kinetic effects. A theoretical understanding of both processes is advanced, and here only a qualitative picture is presented. Equilibrium fractionation refers to processes that proceed slowly enough that at any time, both phases are in equilibrium with respect to each other. It

---

[1] This is strictly true only when neglecting extraterrestrial sources of isotopes or isotope generation through high-energetic cosmic rays; both do not occur for oxygen and hydrogen isotopes except for tritium.

arises from the quantum mechanical effect that the mass of atoms influences the strength of their chemical bonds, in turn affecting the vibrational energy of the molecule. This results in slightly different latent heats of isotopologues, leading to variations in their relative abundances during phase changes at a given temperature. Kinetic effects may arise, e.g., from the difference in molecular diffusivities. This can lead to additional fractionation during phase changes that occur rapidly and/or unidirectionally. One example is the evaporation of ocean water into dry (unsaturated) air where the kinetic effect leads to higher fractionation compared to evaporation under equilibrium conditions with bidirectional transport (Craig and Gordon, 1965). Another example is the condensation from supersaturated vapour, e.g., in clouds (Jouzel and Merlivat, 1984). The difference in molecular diffusivities for the stable water isotopologues have been experimentally determined, among others, by Merlivat (1978).

The isotopic composition of a water sample is usually expressed in delta values (measured in per mil (‰)) as

$$\delta = \left(\frac{R'}{S} - 1 \right) \times 10^3 \,‰, \tag{2.1}$$

where R' is the abundance ratio of the rare to the common ($H_2{}^{16}O$) isotopologue in the sample, and S is the corresponding ratio in some standard reference water. It is international consensus to report delta values relative to the isotopic composition of Vienna Standard Mean Ocean Water (VSMOW, Gonfiantini, 1978) which represents the average isotopic composition of the global ocean (Table 2.1).

Table 2.1. Relative abundances in the standard reference water VSMOW of the four major stable water isotopologues. Numbers taken from Nassar et al. (2007).

Isotopologue	Abundance (%)
$H_2{}^{16}O$	99.731 700
$H_2{}^{18}O$	0.199 983
$H_2{}^{17}O$	0.037 200
$HD^{16}O$	0.031 069

Equilibrium fractionation of the isotopic composition at the transition between two phases a and b is described by the fractionation factor

$$\alpha = \frac{R'_a}{R'_b} \overset{(2.1)}{=} \frac{1+\delta_a}{1+\delta_b}, \tag{2.2}$$

which depends on the type of phase transition (vapour ↔ liquid, vapour ↔ ice), the isotopologue species and on temperature. Commonly used values for α are the ones experimentally determined by Majoube (1971a,b). At 25 °C, the fractionation factor for evaporation ($R'_{\text{liquid}}/R'_{\text{vapour}}$) is approximately 1.009 for $H_2{}^{18}O$ and 1.08 for $HD^{16}O$; thus, the vapour has delta values relative to the liquid of $\delta^{18}O \approx -9\,‰$ and $\delta D \approx -74\,‰$.

Rayleigh distillation refers to the equilibrium fractionation at phase changes with an immediate removal of the newly formed phase. The isotopologue ratio of the remaining phase will then change according to (Yoshimura, 2015)

$$R' = R'_0 F^{\alpha-1}, \tag{2.3}$$

where R'_0 is the initial isotopologue ratio and F the fraction of the original phase remaining. Rayleigh distillation leads to a much stronger change in isotopologue abundance ratio for low fractions of the remaining phase than does equilibrium fractionation (Dansgaard, 1964).

2.1.2 *Relationship with temperature*

The Rayleigh model explains much of the large-scale variations of the isotopic composition of global precipitation, such as the linear relationship between δ^{18}O and δD and the dependence on local temperature. While the evaporation of vapour from the ocean is the mixture of an equilibrium process in a thin boundary layer above the surface and kinetic effects in a subsequent transition zone which mostly depend on local humidity (Craig and Gordon, 1965), the formation of precipitation in clouds can be approximated by Rayleigh distillation since newly formed condensate is removed from the system by rain or snow.

Indeed, the average relationship between δ^{18}O and δD in precipitation on a global scale exhibits a slope around 8, which can readily be explained by the fractionation difference between the $HD^{16}O$ and $H_2{}^{18}O$ isotopologues in the Rayleigh model (Craig and Gordon, 1965; Yoshimura, 2015). Furthermore, the relative abundances of both isotopologue species in precipitation decrease with increasing latitude, elevation and distance from the coast. This is due to the successive distillation by precipitation events of the vapour along its atmospheric trajectory. For each precipitation event, the fraction F of the remaining vapour decreases. Thus, each event causes, according to Eq. (2.3), a relative isotopologue fractionation of the remaining vapour which is independent of the initial vapour composition. Since precipitation events are connected with a decrease in local temperature, the isotopic composition of precipitation can be linked to the atmospheric temperature at the last stage of precipitation formation. A secondary temperature effect arises from the temperature dependence of the fractionation factor itself. Formally, the temperature dependence of the isotopologue ratio of the condensate is

$$\frac{\mathrm{d}R'_\mathrm{c}}{\mathrm{d}\theta} = R'_\mathrm{c}\left(\frac{1}{\alpha}\frac{\mathrm{d}\alpha}{\mathrm{d}\theta} + \frac{\alpha-1}{F}\frac{\mathrm{d}F}{\mathrm{d}\theta}\right), \tag{2.4}$$

where θ is the local condensation temperature. It is derived from taking the derivative with respect to θ of Eq. (2.3), noting that the change in isotopologue ratio, $\mathrm{d}R'$, is only a function of the change in vapour fraction $\mathrm{d}F$. The dependence on the derivative of α with respect to temperature only arises due to the conversion of the isotopologue ratio from vapour to condensate.

The relationship (2.4) strictly applies only to a given atmospheric vapour trajectory. Several effects can complicate the relationship between isotopic composition and local temperature at a given precipitation site. Variations in the location of, or the temperature at the source site change the temperature gradient between source and precipitation site. This influences the amount of distillation along the vapour trajectory, even when the temperature at the precipitation site stayed constant. Furthermore, the atmospheric vapour trajectories themselves can vary for fixed source and precipitation sites, resulting in precipitation events that have different distillation histories. In addition, different vapour masses can mix on their way to the precipitation site, and/or uptake new vapour from the ocean with a different isotopic composition. Finally, Jouzel and Merlivat (1984) showed that kinetic fractionation effects have to be included into Rayleigh models for the formation of snow at high latitudes since it proceeds under supersaturated conditions.

Despite these complications, the present-day isotopic composition of polar snow is to first order governed by local temperatures. Linear relationships have been found for the isotopic composition of surface snow and annual mean temperature both for Greenland (Dansgaard, 1964; Sjolte et al., 2011) and Antarctica (Lorius et al., 1969; Masson-Delmotte et al., 2008), suggesting that distillation histories are fairly constant for a given site and that the isotopic composition is hence mainly determined by the condensation temperature at the final stage of precipitation formation.

These findings have laid the groundwork for inferring past temperatures from isotopologue data measured on firn and ice cores, making the common but crucial assumption that the observed relationship between present-day spatial gradients in surface snow isotopic composition and temperature (spatial slope β, here in $°\mathrm{C}\,‰^{-1}$) also applies to past variations observed at a single site (temporal slope). However, the complicated nature of the distillation histories can significantly change for different climate periods and regions and thus affect the relationship between isotopic composition and local temperature. For Greenland it was shown from independent calibrations of the isotope–temperature relationship, using long-term temporal observations, borehole temperatures or gas isotope ratios, that temporal slopes lie consistently above the present-day spatial slope and are dependent on the timescale: While Greenland present-day δ^{18}O spatial slopes lie in the range of 1.25–$1.6\,°\mathrm{C}\,‰^{-1}$ (Johnsen et al., 1989; Sjolte et al., 2011), temporal slopes for the Holocene are reported, depending on the time period, between 1.7 and $2.5\,°\mathrm{C}\,‰^{-1}$ (Shuman et al., 1995; Beltrami and Taylor, 1995; Cuffey et al., 1994; Cuffey and Clow, 1997; Johnsen et al., 1997; Vinther et al., 2009; Sjolte et al., 2011).

Furthermore, borehole temperature calibrations for the period of the Last Glacial Maximum (LGM) from the GRIP (Johnsen et al., 1995; Johnsen et al., 1997) and GISP2 (Cuffey et al., 1995; Cuffey and Clow, 1997) ice cores imply LGM temporal slopes for δ^{18}O of 3–3.5 °C ‰$^{-1}$, calibration slopes inferred from gas isotope ratios (Kindler et al., 2014) yield values for the entire last glacial period of ~ 1.7–3.3 °C ‰$^{-1}$ with considerable variations on orbital timescales. Masson-Delmotte et al. (2005) conclude, based on simultaneous measurements of δ^{18}O and δD from the GRIP ice core, that the "apparent isotope–temperature slope varies on all time scales". This timescale-dependency of the calibration slope for Greenland is thought to be most likely due to changes in moisture origin and seasonality of precipitation (Jouzel et al., 1997; Masson-Delmotte et al., 2005) as well as in sea-ice cover and atmospheric circulation (Rhines and Huybers, 2014). For Antarctica, an extensive survey of present-day spatial slopes (Masson-Delmotte et al., 2008), using > 1000 surface snow isotopic composition measurements from across the entire continent, yields mean values of 1.25 °C ‰$^{-1}$ for δ^{18}O and 0.16 °C ‰$^{-1}$ for δ^{2}H with an uncertainty of 20 % accounting for the spatial variability of the individual slopes. The low accumulation rates and the lack of abrupt millennial temperature changes challenge the use of borehole temperatures and gas isotopes for an alternative calibration of the isotope–temperature relationship (Jouzel et al., 2003). However, combining available modelling and observational evidence, Jouzel et al. (2003) suggests that the long-term (glacial–interglacial) temporal slope differs, unlike for Greenland, only by a factor of 1.1 ± 0.2 from the present-day spatial slope. However, this does not entirely exclude the possibility of different slopes between the Holocene and the LGM or other timescale-dependencies.

The calibration for different climate states of variations in stable water isotopologue data to variations in temperature is thus complicated and still a debated topic. Nevertheless, reliable estimates of the timescale-dependency of the calibration slopes are not only crucial for quantitative estimates of the mean temperature changes of major climate transitions, but also for quantitative inferences of temperature variability in general (Chap. 7), as the slope directly affects the variability of the inferred temperature time series.

2.1.3 *Measuring of the isotopic composition*

For measuring abundance ratios of stable water isotopologues, current techniques of so-called isotope ratio infrared spectroscopy (IRIS) provide comparable results in terms of precision and accuracy as classical mass spectrometry, with the advantage that related measurement devices are cheaper, smaller and portable (van Geldern and Barth, 2012). Additionally, they can measure different isotopologue species simultaneously. The principle method of IRIS is the excitation of a vaporised water sample with a tuneable infrared laser. While first-generation IRIS instruments determined the relative intensities of the isotopologue-specific spectral lines in the absorption spectrum which are proportional to the abundance ratios (Kerstel et al., 1999), present IRIS devices analyse the decay of the emitted light from the excited isotopologues after the laser beam has been switched off (Cavity Ring-Down Spectroscopy, CRDS; Gupta et al., 2009). The time constant of the decay then can also be related to the relative isotopologue abundances.

The results of the firn isotopic composition presented and analysed in Chaps. 3 and 4 have been measured using CRDS instruments. The raw measurement values have to be calibrated against the VSMOW standard. In addition, CRDS measurements suffer from two undesired effects: the memory effect and instrumental drift (van Geldern and Barth, 2012). The memory effect arises from residual amounts of vapour left over from the previous sample within the analyser cavity. Drift refers to the gradual change in measured isotopologue ratios which can occur for long machine running times even though, e.g., only one sample is analysed. Both effects can be corrected for (van Geldern and Barth, 2012). Since a large number of samples had to be analysed for the works in this thesis, instead of using the widely applied but manual and time-consuming spreadsheet calculations, a script was written for the automated calibration of the measurements together with memory and drift correction based on the procedure presented in van Geldern and Barth (2012). However, as the scope of this thesis does not lie on these technical aspects, we will not expand on this topic here. The script is available as a bundle of functions written in the language R[2] under `https://bitbucket.org/ecus/piccr`. It will be converted into an R package in due time to foster a wider use in the future.

2.2 PROCESSES WITHIN THE FIRN COLUMN

2.2.1 *The firn column of polar ice sheets*

The firn column, i.e. the first approximately 100 m of the polar ice sheets of Greenland and Antarctica, is characterised by a continuous transformation from surface snow to firn and ice, a process accompanied by recrystallisation and densification of the medium, but also by diffusive exchange processes of air and vapour through the interconnecting pore spaces. Since the ice retrieved from ice cores, or also the air enclosed, stores past climatic information but once has undergone the transformation processes in the firn column, a thorough understanding of the mentioned processes is necessary for a

---

[2] R: A Language and Environment for Statistical Computing (R Core Team, 2016).

solid interpretation of the ice-core records. In the following sections, the theoretical groundwork for such an understanding is presented, which also forms the basis for the modelling of the processes as performed in the manuscripts of this thesis.

2.2.2 *The density of firn*

The densification of polar firn is of fundamental interest as it controls, e.g., the depth at which enclosed air is sealed off from the atmosphere, and thereby determines the age difference between the air and the surrounding ice matrix (Freitag et al., 2013b). Since depth–age models are commonly based on firn- and ice-related data (e.g., annual layer counting of isotopic composition or impurities, dating of volcanic ash layers, ice-flow modelling), knowledge of the pore-close-off depth is essential to investigate the temporal relationship of ice- and gas-based climate records.

The mean densification is qualitatively characterised by three stages of hot pressure sintering depending on firn density ρ (Herron and Langway, 1980): (1) sliding of ice grains leading to grain settling and a denser packing for firn densities $\rho \leq \rho_\mathrm{c} = 550\,\mathrm{kg\,m^{-3}}$; (2) power-law creep leading to a deformation at the ice grain boundaries which reduces the pore spaces until the interconnecting channels close off at $\rho \sim 830\,\mathrm{kg\,m^{-3}}$; (3) further densification by compression of the enclosed air bubbles until the density of pure ice ($\rho_\mathrm{i} = 920\,\mathrm{kg\,m^{-3}}$) is reached.

So far no purely physical model of the densification process has been suggested. Instead, existing models are semi-empirical based on expressions for the densification rate which are fitted to observational data. One such widely used model is that by Herron and Langway (1980) which is described in the following. For this, it is convenient to define the porosity of firn by $\phi = 1 - \rho/\rho_\mathrm{i}$ which expresses the fraction of firn that is air. The basic assumption of the model is that the decrease in porosity is proportional to the normal stress from the weight of the overlying firn column,

$$\frac{\mathrm{d}\rho}{\phi(\rho)} = C\rho\,\mathrm{d}z\,, \tag{2.5}$$

where z is depth and C a constant that depends on accumulation rate and temperature at a given site as well as on the densification stage. Given constant accumulation and temperature, the vertical density profile of firn is commonly assumed to be stationary over time, $\partial_t\rho = 0$, so that $\mathrm{d}_t\rho = \left(\dot{b}/\rho\right)\mathrm{d}_z\rho$ where $\dot{b}$ is the mass accumulation rate (in $\mathrm{kg\,m^{-2}\,yr^{-1}}$). Assuming that the dependency of the constant C on accumulation rate and temperature factorises, and using observational data from Greenland and Antarctica, Herron and

Langway (1980) then showed that the densification rates of the first two densification stages can be described by

$$\frac{\mathrm{d}\rho}{\mathrm{d}t} = \begin{cases} k_0 \left(\dot{b}/\rho_\mathrm{w}\right)(\rho_\mathrm{i} - \rho) & \text{for } \rho \leq \rho_\mathrm{c}, \\ k_1 \sqrt{\dot{b}/\rho_\mathrm{w}}\,(\rho_\mathrm{i} - \rho) & \text{for } \rho_\mathrm{c} \leq \rho \leq \rho_\mathrm{max}, \end{cases} \tag{2.6}$$

where t is time, ρ_w the density of water, $\rho_\mathrm{max} = 800\,\mathrm{kg\,m^{-3}}$, and k_0 and k_1 are rate constants according to an Arrhenius equation, $k = a\exp\{-E_0/RT\}$. Here, a and E_0 are the rate factor and activation energy which depend on the densification stage but are otherwise kept constant, and R and T denote the gas constant and firn temperature. Interestingly, for the first stage, when converting the densification rate into a densification gradient, the dependency on accumulation rate drops out, yielding thus a density change with depth that is independent of accumulation.

The solution of Eq. (2.6)[3] describes suitably well the change in average density at Greenlandic and Antarctic sites (Herron and Langway, 1980). For Kohnen Station, a comparison of modelled and observed density profiles is shown in Fig. (2.1). However, the model assumes a homogeneous densification over the entire firn column and thus fails to explain the general variability of observed density profiles (Hörhold et al., 2011, and Fig. 2.1), although some variability can be introduced by stochastically varying the surface density in forward simulations of Eq. (2.6) (Freitag et al., 2013b). The obvious minimum in density variability around $600\,\mathrm{kg\,m^{-3}}$ (Fig. 2.1) observed over a wide range of climatic conditions (Hörhold et al., 2011) was suggested to arise from different rates of densification of initially high and low density layers (ibid.). Furthermore, Hörhold et al. (2012) presented evidence that impurity concentrations of the firn may have a substantial influence on the densification rate. Based on this, Freitag et al. (2013b) showed that by modifying the activation energy E_0 in Eq. (2.6) as a function of measured impurity concentrations in the firn, a strong agreement between modelled and observed density variability can be achieved. Finally, seasonal variations in firn density are also a matter of debate. Zwally and Li (2002) used temperature-dependent rate factors and activation energies, resulting in a stronger temperature dependence of the rate constants k, and showed that this can result in a seasonally varying densification. However, in fact a variety of different models for seasonal density variability has been discussed

---

[3] The solution of Eq. (2.6) for the first two densification stages is

$$\rho(z) = \rho_\mathrm{i}\frac{q(z)}{1+q(z)} \text{ where } q(z) = \begin{cases} \mathcal{R}_0 \exp\left\{\frac{\rho_\mathrm{i}}{\rho_\mathrm{w}} k_0 z\right\}, & \rho \leq \rho_\mathrm{c}, \\ \mathcal{R}_\mathrm{c} \exp\left\{\frac{\rho_\mathrm{i}}{\sqrt{\rho_\mathrm{w}\dot{b}}} k_1 (z - z_\mathrm{c})\right\}, & \rho_\mathrm{c} \leq \rho \leq \rho_\mathrm{max}, \end{cases}$$

with $\mathcal{R}_0 = \rho_0/(\rho_\mathrm{i} - \rho_0)$ where ρ_0 is the firn surface density, $\mathcal{R}_\mathrm{c} = \rho_\mathrm{c}/(\rho_\mathrm{i} - \rho_\mathrm{c})$, and $z_\mathrm{c} = (\rho_\mathrm{w}/\rho_\mathrm{i})k_0^{-1}\ln(\mathcal{R}_\mathrm{c}/\mathcal{R}_0)$.

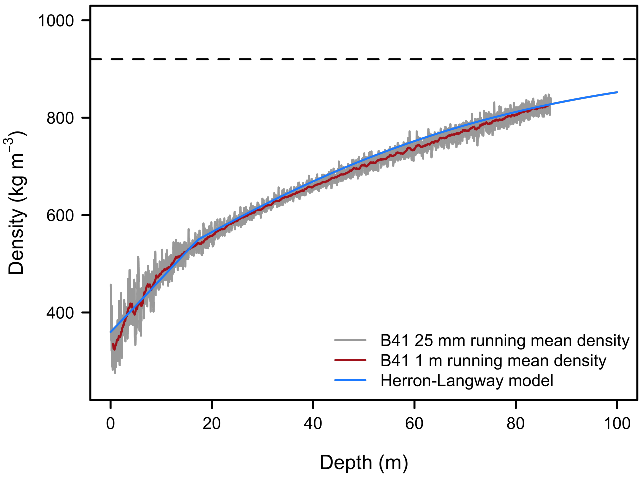

FIGURE 2.1. Observed and modelled firn density profiles at Kohnen Station. The density data as measured on the firn core B41 (Laepple et al., 2016) by high-resolution X-ray Computer Tomography (Freitag et al., 2013a) is compared to the solution according to the Herron–Langway densification model (blue) for Kohnen Station parameters (constant temperature $T = -44.5\,°\mathrm{C}$, $\rho_0 = 360\,\mathrm{kg\,m^{-3}}$, $\dot{b} = 70\,\mathrm{kg\,m^{-2}\,yr^{-1}}$). B41 density data are shown as 25 mm (grey) as well as 1 m (red) running means. The density of ice is given by the horizontal dashed line.

for different sites (Arthern et al., 2010) and the general picture of seasonal density variability is still unclear. In Appendix B, we take a different view on the vertical density layering on seasonal timescales by investigating the actual signal strength of the densification as compared to the horizontal variability arising from stratigraphic noise.

2.2.3 *The temperature profile of firn*

The temperature profile of the firn column is primarily governed by the seasonally varying solar radiation, which creates a heat flux across the boundary from the atmosphere to the top layer of the firn that thereafter diffuses downwards.

The temperature change of a firn parcel is given by the conservation of total energy. For firn, surface forces and internal sources of heat can be neglected. If we further assume that the internal energy is only a function of the firn temperature T, the balance of energy reads

$$\rho c_p(T)\frac{\mathrm{d}T}{\mathrm{d}t} = -\boldsymbol{\nabla}\cdot\mathbf{q} = \boldsymbol{\nabla}K\cdot\boldsymbol{\nabla}T + K\nabla^2 T, \tag{2.7}$$

where $c_p(T)$ is the heat capacity of ice at constant pressure, and $\mathbf{q}$ is the heat flux through the firn. In the second step, we applied Fick's law of heat diffusion, $\mathbf{q} = -K(\mathbf{r})\boldsymbol{\nabla}T$, where $K(\mathbf{r})$ is the thermal conductivity of the firn which depends on position $\mathbf{r}$ due to the dependence on density and temperature (Goujon et al., 2003).

For ice sheets, variations of K in horizontal direction are negligible, hence

$$\rho c_p(T)\left(\frac{\partial T}{\partial t}+\mathbf{v}\cdot\boldsymbol{\nabla}T\right)=K(z)\nabla^2 T+\frac{\partial K}{\partial z}\frac{\partial T}{\partial z}, \tag{2.8}$$

where $\mathbf{v}$ is the velocity of the firn parcel. For the near-surface firn also advection is negligible. Furthermore, the increase in mean density is small within the first metres (Fig. 2.1), and the dependencies of K and c_p on density and temperature are relatively weak (Goujon et al., 2003). Thus, we can treat these parameters to a first approximation as constants which leads to the simple heat transfer equation

$$\frac{\partial T}{\partial t}=\kappa\frac{\partial^2 T}{\partial z^2}, \tag{2.9}$$

where $\kappa := K/(\rho c_p)$ denotes the constant thermal diffusivity of the firn.

For the boundary conditions of a sinusoidally varying surface air temperature (e.g., driven by the seasonal cycle) and $T \to T_0 = \text{const.}$ for $z \to \infty$, Eq. (2.9) can be solved analytically (Paterson, 1994),

$$\begin{aligned} T(z,t) = T_0 &+ A_1 \exp\left(-z\sqrt{\omega/2\kappa}\right)\cos\left(\omega t+\phi_1-z\sqrt{\omega/2\kappa}\right) \\ &+ A_2\exp\left(-z\sqrt{\omega/\kappa}\right)\cos\left(2\omega t+\phi_2-z\sqrt{\omega/\kappa}\right). \end{aligned} \tag{2.10}$$

Here, ω is angular frequency, and we assumed a seasonal surface temperature profile consisting of the first two spherical harmonics of the seasonal cycle with amplitudes A_1 and A_2, and phases ϕ_1 and ϕ_2. For the conditions at Kohnen Station, the temperature of the surface layer varies by nearly 30 K throughout the year, and a constant firn temperature corresponding to the annual mean temperature of $T_0 = -44.5\,^\circ\text{C}$ is reached around a depth of 10 m (Fig. 2.2).

2.2.4 *Vapour diffusion in firn*

Molecular diffusion occurs, owing to the thermal motion of particles, naturally in fluids when spatial concentration gradients of a particular particle species are present. The diffusion process tends to reduce these gradients, eventually resulting in a dynamic equilibrium with uniform particle distribution. In firn, there is a constant exchange of molecules between the solid and the vapour phase. Molecular diffusion in the vapour phase of a certain isotopologue of water then arises for adjacent layers of the firn that exhibit a different isotopic composition and/or a different temperature. In the following, the full equation for molecular diffusion in firn is derived, which follows in principle the derivation of Whillans and Grootes (1985) but includes the firn tortuosity as in Johnsen et al. (2000) and the full dependency on the fractionation factor.

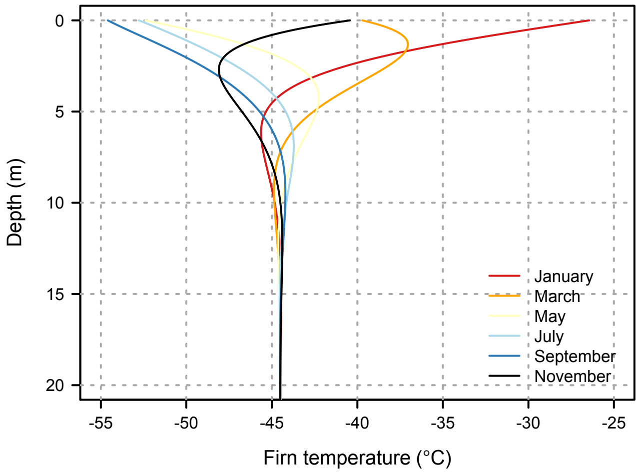

FIGURE 2.2. Modelled firn temperature profiles at Kohnen Station. The firn temperature as a function of depth was calculated for different times of the year according to Eq. (2.10) for the environmental conditions at Kohnen Station (annual mean temperature $T_0 = -44.5\,°\mathrm{C}$, first two harmonics of the seasonal cycle in surface air temperature with amplitudes $A_1 = 13.2\,°\mathrm{C}$, $A_2 = 4.9\,°\mathrm{C}$ and phases $\phi_1 = -3.2\,\mathrm{d}$, $\phi_2 = 6.0\,\mathrm{d}$ (relative to January 1)). Each line corresponds to the temperature profile at day 1 of the indicated month.

The isotopic composition, the density (Fig. 2.1) and the temperature (Fig. 2.2) of firn predominantly vary with depth. Given the common water isotopologue ($H_2{}^{16}O$) with a molar concentration in the vapour N_v^0, and a certain rare isotopologue species (e.g., $H_2{}^{18}O$) with vapour concentration N_v, the vertical diffusive flux of the rare particles is given by

$$F = -\Omega \frac{\partial N_v}{\partial z}. \tag{2.11}$$

Here, Ω is the diffusivity of vapour in firn, which is governed by the vapour diffusivity in air (Ω_a), the firn porosity and the tortuosity τ: $\Omega = \Omega_a \phi / \tau$ (Johnsen et al., 2000). The vapour diffusivity in air is a function of ambient firn temperature and atmospheric pressure and depends on the isotopologue species (Johnsen et al., 2000). The porosity incorporates the blocking effect on the diffusing vapour molecules by the solid phase; in addition, the tortuosity takes into account the shape of the connecting channels within the firn, which reduces the effective porosity (Johnsen et al., 2000). Tortuosity is typically parametrised as a function of firn density, $1/\tau = 1 - b\left(\rho/\rho_\mathrm{i}\right)^2$, with $b = 1.3$ and thus $1/\tau = 0$ for $\rho_\mathrm{co} = \rho_\mathrm{i}\Big/\sqrt{b} \sim 805\,\mathrm{kg\,m^{-3}}$ (Johnsen et al., 2000). ρ_co is hence called the effective pore-close-off density at which the diffusion process ceases. However, this parametrisation is a strong simplification of the real processes and its validity has been questioned recently (van der Wel et al., 2015a).

Given the flux F, the total concentration N in the firn (vapour and ice) of the rare isotopologue species varies with time according to

$$\frac{\mathrm{d}N}{\mathrm{d}t} = -\frac{\partial F}{\partial z} = \frac{\partial}{\partial z}\left(\Omega_a \frac{\phi}{\tau}\frac{\partial N_v}{\partial z}\right), \tag{2.12}$$

which is based on the assumption that the isotopic exchange within ice grains as well as between grains and the surrounding vapour is much faster than the molecular diffusion process in the vapour (Whillans and Grootes, 1985).

N and N_v can be expressed in terms of delta values (Eq. 2.1),

$$N = N^0 S(1+\delta) \quad \text{and} \quad N_v = N_v^0 S(1+\delta_v), \tag{2.13}$$

where N^0 and N_v^0 are the respective concentrations of the common water isotopologue. N_v^0 is given by the ideal gas law, $N_v^0 = \frac{p}{RT}$, where p is the temperature-dependent partial saturation pressure over ice (van der Wel et al., 2015a). By neglecting the small contributions from the rare isotopologues and the vapour, N^0 can be expressed by the mass concentration of the ice, $N^0 \approx \rho/m$, where m is the molar weight of water. Finally, using $1+\delta_v = (1+\delta)/\alpha$ (Eq. 2.2), Eq. (2.12) becomes

$$\begin{aligned}\frac{\mathrm{d}}{\mathrm{d}t}\left(\frac{\rho}{m}(1+\delta)\right) &= \frac{1+\delta}{m}\frac{\mathrm{d}\rho}{\mathrm{d}t} + \frac{\rho}{m}\frac{\mathrm{d}\delta}{\mathrm{d}t} \\ &= \frac{\partial}{\partial z}\left(\frac{\Omega_a\phi}{\tau}\frac{\partial}{\partial z}\left(\frac{p}{RT}\frac{1+\delta}{\alpha}\right)\right).\end{aligned} \tag{2.14}$$

This is the full equation for molecular diffusion of water isotopologues in firn which also includes the temporal evolution of the firn density as a result of the diffusion process (Whillans and Grootes, 1985). In many works on firn diffusion, a much simplified equation is applied, however, often without stating the limitations of this simpler form. For that reason, in the following we perform a scaling analysis of Eq. (2.14) for the upper firn column, where both density and temperature gradients are present, in order to identify the leading-order terms.

We define the typical length scale over which the diffusion process takes place as $\mathrm{L} \sim 10^{-2}\,\mathrm{m}$. Typical firn densities in the upper firn column are of the order of $\mathcal{O}(\rho) \sim 10^2\,\mathrm{kg\,m^{-3}}$ (Fig. 2.1), the ice density of $\mathcal{O}(\rho_\mathrm{i}) \sim 10^3\,\mathrm{kg\,m^{-3}}$. Densification from the top to the bottom of the firn column corresponds to a typical increase in density by $\sim 600\,\mathrm{kg\,m^{-3}}$ over a scale of $\sim 100\,\mathrm{m}$ (Fig. 2.1). The average density gradient is thus $\mathcal{O}(\partial_z \rho) \sim 10\,\mathrm{kg\,m^{-4}}$. Firn temperatures are typically $\mathcal{O}(T) \sim 10^2\,\mathrm{K}$ with constant temperatures below $\sim 10\,\mathrm{m}$ depth and typical gradients of $\mathcal{O}(\partial_z T) \sim 1$–$10\,\mathrm{K\,m^{-1}}$ above (Fig. 2.2). Finally, gradients in isotopic composition are $\mathcal{O}(\partial_z \delta) \sim 10^{-3}\mathrm{L}^{-1} = 10^{-1}\,\mathrm{m^{-1}}$.

The right-hand side of Eq. (2.14) can be split as follows,

$$R^{-1}\left(\frac{\partial \Omega_a}{\partial z} + \Omega_a\frac{\partial}{\partial z}\right)\left\{\frac{\phi}{\tau}\frac{\partial}{\partial z}\left(\frac{p}{\alpha}\frac{1+\delta}{T}\right)\right\}.$$

Inspecting the terms in the left-hand brackets, we find that the term involving the depth derivative of the diffusivity is negligible[4]. Applying the remaining derivative with respect to the right-hand term yields

$$\left\{ -\frac{2b\rho}{\rho_\mathrm{i}^2}\left(1-\frac{\rho}{\rho_\mathrm{i}}\right)\frac{\partial\rho}{\partial z} - \frac{1}{\tau}\frac{1}{\rho_\mathrm{i}}\frac{\partial\rho}{\partial z} + \frac{1}{\tau}\left(1-\frac{\rho}{\rho_\mathrm{i}}\right)\frac{\partial}{\partial z} \right\} \frac{\partial}{\partial z}\left(\frac{p}{\alpha}\frac{1+\delta}{T}\right)$$

with scaling of the terms in the left-hand brackets of

$$\mathcal{O}\left(\frac{2b\rho}{\rho_\mathrm{i}^2}\left(1-\frac{\rho}{\rho_\mathrm{i}}\right)\frac{\partial\rho}{\partial z}\right) \sim 10^{-3}\,\mathrm{m}^{-1} < \mathcal{O}\left(\frac{1}{\tau\rho_\mathrm{i}}\frac{\partial\rho}{\partial z}\right) \sim 10^{-2}\,\mathrm{m}^{-1}$$

$$\ll \mathcal{O}\left(\frac{1}{\tau}\left(1-\frac{\rho}{\rho_\mathrm{i}}\right)\frac{\partial}{\partial z}\right) \sim \mathrm{L}^{-1} = 10^{2}\,\mathrm{m}^{-1}.$$

The derivative with respect to depth of $\frac{p}{\alpha}\frac{1+\delta}{T}$ is

$$\left(\frac{1}{\alpha}\frac{\partial p}{\partial z} + p\frac{\partial\alpha^{-1}}{\partial z} + \frac{p}{\alpha}\frac{\partial}{\partial z}\right)\frac{1+\delta}{T},$$

where the first two terms in the brackets are much smaller than the third term[5]. Hence, we are left with analysing the derivatives of $\frac{1+\delta}{T}$. The first derivative of the term has a scaling of

$$\mathcal{O}\left((1+\delta)\frac{1}{T^2}\frac{\partial T}{\partial z}\right) \lesssim 10^{-3}\,\mathrm{K}^{-1}\,\mathrm{m}^{-1} \sim \mathcal{O}\left(\frac{1}{T}\frac{\partial\delta}{\partial z}\right) \sim 10^{-3}\,\mathrm{K}^{-1}\,\mathrm{m}^{-1}.$$

The second derivative of the leading term $\frac{1}{T}\partial_z\delta$ scales as

$$\mathcal{O}\left(\frac{1}{T^2}\frac{\partial T}{\partial z}\frac{\partial\delta}{\partial z}\right) \lesssim 10^{-4}\,\mathrm{K}^{-1}\,\mathrm{m}^{-2} \ll \mathcal{O}\left(\frac{1}{T}\frac{\partial^2\delta}{\partial z^2}\right) \sim 10^{-1}\,\mathrm{K}^{-1}\,\mathrm{m}^{-2}.$$

The leading-order term of the right-hand side of Eq. (2.14) therefore is $1/T\,\partial_z^2\delta$.

The evolution of the firn density as a result of the diffusion process is given by the evolution of the total molar concentration of the firn,

---

[4] The vapour diffusivity in air depends on temperature T and air pressure P as $\Omega_a = a\,(T/T_0)^b\,(P/P_0)$, where $T_0 = 273.15\,\mathrm{K}$, $P_0 = 1\,\mathrm{atm}$, and $\mathcal{O}(b) \sim 1$ (Johnsen et al., 2000). Thus, $\mathcal{O}(\partial_z\Omega_a) = \mathcal{O}(b\Omega_a/T\,\partial_z T) \lesssim 10^{-1}\,\mathrm{m}^{-1}\mathcal{O}(\Omega_a) \ll \mathcal{O}(\Omega_a\partial_z) \sim \Omega_a/L = 10^2\,\mathrm{m}^{-1}\mathcal{O}(\Omega_a)$.

[5] The partial saturation vapour pressure over ice has a temperature dependence of $p = \exp(c_0 - c_1/T + c_2\ln(T) - c_3 T)$ with $\mathcal{O}(c_1) \sim 10^4$, $\mathcal{O}(c_2) \sim 10^0$ and $\mathcal{O}(c_3) \sim 10^{-2}$ (van der Wel et al., 2015a). The derivative with respect to z is $\partial_z p = p\,(c_1/T^2 + c_2/T - c_3)\,\partial_z T$. Therefore, $\mathcal{O}(1/\alpha\,\partial_z p) \sim \xi_1\mathcal{O}(p/\alpha)$ with $\mathcal{O}(\xi_1) \lesssim 10^1$.
The fractionation factor depends on temperature as $\alpha = a_1\exp(b_1/T)$ for δ^{18}O, and as $\alpha = a_2\exp(b_2/T^2)$ for δD, with $\mathcal{O}(b_1) \sim 10^1$ and $\mathcal{O}(b_1) \sim 10^4$ (Yoshimura, 2015). Hence, $p\partial_z\alpha^{-1} = -\,p/\alpha^2\,\partial_T\alpha\partial zT$, which scales as $\sim \xi_2\mathcal{O}(p/\alpha)$ with $\mathcal{O}(\xi_2) \lesssim 10^{-2}$ for δ^{18}O and $\mathcal{O}(\xi_2) \lesssim 10^{-1}$ for δD.
Both contributions are hence small compared to $\mathcal{O}(p/\alpha\,\partial_z) \sim \xi_3\mathcal{O}(p/\alpha)$ with $\mathcal{O}(\xi_3) \sim 10^2$.

N^0, similar to Eq. (2.12), but including all isotopologue species i; thus

$$\frac{\mathrm{d}N^0}{\mathrm{d}t} = \frac{\partial}{\partial z}\left(\frac{\Omega_a \phi}{\tau}\frac{\partial}{\partial z}\sum_i N_{v,i}\right). \tag{2.15}$$

By noting that $\sum_i N_{v,i} \approx N_v^0$ we find

$$\frac{\mathrm{d}\rho}{\mathrm{d}t} = \frac{m}{R}\frac{\partial}{\partial z}\left(\frac{\Omega_a \phi}{\tau}\frac{\partial}{\partial z}\right)\left(\frac{p}{T}\right). \tag{2.16}$$

Performing a similar scaling analysis of the right-hand side of this equation as carried out above shows that the terms in Eq. (2.16) are all smaller in magnitude than the leading-order term of the right-hand side of Eq. (2.14).

Finally, we express $\mathrm{d}\delta/\mathrm{d}t$ with $\dot{z}\partial_z\delta + \partial_t\delta$, and the vertical velocity $\dot{z}$ with the vertical strain rate in the firn, $\dot{\varepsilon} = \frac{1}{z}\partial_t z$. Keeping only the leading-order term, Eq. (2.14) indeed simplifies to the well-known form

$$\frac{\partial\delta}{\partial t} = \underbrace{\frac{mp\Omega_a}{RT\alpha\tau}\left(\frac{1}{\rho} - \frac{1}{\rho_\mathrm{i}}\right)}_{=:D}\frac{\partial^2\delta}{\partial z^2} - z\dot{\varepsilon}\frac{\partial\delta}{\partial z}, \tag{2.17}$$

where we introduced the effective isotopic diffusivity D.

The scaling analysis shows that gradients in isotopic composition of the ice matrix are indeed the dominating driver of the diffusion process, even in the upper firn column. However, some terms that involve temperature gradients are roughly only one order of magnitude smaller than the related terms in isotopic gradients and might dominate in regions, where they are significantly higher than the average value assumed here.

The solution to Eq. (2.17) can be obtained using Fourier transforms and is the convolution of the original isotope profile $\delta(z, t = 0)$, after correction for the vertical compression due to densification, and a Gaussian,

$$\delta(z,t) = \frac{1}{\sqrt{2\pi\sigma^2}}\int_{-\infty}^{\infty}\delta(z', t = 0)\exp\left\{\frac{(z - z')^2}{2\sigma^2}\right\}\mathrm{d}z'. \tag{2.18}$$

Here, σ is the diffusion length which is given by the differential equation (Johnsen et al., 2000)

$$\frac{\mathrm{d}\sigma^2}{\mathrm{d}t} - 2\dot{\varepsilon}\sigma^2 = 2D, \tag{2.19}$$

and thus depends on ambient firn density, temperature, vapour and atmospheric pressure as well as the isotopologue species. For constant temperature and a Herron–Langway density profile (Eq. 2.6), Eq. (2.19) has an analytical solution (van der Wel, 2012). Alternatively, the equation can be solved numerically which is performed as the basis of the firn diffusion calculations in Chaps. 4 and 5. In the latter work, we assume seasonally varying firn temperatures (such as shown in Fig. 2.2) and calculate the average over individual diffusion lengths of firn parcel trajectories that experience different firn temperature profiles over the year.

Qualitatively, Eq. (2.18) describes a smoothing of the initial isotope profile, as expected for a diffusive process, that erases any initial high-frequency variations in the isotopic composition. This can be seen by taking the absolute square of the Fourier transform of the equation, which yields the power spectral density (PSD)

$$\mathcal{P}(k) = \mathcal{P}_0(k) \exp\{-k^2\sigma^2\}, \tag{2.20}$$

where k denotes wavenumber and $\mathcal{P}_0(k)$ the PSD of the initial isotope profile. For small k (long wavelengths or timescales), the spectrum $\mathcal{P}(k) \sim \mathcal{P}_0(k)$, for large k (short wavelengths or timescales) $\mathcal{P}(k)$ has a strongly "red" character with quadratically decreasing PSD for increasing k on a double logarithmic plot. At the point $k = 1/\sigma$ the PSD has dropped to $1/e$. Hence, an accurate modelling of the diffusion length is important for the interpretation of the power spectra of isotope variations measured on firn and ice cores (Chaps. 5 and 6).

2.3 MODELS OF INTERNAL CLIMATE VARIABILITY

The climate varies on all timescales – covering periods corresponding to subannual and interannual variations up to orbital and tectonic scales, thus from months to millions of years –, which makes it a striking feature of the climate system. Here, a brief overview of observed natural climate variability is given together with simple theoretical models that attempt to describe this variability. This serves as background information for the topics discussed in Chaps. 6 and 7.

The variability of a climate record $X(t)$ is conveniently described by its PSD $\mathcal{P}(f)$, where f denotes frequency. This provides a timescale-dependent picture of the variability since the integral over the PSD for frequencies from f_1 to f_2 gives the variance that is contained in this frequency band,

$$\operatorname{var}(X)(f_1, f_2) = 2\int_{f_1}^{f_2} \mathcal{P}(f)\,\mathrm{d}f. \tag{2.21}$$

Consequently, the total integral for frequencies from $f_1 = f_{\mathrm{R}}$ to $f_2 = f_{\mathrm{Nyq}}$ yields the full variance of the record. Here, f_{R} is the lowest possible frequency for the given length of the record (sometimes called the Rayleigh frequency) and f_{Nyq} the Nyquist frequency, i.e. the highest frequency that can be resolved at the temporal resolution of the record.

Observed climate power spectra, for example of surface or sea surface temperatures, typically show a continuous spectrum of background variability, which increases as a function of timescale, with more or less distinct peaks superposed on it (e.g., Shackleton and Imbrie, 1990; Pelletier, 1998; Huybers and Curry, 2006; Laepple and Huybers, 2014). Climate variations can be classified into internal and external variations, where the former are produced by the climate system itself while the latter are driven by an external forcing. The peaks in observed climate spectra can be attributed to external forcings – e.g., the annual cycle or the orbital cycles of glacial–interglacial changes –, but can also be due to internal interactions within the climate system for constant external forcing (Latif, 2009). By contrast, the broad background spectrum, which constitutes the largest part of the total variability (Wunsch, 2003), is thought to arise from internal processes, either within individual components or through interactions between different components of the climate system. The typically observed increase in power of the background spectrum as a function of timescale is often described in form of a power law with slope β, $\mathcal{P}(f) \propto f^{-\beta}$.

A first qualitative description of the background spectrum can be obtained from the stochastic climate model by Hasselmann (1976) which treats the interaction of two climate components with different response timescales, such as atmosphere and ocean. The basic idea is that the slow component (the ocean, but possible are also sea ice, the ice sheets or the biosphere) shows a damped response to the sum of many statistically independent single influences from the atmosphere. The evolution of the ocean response then follows the following linear stochastic differential equation,

$$\frac{\mathrm{d}T}{\mathrm{d}t} = -\frac{T(t)}{\tau} + F(t). \tag{2.22}$$

Here, T is the ocean response, for example the sea surface temperature, τ the time constant of the damping, and F the stochastic atmospheric forcing. By taking the Fourier transform of this equation, one can easily derive the corresponding PSD of the ocean response,

$$\left|\hat{T}(\omega)\right|^2 = \frac{\left|\hat{F}(\omega)\right|^2}{\tau^{-2} + \omega^2}, \tag{2.23}$$

where ω is angular frequency and hatted quantities denote the respective Fourier transforms of the variables in (2.22). Assuming a white noise atmospheric forcing, the spectrum (2.23) has qualitatively many similarities with observed climate spectra (Fig. 2.3). In the high-frequency range, $\omega \gg 1/\tau$, the spectrum is red and shows a constant increase in PSD with increasing timescale with a slope of $\beta = 2$. For $\omega \ll 1/\tau$, the spectrum is white at a level equal to the atmospheric forcing scaled by the damping constant. This can be interpreted in the sense that the slow component reacts selectively with regard to timescales: while the ocean damps the temporal fluctuations of the atmosphere (air temperature, wind, pressure) on short scales, it exhibits

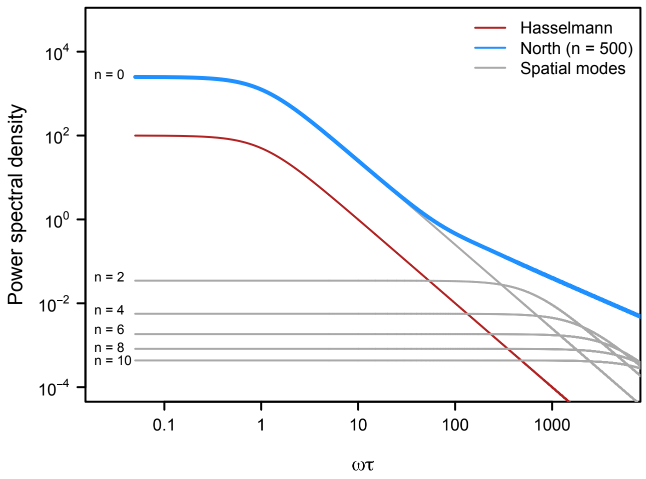

FIGURE 2.3. Power spectral densities according to theoretical models for the internal variability of the climate system. Shown are a Hasselmann spectrum (red) and the local North spectrum as the sum over the first 500 spatial modes (blue) for a horizontal diffusion length of $\lambda = 10$. Additionally, grey lines depict the individual spatial modes in the North model for $n = 0, 2, 4,$ $6, 8$ and 10. The Hasselmann spectrum and the individual spatial modes in the North model show a constant power-law scaling of $\beta = 2$ on short timescales ($\omega\tau > 1$), while the local North spectrum exhibits a slope of $\beta = 1$ for $\omega\tau \gg 1$.

a memory effect by integrating the fluctuations into the system and thereby generating amplified variations on long timescales. One example for a nearly white atmospheric forcing on seasonal to decadal timescales is the North Atlantic Oscillation (NAO) (Latif, 2009).

The Hasselmann model (2.22) is in principle a zero order model since it contains no spatial dimensions. Adding a horizontal diffusion term to Eq. (2.22), $-(\lambda^2/\tau)\nabla^2 T$, where ∇^2 only acts on horizontal coordinates and λ is the horizontal diffusion length (North et al., 2011), yields a spectrum that depends on the horizontal spectral modes n of the temperature variations (Rypdal et al., 2015),

$$\left|\hat{T}(\omega)\right|^2 = \frac{\left|\hat{F}(\omega)\right|^2}{4\pi} \sum_{n=0}^{\infty} \frac{2n+1}{\omega^2 + \tau^{-2}\left[\lambda^2 n(n+1)+1\right]^2}. \tag{2.24}$$

Obviously, the mode $n = 0$ that corresponds to the global average of T is identical to the Hasselmann spectrum (2.23). Thus, the latter can be interpreted as the spectrum of the global average of the temperature response whereas the sum over all spatial modes n in Eq. (2.24) represents the global average of the local temperature spectrum. Interestingly, each mode n is a red noise spectrum with slope $\beta = 2$, similar to the spectrum of the global average, but with different effective damping times that get smaller with increasing n (Fig. 2.3). This can be understood by noting that smaller spatial scales are associated with stronger gradients which thus exhibit a stronger diffusion leading to a faster damping. The average local spectrum, by contrast, exhibits a slope of 1 towards the high-frequency end (Fig. 2.3). This is an important finding since observed climate spectra are derived from proxy data that typically represent a more local view on the variability instead of a global one.

Indeed, observed climate spectra typically show a power-law behaviour with slopes between 1 and 2 (Shackleton and Imbrie, 1990; Ditlevsen et al., 1996; Pelletier, 1998; Wunsch, 2003; Huybers and Curry, 2006). This could be interpreted in the sense that proxy time series record climate variations in between the very localised and a, to some extent, spatially integrated view. However, the determined slopes are dependent on the estimation techniques (Rypdal et al., 2015), and for single proxy records also dependent on the amount of non-climatic noise contained in the records (Laepple and Huybers, 2013; and Chap. 6). Furthermore, the Hasselmann model has been originally applied to the ocean mixed layer for which typical time constants, τ, have been inferred that are of the order of a few years (Frankignoul and Hasselmann, 1977). Such magnitudes cannot explain the observed increasing spectral power of many temperature records on much longer timescales (e.g., Huybers and Curry, 2006).

Another point of interest is the general scaling behaviour of climate spectra. Lovejoy et al. (2013) classify the climate variations in three regimes characterised by distinct power-law slopes. However, if this characterisation is indeed a true property of the climate system is still a matter of debate (T. Laepple, personal communication, 2017), and its discussion goes beyond the scope of the discourse presented here.

3

REGIONAL CLIMATE SIGNAL VS. LOCAL NOISE: A TWO-DIMENSIONAL VIEW OF WATER ISOTOPES IN ANTARCTIC FIRN AT KOHNEN STATION, DRONNING MAUD LAND

Thomas Münch[1,2], Sepp Kipfstuhl[3], Johannes Freitag[3],
Hanno Meyer[1], and Thomas Laepple[1]

[1] *Alfred Wegener Institute Helmholtz Centre for Polar and Marine Research, Telegrafenberg A43, 14473 Potsdam, Germany*
[2] *Institute of Physics and Astronomy, University of Potsdam, Karl-Liebknecht-Str. 24/25, 14476 Potsdam, Germany*
[3] *Alfred Wegener Institute Helmholtz Centre for Polar and Marine Research, Am Alten Hafen 26, 27568 Bremerhaven, Germany*

This chapter is published in:
Climate of the Past, **12** (7), 1565–1581, DOI: `10.5194/cp-12-1565-2016`, 2016.

ABSTRACT. In low-accumulation regions, the reliability of δ^{18}O-derived temperature signals from ice cores within the Holocene is unclear, primarily due to the small climate changes relative to the intrinsic noise of the isotopic signal. In order to learn about the representativity of single ice cores and to optimise future ice-core-based climate reconstructions, we studied the stable-water isotope composition of firn at Kohnen Station, Dronning Maud Land, Antarctica. Analysing δ^{18}O in two 50 m long snow trenches allowed us to create an unprecedented, two-dimensional image characterising the isotopic variations from the centimetre to the 100-metre scale. Our results show seasonal layering of the isotopic composition but also high horizontal isotopic variability caused by local stratigraphic noise. Based on the horizontal and vertical structure of the isotopic variations, we derive a statistical noise model which successfully explains the trench data. The model further allows one to determine an upper bound for the reliability of climate reconstructions conducted in our study region at seasonal to annual resolution, depending on the number and the spacing of the cores taken.

3.1 INTRODUCTION

Ice cores obtained from continental ice sheets and glaciers are a key climate archive. They store information on past changes in temperature in the form of stable water isotopes (EPICA community members, 2006), in greenhouse gas concentrations via trapped air (Raynaud et al., 1993) and in many other parameters such as accumulation rates (e.g., Mosley-Thompson et al., 2001) or aerosols (e.g., Legrand and

Mayewski, 1997). Analysis of the isotope ratios recorded in single deep ice cores provided milestones in the palaeoclimate research, including the investigation of glacial–interglacial climate changes (Petit et al., 1999) and the existence of rapid climate variations within glacial periods (Dansgaard et al., 1993).

In contrast to the coherent view established from polar ice cores for millennial and longer timescales, the reliability of single ice cores as archives of the Holocene climate evolution is less clear (Kobashi et al., 2011). The small amplitude of changes and the aim to reconstruct climate parameters at high temporal resolution poses a challenge to the interpretation of ice-core signals. This is especially true for low-accumulation sites, defined here for accumulation rates below 100 mm w.e. yr^{-1}, which holds for large parts of the Antarctic Plateau[1]. There, the non-climate noise – that part of the isotopic record which cannot be interpreted in terms of temperature variations on regional or larger scales, hence including any meteorological, pre- and post-depositional effects that additionally influence the isotopic composition – may often be too high to accurately extract a climatic temperature signal (Fisher et al., 1985). Despite the challenges, quantifying the Holocene polar climate variability is the key foundation to determine the range of possible future climate changes (e.g., Huntingford et al., 2013, and references therein) as well as to test the ability of climate models in simulating natural climate variability (Laepple and Huybers, 2014).

The quantitative estimation of climate variability from proxy data therefore requires an understanding of the non-climate noise in order to separate it from the climate signal (e.g., Laepple and Huybers, 2013). Several mechanisms influence the isotopic composition of snow prior to and after its deposition onto the ice sheet. On larger spatial scales, non-climate variability may be introduced by different moisture pathways and source regions (e.g., Jones et al., 2014) as well as spatial and temporal precipitation intermittency (Persson et al., 2011; Sime et al., 2009, 2011; Laepple et al., 2011). Irregular deposition caused by wind and surface roughness along with spatial redistribution and erosion of snow is a major contribution to non-climate variance on smaller spatial scales ("stratigraphic noise", Fisher et al., 1985). Wind scouring can additionally remove entire seasons from the isotopic record (Fisher et al., 1983). Vapour exchange with the atmosphere by sublimation–condensation processes (Steen-Larsen et al., 2014) can influence the isotopic composition of the surface layers; diffusion of vapour into or out of the firn driven by forced ventilation (Waddington et al., 2002; Neumann and Waddington, 2004; Town et al., 2008) may represent an additional component of post-depositional

---

[1] Compared to the original publication, the terminology has been changed here and throughout the chapter from "East Antarctic Plateau" to "Antarctic Plateau" for consistency throughout the thesis.

change. Finally, diffusion of water vapour through the porous firn smoothes isotopic variations from seasonal to interannual⋆ or longer timescales, depending on the accumulation rate (Johnsen, 1977; Whillans and Grootes, 1985; Cuffey and Steig, 1998; Johnsen et al., 2000).

In the last two decades, a number of studies analysed the representativity of single ice cores in recording submillennial⋆ climate changes. One well-studied region is the low-accumulation ($\sim$ 40–90 mm w.e. yr^{-1}, Oerter et al., 2000) Dronning Maud Land (DML) on the Antarctic Plateau. Here, Graf et al. (2002) found low signal-to-noise variance ratios (F) in 200-year-long firn-core records for oxygen isotopes ($F = 0.14$) and accumulation rates ($F = 0.04$), implying that the climate signal content of a single core is much smaller than the noise level (14 and 4 %, respectively). On a similar timescale, Karlöf et al. (2006) detected no relationship in electrical properties apart from volcanic imprints between firn cores. Similarly, high-resolution records of chemical trace species from three shallow ice cores (Sommer et al., 2000a,b) showed a lack of intersite⋆ correlation on decadal timescales. These results were supported by process studies comparing observed and simulated snow-pit isotope data (Helsen et al., 2006). Whereas the model–data comparison was successful for coastal high-accumulation regions of DML (400 mm w.e. yr^{-1}), it largely failed on the dryer Antarctic Plateau (70 mm w.e. yr^{-1}). This dependency between accumulation rate and signal-to-noise ratio was further demonstrated in studies across the Antarctic continent (Hoshina et al., 2014; Jones et al., 2014; McMorrow et al., 2002). From high-accumulation (140–520 mm w.e. yr^{-1}) Greenland ice cores, Fisher et al. (1985) estimated signal-to-noise ratios clearly larger than 1.

Despite this large body of literature, quantitative information about the signal-to-noise ratios and the noise itself is mainly limited to correlation statistics of nearby cores. While a relatively good understanding of stratigraphic noise exists in Arctic records (Fisher et al., 1985), this does not apply to low-accumulation regions of Antarctica where the accumulated snow is considerably reworked in and between storms (Fisher et al., 1985).

Here, we provide a direct visualisation and analysis of the signal and noise in an East Antarctic low-accumulation region (64 mm w.e. yr^{-1}) by an extensive two-dimensional sampling of the firn column in two 50 m long snow trenches. Our approach, for the first time, offers a detailed quantitative analysis of the spatial structure of isotope variability on a centimetre to 100-metre scale. This is a first step towards a signal and noise model to enable quantitative reconstructions of the climate signal and their uncertainties from ice cores.

3.2 DATA AND METHODS

Near Kohnen Station in the interior of Dronning Maud Land, close to the EPICA deep ice core drilling site (EDML, $-75.0°$ S, $0.1°$ E; altitude 2892 m a.s.l.; mean annual temperature -44.5 °C; mean annual accumulation rate 64 mm w.e. yr^{-1}; EPICA community members, 2006), two 1.2 m deep and approximately 45 m long trenches in the firn, named T1 and T2, were excavated during the austral-summer field season 2012/2013 using a snow blower. Each trench was aligned perpendicularly to the local snow-dune direction. The horizontal distance between the starting points of T1 and T2 was 415 m.

An absolute height reference was established using bamboo poles by adjusting their heights above ground with a spirit level. A control measurement with a laser level yielded in each snow trench a vertical accuracy better than 2 cm. No absolute height reference between the two trenches could be established, but, based on a stacked laser level measurement, the vertical difference between the trenches was estimated to be less than 20 cm.

Both trenches were sampled for stable-water-isotope analysis with a vertical resolution of 3 cm. In T1, 38 profiles were taken at variable horizontal spacings between 0.1 and ~ 2.5 m. In T2, due to time constraints during the field campaign, only four profiles at positions of 0.3, 10, 30 and 40 m from the trench starting point were realised. The sampling of each trench was completed within 24 h. All firn samples ($N = 1507$) were stored in plastic bags and transported to Germany in frozen state. Stable isotope ratios were analysed using cavity ring-down spectrometers (L2120i and L2130i, Picarro Inc.) in the isotope laboratories of the Alfred Wegener Institute (AWI) in Potsdam and Bremerhaven. The isotope ratios are reported in the usual delta notation in per mil (‰) as

$$\delta = \left(\frac{R_{\text{sample}}}{R_{\text{reference}}} - 1 \right) \times 10^3, \tag{3.1}$$

where R_{sample} is the isotopic ratio of the sample ($^{18}\mathrm{O}/^{16}\mathrm{O}$) and $R_{\text{reference}}$ that of a reference. The isotopic ratios are calibrated with a linear three-point regression analysis using in-house standards at the beginning of each measurement sequence, where each standard has been calibrated to the international VSMOW*/SLAP scale. Additionally, a linear drift-correction scheme and a memory-correction scheme (adapted from van Geldern and Barth, 2012) is applied, using three repeated measurements per sample. The analytical precision of the calibrated and corrected δ^{18}O measurements is assessed by evaluating standards in the middle of each measurement sequence. This yields a mean combined measurement uncertainty of 0.09 ‰ (RMSD). The δ^{18}O trench data are archived under DOI: `10.1594/PANGAEA.861675` (Münch et al., 2016a).

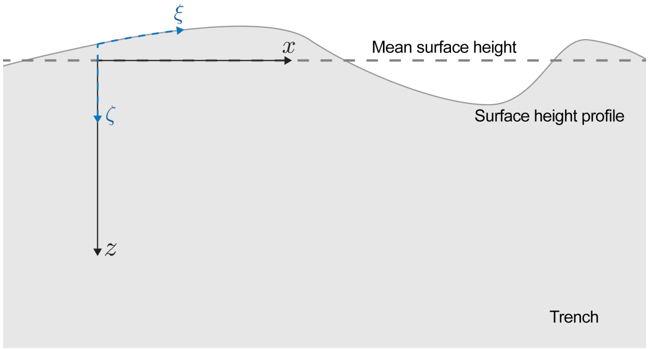

FIGURE 3.1. Coordinate systems used for the analysis of the trench isotope data: (1) a curvilinear coordinate system (ξ, ζ) (blue dashed lines, surface coordinates) with horizontal axis along the surface height profile and vertical axis denoting the depth below the local surface; (2) a Cartesian system (x, z) (black lines, absolute coordinates) defined by the mean surface height.

For the analysis of the measurements, we set up two coordinate systems for each trench (Fig. 3.1). Surface coordinates refer to a local, curvilinear system with the horizontal axis along the surface height profile and the vertical axis denoting the firn depth below the local surface. Absolute coordinates adopt the mean surface height as a reference for a straight horizontal axis, completed by an absolute depth scale.

3.3 RESULTS

3.3.1 *Trench isotope records*

The firn samples obtained from trench T1 provide a two-dimensional image of the δ^{18}O structure of the upper $\sim$ 1 m of firn on a horizontal scale of $\sim$ 50 m (Fig. 3.2a).

The surface height profile of the trench reflects the typical snow topography of the sampling region characterised by small-scale dunes with their main ridges elongated parallel to the mean wind direction (Birnbaum et al., 2010). Trench T1 features one prominent dune located between 25 and 40 m, accompanied by a dune valley between 8 and 18 m, and some smaller-scale height variations. The peak-to-peak amplitude of the large dune undulation is $\sim$ 10 cm; the entire height variations exhibit a standard deviation (SD) of 2.9 cm.

Overall, the trench δ^{18}O record shows a diverse picture. The delta values in T1 (Fig. 3.2a) span a range from -54 to -34 ‰ with a mean of -44.4 ‰ (SD 3.1 ‰). A similar range of -50 to -38 ‰ is observed in T2 (Fig. 3.3) with a mean of -44.0 ‰ (SD 2.7 ‰). We can identify 8 to 10 alternating layers of enriched and depleted isotopic composition in the T1 record. The uppermost layer (first 6 cm relative to the surface) essentially shows enriched (mean of -42.7 ‰) but also

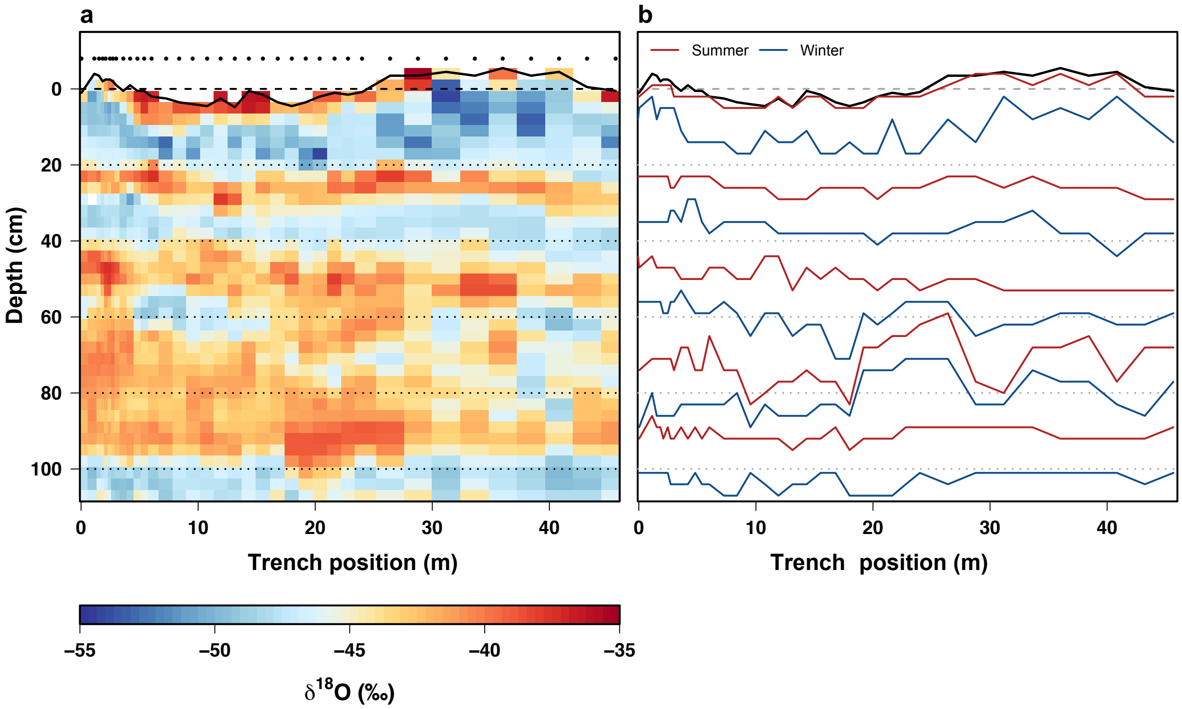

FIGURE 3.2. (**a**) The two-dimensional δ^{18}O data set of trench T1 displayed on absolute coordinates. The solid black line shows the surface height profile, the long-dashed black line the mean surface height. Sampling positions are marked by the black dots above. White gaps indicate missing data. (**b**) The stratigraphy of trench T1 expressed as the seasonal layer profiles tracking the local δ^{18}O extrema as explained in the text.

strongly variable δ^{18}O values between -54 and -34 ‰ (SD 4.4 ‰), thus already covering the range of the entire trench record. Stronger enrichment tends to be found in the valleys; however, the limited data do not allow one to conclude whether this is a general feature. In an absolute depth of 5–20 cm, a band of generally more depleted δ^{18}O values is found exhibiting less horizontal variability compared to the first layer with a range of -54 to -45 ‰ (mean -48.5 ‰, SD 1.9 ‰). The layering appears strongly perturbed in the depth of $\sim$ 60–100 cm for profile positions < 30 m. Here, a broad and diffuse region of rather constant δ^{18}O values around -40 ‰ is observed, together with a prominent, 20 cm thick feature of high delta values between 18 and 28 m.

The four δ^{18}O profiles obtained from trench T2 (Fig. 3.3) show similar features as trench T1. We can identify roughly five cycles in each profile. However, the profiles diverge considerably at depths of 50–90 cm, which coincides with the region of strong perturbations identified in T1.

To further analyse the isotopic layering, we determine the pronounced local maxima and minima of each T1 δ^{18}O profile and visually assign summer and winter to the depths of these extrema. This results in consecutive horizontal curves tracing the vertical positions of seasonal extrema along the trench (seasonal layer profiles, Fig. 3.2b). Assuming that respective isotopic extrema occur at the same point in time (summer/winter), the seasonal layer profiles reflect the surface height profile for a given season. However, considering the highly variable isotopic composition observed at the current trench surface (Fig. 3.2a), this is a rough approximation and the seasonal layer profiles will likely overestimate the past surface height profiles. Nevertheless, the vertical undulations of the layer profiles show peak-to-peak amplitudes of 6–24 cm (average SD 3.7 cm), comparable to the present surface undulations, and the layers are vertically separated by approximately 20 cm, in accord with the local mean annual accumulation rate of snow ($64\,\mathrm{mm\,w.e.\,yr^{-1}}$) and the mean firn density measured in trench T1 ($\rho_{\mathrm{firn}} = 340\,\mathrm{kg\,m^{-3}}$). To study the similarity between the seasonal layer profiles and the present surface height profile, we calculate the standard deviation of their height differences ($\mathrm{SD}_{\mathrm{surface}}$, hence, the SD of each layer profile on surface coordinates). This is compared to the standard deviation of the layer profiles on absolute coordinates ($\mathrm{SD}_{\mathrm{horiz}}$). We find that the first layer profile closely follows the present surface ($\mathrm{SD}_{\mathrm{horiz}} - \mathrm{SD}_{\mathrm{surface}} = 1.8\,\mathrm{cm}$). For the second layer profile, the link with the surface is weaker ($\mathrm{SD}_{\mathrm{horiz}} - \mathrm{SD}_{\mathrm{surface}} = 1.5\,\mathrm{cm}$), and the layer profiles below 20 cm are on average horizontally aligned ($\mathrm{SD}_{\mathrm{horiz}} - \mathrm{SD}_{\mathrm{surface}} = -0.6\,\mathrm{cm}$). This can be explained by an annual reorganisation of the stratigraphy so that aligning the isotopic variations on absolute coordinates is on average more appropriate than the alignment according to a specific surface height profile. The positive autocorrelation with a decorrelation length of $\sim 6\,\mathrm{cm}$ that is found from the vertical T1 δ^{18}O variations after subtraction of the mean trench profile is consistent with this hypothesis.

Due to the on average horizontal stratigraphy of the isotopic composition in the larger part of the trench record all further plots and calculations will be evaluated on absolute coordinates.

3.3.2 *Single-profile representativity*

The isotope record of trench T1 (Fig. 3.2a) allows the quantification of the horizontal isotopic variability of the snow and firn column in our study region. We observe considerable horizontal variability with a mean variance of $\sigma^2_{\mathrm{h,T1}} \simeq 5.9\,(‰)^2$, directly affecting the representativity of single trench profiles. To mimic the potential result obtained from correlating two snow pits taken at a distance of 500 m, similarly done in many firn-core studies (e.g., McMorrow et al., 2002), we calculate the pairwise Pearson correlation coefficient between single profiles of T1 and single profiles of T2. We account for potential surface undulations between the trenches by allowing bin-wise vertical shifts of ±12 cm between the T1 and T2 profiles to maximise their correlation. The estimated correlations (Fig. 3.4) are substantially scattered

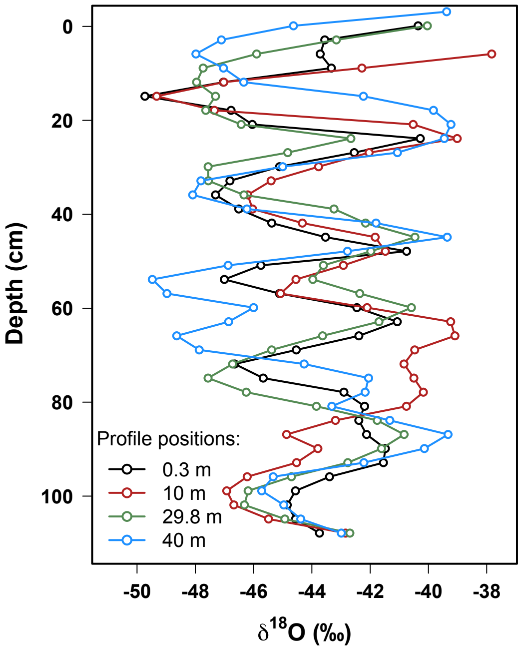

FIGURE 3.3. The four δ^{18}O profiles obtained from trench T2 displayed on absolute coordinates.

around a mean correlation of ~ 0.50 (SD $= 0.13$). The relative majority ($\sim 43\,\%$) of all possible profile pairs ($N = 152$) shows a maximum correlation at a shift of $+3\,$cm, which is well below the estimated upper vertical height difference of the trenches.

3.3.3 *Mean trench profiles*

Spatial averaging is expected to improve the correlation between the trenches compared to the single profiles. We therefore correlate the mean trench profiles of T1 and T2, allowing again for bin-wise vertical shifts of the T2 profile to maximise the correlation.

The mean trench profiles (Fig. 3.5) are highly correlated ($r_{\mathrm{T1,T2}} = 0.81$ for an optimal shift of $+3\,$cm; $p = 0.01$, accounting for the full autocorrelation structure and allowing for vertical shifting), indicating a common isotopic signal reproducible over a spatial scale of at least 500 m. It is interesting to note that this value is above most of the single intertrench* correlations (Fig. 3.4).

In both mean profiles, we observe five seasonal cycles spanning a range of ~ 6–7 ‰ at the surface, but being attenuated further down and exhibiting no clear sinusoidal shape in the depth range of 65–90 cm. Interestingly, this obscured part without clearly depleted δ^{18}O "winter" values is found in both trenches, indicating that this feature persists over at least 500 m and is thus likely of climatic origin, e.g., a winter with unusually low precipitation. Despite the statistic-

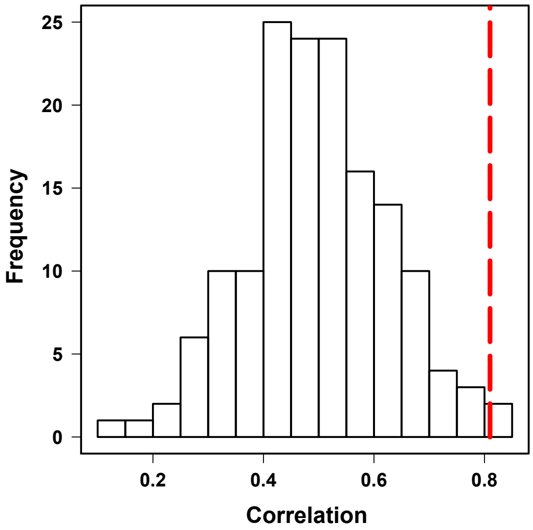

FIGURE 3.4. Histogram of all possible pairwise correlations ($N = 152$) between single profiles of trench T1 and single profiles of trench T2. Displayed are the maximum correlations allowing vertical shifts of the T2 profiles of up to ± 12 cm. Shown in red is the correlation between the mean profiles of T1 and T2 (Fig. 3.5).

ally significant correlation, pronounced differences between the mean profiles are present, such as a significantly more depleted, and partially more enriched, isotopic composition of the T2 mean between 50 and 80 cm.

To analyse annual-mean δ^{18}O time series we use different binning methods to average the seasonal trench data with bins defined by (1) the six local maxima determined from the average of the two mean trench profiles, (2) the five local minima, (3) the midpoints of the ascending slopes flanking the maxima and (4) the midpoints of the descending slopes. To display the data on an absolute time axis we assign the year 2012 to the first annual bin. The annual-mean time series derived from the four possible binning sets are averaged to obtain a single time series for each trench (Fig. 3.5). The correlation of the average annual-mean δ^{18}O time series of $r_{\overline{\text{T1}},\overline{\text{T2}}} = 0.87^{+0.07}_{-0.20}$ (range represents the four binning methods) is comparable to that of the mean seasonal profiles (0.81). However, five observations of annual means are too short to reliably estimate the correlation and its significance.

3.3.4 *Spatial correlation structure*

We have shown that spatial averaging significantly increases the correlation between the trenches. To learn more about the spatial correlation structure of the trench isotope record, we investigate (1) the interprofile⋆ correlation as a function of profile spacing for T1 and

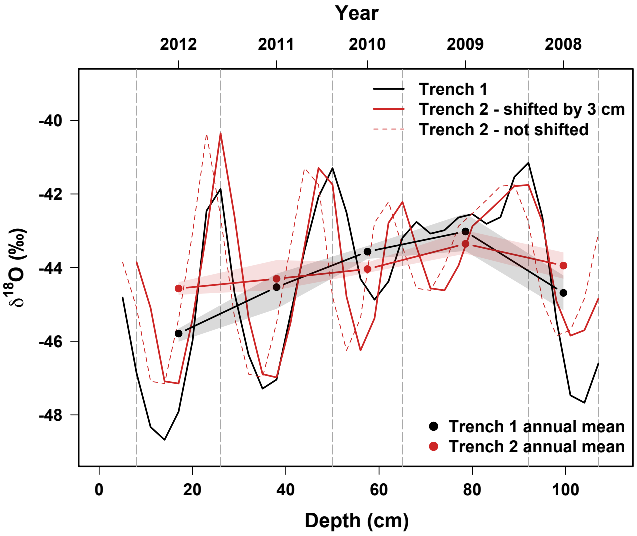

FIGURE 3.5. Comparison of the mean δ^{18}O profiles (lines: seasonal, points: annual mean) from T1 (black) and T2 (red). To maximise the seasonal correlation ($r_{\text{T1,T2}} = 0.81$), trench T2 was shifted by +3 cm. For the first three depth bins, the number of existing observations varies on absolute coordinates between the trench profiles. To obtain non-biased seasonal mean profiles only the depth range covered by all profiles is used. Shading represents the range of the approximate annual-mean profiles due to different binning definitions. Note that their first and last value are biased since the trench data are incomplete here. Vertical dashed grey lines mark the six local maxima of the average of both seasonal mean profiles.

(2) the intertrench correlation between different sets of mean profiles from T1 and the mean T2 profile.

The interprofile correlation is estimated as the mean of the correlations obtained from all possible T1 profile pairs separated by a given spacing, allowing a tolerance in the horizontal position of 5 %. For the intertrench correlation, we define a T1 profile stack as the spatial average across a certain number of T1 profiles separated by a given distance, and determine all possible equivalent stacks. The intertrench correlation with the mean T2 profile is then recorded as the mean across the correlations between the mean T2 profile and all possible T1 stacks.

The interprofile correlation approaches 1 for nearest neighbours and rapidly drops with increasing interprofile spacing before it stabilises around a value of ~ 0.5 for spacings $\gtrsim 10$ m (Fig. 3.6). For the intertrench correlation, we find a steady increase in the correlation with the T2 reference with increasing number of profiles used in the T1 stacks (Fig. 3.7). Additionally, the correlation increases with a wider spacing between the individual profiles of a stack.

The observed decrease of the interprofile correlation with distance suggests a horizontal autocorrelation of the isotopic composition. Indeed, a positive autocorrelation of the horizontal δ^{18}O variations of

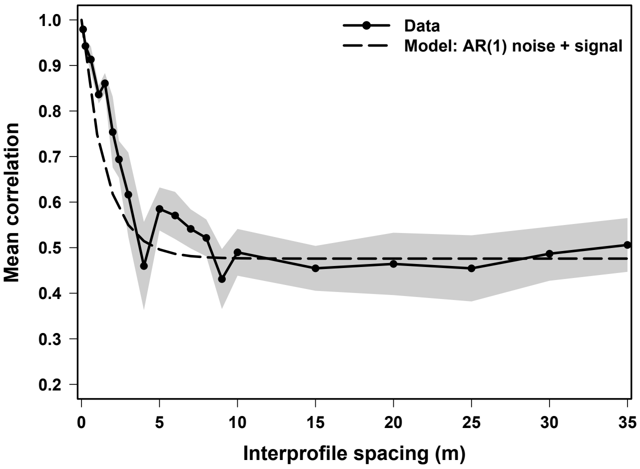

FIGURE 3.6. Observed and modelled interprofile correlation as a function of profile spacing for T1. Observations for a given spacing are the mean across all possible profile pairs. Shading denotes the standard error of the mean assuming maximum degrees of freedom (DOF) of $N = 12$ (estimated from the effective DOF of the horizontal trench data accounting for autocorrelation).

T1 with a decorrelation length of $\lambda \simeq 1.5\,\mathrm{m}$ is found by applying a Gaussian kernel correlation (Rehfeld et al., 2011) which accounts for the irregular horizontal sampling. As we do not expect any climate-related part of the isotopic record to vary on such small spatial scales, we attribute the observed autocorrelation to noise features.

3.3.5 *Statistical noise model*

The interprofile correlation r_{XY} provides an estimate of the signal-to-noise variance ratio F of single profiles (Fisher et al., 1985),

$$F = r_{XY}/(1 - r_{XY}). \tag{3.2}$$

Neglecting the small-scale correlation, we estimate F from the data using the mean interprofile correlation for the profile spacings between 10 and 35 m and find $F = 0.9 \pm 0.1$.

Based on our findings, we develop a simple statistical model: we assume that each trench profile consists of the sum of a common climate signal S and a noise component w independent of the signal. The noise component is modelled as a first-order autoregressive process (AR(1)) in the horizontal direction. Then, the interprofile correlation coefficient between profiles X and Y becomes a function of their spacing d (see Appendix 3.6),

$$r_{XY} = \frac{1}{1 + F^{-1}} \left\{ 1 + F^{-1} \exp\left(-\frac{d}{\lambda} \right) \right\}. \tag{3.3}$$

Here, $F^{-1} = \mathrm{var}(w)/\mathrm{var}(S)$ is the inverse of the signal-to-noise variance ratio. Using our estimate for F and the value for λ obtained in

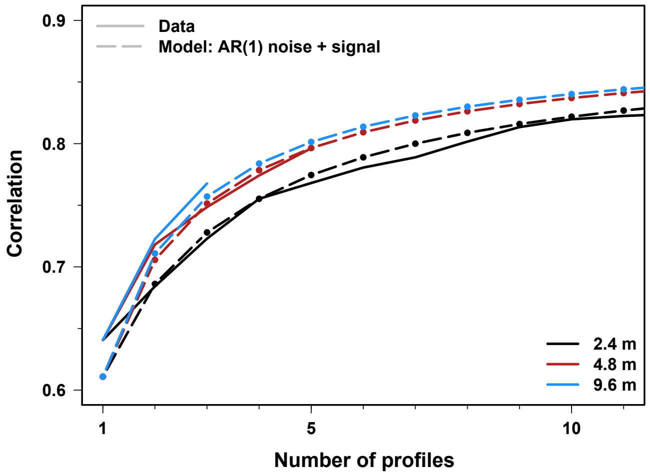

FIGURE 3.7. Observed and modelled correlations between T1 profile stacks and the mean of all T2 profiles depending on the number of profiles in the T1 stack for three selected interprofile spacings. Observed results for given spacing and number of profiles are the mean across the correlations obtained for all possible unique stacks and only calculated when at least 15 stacks are available.

the previous section, the model reproduces the observed interprofile correlations (Fig. 3.6). Applying the same parameter values, the theoretical intertrench correlation (Eq. 3.18) is also in good agreement with the empirical results (Fig. 3.7). This validates the model and the parameter values (F, λ) from the intra-trench ($\sim$ 10 m) to the intertrench spatial scale ($\sim$ 500 m).

3.4 DISCUSSION

Our trench data confirm earlier results that individual δ^{18}O firn-core records from low-accumulation regions are strongly influenced by local noise (Fisher et al., 1985; Karlöf et al., 2006). Going beyond this finding, our two-dimensional δ^{18}O data set also allows one to determine the spatial structure and to learn about the causes of the noise. In this section, we discuss our findings in the context of the possible noise sources and derive implications for seasonal to interannual climate reconstructions based on firn cores.

3.4.1 *Local stratigraphic noise and regional climate signal*

A horizontally stratified trench without horizontal isotopic variations would yield perfectly correlated single profiles. Opposed to that, our records (Table 3.1) show a significant variability in horizontal direction with mean variances $\left(\sigma^2_{\mathrm{h,T1}} \simeq 5.9\,(‰)^2,\ \sigma^2_{\mathrm{h,T2}} \simeq 5.3\,(‰)^2\right)$ that are smaller but of the same order of magnitude as the mean down-core variances $\left(\sigma^2_{\mathrm{v,T1}} \simeq 9.5\,(‰)^2,\ \sigma^2_{\mathrm{v,T2}} \simeq 7.3\,(‰)^2\right)$. In consequence, coherent isotopic features between single profiles separated by the trench distance are only found by chance (Fig. 3.4: the median correlation is 0.49, only for two pairs ($\sim 1.3\,\%$) the correlation is > 0.8). Thus, single firn profiles from our study region are no representative recorders of climatic isotope signals on the vertical scales analysed here.

On the horizontal scale of the trenches ($\sim$ 10–500 m), we expect that stratigraphic noise dominates the isotopic variations (Fisher et al., 1985). The observed length scale of the horizontal decorrelation of the noise ($\lambda \sim 1.5\,\mathrm{m}$) is similar in magnitude as that on which the local small-scale surface height variations occur, indicating that stratigraphic noise is in fact the prominent noise component in our data.

Despite the low single-profile representativity, the trench record contains a climate signal becoming apparent through the interprofile correlation of ~ 0.5 remaining on scales on which the stratigraphic noise is decorrelated ($\gtrsim 10\,\mathrm{m}$). It appears to be regionally ($\lesssim 1\,\mathrm{km}$) coherent as suggested firstly by the comparable values of the interprofile correlation for spacings $\gtrsim 10\,\mathrm{m}$ and the mean correlation between single T1–T2 records (Fig. 3.4), and secondly by the common seasonal signal observed in the mean trench profiles (Fig. 3.5).

Noise is always reduced by averaging profiles; here, the autocorrelation causes nearby profiles to share more common noise variance than profiles at a larger spacing. Therefore, albeit the same number of profiles is averaged, stacks using a larger profile spacing will exhibit less common noise variance and hence a larger proportion of the underlying signal (Fig. 3.7). Our results show a minimum profile spacing of $\sim 10\,\mathrm{m}$ to be optimal.

3.4.2 *Representativity of isotope signals on seasonal to interannual timescales*

For quantitative climate reconstructions from proxy data, a robust estimate of the climate signal is necessary. Based on our statistical noise model, we can estimate the isotopic climate signal content of a profile stack for our study region depending on the number of averaged profiles and their spacing.

To this end, we define the climate representativity of a trench profile stack as the correlation between the stack and a common climate signal (Eq. 3.17). This signal is identified with the coherent isotope signal of the trench records. A physical interpretation of the climate representativity is then the upper bound of the correlation with a local temperature record, for example from a weather station. However, bearing in mind other influences such as meteorology (variable storm tracks, changing moisture source regions, precipitation-

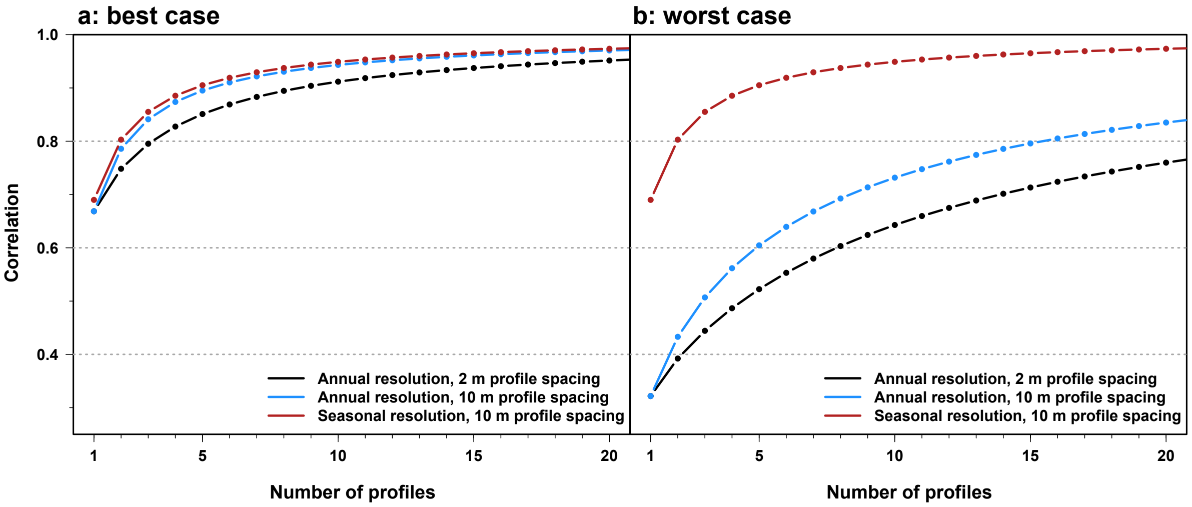

FIGURE 3.8. Representativity of a δ^{18}O firn profile stack expressed as the correlation with a hypothetical climate signal depending on the number of profiles averaged and their interprofile spacing. For annual resolution, the two limiting cases discussed in the text are displayed (**a** best-case scenario, **b** worst-case scenario), each for 2 m (black) as well as 10 m (blue) interprofile spacing. As a reference, in each case the seasonal representativity is shown in red for 10 m interprofile spacing.

weighting), the true correlation will be lower. In the limit of independent noise our definition of climate representativity is equivalent to the expression derived by Wigley et al. (1984).

In general, climate signals are timescale-dependent. For example, the seasonal amplitude of the isotopic signal is much larger than any variations between the years. On the other hand, one expects larger changes of the climate signal on longer timescales, such as glacial–interglacial cycles. Moreover, not only the climate signal but also the noise can be a function of the timescale. One extreme example for this is the non-climate oscillations of the isotopic composition on up to centennial timescales which have been indicated by snow-pit studies around Vostok station and linked to the movement of accumulation waves on various scales (Ekaykin et al., 2002). Since the climate representativity (Eq. 3.17) depends on the ratio F of signal and noise variance, it is in consequence also a function of the timescale.

Here, we assess the climate representativity of firn isotope profiles from our study region for two specific timescales: (1) the original resolution of the trench data and (2) an annual resolution based on binning the trench data.

Analysing the original data, which is dominated by variations on seasonal timescales, the climate representativity can be readily calculated with the model parameters obtained in Sect. 3.3.5. For the analysis at annual resolution, estimates of both annual signal and noise variance are necessary to assess the variance ratio F. However, the shortness of our trench data only allows heuristic estimates (see Appendix 3.6 for details). Specifically, for the annual noise variance

TABLE 3.1. Variance levels of the two trenches: the horizontal variance is the mean variance of all depth layers on absolute coordinates; the down-core variance is the mean vertical variance of all respective trench profiles. The seasonal as well as the annual variance levels denote the variances of the respective mean seasonal and annual δ^{18}O time series of the two trenches (Fig. 3.5). All numbers are in units of $(‰)^2$.

Trench	Horizontal σ_h^2	Down-core σ_v^2	Seasonal $\overline{\sigma}_\mathrm{v}^2$	Annual $\overline{\sigma}_\mathrm{a}^2$
T1	5.9	9.5	5.1	1.15
T2	5.3	7.3	3.3	0.21

TABLE 3.2. Noise variance and standard deviation (SD) of the trench data together with the ratio of measurement uncertainty ($\sigma_\mathrm{CRDS} = 0.09$ ‰) and respective noise SD, given for different resolutions and for the two limiting cases of the annual noise variance. The decadal noise level estimates are calculated from the annual noise variances accounting for full forward diffusion.

Resolution	Variance in $(‰)^2$	SD in ‰	σ_CRDS/SD
seasonal	5.9	2.43	4 %
annual: case I	0.84	0.92	10 %
annual: case II	5.9	2.43	4 %
decadal: case I	0.08	0.28	32 %
decadal: case II	0.56	0.75	12 %

we discuss two limiting cases: for case I we assume that the vertical noise is white (best-case scenario), for case II that the vertical noise shows complete inter-dependence on the subannual* timescale (worst case). The inverse of the annual signal-to-noise variance ratio, $F_\mathrm{annual}^{-1} = \mathrm{var}(w)_\mathrm{annual}/\mathrm{var}(S)_\mathrm{annual}$, used in the model is then ~ 1.2 for case I and ~ 8.7 for case II. A summary of the noise levels is given in Table 3.2.

For single profiles, the climate representativity estimated at seasonal resolution is 0.69 (Fig. 3.8). At annual resolution, single profiles show a representativity of 0.67 in the best-case scenario (Fig. 3.8a) and of 0.32 in the worst-case scenario (Fig. 3.8b).

Similar to the correlation between the trenches (Fig. 3.7), the representativity increases with the number of profiles averaged with a stronger increase for larger interprofile spacings. However, spacings above 10 m do not yield a further increase as the stratigraphic noise is largely decorrelated. To obtain a climate representativity of 0.8 at annual resolution with profiles separated by 10 m, a minimum of 3–16 cores are needed (from best to worst case). Demanding a representativity of 0.9, the number of cores required increases to 6–37.

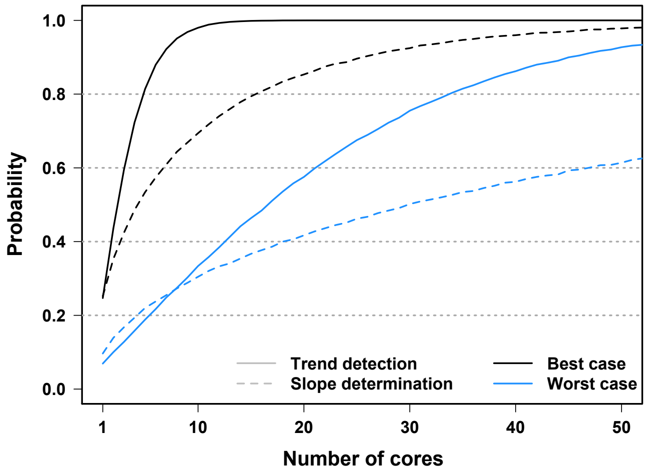

Figure 3.9. Probability of detecting a linear temperature trend of 0.5 °C $(50\,\mathrm{yr})^{-1}$ ($p = 0.05$) (solid lines) and of determining the strength of the trend with an accuracy of 25 % (dashed lines) as a function of the number of firn cores averaged and for the two scenarios of the annual noise variance discussed in the text (black: best case, blue: worst case).

The modelled single-profile climate representativity at annual resolution appears consistent with previous findings from Dronning Maud Land. Graf et al. (2002) estimated a low signal-to-noise variance ratio of $F = 0.14$ obtained from the cross-correlations of 16 annually resolved δ^{18}O records from an area of 500 km × 200 km. Due to the large intercore* spacings, the stratigraphic noise in the records is decorrelated and the variance ratio F can be translated into a single-profile representativity of $r_{SX} = 1/\sqrt{1 + F^{-1}} \simeq 0.35$, consistent with our findings for the worst-case scenario. However, the records analysed in Graf et al. (2002) are also subject to dating uncertainties, additional variability caused by spatially varying precipitation-weighting and other effects. Therefore, the similar representativities are not necessarily caused by the high stratigraphic noise level assumed in the worst-case scenario. In addition, our trench data indicate vertical autocorrelation of the noise (Fig. 3.2b and Sect. 3.3.1). Thus, the true climate representativity for our study region will likely be in between our limiting estimates.

Stratigraphic noise affects not only isotopes but also other parameters measured in ice cores, such as aerosol-derived chemical constituents. Gfeller et al. (2014) investigated the seasonal to interannual representativity of ion records from five Greenland firn cores taken at varying distances from 7 to 10 m in the vicinity of the NEEM drilling site. Using the definition of representativity based on Wigley et al. (1984), they found interannual representativities of ∼ 0.55–0.95, depending on the number of averaged cores and the ion species considered. These numbers are slightly higher than our best-case-scenario results for δ^{18}O, which is expected since the accumulation rate at the NEEM site is about 3 times higher than at Kohnen Station (NEEM community members, 2013).

Our estimates for the climate representativity of firn cores hold as long as the signal-to-noise variance ratio F does not change. Variance-affecting processes such as diffusion and densification have equal influence on signal and noise and thus do not alter the ratio F. On the other hand, only one component might change over time; for example, the noise variance might vary due to changing environmental conditions, or the variability of the climate could have been different in the past for certain time periods. Nevertheless, given the stability of the Holocene climate, we do not expect first-order changes of the signal and noise properties over time. However, we do expect a timescale dependency of the climate signal with more variance associated with longer timescales (e.g., Pelletier, 1998). The signal-to-noise variance ratio and the climate representativity of firn cores will improve considerably on these scales.

3.4.3 *Implications*

Our noise level and implied climate representativity estimates underline the challenge of firn-core-based climate reconstructions at seasonal to annual resolution in low-accumulation regions. For our study site, we now discuss implications of our noise model concerning (1) the required measurement precision of water isotopes in the case of classical isotope thermometry, (2) the potential noise fraction in isotope signals of the EDML ice core and (3) the detectability of a temperature trend.

Our estimates of the stratigraphic noise level are based on the upper 1 m of firn. Due to the shortness of the data our results are limited by insufficient knowledge of the vertical noise covariance structure for interannual and longer timescales for which we now assume white-noise behaviour. The noise of isotopic data obtained from deeper parts of the firn column is affected by diffusion and densification. Densification is only of importance when studying the isotopic time series in the depth domain since in that case constantly sampled data will contain noise levels on varying timescales. We estimate the effect of diffusion and find that at decadal resolution below the firn–ice transition the noise level at Kohnen Station is only 5 % smaller as compared to the undiffused case (Appendix 3.7 and Table 3.2).

The noise of an isotopic signal includes the stratigraphic noise as well as noise caused by the measurement process. Since the stratigraphic noise is a function of the number of analysed cores, and measurement precision is often related to measurement time, obtaining the best signal is a trade-off between measurement precision and the amount of analysed samples.

At seasonal as well as annual resolution, the measurement uncertainty of the trench data of $\sigma_{\text{CRDS}} = 0.09‰$ is much lower ($\sim$ 4–10 %) than the standard deviation of the stratigraphic noise (Table 3.2). This ratio is independent of the temporal resolution if a lower resolution is obtained by averaging annually resolved data as both contributions decrease by the same amount in the averaging process, assuming independence between the samples. In such a case, priority should be given to measuring and averaging across multiple cores in order to reduce the (stratigraphic) noise levels instead of performing high-precision measurements on single cores. As an example, with the cavity ring-down spectrometers used for this work faster measurements are possible by reducing the number of repeated measurements per sample and applying a memory correction (van Geldern and Barth, 2012). We explicitly note that this possibility is limited to classical single-isotope (δ^{18}O) reconstructions as it can affect the data usability for diffusion- (Gkinis et al., 2014; van der Wel et al., 2015b) or deuterium-excess-based (Vimeux et al., 2001) inferences.

If a lower temporal resolution is obtained by a coarser sampling of the cores, the measurement error to stratigraphic noise ratio will depend on the analysed resolution (Table 3.2). For a resolution corresponding to 10 years, our measurement uncertainty might amount to up to 32 % of the stratigraphic noise level, accounting for full diffusion. The noise level of single cores would become comparable to the measurement uncertainty for averages over $\sim$ 104 or $\sim$ 735 years (best- or worst-case scenario of annual noise level).

The deep EPICA DML ice core obtained in the vicinity of Kohnen Station reflects the climate evolution in Antarctica over the last 150 000 years (EPICA community members, 2006). Oerter et al. (2004) studied a core section covering the last 6000 years at decadal resolution. We find a δ^{18}O variance for this section of $\sim$ 0.57 (‰)^2. Using our diffusion-corrected stratigraphic noise variance estimates would imply that $\sim$ 15–100 % (from best to worst case) of the observed decadal variance in the core might be noise (Table 3.2), masking the underlying climate variability. We note that this is only a rough estimate as the shortness of the trench data does not allow one to fully assess the decadal noise covariance. In any case, averaging across multiple cores seems necessary in low-accumulation regions to reconstruct the climate variability of the last millennium. Alternatively, if only the magnitude of variability is of interest, the proxy variability has to be corrected for the noise contribution (e.g., Laepple and Huybers, 2013).

As a final example of applying our noise model, we test the influence of stratigraphic noise on the detectability of a linear trend at Kohnen Station. This is motivated by the finding of Steig et al. (2009) that in the last 50 years the surface temperature over East Antarctica has warmed by about half a degree. While both the climate signal as well as the relationship between local temperature and isotopic signal are complex, we assess the detectability with a simplified model experiment. For this, we assume the climate signal to be a purely linear trend ($0.5\,°\mathrm{C}\,(50\,\mathrm{yr})^{-1}$) and a linear isotope-to-temperature relationship ($1\,‰\,\mathrm{K}^{-1}$), further influenced only by post-depositional noise. In a Monte Carlo approach repeated 10^5 times, we create stacks from 50 yr long δ^{18}O profiles with post-depositional noise variances based on our two limiting cases (Table 3.2), accounting for an average effect of diffusion on the annual noise level over the 50 years (Appendix 3.7) and assuming independent noise between the profiles (interprofile spacings $\gtrsim 10\,\mathrm{m}$), and vary the number of averaged profiles. A trend in the stacked profile is successfully detected for an estimated trend that is significantly larger than zero ($p = 0.05$); the estimated slope is defined to be correct when it lies in a range of 25 % around the true slope. The probability of trend detection/slope determination is then the ratio of successful reconstructions to total number of realisations.

Drilling a single core, the probability of detecting the trend or reconstructing its slope is around 25 % in the best-case and below 10 % in the worst-case scenario (Fig. 3.9). To reliably ($> 80\,\%$ of the cases) detect the warming over the Antarctic Plateau, our results suggest that averaging across at least $\sim$ 5–35 firn cores taken at spacings of 10 m (Fig. 3.9) is needed, depending on the scenario for the annual noise variance. Inferring the right slope would need 3 times that number of cores. We note that more realistic assumptions about the isotopic signal (natural climate and atmospheric variability, varying isotope–temperature relationship, etc.) further complicate the trend detectability.

3.5 CONCLUSIONS

We presented extensive oxygen stable water isotope data derived from two snow trenches excavated at Kohnen Station in the interior of Dronning Maud Land, Antarctica. The two-dimensional approach allowed a thorough investigation of the representativity of single firn-core isotope profiles, as well as of the spatial structure of the signal and noise over spatial scales of up to 500 m and a time span of approximately 5 years.

The trench data confirm previous studies that single low-accumulation ($\leq 100\,\mathrm{mm\,w.e.\,yr^{-1}}$) isotope profiles only show a weak coherent signal at least on subdecadal* timescales. We also demonstrate that the spatial average of a sufficient number of profiles provides representative isotopic signals, consistent with our finding that the local noise has a small horizontal decorrelation length ($\sim 1.5\,\mathrm{m}$). This also suggests stratigraphic noise to be the major contribution to the horizontal isotopic variability. A statistical noise model based on a first-order autoregressive process successfully explains the observed covariance structure and allows one to reproduce the correlation statistics between the trenches.

Based on these results we infer appropriate sampling strategies. At our low-accumulation (64 mm w.e. yr^{-1}) site an optimal spacing of about 10 m is necessary for a sufficient decorrelation of the stratigraphic noise. We estimate the climate representativity of isotope profiles depending on the number of averaged firn cores and the intercore spacing. Our estimates show that at seasonal resolution five cores at the optimal spacing are necessary to obtain representative ($r > 0.9$) isotope signals; at annual resolution up to ~ 8 times as many cores are needed. As climate variations are typically stronger on longer timescales than analysed here, the climate representativity of firn- and ice-core reconstructions for slower climate changes will likely be higher.

We present two examples of how the stratigraphic noise might hamper the quantitative interpretation of isotope in terms of climate variations at our study site. Our data suggest that at least 15 % of the decadal variations seen in the EPICA DML ice core over the last 6000 years might be post-depositional noise, but the climate signal might also be masked by a much higher decadal noise level. A simplified model experiment shows that the faithful reconstruction of the recent positive temperature trend observed over the Antarctic Plateau likely requires averaging across at least 5–35 firn cores. For single-proxy (δ^{18}O) reconstructions this task could be rendered more easily by the fact that the annual noise level is substantially larger than typical measurement uncertainties. Thus, monitoring the measurement error depending on sample throughput could allow fast measurements for the benefit of analysing many cores. Alternatively, using indirect methods based on diffusion (Gkinis et al., 2014; van der Wel et al., 2015b) or gas isotope ratios (Kobashi et al., 2011) might circumvent the problem of stratigraphic noise.

Since the stratigraphic noise is related to irregular re-deposition and erosion of snow and the formation of surface dunes, it primarily depends on the local accumulation rate, besides further factors such as wind strength, temperature, seasonal timing of the precipitation and snow properties. Therefore, we expect that our representativity results improve (worsen) for regions with higher (lower) accumulation rates. In effect, our results are likely applicable for large parts of the Antarctic Plateau, but similar studies in West Antarctica and Greenland – regions with considerably higher accumulation rates – are needed. In addition, studies with deeper trenches that cover a longer time period, complemented by spectral analyses of nearby firn cores, are necessary to enhance our knowledge of the vertical noise covariance structure. This is crucial to determine the climate representativity on longer timescales. Deeper trenches would also allow one to link our representativity results to actual correlations with temperature time series derived from weather stations. The latter is part of ongoing work at Kohnen Station.

3.6 APPENDIX A: DERIVATION OF NOISE MODEL

3.6.1 *Definitions*

We consider isotope profiles $X_i(z)$ at equidistant spacings $\Delta\ell$ where z is depth on absolute coordinates and i refers to the profile's horizontal position along a snow trench, $\ell_i = \ell_0 + i \times \Delta\ell$, with some arbitrary starting position ℓ_0 (Fig. 3.10). This and all subsequent nomenclature is summarised in Table 3.3.

We assume each $X_i(z)$ as a sum of a common signal $S(z)$ and a noise term $w_i(z)$ independent of S,

$$X_i(z) = S(z) + w_i(z). \tag{3.4}$$

The noise $w_i(z)$ is modelled as an AR(1) process in the horizontal direction,

$$w_i(z) = a w_{i-1}(z) + \varepsilon_i(z), \tag{3.5}$$

where a is the autocorrelation parameter with $0 \leq a \leq 1$ and $\varepsilon_i(z)$ are independent random normal variables (white noise). We assume the same variance $\mathrm{var}(w)$ of the noise in both the horizontal and the vertical direction.

The mean of a set of N trench isotope profiles $\overline{X}_{\{i\}}$ (profile stack) is defined by the indices $\{i\} = \{i_1, i_1 + i_2, i_1 + i_2 + i_3, \ldots, i_1 + i_2 + \cdots + i_N\}$. This nomenclature of incremental steps simplifies the expressions obtained later. $\overline{X}_{\{i\}}(z)$ is given by the signal $S(z)$ and the mean of the noise terms,

$$\overline{X}_{\{i\}}(z) = S(z) + \frac{1}{N}\left(w_{i_1} + w_{i_1+i_2} + \cdots + w_{i_1+i_2+\cdots+i_N}\right)(z). \tag{3.6}$$

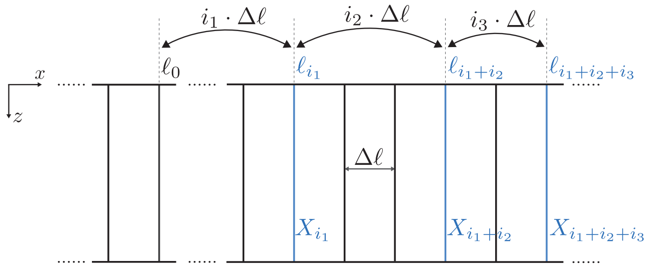

FIGURE 3.10. Sketch of a snow trench used for the derivation of the statistical noise model. Vertical isotope profiles X_i are spaced at constant intervals of $\Delta\ell$ at locations $l_i = l_0 + i\Delta\ell$. The horizontal distance d between two profiles X_{i_1} and $X_{i_1+i_2}$ is defined by the incremental index i_2, $d = i_2\Delta\ell$.

TABLE 3.3. Summary of the nomenclature used for the statistical noise model.

Symbol	Description
z	absolute depth below mean snow height
X_i	trench isotope profile at position ℓ_i
$\Delta\ell$	spacing of adjacent profiles
S	climate signal contained in X_i
w_i	noise contained in X_i
ε_i	white-noise component of w_i
$\overline{X}_{\{i\}}$	profile stack
a	autocorrelation parameter; $a = \exp\left(-\Delta\ell/\lambda\right)$
λ	horizontal noise decorrelation length
d	interprofile distance
N	number of profiles
$\sigma^{*2}_{\{i\}}$	relative effective noise variance of stack $\overline{X}_{\{i\}}$
F	signal-to-noise variance ratio

The Pearson correlation of two single profiles X_i and X_{i+j} is

$$\begin{aligned}\operatorname{corr}\left(X_i, X_{i+j}\right) &= \frac{\operatorname{cov}\left(X_i, X_{i+j}\right)}{\sqrt{\operatorname{var}(X_i)\operatorname{var}(X_{i+j})}} \\ &= \frac{\operatorname{var}(S) + \operatorname{cov}\left(w_i, w_{i+j}\right)}{\operatorname{var}(S) + \operatorname{var}(w)},\end{aligned} \tag{3.7}$$

using the independence of signal and noise and the stationarity of w.

The correlation of a profile stack $\overline{X}_{\{i\}}$ and the signal is given by

$$\begin{aligned}\operatorname{corr}\left(\overline{X}_{\{i\}}, S\right) &= \frac{\operatorname{cov}\left(\overline{X}_{\{i\}}, S\right)}{\sqrt{\operatorname{var}(\overline{X}_{\{i\}})\operatorname{var}(S)}} \\ &= \frac{\operatorname{var}(S)}{\sqrt{\operatorname{var}(\overline{X}_{\{i\}})\operatorname{var}(S)}}.\end{aligned} \tag{3.8}$$

Similarly, the correlation of two profile stacks with indices $\{i\}$ and $\{j\}$, assuming independent noise between the sets, is obtained from

$$\begin{aligned}\operatorname{corr}\left(\overline{X}_{\{i\}}, \overline{X}_{\{j\}}\right) &= \frac{\operatorname{cov}\left(\overline{X}_{\{i\}}, \overline{X}_{\{j\}}\right)}{\sqrt{\operatorname{var}(\overline{X}_{\{i\}})\operatorname{var}(\overline{X}_{\{j\}})}} \\ &= \frac{\operatorname{var}(S)}{\sqrt{\operatorname{var}(\overline{X}_{\{i\}})\operatorname{var}(\overline{X}_{\{j\}})}}.\end{aligned} \tag{3.9}$$

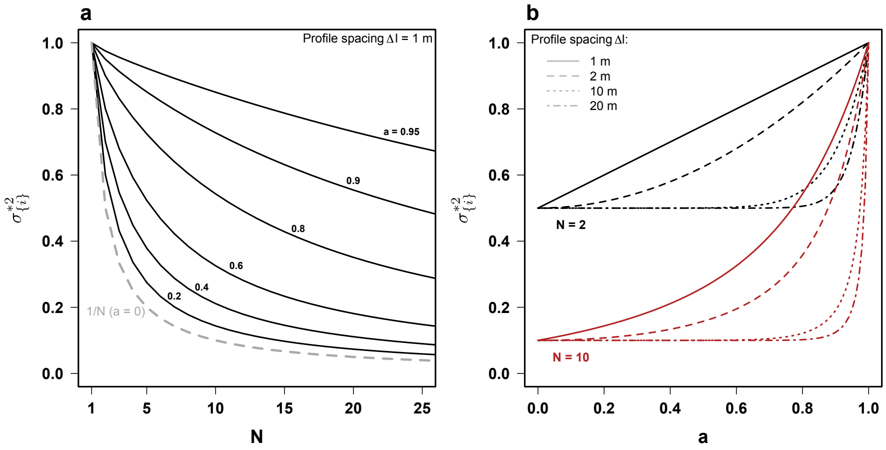

FIGURE 3.11. (**a**) Relative effective noise variance $\sigma^{*2}_{\{i\}}$ of a profile stack $\overline{X}_{\{i\}}$ as a function of the number of profiles averaged for a profile spacing of $\Delta\ell = 1\,\mathrm{m}$ and for different values of the autocorrelation parameter a. The limiting case of white noise ($a = 0$) is indicated by a dashed line. (**b**) $\sigma^{*2}_{\{i\}}$ as a function of the autocorrelation parameter a for different numbers of averaged profiles and profile spacings.

3.6.2 *Derivation of model correlations*

To derive the explicit correlations (3.7)–(3.9) for the AR(1) noise model, we need expressions for the noise variance, $\mathrm{var}(w)$, the noise covariance in horizontal direction, $\mathrm{cov}(w_i, w_{i+j})$, and the variance of a profile stack, $\mathrm{var}(\overline{X}_{\{i\}})$.

The former two are given by (Chatfield, 2004)

$$\mathrm{var}(w) = \frac{\mathrm{var}(\varepsilon)}{1-a^2}, \tag{3.10}$$

$$\mathrm{cov}(w_i, w_{i+j}) = \frac{\mathrm{var}(\varepsilon)}{1-a^2}\, a^j = \mathrm{var}(w)\, a^j. \tag{3.11}$$

The index j can be expressed here by the distance $d = \ell_{i+j} - \ell_i$ between the profiles X_i and X_{i+j} and the spacing of adjacent profiles $\Delta\ell$ as $j = d/\Delta\ell$. Further, for an AR(1) process the lag one autocorrelation is given by $a = \exp\left(-\Delta\ell/\lambda\right)$ with the decorrelation scale λ. It follows from Eq. (3.11) that the horizontal noise covariance decreases exponentially with distance d as

$$\mathrm{cov}(w_i, w_{i+j}) = \mathrm{var}(w) \exp\left(-\frac{d}{\lambda}\right). \tag{3.12}$$

The variance of a profile stack $\overline{X}_{\{i\}}$ is calculated according to

$$\begin{aligned} \mathrm{var}(\overline{X}_{\{i\}}) &= \left\langle \overline{X}^2_{\{i\}}(z) \right\rangle - \left\langle \overline{X}_{\{i\}}(z) \right\rangle^2 = \mathrm{var}(S) \\ &+ \frac{1}{N^2} \left\langle \left(w_{i_1} + w_{i_1+i_2} + \cdots + w_{i_1+i_2+\cdots+i_N}\right)^2 (z) \right\rangle, \end{aligned} \tag{3.13}$$

where $\langle\cdot\rangle$ denotes the expected value. Using the multinomial identity $(\xi_1 + \xi_2 + \cdots + \xi_N)^2 = \sum_{i=1}^{N} \xi_i^2 + 2\sum_{i=1}^{N-1} \sum_{j>i} \xi_i \xi_j$ yields

$$\begin{aligned}\mathrm{var}(\overline{X}_{\{i\}}) = \mathrm{var}(S) + \frac{1}{N^2}\Big\{ & N\mathrm{var}(w) + \\ & 2\Big(\langle w_{i_1} w_{i_1+i_2}\rangle + \langle w_{i_1} w_{i_1+i_2+i_3}\rangle + \cdots + \\ & \langle w_{i_1} w_{i_1+i_2+i_3+\cdots+i_N}\rangle + \langle w_{i_2} w_{i_2+i_3}\rangle + \cdots + \\ & \langle w_{i_2} w_{i_2+i_3+\cdots+i_N}\rangle + \cdots + \langle w_{i_{N-1}} w_{i_{N-1}+i_N}\rangle\Big)\Big\}. \end{aligned} \tag{3.14}$$

By applying Eq. (3.11) for the horizontal covariance of the noise we obtain

$$\begin{aligned} & \mathrm{var}(\overline{X}_{\{i\}}) = \mathrm{var}(S) + \mathrm{var}(w) \times \\ & \underbrace{\frac{1}{N^2}\left\{N + 2\left(a^{i_2} + a^{i_2+i_3} + \cdots + a^{i_2+\cdots+i_N} + a^{i_3} + \cdots + a^{i_3+\cdots+i_N} + \cdots + a^{i_N}\right)\right\}}_{\sigma^{*2}_{\{i\}}} \end{aligned} \tag{3.15}$$

where we define $\sigma^{*2}_{\{i\}}$ as the relative effective noise variance of the profile stack. In the limiting case of $a = 0$ (zero autocorrelation) $\sigma^{*2}_{\{i\}} = 1/N$, in the limit of $a = 1$ (perfect autocorrelation) $\sigma^{*2}_{\{i\}} = 1$. In general, $\sigma^{*2}_{\{i\}}$ is a function of both N and the spacing of the profiles averaged (Fig. 3.11).

For final expressions of the correlation functions (3.7)–(3.9), we define the signal-to-noise variance ratio $F := \frac{\mathrm{var}(S)}{\mathrm{var}(w)}$ and use Eqs. (3.12) and (3.15) to obtain

interprofile corr.:

$$\mathrm{corr}\left(X_i, X_{i+j}\right) = \frac{1}{1+F^{-1}}\left\{1 + F^{-1}\exp\left(-\frac{d}{\lambda}\right)\right\}, \tag{3.16}$$

stack–signal corr.:

$$\mathrm{corr}\left(\overline{X}_{\{i\}}, S\right) = \frac{1}{\sqrt{1 + F^{-1}\sigma^{*2}_{\{i\}}}}, \tag{3.17}$$

stack–stack corr.:

$$\mathrm{corr}\left(\overline{X}_{\{i\}}, \overline{X}_{\{j\}}\right) = \frac{1}{\left\{\left(1 + F^{-1}\sigma^{*2}_{\{i\}}\right)\left(1 + F^{-1}\sigma^{*2}_{\{j\}}\right)\right\}^{1/2}}. \tag{3.18}$$

3.6.3 *Estimation of parameters*

To evaluate the correlation functions (3.16)–(3.18) we need estimates of the decorrelation length λ and of the timescale-dependent variance ratio F^{-1}.

For the trench data at seasonal resolution, we obtain a variance ratio of $F^{-1} \simeq 1.1 \pm 0.1$ from the observed interprofile correlations of

T1 (Fig. 3.6) for profile spacings $\geq 10\,\text{m}$, and an estimate of the decorrelation length of $\lambda \simeq 1.5\,\text{m}$ from the horizontal autocorrelation of the T1 δ^{18}O data. We validate the parameters by comparing the predicted (Eq. 3.18) and observed correlations between profile stacks derived from T1 and T2 (Fig. 3.7). This assumes independent noise between T1 and T2, a valid approximation given that the trench distance ($\sim 500\,\text{m}$) is much larger than λ. Relying on the assumption of equal noise variance in the horizontal and vertical direction, a second estimate of $F^{-1} \sim 1.6$ can be obtained from the observed mean T1 down-core variance (identified with signal and noise) subtracted by the observed mean T1 horizontal variance (i.e. noise, see Table 3.1).

Going from the original seasonal resolution of the trench data to an explicit annual resolution, the short data sets only allow limited estimations. We thus make use of the following simple heuristic arguments. The annual signal variance is estimated from the mean annual δ^{18}O time series of each trench neglecting the residual noise contributions and averaging both variance estimates to obtain $\text{var}(S)_{\text{annual}} \simeq 0.68\,(‰)^2$ (Table 3.1). The annual noise variance, $\text{var}(w)_{\text{annual}}$, is calculated from the seasonal noise variance estimated by the mean horizontal T1 variance of $\text{var}(w) \simeq 5.9\,(‰)^2$. Physically, we expect a vertical autocorrelation of the noise due to the underlying processes (stratigraphic noise, Fisher et al., 1985; Ekaykin et al., 2002; diffusion, Johnsen et al., 2000), which is also indicated by our data (Fig. 1b). However, due to the limited vertical trench data, the vertical noise autocorrelation cannot be reliably estimated and we discuss two limiting cases: in case I the vertical noise is independent (white noise) and the seasonal noise variance therefore reduced by the number of samples included in the annual average ($N \approx 7$); in case II the vertical noise shows complete inter-dependence on the subannual timescale and its variance is not reduced by taking annual means. The resulting annual variance ratios of noise over signal are

$$\begin{aligned} F^{-1}_{\text{annual}} &= \frac{\text{var}(w)_{\text{annual}}}{\text{var}(S)_{\text{annual}}} \\ &\simeq \frac{1}{0.68} \times \begin{cases} 0.84, \\ 5.9 \end{cases} = \begin{cases} 1.2, & \text{for case I,} \\ 8.7, & \text{for case II.} \end{cases} \end{aligned} \tag{3.19}$$

For all longer timescales, we generally assume white-noise behaviour for the noise covariance.

3.7 APPENDIX B: REDUCTION OF NOISE LEVEL BY DIFFUSION

The integral over the power spectrum $P(f)$ of a time series $X(t)$, where f denotes frequency and t time, is equal to the total variance of X (Chatfield, 2004),

$$\text{var}(X) = 2\int_0^{f_N} P(f)\,\text{d}f. \tag{3.20}$$

Here, f_N is the Nyquist frequency according to the sample resolution of X.

For white noise, the power spectrum is a constant, $P_0(f) = P_0 =$ const. Evaluation of Eq. (3.20) then gives $2 f_N P_0$.

In case of diffusion, the initial power spectrum $P_0(f)$ is changed for a given diffusion length σ and local annual layer thickness $\dot{b}$ according to (van der Wel et al., 2015b)

$$P(f) = P_0(f) \exp\left\{ -\left(2\pi\sigma\dot{b}^{-1}f\right)^2 \right\}, \tag{3.21}$$

where $\dot{b}$ is introduced in order to work in the temporal domain, thus with frequency measured in yr^{-1}. For white noise, the integral in Eq. (3.20) is straightforward to solve, yielding the noise variance at a given resolution f_N accounting for diffusion:

$$\begin{aligned} &2P_0 \int_0^{f_N} \exp\left\{ -\left(2\pi\sigma\dot{b}^{-1}f\right)^2 \right\} \mathrm{d}f = \\ &\quad P_0\sqrt{\pi}/(2\pi\sigma\dot{b}^{-1})\,\mathrm{erf}(2\pi\sigma\dot{b}^{-1}f_N). \end{aligned} \tag{3.22}$$

To estimate how much diffusion has reduced the annual trench noise level at the firn–ice transition at decadal resolution ($f_N = 0.05\,\mathrm{yr}^{-1}$), we assume $\dot{b} = 7\,\mathrm{cm\,yr}^{-1}$ and a constant diffusion length of $\sigma = 8\,\mathrm{cm}$ (Johnsen et al., 2000). Evaluation of Eq. (3.22) yields a reduction of the annual noise power of $\sim 0.095[\mathrm{yr}^{-1}]P_0$. Comparing the diffused with the undiffused case shows that at decadal resolution, diffusion only has a relative effect of $\sim 5\,\%$ on the reduction of the annual noise level.

Thus, diffusion only has a minor influence on decadal and longer timescales at our study site. However, on shorter timescales it has to be accounted for. The annual noise levels given in Table 3.2 are therefore only valid for the uppermost part of the firn column where diffusion is almost negligible. In the deeper parts of the firn, they have been affected by diffusion. In our simplified trend detection experiment, we assume over the first 9 m of firn (approximately the last 50 years) an average annual layer thickness of 15 cm and a mean diffusion length of $\sigma \sim 5\,\mathrm{cm}$ (Johnsen et al., 2000). Evaluation of Eq. (3.22) then gives an average reduction of the annual noise level to $\sim 73\,\%$ of the original value.

4

CONSTRAINTS ON POST-DEPOSITIONAL ISOTOPE MODIFICATIONS IN EAST ANTARCTIC FIRN FROM ANALYSING TEMPORAL CHANGES OF ISOTOPE PROFILES

Thomas Münch[1,2], Sepp Kipfstuhl[3], Johannes Freitag[3],
Hanno Meyer[1], and Thomas Laepple[1]

[1] *Alfred Wegener Institute Helmholtz Centre for Polar and Marine Research, Telegrafenberg A43, 14473 Potsdam, Germany*
[2] *Institute of Physics and Astronomy, University of Potsdam, Karl-Liebknecht-Str. 24/25, 14476 Potsdam, Germany*
[3] *Alfred Wegener Institute Helmholtz Centre for Polar and Marine Research, Am Alten Hafen 26, 27568 Bremerhaven, Germany*

This chapter is published in:
The Cryosphere, **11** (5), 2175–2188, DOI: `10.5194/tc-11-2175-2017`, 2017.

ABSTRACT. The isotopic composition of water in ice sheets is extensively used to infer past climate changes. In low-accumulation regions their interpretation is, however, challenged by poorly constrained effects that may influence the initial isotope signal during and after deposition of the snow. This is reflected in snow-pit isotope data from Kohnen Station, Antarctica, which exhibit a seasonal cycle but also strong interannual variations that contradict local temperature observations. These inconsistencies persist even after averaging many profiles and are thus not explained by local stratigraphic noise. Previous studies have suggested that post-depositional processes may significantly influence the isotopic composition of East Antarctic firn. Here, we investigate the importance of post-depositional processes within the open-porous firn ($\gtrsim 10\,\text{cm}$ depth) at Kohnen Station by separating spatial from temporal variability. To this end, we analyse 22 isotope profiles obtained from two snow trenches and examine the temporal isotope modifications by comparing the new data with published trench data extracted two* years earlier. The initial isotope profiles undergo changes over time due to downward advection, firn diffusion and densification in magnitudes consistent with independent estimates. Beyond that, we find further modifications of the original isotope record to be unlikely or small in magnitude ($\ll 1$ ‰ RMSD). These results show that the discrepancy between local temperatures and isotopes most likely originates from spatially coherent processes prior to or during deposition, such as precipitation intermittency or systematic isotope modifications acting on drifting or loose surface snow.

4.1 INTRODUCTION

The isotopic composition of water measured in firn and ice cores is an important climate proxy. The abundance ratios of the stable water isotopologues in falling snow are shaped by different fractionation processes in between the moisture source and the precipitation site, including evaporation (Craig and Gordon, 1965), air-mass advection and Rayleigh distillation (Dansgaard, 1964) and snow formation (Jouzel and Merlivat, 1984). Hence, isotope ratios can be linked to the climatic conditions at the local or moisture source site. For instance, physical modelling of the large-scale hydrological cycle and the fractionation processes has validated the link between the isotopic composition of precipitation and local temperature (Jouzel et al., 1997, 2003, and references therein) previously inferred for polar ice sheets, where observational evidence has suggested a robust relationship at large spatial scales (i.e. continental) between the isotopic composition of snow and annual-mean temperature at the sampling sites (Dansgaard, 1964; Lorius et al., 1969; Masson-Delmotte et al., 2008). Isotope data archived in polar ice cores have therefore become an invaluable means to infer past site temperature variations (e.g., Petit et al., 1999; NEEM community members, 2013) or changes in the moisture sources (e.g., Vimeux et al., 2001; Uemura et al., 2012) and show, at least qualitatively, a globally consistent picture of glacial–interglacial to millennial-scale climate changes (EPICA community members, 2004, 2006; NGRIP members, 2004). However, it is questioned whether the assumption holds in general that pre-depositional fractionation processes alone are the main influence on the isotopic composition of firn and ice, while seemingly fulfilled for large spatial and temporal scales. Particularly in low-accumulation areas for which the snow surface is exposed to the atmosphere for a substantial time, a variety of processes are thought to considerably modify the original atmospheric isotope signal during or after deposition of the snow, thus from seasonal to interannual timescales (e.g., Ekaykin et al., 2014, 2016, Hoshina et al., 2014; Touzeau et al., 2016; Casado et al., 2016).

For the Antarctic Plateau, modifications of the original isotope signal that is imprinted in precipitation are generally expected. In buried snow and firn, the isotopic composition is affected by diffusion of interstitial water vapour (Johnsen, 1977; Whillans and Grootes, 1985; Cuffey and Steig, 1998; Johnsen et al., 2000; Gkinis et al., 2014) and by densification (Hörhold et al., 2011, 2012, Freitag et al., 2013b); however, these processes do not lead to any net change in the isotopic composition. In contrast, the seasonal intermittency of precipitation and accumulation can bias the original signal, induce variability or lead to a combination of both (Sime et al., 2009, 2011; Persson et al., 2011; Laepple et al., 2011). In combination with the low accumulation rates on the Antarctic Plateau, precipitation intermittency also increases the time the surface is exposed to the atmosphere (Town et al., 2008; Hoshina et al., 2014). These conditions might favour fractionation, diffusive and advective processes that can considerably alter the snow's original isotopic composition, acting either post condensation (on falling or drifting snow) or post deposition on snow at the surface or within the open-porous firn column which is no longer subject to erosion but still in contact with the atmosphere. For instance, the exchange of water vapour between the first metre of firn and the overlying atmosphere through diffusion and wind-driven ventilation (Waddington et al., 2002; Neumann and Waddington, 2004; Town et al., 2008) can introduce vapour with a different isotopic signature to the firn and significantly change the isotopic composition. Isotopic exchanges between the top layer of snow and the lower atmosphere have been observed on daily scales at the NEEM site in Greenland (Steen-Larsen et al., 2014) and on diurnal scales at Kohnen Station in East Antarctica (Ritter et al., 2016). Isotopic fractionation associated with sublimation, condensation and recrystallisation processes within the near-surface firn might change the initial isotope signal, as indicated by observations (Moser and Stichler, 1974; Stichler et al., 2001) and lab experiments (Hachikubo et al., 2000; Sokratov and Golubev, 2009). Since these post-depositional processes also depend, besides temperature, on other climatic variables such as wind speed and relative humidity, any seasonal or interannual variations in these variables would induce additional variability in the isotope record. However, for East Antarctica, a quantitative assessment of the individual processes based on firn-core data is still outstanding, and their importance for shaping the isotope signal in the near-surface firn remains poorly constrained.

An additional, important source of variability in low-accumulation firn-core records is the spatial variability from stratigraphic noise (Fisher et al., 1985) caused by uneven deposition and the constant wind-driven erosion, redistribution and vertical mixing of the snow surface. A previous study from Kohnen Station in Dronning Maud Land, East Antarctica, has shown that the spatial variability can be overcome by averaging across a suitable number of single profiles extracted from snow trenches (Münch et al., 2016b). This yielded a spatially representative isotope signal on a horizontal scale of approximately 500 m. However, contrasting the isotope data with instrumental observations from a nearby automatic weather station (AWS, Reijmer and van den Broeke, 2003) suggests that this regional signal does not necessarily represent a regional temperature signal (Fig. 4.1). Whereas the isotope record shows strong year-to-year variability, the observed temperature variations are characterised by a regular seasonal cycle and small interannual changes. This discrepancy stresses the importance of contributions other than regional

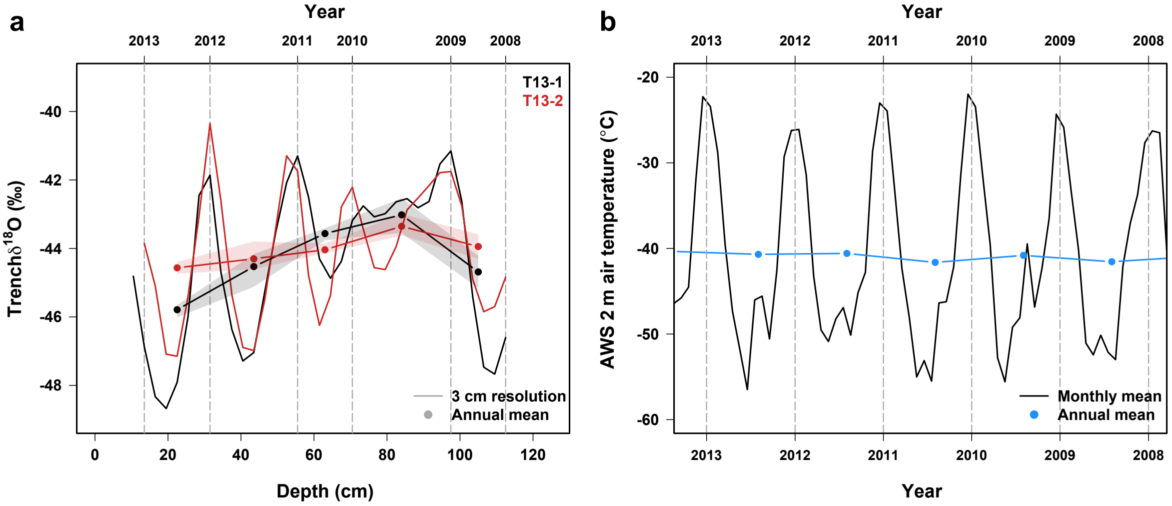

FIGURE 4.1. Comparison of oxygen isotope data and 2 m air temperature at Kohnen Station, Antarctica. (**a**) Mean δ^{18}O profiles of trenches T13–1 (black) and T13–2 (red) (modified after Münch et al., 2016b) on original 3 cm (lines) as well as annual resolution (points with uncertainty shading from shifting the range of the annual bins). (**b**) 2 m air temperature (black lines: monthly means; blue points: annual means) recorded by the automatic weather station AWS9 located at Kohnen Station < 1 km from the trench excavation sites (Fig. 4.2). Note the different timescales (**a** is based on counting and binning the extrema of the isotope data, **b** shows true calendar dates). The mean of the 2 m air temperature shown here lies about 3.5 °C above the published local 10 m firn temperature (Table 4.1).

temperature alone to the formation of the isotope signal, such as precipitation intermittency and changes during or after deposition. Since quantitative knowledge on seasonal and interannual variations of accumulation amounts is still sparse on the Antarctic Plateau (Reijmer and van den Broeke, 2003; Helsen et al., 2005), in this study we investigate whether post-depositional isotope modifications in the open-porous firn contribute to the observed discrepancy between the isotope data and local temperatures at Kohnen Station.

One way to address the question of post-depositional modification is to compare two firn-core isotope profiles obtained at different times and to measure the nature in which the first profile has been modified. However, due to stratigraphic noise, the comparison of two single records sampled at different times will always confound temporal isotope changes and spatial variability. Therefore, in this study we present and use data from a new extensive snow trench campaign yielding 22 profiles of isotopic composition from two trenches and compare these with the data of the previous trench campaign conducted two years earlier. By generating representative records from the spatial averaging of single profiles, together with the theoretical understanding of stratigraphic noise, our study allows us for the first time to quantitatively follow the isotopic changes over a time span of two years. We use independent knowledge on firn diffusion and densification to subtract these effects from the observed temporal

TABLE 4.1. Information on the EPICA Dronning Maud Land (EDML) drilling site at Kohnen Station, Antarctica. Listed are approximate position (latitude, longitude), elevation, 10 m firn temperature $\overline{T}_{\mathrm{firn}}$, mean annual accumulation rate of snow $\overline{b}$ and mean daily wind speed $\overline{v}_{\mathrm{wind}}$ (±1 standard deviation).

Drilling site	Lat. °N	Lon. °E	Elev. m a.s.l.	$\overline{T}_{\mathrm{firn}}$ °C	$\overline{b}$ mm w.e. yr^{-1}	$\overline{v}_{\mathrm{wind}}$ $\mathrm{m\,s}^{-1}$
EDML	-75.0^{a}	0.1^{a}	2892^{a}	-44.5^{a}	$64^{a}/82.5^{b}$	4.4 ± 2.3^{c}

[a] EPICA community members (2006). [b] Mean of snow stake measurements 2013–2015.
[c] AWS9 data 1998–2013 (Reijmer and van den Broeke, 2003).

modifications. Therefore, beyond simply stating the problem of local isotope–temperature discrepancy, we go further and can quantitatively estimate the influence of post-depositional change for our study site. This is an important step towards better constraining the isotope signal formation in East Antarctic firn.

4.2 DATA AND METHODS

4.2.1 *Sampling and measurements*

A pair of firn trenches, each with a horizontal length of 50 m and a depth of 3.4 m, was excavated using a snow blower in the austral summer field season 2014/2015 near Kohnen Station (Alfred-Wegener-Institut Helmholtz-Zentrum für Polar- und Meeresforschung, 2016), the location of the EPICA Dronning Maud Land deep ice core drilling site (Fig. 4.2 and Table 4.1). This campaign extends the published oxygen isotope data set obtained from two shallower (∼ 1 m) trenches in 2012/2013 (Münch et al., 2016b). From the new trenches, we present the top 1.75 m of the data which are expected to cover the period imprinted in the trenches of the first campaign. To avoid contamination, the new trench positions were shifted relative to the previous ones by 160 and 300 m, respectively, and are separated by 550 m (Fig. 4.2). In the remaining part of the manuscript, "T13" will refer to the pair of previous trenches from 2012/2013, "T15" to the pair of new trenches from 2014/2015.

Fieldwork for the new T15 trench campaign was conducted as follows: horizontal profiles of the surface height variations were obtained along each trench using a levelling instrument. The uncertainty of these profiles is estimated from the reading accuracy of the levelling rod of 0.5 cm. The windward walls of the trenches were cleaned after excavation by slicing off a thin firn layer. Firn profiles were then sampled directly off the wall with a vertical resolution of 3 cm and a horizontal spacing of 5 m, yielding 11 profiles in each trench. The vertical resolution is small enough to evaluate the sea-

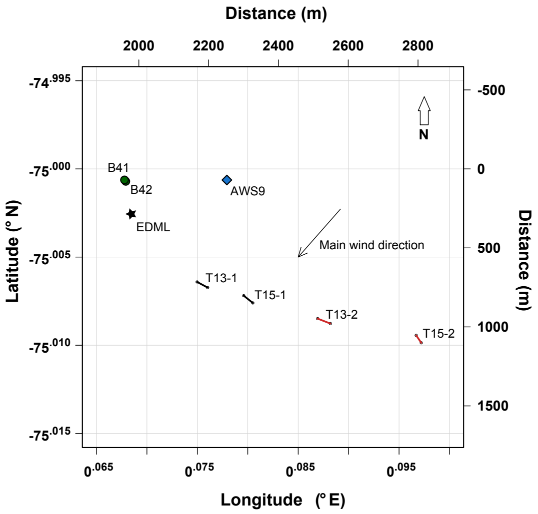

FIGURE 4.2. Map of the study area at Kohnen Station. Snow trenches are shown as black and lines, firn-core sites as green-filled circles. The drilling site of the EPICA Dronning Maud Land (EDML) ice core is shown as a black star, the position of the automatic weather station (AWS9) as a blue-filled diamond. The main wind direction (57° from geographic north, Birnbaum et al., 2010) is indicated with a black arrow. The trenches were aligned perpendicularly to the local snow-dune direction.

sonal cycle of the isotope data of ~ 20 cm (Münch et al., 2016b); the interprofile distance of 5 m corresponds approximately to three times the decorrelation length of the stratigraphic noise observed in the T13 record (Münch et al., 2016b). At both trenches, excavation and subsequent sampling of the profiles was conducted in two consecutive stages (2 times ~ 1 m depth); each stage was completed within 24 h. All firn samples ($N = 1214$) were stored in plastic bags, tightly packed, transported to Germany in frozen state and analysed for oxygen (^{18}O/^{16}O) and hydrogen (^{2}H/^{1}H) isotope ratios at the isotope laboratory of the Alfred Wegener Institute (AWI) in Potsdam, using a cavity ring-down spectrometer (L2130i, Picarro Inc.). The results are reported in the usual delta notation (oxygen isotopes: δ^{18}O, hydrogen isotopes: δD) in per mil (‰) relative to the international VSMOW/SLAP[1] scale. Calibration and correction of the raw measurements was performed as described in Münch et al. (2016b). The mean combined measurement uncertainty is 0.08 ‰ for δ^{18}O (root mean square deviation, RMSD) and 0.8 ‰ for δD, assessed by evaluating a standard not used in the calibration and correction procedure. All data are archived under DOI: `10.1594/PANGAEA.876639` (Münch et al., 2017b).

---

[1] VSMOW (Vienna Standard Mean Ocean Water) and SLAP (Standard Light Antarctic Precipitation) are reference waters with VSMOW being defined as 0 ‰ both for oxygen and hydrogen isotopes, and, by convention, SLAP being fixed to -55.5 and -428 ‰ for δ^{18}O and δD, respectively.

4.2.2 *Trench depth scale*

Following Münch et al. (2016b), we record and display the trench isotope data with respect to an absolute height reference given by the respective maximum of the surface height profile of each trench. Note that the surface layer of the trench records is incomplete on this depth scale (up to $\sim$ 10 cm for T13 and $\sim$ 18 cm for T15) due to the surface undulations. Averaging of trench profiles is performed relative to the absolute height reference. Therefore, the number of data points contributing to a mean profile is lower and varies in the surface layer. This part is marked by dashed lines for all mean profiles and is excluded from all quantitative calculations. Our conclusions are therefore limited to firn depths below $\sim$ 10 cm but are, however, as will be shown, not essentially changed when including the surface layer.

4.2.3 *Spatial variability of average trench profiles*

Spatial variability arising from stratigraphic noise is a major contribution to the overall variability of individual trench isotope profiles (Münch et al., 2016b). Its magnitude ω can be estimated from the horizontal variability of the trench isotope record. Averaging across individual trench profiles reduces the total noise variability. Specifically, stratigraphic noise can be modelled by a first-order autoregressive process with a horizontal decorrelation length for the study region of $\lambda \simeq 1.5\,\mathrm{m}$ (Münch et al., 2016b). Then, the residual noise variability of a mean profile built by averaging across N individual records is

$$\varepsilon_{\mathrm{res}} = \frac{\omega}{N^2}\Big(N + f(N,\, d,\, \lambda)\Big) \equiv \frac{\omega}{N_{\mathrm{eff}}}, \tag{4.1}$$

where $f(N, d, \lambda)$ is a function of N, λ and of the interprofile distances d. Equation (4.1) can equivalently be expressed through the effective number of records, N_{eff}. For independent noise (zero autocorrelation, $\lambda \to 0$), $f(N, d, \lambda \to 0) \to 0$ and thus $N_{\mathrm{eff}} \to N$.

4.2.4 *Quantification of downward advection, firn densification and firn diffusion*

We expect that within two years the original T13 isotope profiles have been compressed through densification of the firn, advected downwards due to new snow fall and affected by firn diffusion. To quantify these effects, certain site-specific parameters have to be known.

Firn densities are provided independently of the trench data by high-resolution X-ray Computer Tomography data (Freitag et al., 2013a) of the firn cores B41 and B42 (core distance $\sim$ 10 m, Laepple et al., 2016) drilled in vicinity to the trenches ($\sim$ 1 km, Fig. 4.2). The

Table 4.2. Sampling and statistical properties of the trench δ^{18}O records from the field seasons 2012/2013 (T13, Münch et al., 2016b) and 2014/2015 (T15, this study). Listed are number and distance of sampled profiles, δ^{18}O values and variance, correlation of mean trench profiles and estimated signal-to-noise variance ratios (SNR) after Münch et al. (2016b). Correlations are maximised through allowing relative vertical shifts (optimal shift given in brackets). 67 % confidence intervals (CI) for the variance estimates account for autocorrelation of the data. Average signal-to-noise ratios are given with an uncertainty of 1 standard error (SE).

Trench record	T13–1	T13–2	T15–1	T15–2
Number of profiles:	38	4	11	11
Profile distances (m):	~ 0.1–2.5	10, 20	5	5
δ^{18}O (‰):				
range: min/max	$-54/-34$	$-50/-38$	$-56/-32$	$-55/-33$
mean (SD)	-44.4 (3.1)	-44.0 (2.7)	-44.7 (3.8)	-44.5 (3.8)
δ^{18}O variance ((‰)^2):				
mean horizontal (67 % CI)	5.9 (5.2–7.0)	5.3 (4.2–7.0)	7.0 (6.1–8.3)	6.6 (5.7–7.7)
mean vertical (67 % CI)	9.5 (8.3–11.1)	7.3 (5.9–9.6)	13.8 (12.0–16.3)	14.2 (12.3–16.8)
Mean profile correlation (optimal shift)	0.81 (+3 cm)		0.91 (-0.5 cm)	
SNR (± 1 SE)	0.9 ± 0.4	0.5 ± 0.5	1.0 ± 0.3	1.5 ± 0.5

average firn density in the first metre is $\sim 330\,\mathrm{kg\,m^{-3}}$. The densification rate relative to the surface is $\sim 2\,\%\,\mathrm{m^{-1}}$ when regressing density against depth over the first 2 m, $\sim 7\,\%\,\mathrm{m^{-1}}$ when regressing over the first 5 m.

The local annual accumulation rate of snow was 28.8 ± 0.4 cm (± 1 standard error) in the year 2013 and 20.8 ± 0.3 cm in 2014, which was estimated from an array of snow stake measurements conducted near the trench excavation sites. In general, the recent local accumulation rate strongly depends on the measurement site, with values ranging from 20–30 cm of snow per year which is up to 50 % larger than the published longtime mean (Table 4.1).

In case of isothermal firn, diffusion of interstitial water vapour leads to overall smoothing of an isotope profile which can be described as the convolution with a Gaussian kernel (Johnsen et al., 2000). The amount of smoothing (the width of the Gaussian convolution kernel) is controlled by the diffusion length σ which increases monotonically in the upper firn layer (Johnsen et al., 2000). We model σ according to Gkinis et al. (2014) with diffusivity after Johnsen et al. (2000). Firn density is the main driver for the depth dependency of the diffusion length. For the calculations we smooth the stacked B41/B42 density data by fitting a quadratic polynomial in the square root of the depth. For the concept of differential diffusion, we consider a firn layer which is located at the average depth z_1 and has thickness Δz over which the increase in diffusion length ($\Delta\sigma$) is small compared to the layer thickness, $\Delta\sigma / \Delta z \ll 1$. Now the firn layer is advected downwards to the depth z_2. The total amount of diffusion that acted since the layer has been at the surface is the convolution of the layer's initial isotope profile at the surface, δ_0, with a diffusion length $\sigma(z_2)$. Equivalently, since the Gaussian convolution is a linear operation, we can express this as the diffusion of δ_0 with $\sigma(z_1)$, followed by diffusion of the resulting profile with the differential diffusion length:

$$\tilde{\sigma} = \sqrt{\sigma^2(z_2) - \sigma^2(z_1)}\,. \tag{4.2}$$

For the T13 isotope profiles, we account for an approximate average effect of differential diffusion over two years by considering the average diffusion lengths calculated over the depth of the T13 profiles before and after downward advection, neglecting the seasonal variations in firn temperature.

4.2.5 *Statistical tests*

We use the Kolmogorov–Smirnov (KS) test to assess whether distributions of differences between mean trench profiles vary. Autocorrelation of the data is accounted for with a modified version of the standard test adopting effective degrees of freedom of $n(1 - a)$ (Xu,

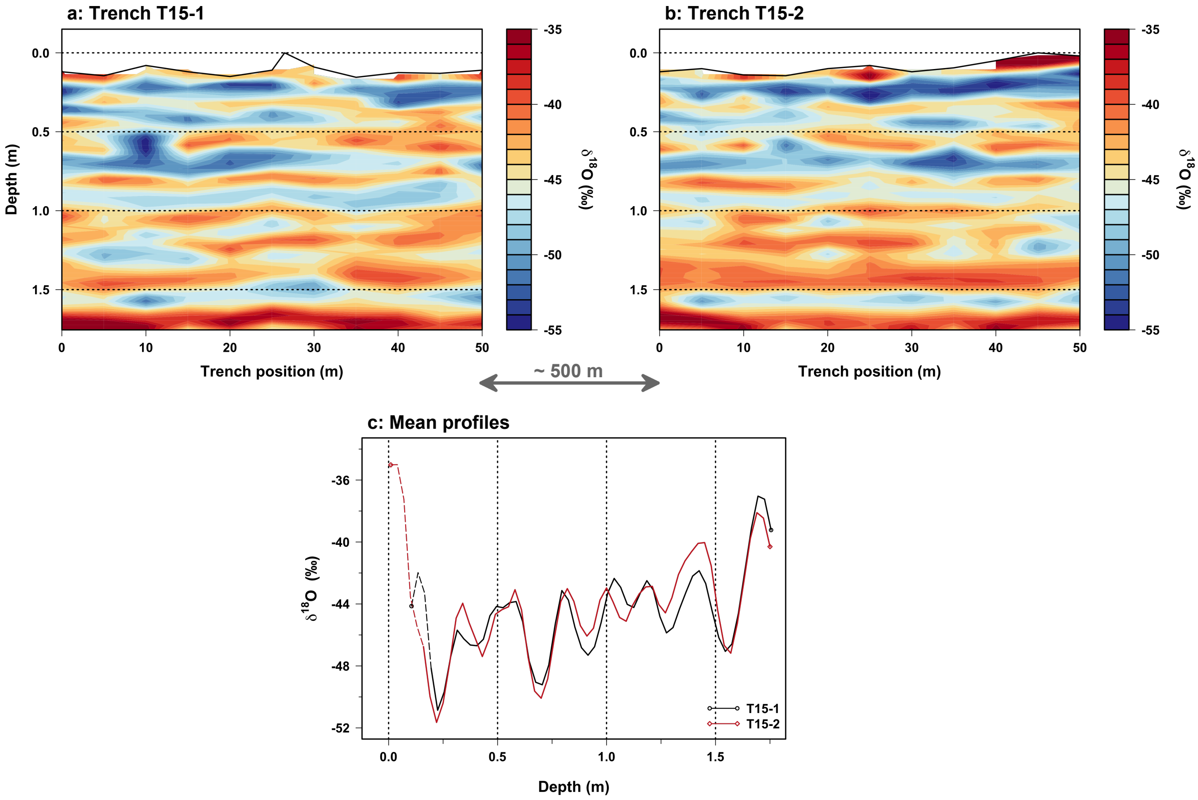

FIGURE 4.3. The new T15 δ^{18}O data set. Displayed are the isotope records of trench T15–1 (**a**) and trench T15–2 (**b**) as two-dimensional colour images, and the mean profiles from averaging across the individual profiles of each trench (**c**), displayed for the optimal vertical shift of the T15–2 mean profile (see text). The trench surface height profiles are given by solid black lines, the near-surface part of each mean profile is marked by dashed lines since the trench data are incomplete there (see Sect. 4.2.2). The vertical scale in (**a, b**) is strongly exaggerated.

2013). Here, n is the total number of data points for each profile and a the estimated autocorrelation parameter at lag 1. The KS test compares the empirical cumulative distribution functions of the data and is thus sensitive to differences in both mean and variance.

4.3 RESULTS

4.3.1 *New T15 isotope data and qualitative comparison with T13*

The two new T15 δ^{18}O trench records measured in 2014/2015 (Fig. 4.3a, b) are qualitatively consistent with the T13 data (Münch et al., 2016b) measured two years earlier. The isotopic variability within the first metres of firn is characterised by roughly horizontal, alternating layers of enriched and depleted isotopic composition (Fig. 4.3a, b) which are separated on average by the annual layer thickness of snow (20–30 cm) and thus likely indicative of the climatic seasonal cycle. In addition, stratigraphic noise leads to significant horizontal variability, visible through discontinuous and inhomogeneous layering as well as patchy features, for example at the surface of trench T15–2 (Fig. 4.3b).

We find similar statistical properties for the data of each trench campaign (Table 4.2). The higher variances in the vertical direction of the T15 records are partly expected for autocorrelated data in combination with a larger record length, in addition to the contribution by the strongly enriched layer around 170 cm depth.

Averaging across all individual profiles of each T15 trench reduces the noise level and yields mean profiles that are highly correlated (correlation $r = 0.91$, RMSD ~ 1.2 ‰, Fig. 4.3c) and thus spatially representative. We maximised this match by allowing vertical shifts of the T15–2 mean profile. Using linearly interpolated data on a resolution of 0.5 cm, we find an optimal shift of -0.5 cm. We note the exceptionally high delta values at the top of the T5–2 mean profile which stem from a prominent dune at the trench surface (Fig. 4.3). However, on the absolute depth scale this top part has no overlap with the T15–1 mean profile and therefore does not contribute to the total T15 mean profile discussed below. Despite their representativity, the T15–1 and T15–2 mean profiles show strong year-to-year variability confirming the discrepancy to local temperature previously found for T13 (Fig. 4.1). This also becomes apparent through the increase in average T15 summer maxima (Fig. 4.3c) which is statistically significant ($p < 0.01$) but not captured by the evolution of local summer temperatures (Fig. 4.1).

Our first findings show that at our study site both the nature of the regional isotope signal and the stratigraphic noise are comparable between the two trench campaigns. In the following sections we quantitatively assess to what extent the original T13 signal can be recovered with the T15 trenches obtained two years later. For this task, we use a single data set for T13 and T15 from averaging across each pair of mean profiles (Fig. 4.4), accounting for the optimal vertical shifts that maximise each intertrench correlation (Table 4.2).

4.3.2 *Expected isotope profile changes between 2013 and 2015*

We analyse to what extent the T13 record can be recovered from the new T15 data, and which changes have modified the original record. Within the two years, we expect that the T13 isotope profiles are advected downwards, compressed by densification and smoothed by firn diffusion. Testing for additional isotope modifications hence requires first estimating the magnitudes of those expected processes. We do this in two ways: firstly, we use data that is independent of the trench records. Secondly, to check consistency with the first estimate, we determine the optimal parameter set that minimises the difference between the T13 and T15 mean profiles.

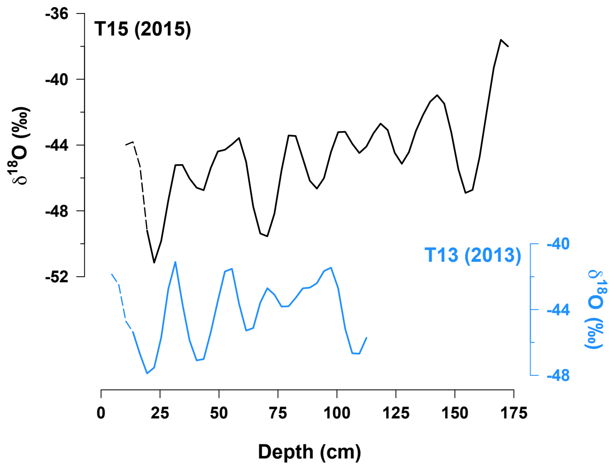

FIGURE 4.4. The mean oxygen isotope profiles of the T15 (this study) and T13 (Münch et al., 2016b) trenches on their original depth scale. The incomplete surface layer of the trenches is marked by dashed lines.

Using the available independent snow stake and density data, we obtain the following estimates: the annual accumulation rates suggest a downward advection of the T13 profiles after two years of $\sim 50\,\text{cm}$. Further, we expect additional diffusional smoothing of the T13 δ^{18}O profiles according to a differential diffusion length (Eq. 4.2) of $\tilde{\sigma} \sim 1.9\,\text{cm}$. The estimated densification rate at the study site of ~ 2–$7\,\%\,\text{m}^{-1}$ implies a compression of the T13 profiles after two years of approximately 1–4 cm.

For the second estimate, we vary the three parameters (downward advection Δ, differential diffusion length $\tilde{\sigma}$, compression γ) in order to minimise the root mean square deviation between the T15 and T13 mean profiles. To avoid an influence on our results, we choose the range of tested parameter values independently of the trench data: for the downward advection, we apply vertical shifts between 40 and 60 cm, comprising the snow-stake-based range of the recent annual accumulation rates. We vary the differential diffusion length from 0 to 8 cm, which is equivalent to additional diffusional smoothing of the original T13 mean profile from zero to the maximum possible amount at the firn–ice transition. Finally, compression is applied for values between 0 and 10 cm (equivalent to 0 to $\sim$ 5 times the observed average densification rate). We obtain the best agreement (RMSD $= 0.92\,‰$, Fig. 4.5; $r = 0.93$) between the T15 and the modified T13 mean profile ($=$T13*) for the optimal parameters $\Delta_{\text{opt}} = 50.5\,\text{cm}$, $\tilde{\sigma}_{\text{opt}} = 2.3\,\text{cm}$ and $\gamma_{\text{opt}} = 3.5\,\text{cm}$ (Fig. 4.6). These trench-based parameter estimates agree reasonably well with the independent estimates from above, showing that the trench data are compatible with our assumptions and parameterisations for downward advection, densification and diffusion. Indeed, using the independent parameter estimates ($\Delta_{\text{ind}} = 50\,\text{cm}$, $\tilde{\sigma}_{\text{ind}} = 1.9\,\text{cm}$, $\gamma_{\text{ind}} = 2.2\,\text{cm}$ from mean over

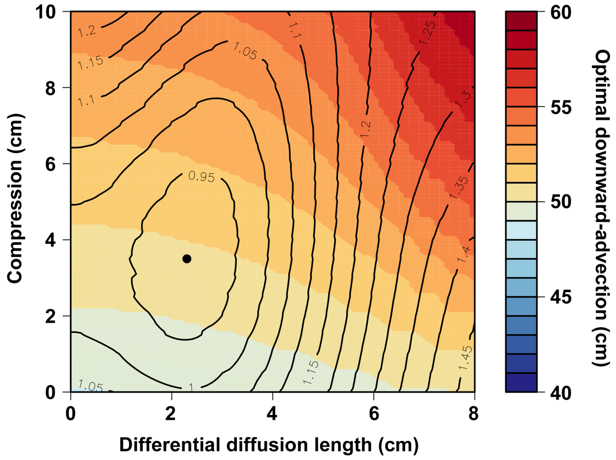

FIGURE 4.5. Effect of downward advection, firn diffusion and linear compression due to densification on the misfit (root mean square deviation, RMSD) between the T15 and the modified T13 mean profile. We record the RMSD for each point in the three-dimensional parameter space of downward advection, compression and diffusion. For each diffusion–compression pair, the figure shows the local minimum in RMSD (contour lines) from varying across the range of advection values, hence the RMSD for the optimal downward advection (colour scale). The global minimum in RMSD is marked with a black dot. Varying the downward advection has in fact the largest influence on the RMSD.

estimated densification rate) to modify the original T13 mean profile (= T13**) results in a deviation from T15 (RMSD $= 0.94\,‰$, $r = 0.93$) that is only slightly higher compared to T13*.

We note that the largest portion of optimising the fit between T15 and T13* is accounted for by the downward advection. This is obvious from only shifting the T13 mean profile vertically to find the maximum correlation with T15, without accounting for diffusion and densification. We find an optimal shift of 48.5 cm ($r = 0.88$) with a minimum misfit of RMSD $= 1.07\,‰$ (Fig. 4.5). Thus, the gain in RMSD is only small when adding diffusion and densification according to T13* (black dot in Fig. 4.5) or T13**, but still appears significant given the above-found consistency in the magnitude of the trench-based and independent estimates. This is further supported by the fact that no second minimum in RMSD exists outside the region bounded by the contour line of only downward advection (RMSD $= 1.07\,‰$, Fig. 4.5) where the magnitudes of diffusion and densification are unrealistically high.

The visual agreement of the trench mean profiles after modifying T13 according to downward advection, diffusion and densification is remarkable regarding cyclicity and, to a lesser extent, the amplitude of the isotope variations (Fig. 4.6b). However, deviations occur throughout most of the record's overlap (Fig. 4.6b) and are even amplified where the amplitude of the T13 profile prior to dif-

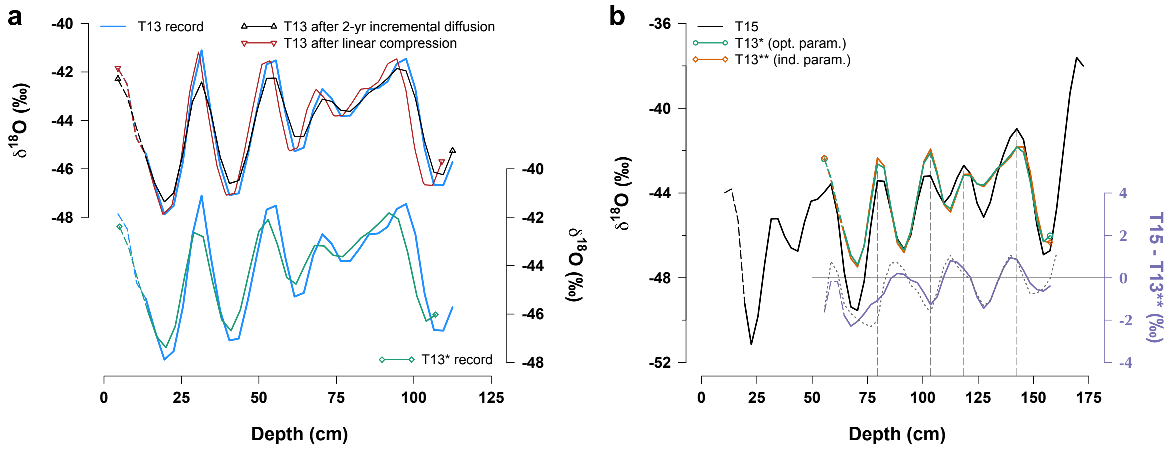

FIGURE 4.6. Expected changes of the T13 and comparison to the T15 mean profile. (**a**) Upper panel: the original T13 mean profile (blue) and its modification by diffusion (black: 2-year diffusion with differential diffusion length $\tilde{\sigma} = 2.3\,\text{cm}$) as well as densification (red: linear compression of $\gamma = 3.5\,\text{cm}$). Lower panel: the original T13 mean profile (blue) compared to the joint effect of 2-year diffusion and linear compression (green, T13*). (**b**) The T15 mean profile (black) in comparison to the T13 mean profile after modifying the latter according to (1) the optimal parameters for downward advection, incremental diffusion and linear densification (green, T13*) and to (2) the corresponding parameters obtained independently from the trench records (orange, T13**). Additionally, the difference between T15 and T13** is shown (violet lines, axis to the right). For comparison, the grey dotted line marks the difference between T15 and T13 only shifted optimally ($\Delta = 48.5\,\text{cm}$). Vertical dashed lines indicate the isotopic summer maxima which are not in phase with the difference curve.

fusion was smaller than for T15 (depths of $\sim 70\,\text{cm}$ and around ~ 125–$140\,\text{cm}$). Here, locally additional diffusion does not lead to an improved match, although overall it reduces the mismatch between the profiles (Fig. 4.5). In general, the profile deviations are relatively large compared to the influence of firn diffusion and densification on the original T13 profile (Fig. 4.6a), which calls for studying further processes in order to explain them.

4.3.3 *Do the remaining differences represent temporal or spatial variability?*

We have shown that downward advection, firn diffusion and densification contribute to the temporal modification of the original T13 profiles as expected from independent data and theoretical considerations. Taking these processes into account leads to a good match of the trench mean profiles (Fig. 4.6b). Most of the match is achieved by accounting for the downward advection; adding the effects of diffusion and densification yields a slightly greater improvement (gain in RMSD of $\sim 0.15\,‰$). However, deviations between the profiles on the order of $\sim 1\,‰$ RMSD still remain. These can have two causes: firstly, additional temporal changes driven by unaccounted post-depositional processes such as firn ventilation or sublimation; secondly,

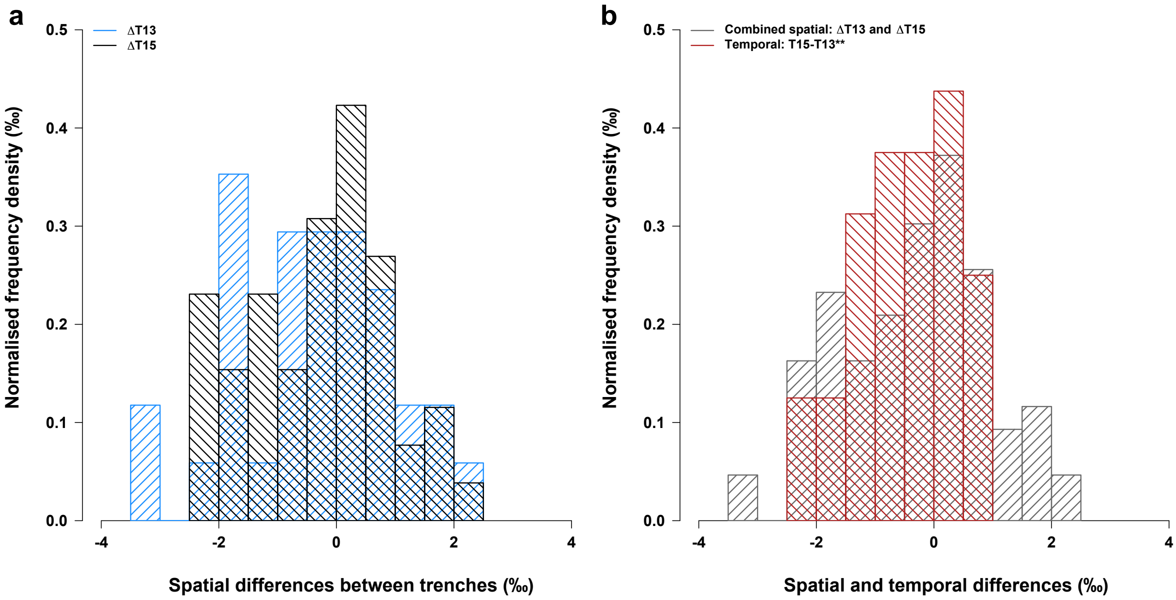

FIGURE 4.7. Variability of the trench data sets. The histograms depict (**a**) the distribution of the spatial differences between the two mean profiles of the T13 (T13–1 vs. T13–2, blue) and the T15 trenches (T15–1 vs. T15–2, black), and (**b**) the combined distribution from (**a**) (grey) compared to the distribution of the temporal differences between the T15 and the T13** mean profiles (red). All distributions' mean values are not significantly different from zero (all $p \geq 0.4$, accounting for autocorrelation).

remaining spatial variability, since we average a large but finite number of records which do not originate from the exact same position. We can thus deduce the importance of additional post-depositional change for our study site if we quantify the contribution of spatial variability. In the following, this is done in two ways: (1) by using the statistical model for stratigraphic noise and (2) by analysing the distributions of the profile differences.

According to the statistical noise model, the effective number of profiles that contribute to the T13 and T15 mean profiles (Eq. 4.1) is $N_{\text{eff}} = 13$ for T13 and $N_{\text{eff}} = 20$ for T15. The residual noise of the mean profiles arising from spatial variability is thus the noise level before averaging ($\omega \sim 5$–7 (67 % CI: 4–8) $(‰)^2$, Table 4.2) divided by 13 and 20, respectively. We assume that the residual noise terms are independent of each other. Therefore, the uncertainty of the difference between the T13 and T15 mean profiles due to stratigraphic noise is the sum of each residual spatial variability or ~ 0.6–0.9 (0.5–1.0) $(‰)^2$. For comparison, the square of the RMSD between the T13* (T13**) and T15 mean profile (the temporal variability) is 0.85 (0.88) $(‰)^2$. This agreement between RMSD and estimated residual spatial variability indicates that the remaining profile differences between the modified T13 mean profile and T15 (Fig. 4.6b) are likely consistent with stratigraphic noise. We note, however, that the squared RMSD lies towards the upper end of the estimated range of residual stratigraphic noise. This also applies to the RMSD between the T15–1 and

T15–2 mean profiles (square of RMSD of $1.44\,(‰)^2$ vs. uncertainty from residual stratigraphic noise of $\sim$ 1.0–1.4 (0.8–1.6) $(‰)^2$). This could indicate that part of the spatial variability on the scale of the intertrench distances ($\sim$ 500 m) is not explained by our stratigraphic noise model.

We therefore make a formal statistical test comparing spatial and temporal variability, which accounts for the full extent of spatial uncertainty and makes no assumption about the covariance of the noise, by analysing the deviations between the mean trench profiles. We find that the spatial differences between the mean profiles of each trench campaign (T13–1 vs. T13–2 and T15–1 vs. T15–2, Fig. 4.7a) are statistically indistinguishable ($p > 0.5$ from modified KS test, combining all possible directions of calculating the differences), meaning that the statistical distributions of the intertrench-scale spatial variability are not significantly different between the years 2013 and 2015. This suggests that we can combine these spatial differences as a joint measure of spatial variability and compare them to the temporal differences between the T15 and the modified T13 mean profile (Fig. 4.7b). By applying the modified KS test once more, again the null hypothesis that both differences follow the same distribution cannot be rejected (all $p > 0.5$ for using $\mathrm{T13}^{**}$ to avoid overfitting). Thus, the temporal differences between $\mathrm{T13}^{**}$ and T15 likely just arise from the fact that the trenches have different locations and can be therefore explained by spatial variability alone.

In summary, both methods show no evidence for any temporal changes of the trench record over the course of two years apart from downward advection accompanied by firn diffusion and densification. The remaining deviations that are observed between the mean profiles of the two trench campaigns can be entirely explained by residual spatial variability arising from stratigraphic noise.

4.4 DISCUSSION

We presented and analysed a new extensive data set of 22 oxygen isotope profiles obtained at Kohnen Station from two 50 m long and $\sim$ 180 cm deep snow trenches. The new trench campaign was designed such that it allows for a direct comparison with a trench data set obtained from the same site two years earlier in order to test for post-depositional effects. In the following, we first discuss our results concerning the expected processes that have influenced the trench isotope profiles over the observed time period, then we discuss our findings regarding the possibility of additional post-depositional changes.

4.4.1 *Densification, diffusion and stratigraphic noise*

We found a strong resemblance between the mean oxygen isotope profiles from the trench field campaigns of 2013 and 2015 (Fig. 4.6b), achieved mostly by accounting for the downward advection and further improved by adding the effects of water vapour diffusion within the firn and firn densification that occurred over the two years (Fig. 4.5). The estimated magnitudes of these processes obtained from matching both records are consistent with independent estimates from snow stakes, diffusion theory and independent density profiles.

The estimated small compression of the T13 profiles is reasonable given the low densification rate observed in the top metres of nearby firn cores. However, our assumption of a linear profile compression with depth is certainly a rough approximation given the actually observed seasonal firn density variation (Laepple et al., 2016), which might indicate a stronger density change with depth of summer compared to winter layers. However, in general the seasonality of densification in Antarctic firn is largely unclear (Laepple et al., 2016, and references therein).

Our data-based estimate of differential firn diffusion agrees with theoretical expectations and in total leads to a further reduction in RMSD between the T13 and T15 mean profiles compared to the case of downward advection and densification alone (Fig. 4.5). More specifically, the diffusion correction improves the match of the trench mean profiles in the medium depth range but also results in higher deviations of the profile minima at the top and bottom parts of the overlap (Fig. 4.6), where the amplitude of the T13 profile had been smaller than for T15 already prior to diffusion. Part of this mismatch might be reduced by accounting for the seasonally varying firn temperature resulting in stronger (weaker) attenuation of summer (winter) layers caused by the seasonal difference in diffusion length which is largest close to the surface (Simonsen et al., 2011). In general, firn diffusion is still an active area of research (van der Wel et al., 2015a), and progress in this field could conceivably result in an improved understanding of our data.

Stratigraphic noise is a major contribution to the overall variability of isotope profiles (Fisher et al., 1985; Karlöf et al., 2006; Münch et al., 2016b). Our large trench data set allows a significant reduction of the noise level by averaging across the single profiles. This is done in two steps: first we average across the local (intra-trench) scale, then we average the resulting mean profiles to account for potential uncertainties on the 500 m (intertrench) scale. Furthermore, we can estimate the remaining uncertainty of the trench mean profiles based on our theoretical understanding of stratigraphic noise. As a result, we found that the difference of the T13 and T15 mean profiles still exhibits an uncertainty of ~ 0.77–$0.95\,‰$ (SD). Thus, the trench data allow us to detect any additional post-depositional changes of the T13 profiles that exceed a detection limit of $\sim 1\,‰$ RMSD. Obviously, a lower detection limit would be beneficial but is in practice constrained by the amount of field work, given the high local stratigraphic noise level as observed from the mean horizontal isotope variability (Table 4.2).

4.4.2 *Additional post-depositional modifications*

Based on the above results we have shown that the remaining differences between the 2013 and 2015 data sets are, after accounting for downward advection, firn diffusion and densification, likely consistent with spatial variability from stratigraphic noise. In other words, we conclude that at our study site the impact of any additional post-depositional changes of the isotopic composition of the firn below $\sim 10\,\mathrm{cm}$ is on average below the residual stratigraphic noise level, thus $\ll 1\,‰$ RMSD. We limited our conclusion to this depth range due to the applied absolute depth scale resulting in a lower and varying number of available data points in the surface layer. However, looking at this part of the modified T13 mean profile (dashed lines of $\mathrm{T13}^{*}$ or $\mathrm{T13}^{**}$, Fig. 4.6b) also does not show any solid evidence of additional post-depositional changes.

Our conclusion is also supported by comparing the nature of the differences between the mean profiles (Fig. 4.6b) with the expected effect of post-depositional modification processes. Studied processes all point to isotopic enrichment, such as sublimation (Stichler et al., 2001; Sokratov and Golubev, 2009) and wind-driven firn ventilation (Town et al., 2008). Specifically, the latter modelling study showed that firn ventilation can result in isotopic annual-mean enrichment from the strong enrichment of isotopic winter layers, compensating an observed slight depletion of summer layers. For South Pole conditions (annual-mean temperature $-50\,°\mathrm{C}$, accumulation rate $84\,\mathrm{mm\,w.e.\,yr^{-1}}$, mean surface wind speed $5\,\mathrm{m\,s^{-1}}$), the effect amounts to $\sim 3\,‰$ for firn ventilation until the layers are advected below the influence of the atmosphere, thus after several years (Town et al., 2008). The environmental conditions at the South Pole are comparable to Kohnen Station (Table 4.1), suggesting a similar influence of ventilation on the isotopic composition of the firn. The higher temperatures at Kohnen Station would even imply a slightly stronger enrichment (Town et al., 2008). However, if we analyse the difference curve of the T15 and $\mathrm{T13}^{**}$ mean profiles (Fig. 4.6b) we find no evidence for firn ventilation. Comparing the direct seasonal counterparts, the first winter layer, which was closest to the surface at the time of excavation of T13 and thus presumably being under strongest influence of the atmosphere, is more depleted in isotopic composition in T15 than in $\mathrm{T13}^{**}$, in contrast with the expectation from firn ventilation. Moreover, despite the fact that the first three summer layers exhibit more depleted values, which would be in line with ventilation, the remaining summer layers do not confirm this finding, and none of the average annual differences show enrichment: for the first annual cycle, T15 exhibits an average difference from $T13^{**}$ of -1.6 ‰ (-1.3 ‰ including the surface region), for the other annual cycles the averages are -0.4, ± 0 and -0.1 ‰. Also in general, the difference curve (Fig. 4.6b) does not show any clear seasonal timing which might be expected for a systematic post-depositional modification. Instead, minimum and maximum differences appear rather randomly across the seasons. In addition, the global average difference of about -0.45 ‰ is not significantly different from zero ($p = 0.4$, accounting for autocorrelation). We nevertheless note that the RMSD of the first overlapping annual cycle is above our stated detection limit for post-depositional change. However, this limit applies to the average over the record's entire overlap and does not account for the possibility of autocorrelated differences. Finally, we note the seeming increase with depth of the annual-mean differences towards more positive values (Fig. 4.6b), which is also indicated by the slight skewness of the corresponding histogram (Fig. 4.7b). However, the trend is not strongly significant ($p = 0.12$, accounting for autocorrelation), and the KS test of the distribution of the differences showed that mean and variability of the residual temporal differences are likely explained by the spatial distribution alone. In addition, we obtain similar results (not shown) when we apply our analysis to the trench d-excess ($d := \delta\text{D} - 8 \cdot \delta^{18}\text{O}$) data, a second-order parameter that is potentially more sensitive to post-depositional fractionation processes (Touzeau et al., 2016). The spatial and residual temporal differences between the corresponding d-excess mean profiles follow the same distribution ($p > 0.5$), and the histogram of the temporal differences is even more symmetric than for $\delta^{18}\text{O}$.

In summary, all evidence suggests that post-depositional modifications from firn ventilation or sublimation are unlikely to contribute to the deviations between the T15 and the modified T13 mean profiles and that the shape of the difference curve only arises from the statistical nature of stratigraphic noise, smoothed by diffusion. We nevertheless note the possibility that additional post-depositional changes are still present at Kohnen Station but not detectable in our analysis. Wind-driven firn ventilation might exist with an effect that is, however, much weaker than expected and thus masked by the stratigraphic noise level. One possible explanation for the discrepancy between the firn ventilation model results and our data could be that the model misrepresents the isotopic signature of the surface vapour advected into the firn. Another possibility is weaker firn temperature gradients at Kohnen Station compared to the South Pole, preventing significant vapour deposition. Assessing these possibilities in detail is, however, beyond the scope of our study. Interestingly, if the seeming trend in difference values was significant, it would suggest an oriented post-deposition process that is yet unknown. In any case, the stronger profile differences for the first overlapping annual cycle might indicate modification processes that are constrained to the very surface layer. In addition, the RMSD between T15 and T13* can be further minimised if one allows shifts in the mean value of the T13 profile (new minimum RMSD of -0.82 ‰ for a shift in mean of -0.4 ‰) which is an interesting observation, yet without any obvious explanation. However, based on the presented evidence, these possibilities are speculative and further field studies are needed to test them.

Our study underlined the pronounced discrepancy at Kohnen Station between interannual variations of isotope ratios in the firn and local temperatures and showed that this feature is not only spatially (over distances of ~ 500 m) but also temporally representative over a period of two years. Furthermore, given the sum of our above findings, it is unlikely that post-depositional modifications of the isotopic composition of the open-porous firn (below depths of ~ 10 cm and probably also not in shallower depths) are the cause of the observed discrepancy. Since a strong relationship between isotopes in precipitation samples and local temperature has been observed at different sites of the Antarctic Plateau (Fujita and Abe, 2006; Touzeau et al., 2016), this cause must instead be sought in processes working directly at or above the firn surface. At least two explanations for this seem possible. (1) Seasonal variation and intermittency of precipitation cause the discrepancy between isotope and local temperature data (Sime et al., 2009, 2011; Persson et al., 2011; Laepple et al., 2011). At Kohnen Station, a large part of the annual accumulation is assumed to occur in winter since little or no precipitation is observed in the summer field seasons. However, the exact seasonal and interannual variation of accumulation is still unclear due to the lack of sufficiently precise, year-round observations (Helsen et al., 2005). The available surface height changes derived from sonic altimeters of automatic weather stations are difficult to separate into events of drifting snow and true snowfall (Reijmer and van den Broeke, 2003). (2) Isotope modification occurring directly at or above the surface is the key driver for shaping the interannual isotope variations. Such processes might be acting on falling, loose or drifting snow, or on the top layer (first few centimetres) of deposited snow (Ritter et al., 2016; Casado et al., 2016). The fact that our trench records are reproducible on spatial scales of at least 500 m implies that the atmospheric parameters and conditions controlling potential processes would also need to be spatially coherent.

4.5 CONCLUSIONS

Many studies, including our present one, show that interannual isotope records from the dry Antarctic Plateau are inconsistent with local temperature variations. However, beyond simply stating the problem, we take two steps further: (1) we use the average over 2×11 isotope profiles to obtain a spatially representative record. (2) We designed our study such that it allows for testing for post-depositional effects over a time span of two years.

Our results provide important constraints on the formation of the stable water isotope signal and its propagation with depth in East Antarctic firn: the trench records show a pure downward advection of the isotope signal within the open-porous firn ($\gtrsim 10\,\mathrm{cm}$ depth), further influenced only by firn diffusion and densification, with no evidence for substantial additional post-depositional modification. Hence, once the signal is archived at this stage, we do not expect any significant change in the mean values deeper down, reinforcing the credibility of palaeoclimate studies using ice core isotope data. However, from our analysis we can constrain post-depositional changes only down to the level of stratigraphic noise. Therefore, qualitatively, firn ventilation and sublimation might still be present with effects that are, however, very small or constrained merely to the surface layer for which the lower number of data points in our study prevents quantitative analyses. These constraints lead us to conclude that the observed discrepant isotope–temperature relationship on the interannual timescale must be caused either by processes prior to or during deposition.

To improve our understanding of the interannual isotope signal, we suggest a mixture of field and modelling efforts. Year-long isotope studies (e.g., in seasonal intervals) with a focus on the near surface would help to constrain isotope modifications at the interface of surface snow and atmosphere. Further, the role of precipitation and accumulation intermittency has to be clarified, e.g., through measuring wet-deposition tracers and improved accumulation measurements. These studies should optimally be accompanied by monitoring and modelling the atmospheric water vapour isotopic composition as well as modelling the potential exchange and fractionation processes between the loose or deposited snow at the surface and the overlying atmosphere.

Our results again underline the role of stratigraphic noise for the total variability of isotope records. Spatial averaging is thus essential for improving the signal-to-noise ratio and thereby separating spatial from temporal variability. Alternatively, single records can only be compared faithfully for temporal changes when their spatial separation is well below the spatial decorrelation length of the stratigraphic noise, which minimises the amount of spatial variability between the records. The effects of potential isotope modifications depend substantially on the time the surface is exposed to the atmosphere, thus on accumulation rate and seasonal timing of precipitation. Comparable recovering efforts at other ice-coring sites are hence highly needed. Our data indicate that present models might overestimate the expected influence of wind-driven firn ventilation; however, regions with higher wind speeds and lower accumulation rates might still be susceptible towards post-depositional changes within the open-porous firn. A deeper understanding of the isotope signal formation in Antarctic firn is, beyond holding intrinsic interest, essential for deciphering the temperature signal archived in ice core records and thus crucial for their palaeoclimatic interpretation.

5

ON THE SIMILARITY AND APPARENT CYCLES OF ISOTOPIC VARIATIONS IN EAST ANTARCTIC SNOW PITS

THOMAS LAEPPLE[1], THOMAS MÜNCH[1,2], MATHIEU CASADO[3], MARIA HOERHOLD[4], AMAELLE LANDAIS[3], AND SEPP KIPFSTUHL[4]

[1]*Alfred Wegener Institute Helmholtz Centre for Polar and Marine Research, Telegrafenberg A43, 14473 Potsdam, Germany*
[2]*Institute of Physics and Astronomy, University of Potsdam, Karl-Liebknecht-Str. 24/25, 14476 Potsdam, Germany*
[3]*Laboratoire des Sciences du Climat et de l'Environnement – IPSL, UMR 8212, CEA-CNRS-UVSQ, Gif sur Yvette, France*
[4]*Alfred Wegener Institute Helmholtz Centre for Polar and Marine Research, Am Alten Hafen 26, 27568 Bremerhaven, Germany*

This chapter is published in:
The Cryosphere, **12** (1), 169–187, DOI: `10.5194/tc-12-169-2018`, 2018.

ABSTRACT. Stable isotope ratios δ^{18}O and δD in polar ice provide a wealth of information about past climate evolution. Snow-pit studies allow us to relate observed weather and climate conditions to the measured isotope variations in the snow. They therefore offer the possibility to test our understanding of how isotope signals are formed and stored in firn and ice. As δ^{18}O and δD in the snowfall are strongly correlated to air temperature, isotopes in the near-surface snow are thought to record the seasonal cycle at a given site. Accordingly, the number of seasonal cycles observed over a given depth should depend on the accumulation rate of snow. However, snow-pit studies from different accumulation conditions in East Antarctica reported similar isotopic variability and comparable apparent cycles in the δ^{18}O and δD profiles with typical wavelengths of $\sim$ 20 cm. These observations are unexpected as the accumulation rates strongly differ between the sites, ranging from 20 to 80 mm w.e. yr^{-1} ($\sim$ 6–21 cm of snow per year). Various mechanisms have been proposed to explain the isotopic variations individually at each site; however, none of these are consistent with the similarity of the different profiles independent of the local accumulation conditions.

Here, we systematically analyse the properties and origins of δ^{18}O and δD variations in high-resolution firn profiles from eight East Antarctic sites. First, we confirm the suggested cycle length (mean distance between peaks) of $\sim$ 20 cm by counting the isotopic maxima. Spectral analysis further shows a strong similarity between the sites but indicates no dominant periodic features. Furthermore, the apparent cycle length increases with depth for most East Antarctic sites, which is inconsistent with burial and compression of a regular seasonal cycle. We show that these results can be explained by isotopic diffusion acting on a noise-dominated isotope signal. The firn diffusion length is rather stable across the Antarctic Plateau and thus leads to similar power spectral densities of the isotopic variations. This in turn implies a similar distance between isotopic maxima in the firn profiles.

Our results explain a large set of observations discussed in the literature, providing a simple explanation for the interpretation of apparent cycles in shallow isotope records, without invoking complex mechanisms. Finally, the results underline previous suggestions that isotope signals in single ice cores from low-accumulation regions have a small signal-to-noise ratio and thus likely do not allow the reconstruction of interannual to decadal climate variations.

5.1 INTRODUCTION

Stable isotope δ^{18}O and δD records from ice cores can be used to infer past local temperature variations (Dansgaard, 1964) and as such are an important climate proxy at interannual to glacial–interglacial timescales (Jouzel et al., 2007; Johnsen et al., 2001). The ice thickness and accumulation rate affect the temporal scale and resolution of the climate reconstructions that can be obtained from a given ice core. In central East Antarctica, low accumulation rates and deep ice cores allow climate reconstructions to be made that cover the last 800 000 years (EPICA community members, 2004), while the higher accumulation rates in coastal areas allow for higher-resolution reconstructions in which the seasonal climate signal can be recovered from the ice isotopic composition (Morgan, 1985; Masson-Delmotte et al., 2003; van Ommen and Morgan, 1997; Küttel et al., 2012).

High-resolution isotope data, thought to correspond to subannual variations, are now routinely measured at deep ice-core sites (Gkinis et al., 2011); however, it is unclear to what extent isotope signals on timescales shorter than multidecadal can be interpreted as indicating climate (Ekaykin et al., 2002; Baroni et al., 2011; Pol et al., 2014; Münch et al., 2016b), especially for the low-accumulation regions that are typical on the Antarctic Plateau ($< 100\,\mathrm{mm\,w.e.\,yr^{-1}}$). As the link is complex between isotopic composition and the climatic conditions creating them (Jouzel et al., 1997), numerous studies have sampled the upper metres of firn in order to compare the isotopic variations with instrumental climate data (Masson-Delmotte et al., 2008; Fernandoy et al., 2010; Steen-Larsen et al., 2014). Many of these have reported oscillations in snow-pit records from the Antarctic Plateau, including those at Vostok, Dome C (EDC), Dome A, Dome F (DF), South Pole (SP) and Kohnen Station at the EPICA Dronning Maud Land drilling site (EDML) (Jouzel et al., 1983; Petit et al., 1982; Ekaykin et al., 2002; Hoshina et al., 2014, 2016; Münch et al., 2016b). Interestingly, despite the very different accumulation rates at these sites, which range from 6 to 21 cm of snow per year, their isotope profiles appear to have very similar peak-to-peak distances (Fig. 5.1), and a recent systematic counting effort of isotopic maxima in firn profiles (Casado et al., 2017) suggested a characteristic wavelength of 15–25 cm across all analysed East Antarctic sites.

For sites such as EDML and SP, their apparent cycle lengths match well with their annual snow layer thicknesses and consequently their cycles have been explained as reflecting seasonal climate variation (Oerter et al., 2004; Münch et al., 2016b; Jouzel et al., 1983; Whitlow et al., 1992). However, this explanation is not consistent with the same cycle length being observed at lower accumulation sites, where the annual snow layer thickness is often less than 10 cm (Petit et al., 1982). Instead, a range of alternative explanations have been proposed for the oscillations at individual sites. At Vostok, Ekaykin et al. (2002) attributed the oscillations to horizontally moving dunes (Frezzotti et al., 2002) leading to isotopic cycles during burial. However, similar cycles are found at core sites with different dune features, wind speeds and accumulation rates, and thus a varying speed of dune movement and burial. At EDC, Petit et al. (1982) explained the mismatch between seasonal and isotopic cycles as being due to missing years resulting from the combined effects of successive precipitation-free months, erosion associated with blowing snow and firn diffusion. In a multi-site study, Hoshina et al. (2014, 2016) suggested that the multi-year oscillations could be formed by the combination of variable accumulation and post-depositional modifications, such as ventilation. Finally, the coarse sampling resolution in some studies (5 cm or longer) would not resolve the seasonal cycle, but similar characteristics were found for profiles sampled at a range of resolutions (Ekaykin et al., 2002). Thus, none of the existing interpretations explain why the apparent observed cycles are so similar across sites and largely independent of the accumulation rate and related climatic conditions.

Here we combine a statistical analysis of isotope profiles from eight Antarctic Plateau sites with theoretical considerations and numerical simulations of the firn signal. We suggest that the presence of apparent cycles in the firn, and their largely invariant length, can be explained by a combination of deposition-related noise in the surface isotope signal and isotopic diffusion (Johnsen et al., 2000), which is rather constant across the Antarctic Plateau.

5.2 DATA AND METHODS

We first introduce the data set and the method used to compare the power spectral density of observed isotope profiles with those from a null model of diffused noise. We then provide an analytic solution for the expected distance between isotopic maxima (“cycle length”) and a method to estimate this cycle length from the observed firn

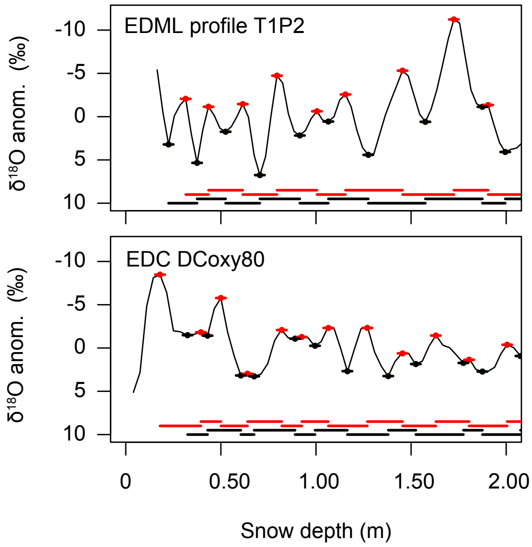

Figure 5.1. Example isotope profiles from EDML and EDC. Both profiles are visually similar despite the differing time periods covered, ∼ 10 yr for EDML and ∼ 25 yr for EDC, and annual snow layer thicknesses, ∼ 21 cm for EDML and ∼ 8 cm for EDC. Also shown is an example of the automatic estimation of isotopic cycle length. Red and black dots show the identified maxima and minima. The short horizontal lines overlaying these dots indicate the ±6 cm region a maximum (minimum) must be above (below) to be identified as an extremum. The longer black and red horizontal lines at the bottom of the figure indicate the identified distances between subsequent maxima or minima. For more examples of isotope profiles see Casado et al. (2017).

profiles. Finally we provide a minimal numerical forward model for the isotopic variations.

5.2.1 *Data*

We analyse data from eight sites on the Antarctic Plateau, for which vertical isotope profiles of δ^{18}O or δD are available with lengths of at least 2 m and minimum resolutions of 3.5 cm per sample (Fig. 5.2 and Table 5.2 on p. 104). We focus our analysis on the upper 4 m of firn within which cycles have been described and interpreted. For SP and EDML, a combination of snow-pit and shallow firn-core data allows us to extend the analysis down to a snow depth of 18 m. All records have been published (Table 5.2), except those for EDML for which we use 22 3.4 m deep profiles sampled from snow trenches (T15) as described and partly analysed in Münch et al. (2017a), together with new isotope data from the firn cores B41 and B50. These two cores were drilled close to Kohnen Station in 2012–13, approx-

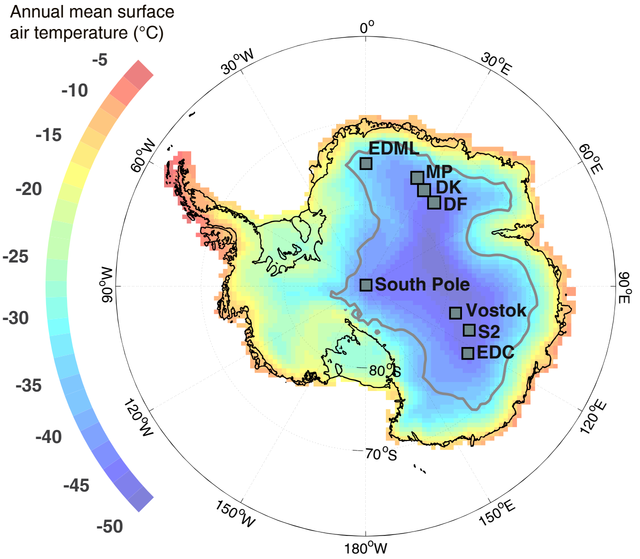

FIGURE 5.2. Location of the sampling sites used in this study (solid squares). The 2500 m a.s.l. elevation contour is marked by a grey line; colours indicate the annual mean surface air temperature (Nicolas and Bromwich, 2014).

imately 1 km apart (Alfred-Wegener-Institut Helmholtz-Zentrum für Polar- und Meeresforschung, 2016). Isotope ratios were analysed at a resolution of 3 cm, using a laser instrument at the Alfred Wegener Institute (AWI) in Bremerhaven and following the protocol described in Masson-Delmotte et al. (2015).

5.2.2 *Spectral analysis*

Spectra are estimated using Thomson's multitaper method with three windows (Percival and Walden, 1993). The depth profiles are linearly detrended before analysis. For profiles with non-equidistant sampling, the data are interpolated to the lowest resolution after low-pass filtering to avoid aliasing effects as described in Laepple and Huybers (2013). In the case of multiple profiles at a single site we show the mean of the individual spectra.

Significance testing of the power spectral density is performed against a null hypothesis of noise affected by firn diffusion. More specifically, we assume the sum of white (temporally independent) noise subject to isotopic diffusion with a depth-dependent diffusion length and additive white measurement noise. The diffusion length is calculated using the site-specific accumulation rates as well as temperature and density profiles as described in Sect. 5.2.5. There is no simple closed form expression for the power spectrum of a diffused signal under varying diffusion lengths. We thus resort to a Monte Carlo procedure by simulating diffused white noise profiles on a 2 mm resolution, resampling them to the actual resolution of the observed profiles to include the effect of discrete sampling, adding measurement noise and then estimating the spectra on these surrogate data sets using the same method as for the observed profiles. The variance of the diffused white noise signal and the measurement noise are free parameters and are chosen to minimise the root mean square deviation of the observed and the null-hypothesis spectrum. Finally, we scale the null-hypothesis spectrum by the 95 % quantiles of a χ^2 distribution to obtain critical significance levels. These mark the range of spectral power expected if the time series were diffused noise. This level has to be overcome for a peak to be locally (thus at a given frequency) significant. The degrees of freedom (DOF) of the χ^2 distribution are the product of the DOF from the spectral estimator and the effective number of independent profiles. We assume independence between profiles for all sites except for the EDML trench data. For this data set consisting of 22 nearby profiles that were sampled in a single season, we assume 5 effective DOF.

5.2.3 *Rice's formula for the expected number of local extrema*

The "wiggliness" of time series, assuming a stationary random process, is determined by the first moments of the spectral density. This relationship, known as Rice's formula (Rice, 1944, 1945), was shown to have important implications for interpreting palaeoclimate records (Wunsch, 2006) and can be used to derive the expected number μ of local extrema (maxima and minima) per unit time. Specifically, for a stationary Gaussian process (e.g., Lindgren, 2012), μ is

$$\mu_{\max} = \mu_{\min} = \frac{1}{2\pi}\sqrt{\frac{\Omega_4}{\Omega_2}}, \tag{5.1}$$

where Ω_2 and Ω_4 denote the second and the fourth moment of the spectral density of the Gaussian process.

A diffused white noise process has the power spectral density $P_0 \cdot \exp\left(-\omega^2\sigma^2\right)$ (van der Wel et al., 2015b), where P_0 is the total power of the undiffused white noise, σ the diffusion length and ω angular frequency. The second and fourth moments are $\Omega_2 = \frac{\sqrt{\pi}}{4}\sigma^{-3}$ and $\Omega_4 = \frac{3\sqrt{\pi}}{8}\sigma^{-5}$. Thus, from Eq. (5.1) the average difference between two maxima is

$$\Delta z_{\max} = 1/\mu_{\max} = 2\pi\sqrt{\frac{2}{3}}\,\sigma, \tag{5.2}$$

which is a linear function of the diffusion length σ – a remarkably simple relationship.

5.2.4 *Automatic estimation of the isotopic cycle length and amplitude*

To investigate the isotopic variations in a way similar to visual cycle counting (Casado et al., 2017), we use an automatic procedure to identify the minima and maxima in isotope profiles. For the sake of simplicity we call the typical distance between subsequent maxima (or minima) cycle length, noting that this does not imply a periodicity that would appear as a peak in the power spectrum.

To improve robustness against measurement noise, we define a local maximum (or minimum) as that value of a profile which is above (or below) all other values within a window of ±6 cm centred at the given point. This naturally limits the minimum possible cycle length to 6 cm; however, as the accumulation rates at our sites vary from 6 to 21 cm of snow per year, we expect that most cycles are longer than this and the results are thus insensitive to this choice. Since we apply the same method to the observations as well as to the simulations, their intercomparison is unbiased.

We determine all local extrema for each observed or simulated profile in the described manner and record the distances between subsequent extrema (i.e. the distances between two neighbouring maxima as well as between two neighbouring minima) as a function of depth (midpoint of depth between the two extrema, Fig. 5.1). We sort the recorded distances (cycle lengths) into depth range bins, e.g., 1.5–2 m depth, forming a distribution of distances for each specific bin. For the simulations, and also for several of our study sites, multiple profiles are available, allowing a better estimate of the cycle length as a function of depth to be made by binning the distances from multiple profiles together. The bin width is chosen as a trade-off between maximising the resolution and minimising the variance of the estimation. Specifically, we choose 1 m for sites with one or two profiles (S2, DF, DK, MP, SP, EDML below 3.4 m snow depth) and 0.5 m for sites with more than two profiles (EDC, Vostok and EDML above 3.4 m snow depth). For the resulting distributions, we report the mean and 2 standard errors ($2 \times \mathrm{se}$). To estimate the standard error, we assume independence of the profiles except for EDML, where we assume 5 effective DOF as in the spectral analysis.

5.2.5 *Minimal forward model for vertical isotope profiles*

As a tool to understand the observations, we construct the following minimalistic model to simulate artificial isotope profiles in the upper metres of Antarctic firn. We approximate the local climate conditions by the local near-surface air temperatures, $T_{\mathrm{air}}(t)$, and assume that these shape the isotope signal of freshly formed snow, $\delta^{18}\mathrm{O}_{\mathrm{snow}}(t)$. Subsequently, the snow is transported to the surface by precipitation where it is redistributed and mixed by wind, giving rise to the surface

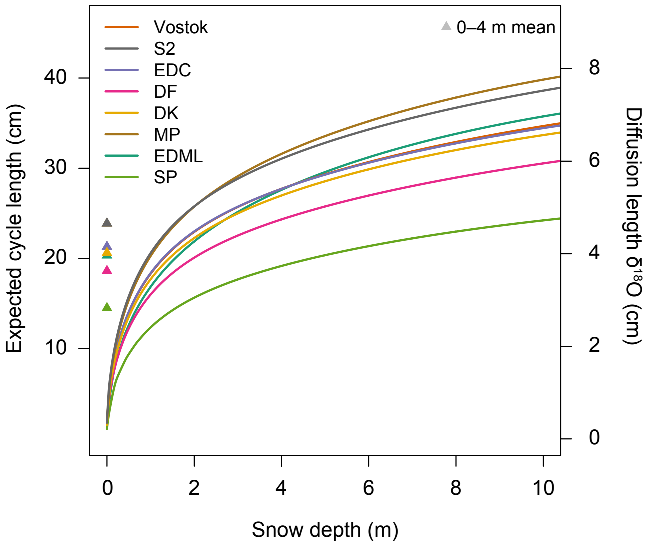

FIGURE 5.3. Modelled diffusion lengths for the different sites. The diffusion lengths for δ^{18}O (right scale) are shown against depth. Also shown are the implied cycle lengths (left scale) assuming diffused white noise. For most sites, the mean cycle lengths in the top 4 m (triangles) are around 20 cm.

isotope signal $\delta^{18}\mathrm{O}_{\mathrm{surface}}(t)$. Finally, the surface signal is buried in the firn column which is accompanied by diffusional smoothing of the signal and densification of the layers (Münch et al., 2017a). Analysing a snow pit or firn core during this process then represents a snapshot of the firn isotope signal $\delta^{18}\mathrm{O}_{\mathrm{firn}}(z)$. We describe the process here for δ^{18}O but the analogous approach also applies to δD. We will now discuss these steps in detail.

On monthly to multidecadal timescales, the local temperatures in Antarctica are dominated by the seasonal cycle. At our studied sites, the seasonal cycle explains more than 90 % of the variance in the temperature evolution of the last decades (ERA-Interim reanalysis; Dee et al., 2011) when evaluated on a monthly resolution and considering the first two harmonics of the seasonal cycle (Table 5.1). We therefore approximate the local climate conditions by parameterising the seasonal cycle in temperature as

$$T_{\mathrm{air}}(t) = T_0 + A_1 \cos(\omega t + \phi_1) + A_2 \cos(2\omega t + \phi_2) + \epsilon_T. \quad (5.3)$$

Here, ω is angular frequency, t time, T_0 is annual mean temperature, A_1, A_2 and ϕ_1, ϕ_2 denote amplitude and phase of the first two harmonics of the seasonal cycle, and ϵ_T is the remaining temperature variability. We estimate the parameters from temperature observations of nearby automatic weather stations (Table 5.1). For our study sites, ϕ_1 and ϕ_2 are small ($< 5°$) and are for simplicity set to zero. For converting the near-surface air temperatures into oxygen isotope

TABLE 5.1. Meteorological conditions and model parameters at the study sites. Listed are the annual mean temperature (T_0), amplitude of the first two harmonics of the seasonal cycle (A_1, A_2), annual mass accumulation rate ($\dot{b}$), firn surface density (ρ_0), average atmospheric pressure (P_0) and fraction of variance in ERA-Interim monthly surface temperature explained by the seasonal cycle alone (F_{seas}). If borehole temperature measurements exist, we use the 10 m firn temperature for T_0 instead of air temperature observations, as they provide a more accurate estimate of the relevant temperature for the diffusion. If no temperature observation exists, the temperature from the nearest site was used by adding the temperature anomaly between the sites from reanalysis data (Dee et al., 2011).

Site	T_0 °C	A_1 °C	A_2 °C	$\dot{b}$ $\mathrm{kg\,m^{-2}\,yr^{-1}}$	ρ_0 $\mathrm{kg\,m^{-3}}$	P_0 mbar	F_{seas} %
Vostok[a]	−57.0	16.7	6.6	21	350	624	97
S2[b]	−55.1	17.4	6.3	21	350	642	97
EDC[c]	−54.9	17.4	6.3	27	350	642	95
DF[d]	−57.3	16.4	6.6	27.3	350	592	95
DK[e]	−53.1	16.7	6.6	35.5	368	592	94
MP[f]	−48.6	15.5	6.6	40.9	372	592	93
EDML[g]	−44.5	13.2	4.9	72	345	677	93
SP[h]	−50.8	15.7	6.4	80.0	350	682	95

[a] Ekaykin et al. (2002) and Lefebvre et al. (2012). [b] Touzeau et al. (2016), A_1, A_2 and P_0 adapted from EDC. [c] Touzeau et al. (2016). [d] Kameda et al. (2008). [e] Hoshina et al. (2014), A_1, A_2 and P_0 adapted from DF. [f] Hoshina et al. (2014), A_1, A_2 and P_0 adapted from DF. [g] EPICA community members (2006). [h] Casey et al. (2014).

ratios, we use the mean Antarctic spatial slope of $\beta = 0.8$ ‰ °C^{-1} (Masson-Delmotte et al., 2008):

$$\delta^{18}\mathrm{O}_{\mathrm{snow}}(t) = \beta T_{\mathrm{air}}(t) + \epsilon_\delta, \tag{5.4}$$

where ϵ_δ reflects the isotopic variability not captured by the linear relationship. We neglect the intercept of the calibration since the absolute isotope values have no influence on the results of our analyses and note that our results, except for the spectral comparison (Fig. 5.8), are independent of the amplitudes and thus the choice of the calibration. A strong temporal relationship has been confirmed between the seasonal cycle of local temperature and the stable isotope ratios measured in precipitation samples (Eq. 5.4) at several sites in East Antarctica (Fujita and Abe, 2006; Touzeau et al., 2016; Stenni et al., 2016) although the estimated slopes vary from 0.3 to 1 ‰ °C^{-1} between sites.

Going from the isotope signal in the snow to the surface signal, the variability of the seasonal cycle is affected by aliasing due to precipitation intermittency (Helsen et al., 2005; Sime et al., 2009; Laepple et al., 2011; Persson et al., 2011), by redistribution of snow (Fisher et al., 1985; Münch et al., 2016b; Laepple et al., 2016) and by interannual variation in the accumulation rate and the accumulation seasonality (Cuffey and Steig, 1998). We note that exchange between atmospheric water vapour and the snow might further influence $\delta^{18}\mathrm{O}_{\mathrm{surface}}$ (Steen-Larsen et al., 2014; Touzeau et al., 2016; Casado et al., 2017) and we do not account for these effects. However, even in this case, the variations in $\delta^{18}\mathrm{O}_{\mathrm{surface}}$ might still follow the temperature variations. To a first approximation, precipitation intermittency, snow redistribution and interannual accumulation variability do not affect the total variance of the input signal but rather mainly redistribute its energy across frequencies, similar to the effect of aliasing (Kirchner, 2005). Thus, to simplify matters, we describe the combination of these processes together with ϵ_T and ϵ_δ by temporally independent (i.e. white) noise and set the variance of the total surface signal (seasonal cycle + noise) to the variance of the original seasonal cycle in the snow (Eq. 5.4). The choice of white noise is the simplest option here and the results are not sensitive to this assumption (Appendix 5.6).

Our model for the isotopic surface signal then is

$$\delta^{18}\mathrm{O}_{\mathrm{surface}}(t) = \beta\left((1-\xi)^{1/2} T_{\mathrm{air}}(t) + \xi^{1/2}\sigma_{T_{\mathrm{air}}}\epsilon(t)\right), \qquad (5.5)$$

where $\sigma_{T_{\mathrm{air}}}$ is the standard deviation of the seasonal cycle in temperature (Eq. 5.3) and $\epsilon(t)$ are independent normally distributed random variables (white noise) with zero mean and standard deviation = 1. The parameter $0 \leq \xi \leq 1$ determines the fraction of noise in the surface signal: $\xi = 1$ represents the case of pure noise (completely reshuffled seasonal cycle) and $\xi = 0$ the case of a fully preserved seasonal cycle.

The model also includes one implicit parameter, the resolution at which we evaluate the variance of the noise $\epsilon(t)$. This is required as, in contrast to the seasonal cycle, white noise is not a band-limited signal. Descriptively, the parameter $\epsilon(t)$ represents the smallest spatial scale on which isotopic variations are possible. We assume 1 cm here, thus implying the complete mixing of any variations occurring on smaller spatial scales.

Finally, the burial of the surface snow transfers the surface signal time series into the depth profile $\delta^{18}\mathrm{O}_{\mathrm{firn}}(z)$. We approximate this process assuming a constant accumulation rate given by the present-day observations (Table 5.1) as the intra-seasonal and interannual variations in accumulation are already included in $\epsilon(t)$. During burial, the isotope signal is influenced by densification, layer thinning by ice flow and isotopic diffusion. Thinning of the layers is negligible in the top metres analysed here and therefore neglected in our analysis. Densification is modelled using the Herron–Langway model (Herron and Langway, 1980), assuming constant surface density and temperature for each site which are set to the modern observations (Table 5.1). The results are not sensitive to these simplifications since the overall effect of densification is small in the top metres of firn.

The effect of firn diffusion on the original isotope signal $\delta^{18}\mathrm{O}_{\mathrm{surface}}$ is modelled as the convolution with a Gaussian kernel (Johnsen et al., 2000) which leads to an overall smoothing of the input signal. The amount of smoothing is governed by the width of the convolution kernel given by the diffusion length σ, which is sensitive to ambient temperature, pressure and the density of the firn (Whillans and Grootes, 1985). We treat the dependency on density according to Gkinis et al. (2014), with diffusivity after Johnsen et al. (2000). The temperature dependency of the diffusion length is highly nonlinear, with warmer temperatures leading to a stronger change. Thus, the seasonal cycle in firn temperature in the top metres increases the effective diffusion length. To approximate this effect, we follow the approach of Simonsen et al. (2011). We model the seasonal cycle in firn temperature according to the general heat transfer equation, driven by surface temperatures for constant thermal diffusivity and negligible heat advection (e.g., Paterson, 1994). We then calculate the diffusion length for parcels starting in every month of the year and compute the average diffusion length over all parcel trajectories. For the sake of simplicity, we assume a constant density for the firn temperature modelling, which is set to the observed surface densities (Table 5.1).

The resulting effective diffusion lengths for our study sites are shown in Fig. (5.3). Interestingly, the combined effect of lower accumulation rates and colder temperatures largely compensate each other, leading to a rather constant diffusion length across the Antarctic Plateau.

5.3 RESULTS

5.3.1 *Spectral analysis of the isotope profiles*

Despite originating from very different accumulation conditions, the power spectra of $\delta^{18}\mathrm{O}$ are remarkably similar across all analysed profiles (Fig. 5.4). The similarity of the diffused white noise null plus measurement noise spectra (blue shading) and the actual power spectra (black) suggests that the shape of the spectra are dominated by diffusion. Most sites show spectra fully consistent with diffused white noise and do not show a significant periodicity at any frequency, including frequencies corresponding to $\sim 20\,\mathrm{cm}$ (vertical grey dashed line). DF shows some significant deviation at the metre scale, corresponding to multidecadal variations. DF, MP, EDML and SP show locally significant peaks at frequencies close to the annual snow layer thickness (vertical red dashed line). However, even for these sites, the energy potentially related to the seasonal cycle is small, especially considering that the presumably driving temperature signal is dominated by the seasonal cycle.

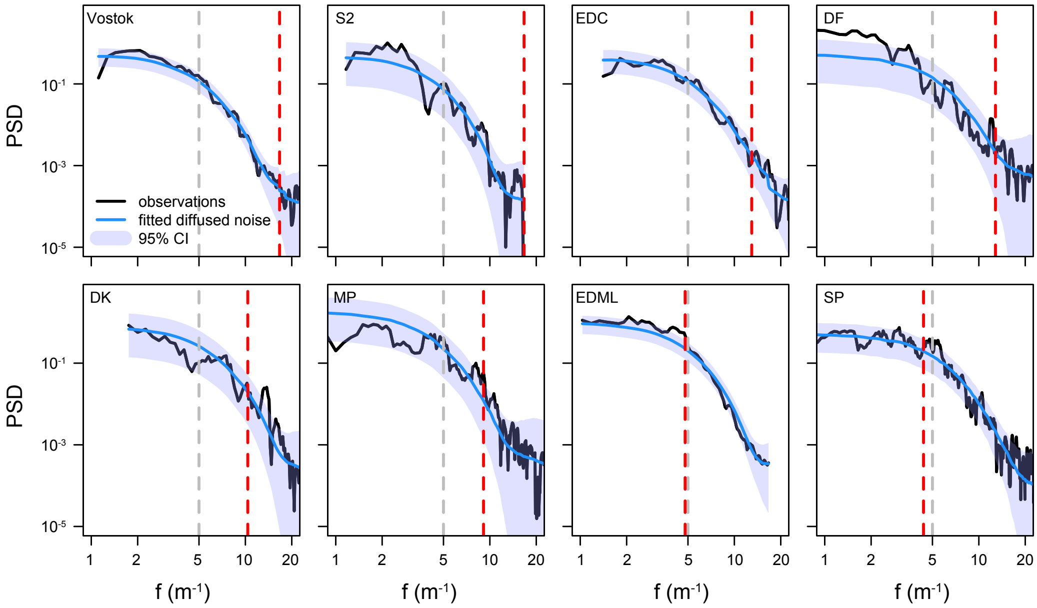

FIGURE 5.4. Power spectra of the firn δ^{18}O variations in the firn profiles. The null hypothesis of diffused white noise (blue) and the corresponding critical significance threshold values (shaded blue) are shown. For each site, the frequency corresponding to the annual snow layer thickness is shown as a vertical red dashed line, and the frequency corresponding to 20 cm is shown as a vertical grey dashed line.

5.3.2 *Theoretical and observed cycle length in isotope profiles*

The similarity of the power spectra between different sites, their similarity to the spectrum of diffused noise, and the lack of evidence for periodic oscillations suggests that the apparent cycles might be independent of periodic variations in the climate signal and instead represent a property of diffused noise. We note that "noise" here just describes isotopic variations that are largely independent in time and thus exhibit a largely timescale-invariant ("white") power spectrum. This neither implies a non-climatic nor negates a climatic origin of these variations. The expected cycle length for a diffused white noise signal is given by Rice's formula (Eq. 5.2) and equals $\sim$ 5 times the diffusion length. This represents the limiting case where all initially climate-related isotopic variations would be reshuffled by precipitation intermittency and redistribution, leading to completely uncorrelated isotopic variations at the snow surface. Using the calculated diffusion lengths for the upper 4 m of firn gives, for δ^{18}O, expected mean cycle lengths from 15 (SP) to 22 cm (Vostok and EDC), which are similar to those observed in isotope profiles by manual counting (Casado et al., 2017).

For a more quantitative comparison, we analyse the cycle lengths from measured δ^{18}O and δD profiles using automated counting and compare them with the theoretical predictions from Rice's formula

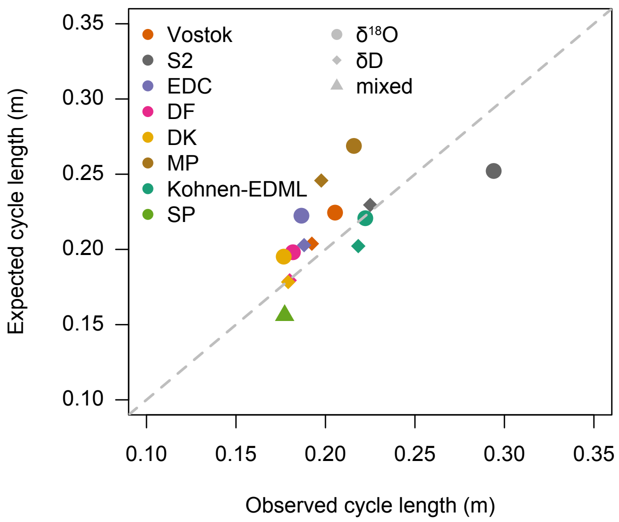

Figure 5.5. Comparison of expected and observed cycle length for all sites. The cycle length is evaluated between 1 and 4 m snow depth (or the maximum depth for shallower snow pits). Results are shown separately for δD and δ^{18}O except for SP, where a combined value is used since here δD and δ^{18}O are not available from the same profiles. The expected cycle length is directly derived from the diffusion length assuming a pure white noise surface signal. Note that cycle lengths are larger than those provided in Fig. 5.3 as the first metre is excluded from this analysis.

(Fig. 5.5). We compare here the depth range 1–4 m (or the maximum profile depth) as counting cycles in the topmost metre is more uncertain since the cycle length is a strong function of depth. The comparison confirms the qualitative results and even shows a similarity between the variations in the observed and predicted cycle lengths ($r = 0.63$, $p = 0.06$). For most sites, δ^{18}O profiles show a larger cycle length than δD, which is expected since the diffusion length for δ^{18}O is slightly ($\sim$ 10 %) larger, although this is largely within the uncertainties of the estimates.

This similarity between observed cycle lengths and those predicted from diffused white noise is surprising, as we have not yet included any climate signal, such as the seasonal cycle, in our analysis. To better understand the combined influence on the firn signal of noise, the seasonal cycle and the diffusion process, we now analyse the extent to which simulated firn profiles depend on the input signal.

5.3.3 *Illustrative examples of the cycle length–depth dependency*

In contrast to the diffusion length, which is a function of snow depth, the climate signal should be largely invariant over time and thus,

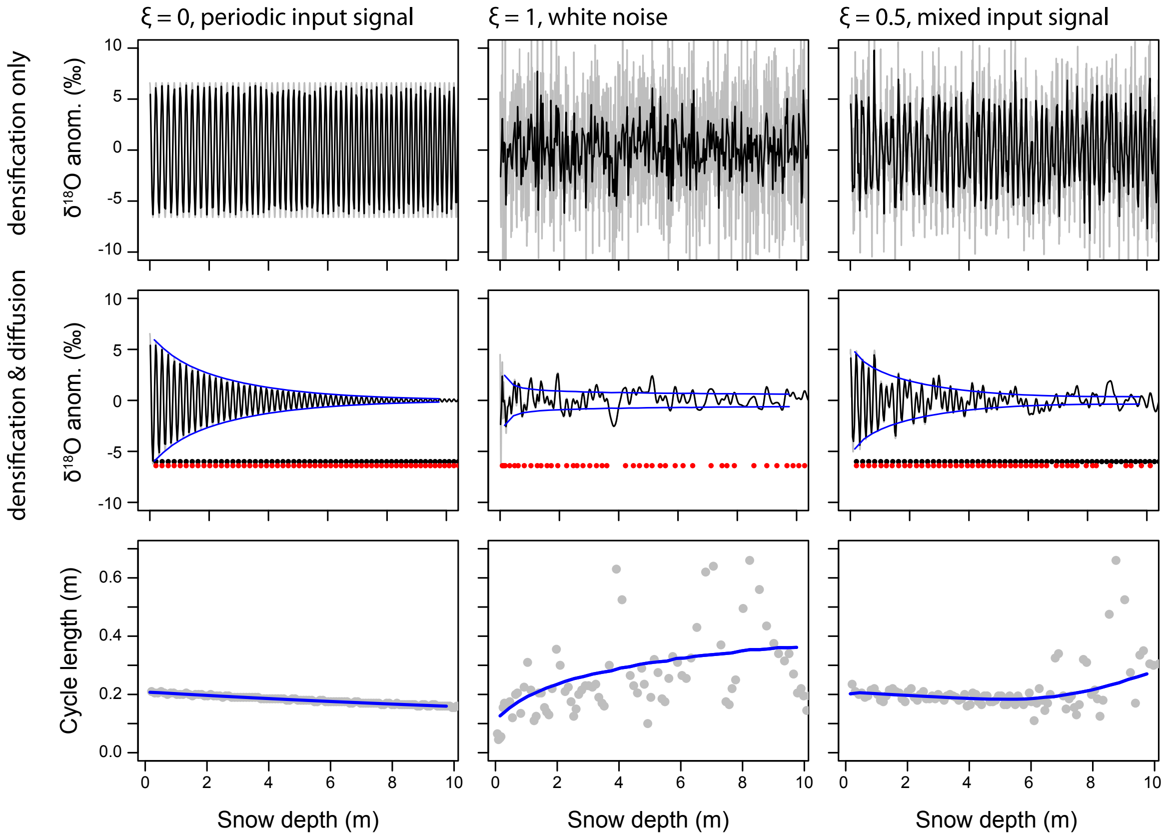

FIGURE 5.6. Illustrative examples of the effect of noise and firn diffusion on the cycle length and amplitude for three input time series ($\xi = 0, 1, 0.5$). Top row: input signal after densification. Middle row: signal after densification and diffusion. The raw (2 mm resolution) data (grey) and 2 cm averages (black) mimicking a typical sampling resolution are shown. In addition, the mean expected amplitude from the Monte Carlo simulations (blue), the positions of the expected maxima of a purely periodic signal (black dots) and the positions of the actual maxima (red dots) are provided. Bottom row: mean expected cycle length (blue) and actual distance (grey) between pairs of maxima (or minima).

in first order, independent of the depth. Therefore, investigating the depth dependency of the cycle length in isotope profiles should provide us with additional insights about the origin of the variations.

To understand the depth dependency of the cycle length, as well as of the signal amplitudes, we provide three examples of simulated depth profiles (A–C) illustrating the effect of firn diffusion and noise (Fig. 5.6), using the environmental and depositional conditions of the EDML site (Table 5.1).

(A) We assume a purely periodic surface isotope signal, such as the seasonal cycle ($\xi = 0$; Fig. 5.6, left column). The cycle length, measured in snow depth units, is determined by the input signal and decreases slowly with depth due to densification. In the specific case of EDML, the cycle length is approximately 21 cm, which is determined by the local accumulation rate of $\sim 72\,\mathrm{mm\ w.e.\ yr^{-1}}$ and a firn density of $345\,\mathrm{kg\,m^{-3}}$. Diffusion attenuates the initial amplitude A_0

of the signal with depth (Fig. 5.6, central plot in left column) according to $A = A_0 \exp\left(-\frac{1}{2}\omega^2\sigma^2\right)$ (Johnsen et al., 2000).

(B) We assume that the input signal is white noise ($\xi = 1$; Fig. 5.6, central column). Possible mechanisms for such a signal would be precipitation intermittency and snow redistribution having completely reshuffled the initial seasonal signal. In this case, the expected cycle length is proportional to the diffusion length as predicted by Rice's formula and thus monotonically increases with depth. For the simulated conditions, this increase is larger than the decrease from layer thinning due to densification. The observed cycle length for a given simulation (grey dots) follows this expectation but its variability is much larger, compared to case (A), given that we now observe a stochastic instead of a deterministic periodic signal. The amplitude of the signal, as measured for example by the peak-to-peak distances, decreases near the surface and then remains largely constant. This can be heuristically understood by considering the two compensating effects: for a given cycle length or frequency ω, diffusion reduces the amplitude as $\exp\left(-\frac{1}{2}\omega^2\sigma^2\right)$. For a constant cycle length, the increasing σ with depth thus leads to an amplitude reduction. However, since the effective cycle length increases proportional to σ, both contributions cancel and lead to a constant amplitude. For the investigated case, the cycle length again is around 20 cm in the top 4 m but here it is determined, in contrast to (A), only by the diffusion length and is not set by the input surface signal.

(C) Finally we consider a mixture of cases (A) and (B), assuming that the input signal is equally partitioned (in variance) between white noise and periodic signal ($\xi = 0.5$; Fig. 5.6, right column). In the top ~ 6 m, the seasonal cycle dominates the diffused signal. Then, as the amplitude of the periodic cycle is reduced, while the diffusion length increases, the diffused noise comes into play and starts to dominate the signal. The observed cycle length of isotopic maxima in this specific simulation (grey dots) thus is a mixture of cases (A) and (B), first following the annual layer thickness before transitioning to the random distances set by the properties of the diffused noise. The expected cycle length (blue line), which corresponds to the mean cycle length obtained from averaging across multiple sites or across some metres of the profile, decreases in the top 5 m but then increases smoothly further down in the profile. If one counted the maxima of the isotope profile (red dots), one would reliably count the periodic signal in the upper part of the core before one would start to occasionally miss some maxima (black dots) that would otherwise be there without noise, resulting in an under-counting of the seasonal cycle in the lower part of the core.

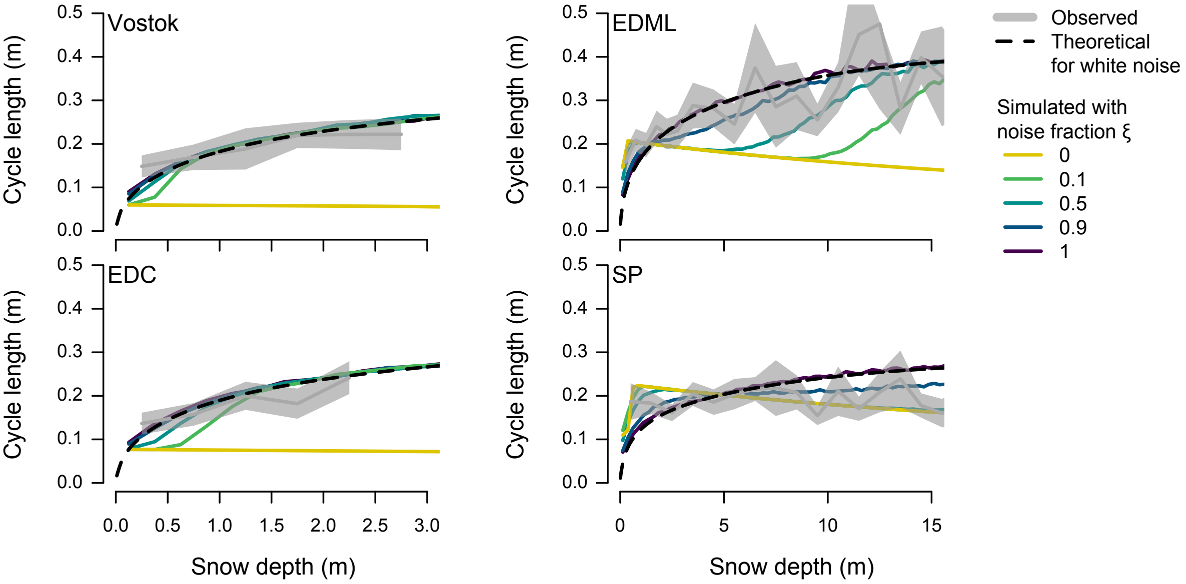

FIGURE 5.7. Comparison of numerically predicted and observed δ^{18}O cycle statistics as a function of depth for all sites with multiple profiles. Observed cycle lengths (grey line) and a 2 standard error estimation uncertainty (grey band) are shown. Simulated cycle lengths are shown for various noise fractions in the input signal (coloured lines). In addition, the theoretical cycle length for pure white noise is shown (dashed black).

5.3.4 *Predicted and observed depth dependency of the cycle length*

These examples (Fig. 5.6) demonstrate that very different input signals (pure noise or pure seasonal cycle) can create similar mean cycle lengths in the top metres of the firn, but they show a distinct depth dependency. We therefore estimate cycle lengths as a function of snow depth for all our East Antarctic study sites (Fig. 5.7), in an attempt to distinguish between these two cases. We focus on sites for which multiple isotope profiles are available (Vostok, EDC, EDML and SP) as they allow better estimates of the variability; however, qualitatively similar results are obtained for all sites (Appendix 5.7; Fig. 5.10). These results are compared to those estimated from artificial profiles simulated for different noise fractions of the input signal, ranging from the pure seasonal cycle case ($\xi = 0$) to pure white noise ($\xi = 1$). As a reference, we additionally show the analytical result (black dashed line) for the cycle length of diffused white noise according to Rice's formula (Eq. 5.2).

At all sites except SP, an increase in the estimated cycle length (grey bars) is observed with depth (Fig. 5.7, left column). This behaviour is well reproduced by simulations that assume a high noise fraction ($\geq 50\,\%$). For all but the SP site, the observed cycle length also follows the theoretical prediction for a pure white noise signal (black dashed line). This behaviour is in strong contrast to the cycle length

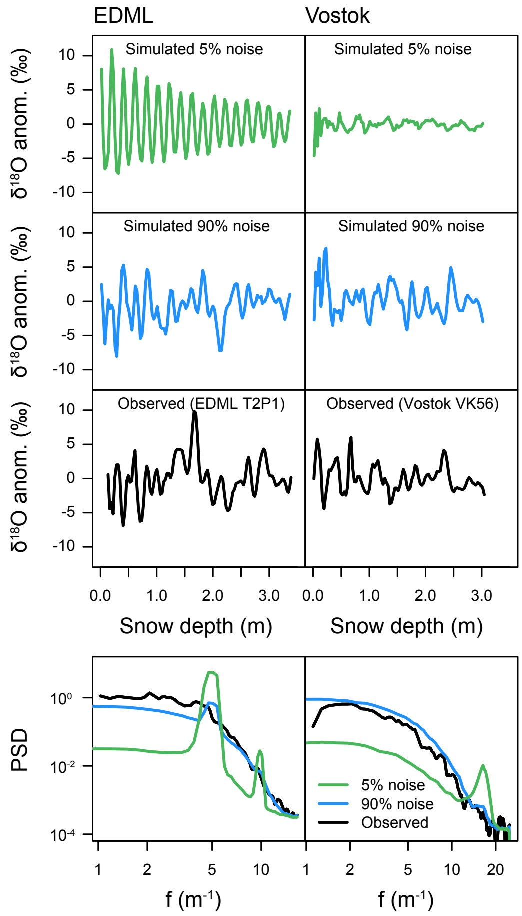

FIGURE 5.8. Visual comparison of measured and simulated profiles for EDML (left) and Vostok (right panel). Upper row: simulations for 5 % noise, representing a pure climate signal. Middle row: simulations for 90 % noise. Bottom row: power spectra of the simulated and observed isotope profiles. The observed spectra are the mean of all spectra from the profiles available for the site. The simulated spectra are the mean spectra over 100 realisations of the isotope profiles.

in the 0 %-noise case (yellow), which decreases with depth due to the thinning of the annual layer thickness by densification.

For the very low-accumulation sites, Vostok and EDC, a small noise fraction already (10 %) leads to the "diffused noise" behaviour below a depth of 0.5 m (Vostok), or 1 m (EDC), since the seasonal cycle is already strongly damped by diffusion in the first metre. Thus, in these cases, just analysing the behaviour of the cycle length does not strongly constrain the fraction of noise vs. seasonal cycle of the surface isotope signal. In contrast, for EDML, the larger annual layer thickness and the stronger diffusion caused by the warmer temperatures lead to strongly diverging behaviour of the expected cycle lengths dependent on the ratio of noise to seasonal signal in the input. Interestingly, even at this relatively high-accumulation site, the observed cycle length increases and follows that expected and shown for simulations that assume a high noise fraction (90 or 100 %). In contrast, a decreasing cycle length would be expected for densification of a pure, noise-free, seasonal signal. For SP, the smaller diffusion length relative to EDML results in a weaker dependency of the expected cycle lengths on the input signal. The observed cycle length is rather constant and thus lies in between the cases of 0 and 90 % noise.

In summary, the presented evidence suggests that, with the exception of SP, diffused noise is the dominant source of the apparent cycles at the studied sites.

5.3.5 *Simulated and observed profiles and power spectra for EDML and Vostok*

As a visual test of our finding, we compare the depth profiles and power spectra of simulated and observed example profiles for the two representative sites EDML (72 mm w.e. yr^{-1} accumulation) and Vostok (21 mm w.e. yr^{-1} accumulation) (Fig. 5.8). We analyse noise fractions of 5 % (seasonally dominated) and 90 % (noise dominated). The first represents the expected case for a perfect temperature proxy (perfect linear isotope-to-temperature relationship, no precipitation intermittency or redistribution, constant accumulation) as the seasonal cycle explains roughly 95 % of the total temperature variance over the last decades (Table 5.1). The second case represents the noise fraction that creates realistic cycle lengths and amplitudes compared to the observations (Fig. 5.7). For each site, a single isotope profile is shown but similar results are obtained for any of the profiles.

We first analyse the low (5 %) noise case (Fig. 5.8, top row). For EDML, the effect of diffusion on the amplitude of the seasonally dominated signal is moderate and only leads to a reduction in amplitude of about 50 % in the top 3.5 m. For Vostok, the annual layer thickness is much smaller and the diffusion therefore already destroys most of the seasonal signal in the top half metre, leaving only a very small diffused signal. For both sites, the diffused signal looks very much unlike the observed isotope profiles (third row). For EDML, the diffused signal (top row) is very regular, whereas the observed profile (third row) shows strong interannual variations. For Vostok, the amplitude of the simulated diffused signal is much smaller than the observed amplitude of the profile.

In contrast, the high (90 %) noise cases (second row) share, for both sites, many properties with the observations. While we do not expect any correlation between the simulated and observed profiles, since the simulated profiles are by construction largely random, the amplitude, interannual variations and cycle lengths are all similar.

These findings are confirmed by comparing the power spectra of the simulations and observations. As shown earlier (Fig. 5.4) the observations show a broadband spectrum with no clear periodicity. For EDML, the power spectrum of the low (5 %) noise simulation (Fig. 5.8, bottom row) shows clear peaks at the periods corresponding to the annual and biannual layer thickness. The broadening of the peaks arises from the varying layer thickness due to densification. In the frequency range outside the peaks, the power spectral density, which is a measure of the timescale-dependent variance of the signal, is about 1 order of magnitude lower than observed. In contrast, the simulations of the high-noise case result in a power spectrum that is nearly indistinguishable from the observations. For Vostok, a similar behaviour is observed. Here, the annual peak corresponding to the layer thickness of the seasonally dominated signal is smaller, since it is strongly damped by diffusion. Again, the variance outside the peak is much too small compared to the observations, whereas the noise-dominated signal has a power spectrum nearly indistinguishable from the observations.

5.4 DISCUSSION AND SUMMARY

Stable isotope ratios in firn are usually interpreted as temperature proxy. Therefore, to a first approximation, vertical isotopic variations in a snow pit should reflect the temperature variations. The naive expectation is thus that a 3 m deep profile containing 25 years and 25 seasonal cycles of climate should look very different from a 3 m profile at a higher accumulation site that only contains 10 years of temperature variations. However, our results show that this is not the case for many low-accumulation ($< 100\,\mathrm{mm\,w.e.\,yr}{-1}$) sites on the Antarctic Plateau, whose isotope profiles appear remarkably similar (Fig. 5.1), and this similarity is not limited to the time series but also applies to the power spectra, which are largely indistinguishable between the sites (Fig. 5.4). The visual similarity of the isotope profiles is further confirmed by systematically analysing the "cycle length" between isotopic maxima or minima (Fig. 5.5).

To explain these findings, we constructed a simple forward model for isotope signals in firn cores, similar to the ice-core proxy system model of Dee et al. (2015) or the "virtual-ice-core model" of van der Wel et al. (2011). Our model, driven by a mixture of the seasonal cycle and white noise as input, allows the simulation of realistic isotope profiles in terms of power spectral density, amplitude and cycle length (Fig. 5.8). Importantly, to obtain realistic simulations of the observed firn profiles, we had to assume a high noise level in the input signal that represents the temporal variations of stable isotope ratios at the surface (Figs. 5.7 and 5.8). Such a high noise level is consistent with the effect of precipitation intermittency (Helsen et al., 2005; Sime et al., 2009; Persson et al., 2011) and the stratigraphic noise caused by the redistribution of snow (Fisher et al., 1985; Laepple et al., 2016; Münch et al., 2016b). Both mechanisms distort the original signal and thereby redistribute the energy from the seasonal periodic cycle to largely uncorrelated variations. In theses cases the statistical properties, especially the power spectra of the isotope profiles, are mainly determined by isotopic diffusion, which is rather constant on the Antarctic Plateau (Fig. 5.3). In turn, similar power spectra imply a similar characteristic spacing between maxima or minima, a fundamental property of stochastic processes known as Rice's formula (Rice, 1944, 1945).

We applied Rice's formula to the problem of isotopic variations and showed that, assuming a white noise signal before diffusion, the expected spacing between isotopic maxima or minima ("cycle length") is ~ 5 times the diffusion length (Eq. 5.2) and thus on the order of 15–25 cm in the top metres of Antarctic firn. It is important to emphasise that such a characteristic spacing of minima or maxima does not imply a periodic deterministic signal that would appear as a peak in the power spectrum, as it is also the property of purely stochastic variations.

While in instrumental climate observations, a deterministic cycle (e.g., variations driven by the seasonal cycle) would be clearly distinguishable from the realisation of a purely stochastic process, this is less clear for snow pits or firn cores. Here, intra-seasonal and interannual changes in accumulation distort the seasonal cycle (Cuffey and Steig, 1998) and might therefore smooth out potential periodic peaks in the power spectrum. However, we further showed that the depth dependency of the cycle length allows discrimination between a deterministic signal (e.g., the seasonal cycle) and a stochastic signal affected by isotopic diffusion. The first case leads to a decrease in cycle length with depth by thinning of the annual layers due to densification, while the latter leads to an increase in cycle length with depth due to the increasing diffusion length (Figs. 5.6 and 5.7).

Defining noise as deviations from the surface isotope signal that are unexplained by the local temperature time series, the depth dependency of the cycle length and amplitude suggests a significant proportion of noise in the surface isotope signal at all analysed sites (Fig. 5.7). While missing knowledge concerning the properties (i.e. the spectral shape) of the noise before diffusion impedes quantitative estimates, with the exception of SP, a noise level of 50–90 % of the total variance seems realistic for all sites analysed in this study. For SP, the result suggests a noise level of 10–50 %. These noise fractions are estimated from snow pits of several metres length and evaluated on the centimetre scale. They therefore correspond to variations from subannual to decadal timescales.

This assertion may seem particularly troubling for the EDML site, as here the accumulation rate, as determined from snow stakes or volcanic markers in firn cores, corresponds to an annual layer thickness of $\sim$ 20 cm of snow, and the cycles were usually interpreted as annual cycles (Oerter et al., 2004). In contrast, our study suggests that, at least below a depth of 3 m, the isotopic "cycles" in single profiles or cores are not dominated by the seasonal signal but rather by diffused noise (Fig. 5.7), leading to the observed increase in cycle length with depth. While challenging the earlier interpretation of the variations, the new finding is consistent with the high stratigraphic noise level (50 % variance) independently estimated by comparing horizontal and vertical variability in snow trenches (Münch et al., 2016b) and the low reproducibility between nearby firn cores in this region (Karlöf et al., 2006).

For the three sites along the East Antarctic divide analysed here (DF, MP, DK) and later an extended set of sites, Hoshina et al. (2014, 2016) interpreted the multiyear cycles as the result of variable accumulation rates in combination with post-depositional changes at the surface, such as ventilation or condensation–sublimation effects. Both studies further argued for several significant periodic cycles in partly the same firn profiles. This interpretation differs from our finding of no significant periodicities in the power spectra of these sites (Fig. 5.4). In contrast to our study, Hoshina et al. (2014, 2016) tested the spectral peaks against undiffused white noise. We argue that this null hypothesis will always lead to spurious significant peaks in firn profiles (Appendix 5.8) as the true background spectrum is modified by diffusion and is therefore not appropriate. For Vostok, Ekaykin et al. (2002) argued that the spatial dune structure results in temporal isotope variations after burial leading to the cycles. For EDC, Petit et al. (1982) discussed the potential of missing months on the isotope record, due to precipitation intermittency and erosion as well as firn diffusion, to create the structure of the isotopic variations. All four studies propose mechanisms that distort or destroy the regular seasonal cycle of stable isotope ratios and thus create noise in the isotopic record. However, we argue that not these processes but rather the diffusion sets the first-order spectral structure of the signal, including the observed "cycle length", and that this explains the similarity across sites.

At first sight, our results seem to contradict the finding that firn-core isotope profiles are significantly correlated with impurities such as Na^+ (Hoshina et al., 2014, 2016), especially in very low-accumulation regions. However, such a relationship is expected when the initial surface signals of isotopes and impurities are correlated and when this correlation is not limited to high-frequency variations. For example, when both the isotopes in snowfall and the impurities show a seasonal cycle, and both are deposited and redistributed together (i.e. wet deposition of impurities), this will result in correlated surface signals. For the typical variability of observed impurity profiles, this correlation is partly preserved even after diffusion (Appendix 5.6; Fig. 5.9).

Similar noise levels in the isotope and impurity signals at the surface, caused by common deposition and redistribution processes, would also imply that little or no seasonality is preserved in the impurity records at those sites for which we find a high noise level. This is consistent with the missing seasonality in the impurity signal at sites with very low accumulation (Hoshina et al., 2014, 2016) but less clear for EDML, where a seasonal cycle in impurities seems to be preserved (Sommer et al., 2000b). The latter suggests either that at EDML the surface seasonality of the impurity signal is stronger than that of the isotope signal, that both atmospheric signals are corrupted differently on their way to the snow or that the noise level is on the lower side of our estimates.

Our result also has implications for estimating isotopic diffusion and for the usage of layer counting. Assuming a white noise input signal, the observed cycle length is proportional to the diffusion length (Eq. 5.2). The agreement between the observed and simulated cycle length (Fig. 5.7), and the observed spectra and diffused noise spectra (Fig. 5.8), thus provides some confirmation of the classical diffusion model (Johnsen et al., 2000). Recently it has been argued that the diffusion model of Johnsen et al. (2000) overestimates diffusion lengths in the top metres of the firn, at least in Greenland (van der Wel et al., 2015a). Focusing on the same data set might potentially allow this to be formally tested but this is beyond the scope of this study.

Our findings further support the assumption of an initially white spectrum as it is used in isotopic diffusion studies (e.g., Gkinis et al., 2014), since the white noise assumption for the surface signal allows a good reproduction of the observed power spectra (Fig. 5.4) and of the observed cycle lengths (Fig. 5.7).

We showed that the level of noise in the input signal also determines the depth dependency of the amplitude of the variations. The boundary case of a diffused pure seasonal cycle leads to an exponential decrease of amplitude with depth (Johnsen et al., 2000), whereas a diffused white noise signal results in a slower decrease of the peak-to-peak amplitude (Fig. 5.6). All isotope signals in snow or firn will be noise affected due to stratigraphic noise (Fisher et al., 1985; Laepple et al., 2016; Münch et al., 2016b) and precipitation intermittency (Helsen et al., 2005; Sime et al., 2009; Persson et al., 2011). Therefore, estimates of the diffusion strength based on analysing the decay of the seasonal cycle amplitude by measuring the peak-to-peak amplitude in the time domain (Cuffey and Steig, 1998) might be biased low if they do not account for the noise. Related to this issue, our results also underline the fact that layer counting in isotope profiles should only be performed after undiffusing the isotope signal (Cuffey and Steig, 1998) or using non-diffused parameters such as impurities. Our results suggest that layers in the deeper parts of the firn could be systematically missed by simply counting the local extrema in isotope profiles

(Fig. 5.6), leading to age models that are biased towards "younger" ages.

The combination of isotopic diffusion with strong variability at the surface that is not directly related to temperature also limits the effective resolution of climate signals that can be obtained by analysing firn-core isotopic records. While the problem of diffusion could be overcome by undiffusing the signal (Cuffey and Steig, 1998), this procedure also inflates the noise. Therefore, methods to reduce the noise by averaging across cores (Münch et al., 2016b), or the use of other parameters, have to be employed when aiming for high-resolution climate reconstructions at low-accumulation sites.

5.5 CONCLUSIONS

We provide an explanation of why snow pits across different sites in East Antarctica show visually similar variations in stable isotope ratios δ^{18}O and δD. We argue that the similar power spectra and apparent cycles of around 20 cm in near-surface isotope profiles are the result of a seasonal cycle in isotopes, noise, for example from precipitation intermittency, and diffusion. The near constancy of the diffusion length across many ice-coring sites (Fig. 5.3) explains why the structure and cycle length is largely independent of the accumulation conditions. At some sites, such as EDML, the cycle length implied by the isotopic diffusion coincides with the annual snow layer thickness in the upper metres of the firn. This calls for a careful consideration of the effects of noise and diffusion when interpreting isotopic variations.

Our hypothesis does not exclude the existence of a climatic signal in the isotope time series, as any low-frequency surface signal would still be preserved in the diffusion process, and thus does not question the relevance of stable isotope ratios as a palaeotemperature proxy. However, in particular for low-accumulation areas we show that the typical spacing of extrema in isotope profiles can be explained without invoking multidecadal climate changes or other climate-related hypotheses.

Our results underline previous findings that δ^{18}O and δD signals in low-accumulation regions have a small signal-to-noise ratio. Therefore, methods to reduce the noise such as averaging across cores have to be employed when aiming for high-resolution climate reconstructions. Finally, systematically analysing the spectral shape of isotopic variability and not just the potential periodicities and cycles might be a promising way forward to quantitatively understand the isotopic variability in polar firn cores (Fig. 5.8).

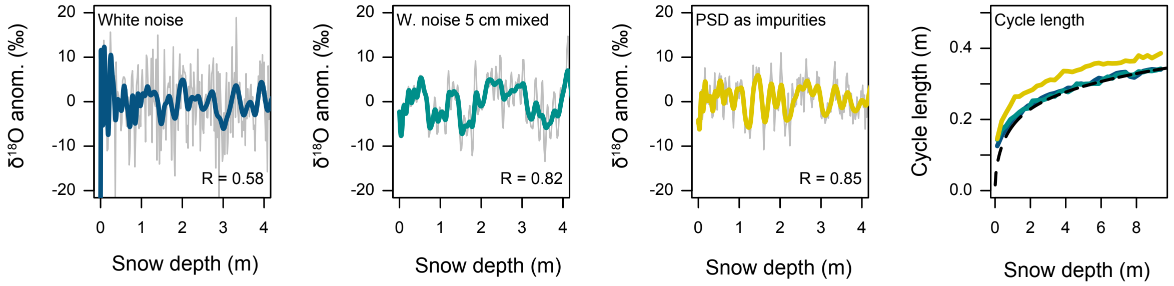

FIGURE 5.9. Sensitivity of the cycle length to the temporal correlation structure of the assumed input signal. Thin lines show the undiffused signal, while thick coloured lines the signal after diffusion. The correlation between the undiffused and the diffused signals is provided in the panels. For the more structured signals (mixed white noise and variability mimicking impurities), a larger fraction of the signal is preserved, leading to higher correlations. The resulting cycle length (right panel, coloured lines) is only weakly dependent on the input signal and is close to the theoretical result for white noise (Rice's formula, dashed line).

5.6 APPENDIX A: SENSITIVITY TO THE INPUT SIGNAL

Our previous calculations assumed an isotope surface signal that is a mixture of a seasonal cycle and uncorrelated (white) noise. While uncorrelated noise is the simplest hypothesis, it is likely that the surface signal exhibits more structure. Potential processes that lead to autocorrelation include precipitation events that deposit several centimetres of snow with similar isotopic composition, as well as mixing and redistribution by wind drift that might vertically homogenise the snow surface.

Unfortunately, the surface isotope signal before diffusion is largely unknown. To obtain a reasonable surrogate for the power spectrum of the surface isotope signal, we therefore resort to observed major ion profiles. This is motivated by the fact that, assuming an atmospheric source, wet deposited impurities are also influenced by precipitation intermittency and snow redistribution and might therefore show a similar variability structure as isotope signal at the surface. However, in contrast to the isotopic composition, impurities are not affected by diffusion and therefore the variability in measured impurity firn profiles should in a first approximation reflect the temporal surface variability.

Interestingly, major ion profiles in snow pits (e.g., Hoshina et al., 2014, 2016) are clearly distinguishable from white noise. This suggests that at least some correlated structure is preserved or created in the depositional process.

To test the effect of autocorrelated noise in the input signal on the resulting cycle length, we simulate profiles assuming three different input signals: (1) white noise, (2) white noise subject to a 5 cm mixing

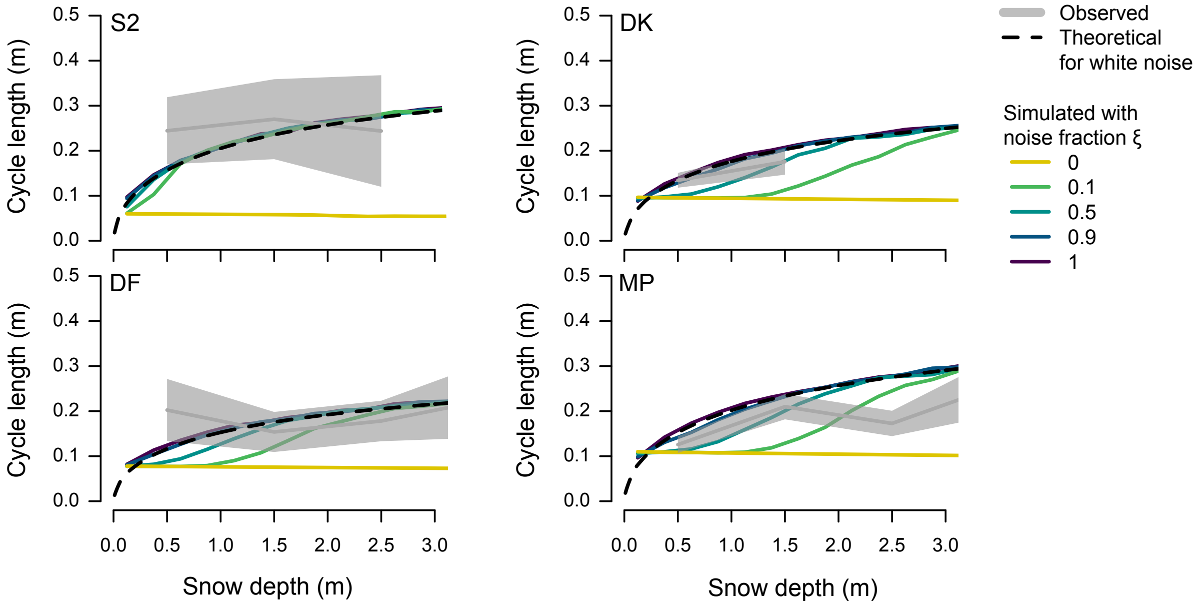

FIGURE 5.10. As Fig. 5.7 but for the remaining sites which only have a single isotope firn profile. Observed cycle lengths (grey line) and a 2 standard error estimation uncertainty (grey band) are shown. Simulated cycle lengths are shown for various noise fractions in the input signal (coloured lines). In addition the theoretical cycle length for pure white noise is shown (dashed black).

(low-pass filtered with a finite response filter with cut-off frequency $1/10\,\mathrm{m}^{-1}$) and (3) noise constructed with a similar temporal structure as observed impurity profiles, acting as a surrogate for the isotopic surface variability. For the latter, we estimate the mean power spectrum of the 4 m long Na^{+} impurity profiles of DF and MP (Hoshina et al., 2014) and generate new random time series from this spectrum.

The results (Fig. 5.9) show that although the input signal strongly differs, the diffused signal is very similar. The resulting cycle lengths for the white noise and the mixed white noise inputs are identical, and both are close to the theoretical expectation (dashed line). The cycle length of the impurity-based simulation is slightly higher ($\sim$ 3 cm offset).

We note that while the cycle length is similar, the correlation between the input and the diffused signal is larger for the more structured input signals as a larger fraction of low-frequency variability is preserved after diffusion.

5.7 APPENDIX B: OBSERVED AND SIMULATED CYCLE LENGTHS FOR THE SITES WITH ONE (SINGLE) AVAILABLE PROFILE

In the main text, we showed the observed and simulated cycle length statistics for the sites with multiple profiles (Fig. 5.7), as they allow a better estimation of the cycle length. The four remaining sites with

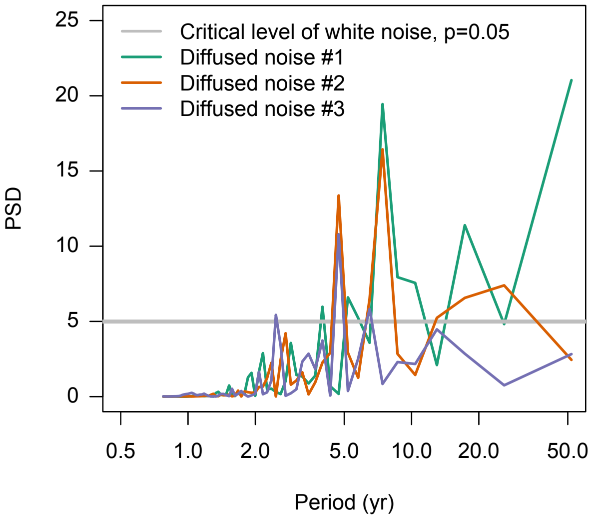

FIGURE 5.11. Demonstration of spurious peaks when testing against a white noise null hypothesis. Coloured lines show power spectra for three realisations of purely random firn profiles. The grey horizontal line shows the critical level ($p = 0.05$) that has to be overcome to be locally significant against white noise. As the simulated firn profiles are subject to firn diffusion, and thus have a red power spectrum, they show random peaks higher than the critical level.

single profiles (Fig. 5.10) also show cycle lengths consistent with the high noise level simulations.

The depth dependency of the cycle length is less clear, which is likely caused by the large estimation uncertainty. In addition, MP shows a systematically smaller observed cycle length than the simulations. Potential reasons could be either uncertainties in the isotopic data set (independent noise leads to more minima and maxima and thus a smaller cycle length) or our choice of climatic parameters (accumulation rate, firn temperature).

5.8 APPENDIX C: SPURIOUS SIGNIFICANCE WHEN USING A WHITE NOISE NULL HYPOTHESIS

To demonstrate the effect of a white noise null hypothesis on the spectral analysis of oxygen / hydrogen isotope ratios in snow and firn, we simulate random δ^{18}O profiles using our minimal forward model. To mimic Hoshina et al. (2014), we use the site parameters for DF and a pure white noise ($\xi = 1$) input signal that is subject to the site-specific densification and diffusion. The final data are averaged to 3 cm to mimic a typical sampling interval. We estimate the power spectrum using a raw periodogram and show the $p = 0.05$ significance level of a white noise null hypothesis. For all three realisations of purely random firn profiles, the spectra show energy well above the white noise significance level (Fig. 5.11). This demonstrates the need for using a null hypothesis that accounts for the isotopic diffusion.

TABLE 5.2. Summary of the drilling and snow-pit sites used in this study. For each site we list latitude, longitude and elevation a.s.l. and for each corresponding record its name, the analysed depth, sampling resolution, measured proxy and original data reference. Some profiles have single missing measurements that are not included in the provided sampling resolution. The 35 missing δ^{18}O samples in DCoxy80 were filled by linear regression to δD. For SP, δD was converted to δ^{18}O using a slope of 8 to get a complete δ^{18}O data set.

Site	Lat.	Lon.	Elevation	Name	Depth	Resolution	Proxy	Reference
	°N	°E	m a.s.l.		m	cm		
Vostok	−78.5	106.8	3488	VK14	2.5	2	δ^{18}O, δD	Ekaykin et al., 2002
				ST61	3.1	2	δ^{18}O, δD	Ekaykin et al., 2002
				ST73	3.1	2	δ^{18}O, δD	Ekaykin et al., 2002
				ST30	3	2.0–3.5	δ^{18}O, δD	Ekaykin et al., 2002
				VK56	3	3	δ^{18}O, δD	Touzeau et al., 2016
EDC	−75.1	123.3	3233	DCoxy5	2	1–2	δ^{18}O†, δD	Casado et al., 2017
				DCoxy80	2.5	3.3–3.6	δ^{18}O, δD	Casado et al., 2017
				Vanish12	2	3	δ^{18}O, δD	Touzeau et al., 2016
DF	−77.3	39.7	3810	DF	4	2	δ^{18}O, δD	Hoshina et al., 2014
DK	−76.8	31.8	3733	DK	2	2	δ^{18}O, δD	Hoshina et al., 2014

(continued on next page)

TABLE 5.2. *(continued)*

Site	Lat.	Lon.	Elevation	Name	Depth	Resolution	Proxy	Reference
	°N	°E	m a.s.l.		m	cm		
S2	−76.3	120.0	3229	S2	3	2.9–3.0	δ^{18}O, δD	Touzeau et al., 2016
MP	−74.0	43.0	3656	MP	4	2	δ^{18}O, δD	Hoshina et al., 2014
EDML	−75.0	0.1	2892	T15 (22 profiles)	3.4	2.2–3.0	δ^{18}O, δD	Münch et al., 2017a and this study
				B41	12 *	2	δ^{18}O, δD	this study
				B50	12 *	2	δ^{18}O, δD	this study
SP	−90.0	0.0	2835	SP78P	10	2	δ^{18}O‡, δD	Jouzel et al., 1983
				SP78C	17.9**	1.9–2.5	δD	Jouzel et al., 1983
				SP92	6	0.9–1.4	δ^{18}O	Whitlow et al., 1992

[*] Top 3 m removed from analysis due to bad core quality. [**] No data available for first 9.6 m.
[†] Incomplete. Missing values linearly interpolated. [‡] Only 0–4.9 m depth.

6

WHAT CLIMATE SIGNAL IS CONTAINED IN DECADAL TO CENTENNIAL SCALE ANTARCTIC ISOTOPE VARIATIONS?

Thomas Münch[1,2] and Thomas Laepple[1]

[1]*Alfred Wegener Institute Helmholtz Centre for Polar and Marine Research, Telegrafenberg A43, 14473 Potsdam, Germany*
[2]*Institute of Physics and Astronomy, University of Potsdam, Karl-Liebknecht-Str. 24/25, 14476 Potsdam, Germany*

This chapter is a manuscript in preparation.[1]

ABSTRACT. Ice-core-based records of isotopic composition are a proxy for temperature, and can thus in principle provide information on polar climate variability over a large range of timescales. However, single isotope records are strongly affected by a multitude of processes that create noise overlaying the true temperature variability. The crucial question of isotope-based climate reconstructions is thus on which temporal scales the actual signal dominates the noise. Estimates of this timescale-dependency of the signal-to-noise ratio (SNR) are however still largely missing. Here we present a simple model to estimate the temperature variability of isotope records by separating the climate signal from the noise in the spectral domain, based on information from multiple cores. We apply our model to firn-core arrays from Dronning Maud Land (DML) in East Antarctica and from the West Antarctic Ice Sheet (WAIS). For DML, we find an increase of the signal-to-noise ratio for longer timescales by one order of magnitude, ranging from 0.1 at decadal to 1 at multicentennial scales. The corrected spectrum of climate variability also shows increasing variability towards longer timescales, contrary to the classical inference from single records. In contrast, the timescale-dependency of both signal-to-noise ratio and climatic signal are less clear for West Antarctica, with the SNR staying close to constant over decadal to centennial timescales. We speculate that this is related to differences in the spatial and temporal scales of the precipitation weighting. Our approach provides a basis for separating local proxy from coherent climate variability which is applicable to a large set of palaeoclimate records.

6.1 INTRODUCTION

In order to study the polar climate variability on timescales beyond instrumental temperature observations ice cores represent a key archive. The isotopic composition of water stored in the firn and ice is inter-

---

[1] A revised version of this manuscript has been submitted to Climate of the Past Discussions after submission of the thesis.

preted as a proxy for temperature (Dansgaard, 1964; Jouzel and Merlivat, 1984; Jouzel et al., 2003), and hence ice-core isotope records can in principle provide information on temperature variability over a wide range of timescales from subannual to glacial–interglacial variations, thus covering roughly six orders of magnitude. This offers the possibility to study the timescale-dependency of the climate variations which is thought to be an inherent property of the climate system depending on the underlying dynamics (Hasselmann, 1976; North et al., 2011; Rypdal et al., 2015; Lovejoy et al., 2013).

However, the interpretation of isotope records in terms of local atmospheric temperatures is complicated by a multitude of processes that distort the original relationship which is observed in precipitation (e.g., Fujita and Abe, 2006; Touzeau et al., 2016; Sjolte et al., 2011; Steen-Larsen et al., 2011). A record of isotopic composition is only created, to a first approximation, if there is snowfall. The intermittency of precipitation is known to strongly affect the isotopic composition of a certain snow layer. It can bias its mean value, e.g., the annual average, through the seasonal timing of precipitation (Sime et al., 2009; Laepple et al., 2011), but also induce variability when this seasonal distribution changes from year to year (Persson et al., 2011). The uneven deposition, as well as the steady and strong winds at the surface that lead to constant erosion, drift and vertical mixing of the surface snow, create strong spatial variability (Fisher et al., 1985; Münch et al., 2016b, 2017a). Finally, when the snow is deposited, the diffusion of vapour through the firn column (Johnsen, 1977; Whillans and Grootes, 1985; Johnsen et al., 2000) smoothes the isotope variations, reducing the power at high frequencies (van der Wel et al., 2015b), but also strongly shapes the apparent isotopic variability (Laepple et al., 2018).

The combined effect of these processes that, to a first approximation, are not directly linked to variations in temperature, represents a significant amount of noise in the isotopic record, especially in low-accumulation regions on the Antarctic Plateau. This noise strongly questions the representativity of single ice-core measurements (Karlöf et al., 2006; Münch et al., 2016b) and the interpretation of isotope in terms of temperature variability (Laepple et al., 2018). This is especially true when the climate signal itself is only relatively weak. While for the strong glacial–interglacial variations, deep ice cores record a consistent picture of the changes (e.g., Jouzel et al., 2007), it is questioned whether the recorded Holocene variability in single cores depicts the true temperature variability (Kobashi et al., 2011). Spatial averaging of isotope records thus represents an important attempt to reduce the overall noise level (Münch et al., 2016b; Stenni et al., 2017).

However, while the study by Münch et al. (2016b) provides a first insight into the relationship of climate signal and noise for short spatial and temporal scales, the link to longer scales, important for the interpretation of Holocene temperature reconstructions, is still missing, and the relative influence of the noise compared to the climate signal is unclear on these timescales. Furthermore, knowledge on the spectral shape of the noise would allow to correct the isotope-inferred variabilities for the noise contribution.

Here, we present a simple spectral method to separate the local noise from spatially coherent signals based on information from multiple isotope records. We apply our model to spatial arrays of firn cores from Dronning Maud Land in East Antarctica and from the West Antarctic Ice Sheet in order to derive an improved estimate of the temperature variability in the two regions, and to learn about the timescale-dependency of the signal-to-noise ratio. While our results for Dronning Maud Land confirm the noise levels inferred in previous studies on short temporal scales, and also suggest white noise on longer timescales, the comparison of the two Antarctic regions reveals strong, unexpected discrepancies. These potentially indicate significant differences in precipitation weighting and show that the underlying processes are not yet fully understood.

6.2 DATA AND METHODS

6.2.1 *Isotope records from Dronning Maud Land and West Antarctica*

We analyse isotope records from two arrays of annually dated firn cores: (1) from Dronning Maud Land (DML) on the Antarctic Plateau and (2) from the West Antarctic Ice Sheet (WAIS).

From DML we use a total of 15 records obtained during the EPICA (European Project for Ice Coring in Antarctica) pre-site survey (Oerter et al., 2000) which cover at least the last $\sim$ 200 yr (Table 6.1, Graf et al., 2002), forming our first data set. Three of these records (B31–B33) cover the last $\sim$ 1000 yr and are therefore included in a second separate data set. The core B32 is near ($\sim$ 1 km) to the deep EPICA DML (EDML) ice-core site at Kohnen Station (EPICA community members, 2006). The chronologies of the records are based on seasonal layer counting of chemical impurity records constrained by tie points from the dating of volcanic ash layers (Graf et al., 2002). The uncertainty of the dating is reported in the original publication to be $\sim$ 2 % of the time interval to the nearest tie point. This corresponds to a maximum time uncertainty of $\sim$ 1.2 yr for the short and of $\sim$ 3.5 yr for the long records. Since our spectral model (Sect. 6.2.2) relies on equal time intervals covered by the records in each data set, we restrict the time spans for the first data set to 1801–1994 CE and for the second data set to 1000–1994 CE.

From WAIS we collect five cores obtained within the US ITASE (International Trans-Antarctic Scientific Expedition) project (Mayewski et al., 2005) which cover the time interval of 1800–2000 CE (Table 6.1,

TABLE 6.1. Overview of the firn cores (sorted into three data sets) used in this study. Listed are the time span each core array covers (in yr CE), the region (range of latitude/longitude), the number of cores in each array (N), the range of the local accumulation rates ($\dot{b}$) and 10 m firn temperatures (T_{firn}) as reported in the original studies, and the range of intercore distances (d).

Core array (Time span)	Region	N	$\dot{b}$ $\mathrm{kg\,m^{-2}\,yr^{-1}}$	T_{firn} °C	d km
DML1[a] (1801–1994)	74.5–75.6° S 6.5° W–6.5° E	15	40–90[d]	$-(40–46)$[d]	1–370
DML2[b] (1000–1994)	75.0–75.6° S 3.4° W–6.5° E	3	50–60[d]	$-(44–46)$[d]	120–280
WAIS[c] (1800–2000)	77.7–80.6° S 111.2–124.0° W	5	140–220[e]	~ -30[f]	20–340

[a] Firn cores FB9804, FB9805, FB9807–FB9811, FB9813–FB9817, B31–B33 (Graf et al., 2002)
[b] Firn cores B31–B33 (Graf et al., 2002) [c] Firn cores WDC2005A, ITASE-1999-1, ITASE-2000-1, ITASE-2000-4, ITASE-2000-5 (Steig et al., 2013) d Oerter et al. (2000) e Kaspari et al. (2004) f WAIS Divide Project Members (2013)

Steig et al., 2013), including the core WDC2005A which is part of the WAIS Divide deep ice core (WDC; WAIS Divide Project Members, 2013). The selection of the cores is based on the constraint to cover a relatively coherent region on the West Antarctic Ice Sheet but to ensure, at the same time, a sufficiently long time duration of the records for a meaningful comparison with the DML cores. Dating of the cores was done through annual layer counting of chemical trace species, validated by identification of volcanic tie points (Steig et al., 2005). The absolute time uncertainty is reported to be about ±2 yr. The local accumulation is 2–4 times as high as at EDML (Table 6.1).

Prior to spectral analysis, missing years in the records ($\sim 1.6\,\%$ of all data points) have been linearly interpolated. Spectra are then estimated using Thomson's multitaper method with three windows (Percival and Walden, 1993) with linear detrending before analysis. This approach is known to introduce a small bias at the lowest frequencies, and we omit the lowest frequency from all shown spectra. For display purposes, the spectra are displayed on logarithmic axes and smoothed using a Gaussian kernel with constant width in logarithmic frequency space. To avoid biased estimates at low- and high-frequency boundaries, the kernel is truncated on both sides to maintain its symmetry.

6.2.2 *Model for the separation of signal and noise in the spectral domain*

We assume that the power spectral density of a single isotope record, $\mathcal{X}_i(f)$, is the sum of a common (climate) signal and an independent noise component, thus $\mathcal{X}_i(f) = \mathcal{C}(f) + \mathcal{N}_i(f)$. We further assume that the statistical properties of the individual noise terms are the same for all N records. We can use the average over all individual spectra as a measure for the single records' power spectral density to reduce the spectral uncertainty,

$$\mathcal{M}(f) = \frac{1}{N}\sum_{i=0}^{N} \mathcal{X}_i(f) = \mathcal{C}(f) + \mathcal{N}(f). \tag{6.1}$$

By contrast, assuming that the noise is independent between the single records, the average over the N isotope records in the time domain (the "stacked" record) has a power spectrum of

$$\mathcal{S}(f) = \mathcal{C}(f) + \frac{1}{N}\mathcal{N}(f). \tag{6.2}$$

From the system of equations (6.1) and (6.2) we can derive expressions for the spectrum of the common signal and the noise,

$$\mathcal{C}(f) = \mathcal{S}(f) - \frac{1}{N}\mathcal{N}(f), \tag{6.3a}$$

$$\mathcal{N}(f) = \frac{N}{N-1}\Big[\mathcal{M}(f) - \mathcal{S}(f)\Big]. \tag{6.3b}$$

We explicitly note that this model does not necessarily yield the true climatic signal of atmospheric temperature variations, since any spatially coherent variations on a given timescale will contribute to the estimated signal $\mathcal{C}(f)$.

6.2.3 *Timescale-dependent estimate of the signal-to-noise ratio*

The signal-to-noise variance ratio F as a function of the timescale is defined as the ratio of the signal and noise spectra,

$$F(f) = \frac{\mathcal{C}(f)}{\mathcal{N}(f)}. \tag{6.4}$$

The signal-to-noise ratio after averaging the isotope records onto a certain temporal resolution Δt (the "averaging period") is obtained from first integrating the signal and noise spectra and then taking the ratio,

$$\overline{F}(f_{\mathrm{Nyq}}) = \frac{\int_{f_0}^{f_{\mathrm{Nyq}}} \mathcal{C}(f)\,\mathrm{d}f}{\int_{f_0}^{f_{\mathrm{Nyq}}} \mathcal{N}(f)\,\mathrm{d}f}, \tag{6.5}$$

where f_0 is the lowest frequency of the spectral estimates and f_{Nyq} the Nyquist frequency corresponding to the averaging period, thus $1/(2\Delta t)$.

The correlation between the common signal and a "stacked" record, built from the spatial average of N individual records, is on the given temporal resolution then

$$\mathrm{corr}(f_{\mathrm{Nyq}}) = \frac{1}{\sqrt{1 + \left(N\overline{F}(f_{\mathrm{Nyq}})\right)^{-1}}}. \tag{6.6}$$

6.2.4 *Estimates of the effect of vapour diffusion and time uncertainty*

Both vapour diffusion in the firn (Johnsen et al., 2000) as well as time uncertainty influence our spectral estimates. Diffusion reduces the high-frequency variance of all single records and thus damps the spectral power of the spectral estimates at the corresponding frequencies (van der Wel et al., 2015b). This affects our noise estimates on the fast timescales, but to a first approximation it does not affect the estimated signal-to-noise ratios and correlations. However, due to the reduced high-frequency signal variances, the measurement noise gains in importance affecting the estimated signal spectra. Time uncertainty does not affect the overall shape of broadband spectra (Rhines and Huybers, 2011) but diminishes the correlation between the records (Haam and Huybers, 2010). The latter effect is strongest on timescales close to the Nyquist frequency of the records' original resolution and leads to an overestimation of the noise variance there.

We do not attempt to make a full correction for the effects but instead estimate the frequency range that is influenced. In case of diffusion with a constant diffusion length σ, the initial power spectral density is reduced to a value of $1/e$ at a frequency corresponding to $\ell/(2\pi\sigma)$ where ℓ is the annual layer thickness (van der Wel et al., 2015b). Assuming a constant diffusion length of 8 cm (Johnsen et al., 2000) and annual layer thicknesses of 7 cm of ice for the EDML site (EPICA community members, 2006) and of 22 cm for the WAIS Divide ice-core site (Kaspari et al., 2004), this corresponds to time periods of roughly 7 and 2.3 yr, respectively. By simulating surrogate records in a Monte Carlo approach we find the influence of the reported time uncertainties of the records to be weak on timescales more than twice of the assumed time uncertainty. Thus, as a heuristic estimate, we choose the decadal timescale as a threshold above which our estimates are largely unaffected by diffusion and time uncertainty.

6.2.5 *Present-day spatial decorrelation scales of atmospheric temperatures for DML and WAIS*

Our spectral model to separate signal and noise based on a spatial array of isotope records makes the fundamental assumption of a spatially coherent signal across the region covered by the cores. To test this assumption for present-day conditions, we estimate the spatial

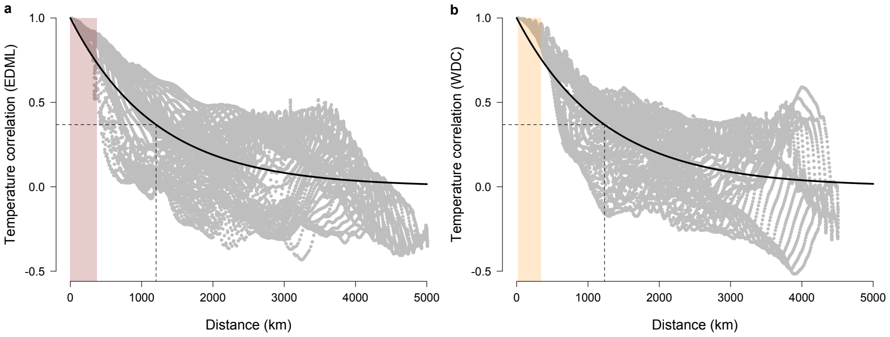

Figure 6.1. Present-day temperature decorrelation across DML and WAIS. Shown are the correlations of annual-mean temperatures (grey dots) of the ERA-Interim reanalysis (Dee et al., 2011) between the locations of the EDML (**a**) and WDC (**b**) ice core (nearest gridbox), respectively, and all other gridboxes on the Antarctic continent. Black lines show an exponential fit to the data; dashed lines indicate the point at which the correlations in the model have dropped to $1/e$ (at 1202 (1232) km for EDML (WAIS)). Coloured shadings indicate the distances between the cores of the studied arrays (Table 6.1).

decorrelation scales of annual-mean temperatures for DML and WAIS from the temperature fields of the ERA-Interim reanalysis (Dee et al., 2011). For this, we calculate the correlations between the temperature time series at the location of the EDML (75° S, 0° W) and of the WDC ice core (79.5° S, 112° W), respectively, with every other gridbox of the Antarctic continent. We then fit an exponential model to the correlations of the form $\exp(-d/\Delta)$, where d is the distance between the given location (EDML or WAIS) and a gridbox and Δ the fit parameter. From this we report Δ as the present-day spatial temperature decorrelation scale (Fig. 6.1).

Based on the analysis we find decorrelation scales of $\sim 1200\,\text{km}$ for both regions. These are large compared to the individual intercore distances (Table 6.1) which suggests that annual-mean temperatures are spatially coherent across the studied regions. In fact, the individual correlations between the reanalysis temperatures at EDML and WDC and the other core sites are close to 1 and even almost exclusively above the ones predicted from the simple exponential model (Fig. 6.1). Since the spatial coherence of climate variations typically increases with increasing timescale, it is reasonable to assume that the studied firn cores in each region should record a coherent temperature signal.

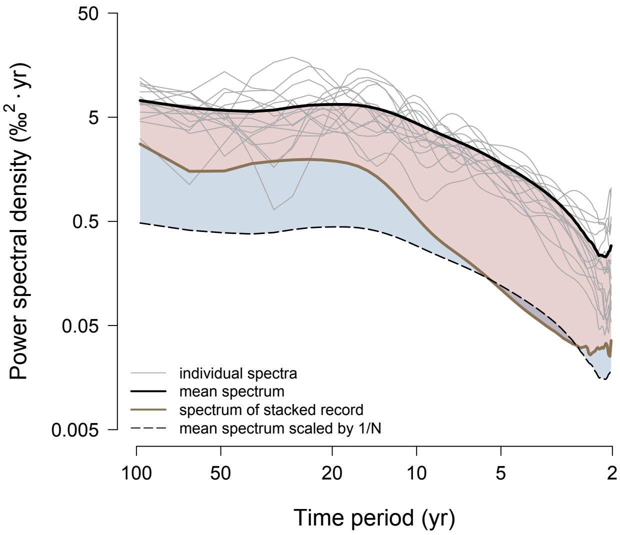

Figure 6.2. Detailed results of estimated power spectral densities for the 200 yr long records from Dronning Maud Land for illustration of the steps involved in our spectral correction model. Thin grey lines show the individual spectra for each record, the mean across these is indicated by the black line. The dashed black line shows the null hypothesis of assuming that all isotope variations are noise (i.e. the mean spectrum divided by the number of records). In contrast, the brown line depicts the spectrum after averaging all records in the temporal domain (the "stack"). Red and blue shadings are proportional to the average noise and signal content, respectively, of the single records. Note that all axes are in logarithmic units; and that the x axis is given in periods in yr, thus the frequency of the variations increases to the right.

6.3 RESULTS

6.3.1 *Illustration of the model approach*

We first present detailed results based on the 200 yr long records from DML (Fig. 6.2) in order to illustrate the individual steps involved in our spectral model of separating signal and noise (Sect. 6.2.2).

Each of the 15 records of the firn-core array provides an estimate of the single records' power spectral density (thin grey lines in Fig. 6.2), and thus a timescale-dependent representation of the isotope variations in the study region. The differences between the spectra are not only due to differences in the isotopic variability between the records, but also caused by the spectral uncertainty due to the finite length of the records. Hence, in order to provide a more robust estimate of the single records' spectrum, we calculate, and use throughout the following, the average over all individual spectra (thick black line in the figure). This mean spectrum shows a close-to-constant spectral power above decadal timescales, i.e. is "white", and a strong decrease

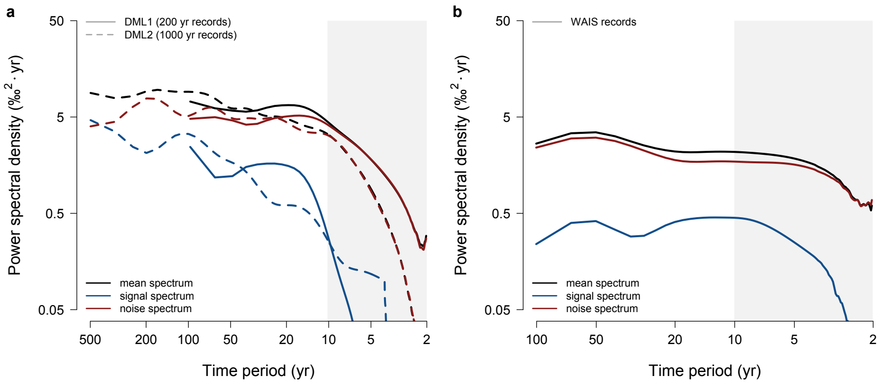

FIGURE 6.3. Results of the spectral correction model for (**a**) the records from Dronning Maud Land and (**b**) the records from the West Antarctic Ice Sheet. Shown are the mean spectra across the individual records (black) together with the estimated signal (blue) and noise (red) spectra. For Dronning Maud Land, both the results for the short, 200 yr long records (solid lines) and the longer records covering the last 1000 yr (dashed lines) are included. The unreliable part of the spectra on subdecadal timescales is shaded in grey.

in spectral power towards higher frequencies caused by vapour diffusion in the firn.

In addition, we show the mean spectrum divided by the number of records (here, $N = 15$; dashed black line). This spectrum represents the null hypothesis assuming that all isotope variations present in the firn-core records are just independent noise, as averaging across N records of noise with the same statistical properties will reduce the total noise variance by a factor of $1/N$. By contrast, averaging across records that contain noise and additionally a common, i.e. spatially coherent, signal, will result in a spectrum where the noise component is also reduced by $1/N$, but with the common signal left unaltered (Eq. 6.2). For the average of the DML records (the "stack") we find that on fast timescales (periods of 2 to ~ 7 yr) the variability of each individual record is consistent with the null hypothesis of only noise (represented by the red shading in Fig. 6.2), as the spectrum of the stack and the mean spectrum divided by N fall on top of each other. By contrast, on longer timescales the individual records contain a common signal (represented by the blue shading) that "survives" the averaging process and increases in power with increasing timescale.

The spectrum of the stack is thus indicative of the common signal contained in the records but also contains a residual amount of noise which has to be corrected for (Eq. 6.3a). This finally yields (Fig. 6.3a) the signal spectrum and the spectrum of the noise (Eq. 6.3b).

Finally, we note that for timescales of ~ 3 to 7 yr the spectrum of the stacked record lies slightly under the mean spectrum scaled by $1/N$ which is unphysical as it would suggest negative signal variance. This discrepancy is either due to the spectral uncertainty of the estimates and/or caused by the effect of time uncertainty. We thus have to treat

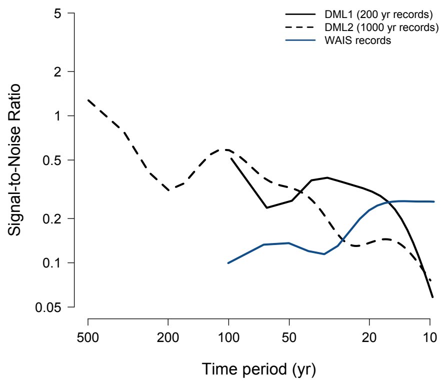

FIGURE 6.4. Timescale-dependency of the signal-to-noise ratios of the DML (black) and WAIS (blue) isotope records, based on Eq. (6.4). For Dronning Maud Land, both the results for the short, 200 yr long records (solid lines) and the longer records covering the last 1000 yr (dashed lines) are shown. The plot is restricted to decadal and longer time periods due to the high uncertainty of the ratios on higher frequencies.

the results on these timescales very cautiously. For the integration of the signal-to-noise ratios (Eq. 6.5) we set the signal spectrum to zero for these regions.

6.3.2 *Timescale-dependency of estimated DML and WAIS signal and noise variability*

Unlike the average spectrum across all individual isotope variations, the signal spectrum of the 200 yr long DML isotope records shows a strong increase in power spectral density with increasing timescale (Fig. 6.3a). This is confirmed by the 1000 yr long records whose signal exhibits a similar power spectrum for the range of overlapping timescales. This is partly expected since the three longer cores are also included in the larger data set of shorter records, but also holds over the entire last 1000 yr. In addition, the signal spectrum of the long cores shows a consistently further increase for longer timescales than covered by the short records, and, interestingly, a similar slope towards subdecadal timescales, although our results are highly uncertain there. By contrast, the signal spectrum of the firn cores from the West Antarctic Ice Sheet (Fig. 6.3b) exhibits a nearly flat appearance, with even diminishing power spectral density towards centennial timescales.

An equivalent difference can be seen in the respective noise spectra (Fig. 6.3). While the DML noise spectra are essentially white on multidecadal and centennial timescales, the WAIS noise spectrum suggests an increase of spatially incoherent isotope variations on multidecadal timescales, in line with the decrease in signal power for the same fre-

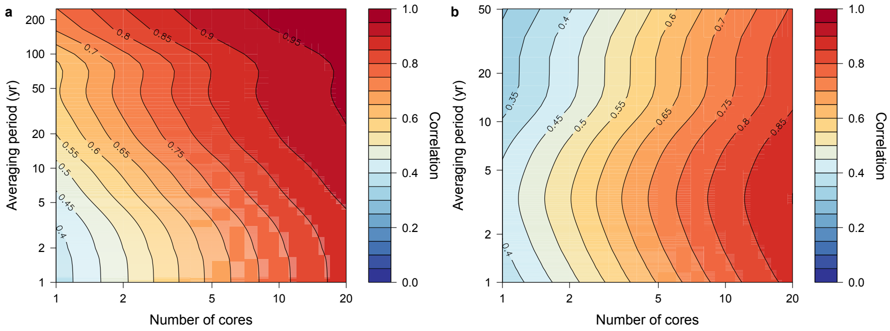

FIGURE 6.5. Correlation of stacked isotope records with the common signal as a function of the averaging period and the number of firn cores included in the average. The correlations are based on Eq. (6.6) using the estimated signal-to-noise ratios for (**a**) the 1000 yr long DML and (**b**) the WAIS records. Parts in the high-frequency range (above decadal resolution) which are affected by the unphysical negative signal variances caused by the high uncertainty of the spectral estimates in this frequency band (see text) have been set to zero for the calculations.

quency band. For both regions, the noise spectra show an exponential decrease towards the high-frequency end.

As a direct result of the previous findings, the timescale-dependency of the signal-to-noise ratios is also strongly different between the two regions (Fig. 6.4). The signal-to-noise ratio for the DML region is low at decadal timescales ($\lesssim 0.1$) but then shows a continuous increase with timescale, reaching values around 1 for multicentennial timescales. In sharp contrast to DML, the estimated WAIS signal-to-noise ratio starts at a higher value at the decadal scale (~ 0.3) but then decreases to values around 0.1 for centennial timescales; however, the statistical significance of this decrease is unclear.

A complementary picture is obtained for the expected correlation of a stacked record with the underlying signal as a function of the number of records averaged and the temporal averaging period (Eq. 6.6 and Fig. 6.5). For DML, the correlation between an individual record on interannual resolution is rather low at roughly 0.3–0.4 (Fig. 6.5a). However, these numbers have to be taken with care due to the considerable uncertainties of the estimated spectra in this frequency band. Similar values are obtained for the WAIS region (Fig. 6.5b). For longer averaging periods, the correlation for DML shows a steady increase with the averaging period, in line with the increase in signal-to-noise ratio, reaching values above 0.6 for single records and centennial periods. The correlation increases further with the number of cores averaged, since the residual amount of noise contained in a stacked record scales with $1/N$. Again in contrast to these findings, for WAIS the correlation with the underlying signal is rather insensitive to the averaging period, remaining relatively constant over averaging periods from annual to 50 yr resolution, and increasing only with the number of averaged records.

6.4 DISCUSSION

6.4.1 *Interpretation of the noise spectra*

The DML noise spectrum as inferred from both data sets shows a close-to-constant noise level across the range from decadal to multi-centennial timescales (Fig. 6.3a) which suggests that the underlying processes that create the noise do not depend on the timescale. These results are promising, as white noise is usually the simplest assumption that is made in order to model the statistics of noise, and our results give a first indication for the validity of such an assumption for Antarctic isotope records. On the other hand, our results might indicate an increase in noise level on multidecadal timescales for the WAIS region (Fig. 6.3b), suggesting that white noise is not the only possible spectral shape for the non-coherent part of the isotope variations. However, this assertion is strongly dependent on the uncertainty of the noise estimate which we have not fully covered here.

For both study regions, the noise spectra show an exponential decrease towards the high-frequency end which can be explained by vapour diffusion in the firn. This is suggested by the stronger decrease observed for DML, which is consistent with the lower local accumulation rates compared to WAIS (Table 6.1), leading to higher diffusion lengths (Johnsen et al., 2000) and thus a stronger smoothing. A further confirmation is the stronger decrease seen for the noise spectrum of the 1000 yr long DML records. This is expected since the older parts of the cores have experienced a stronger diffusional smoothing as the diffusion process had more time to act since deposition of the snow. This qualitative confirmation of the diffusion process could be formally tested by modelling the effect on surrogate time series. Such an approach would also allow to estimate the original noise spectrum prior to diffusion which could be compared to estimates based on shorter data (Münch et al., 2016b). However, this would require detailed knowledge on the relevant parameters at every core site, which is beyond the scope of this study.

6.4.2 *Interpretation of the signal spectra*

Our estimate of the DML signal spectrum (Fig. 6.3a) shows an increase in power spectral density with timescale. Fitting a power law of the form $f^{-\beta}$, where f denotes frequency, yields a slope of the signal spectrum of roughly $\beta \sim 0.8$ for variations above decadal scales. This is considerably higher as the slope of the average spectrum of the single records ($\beta \sim 0.3$). This suggests that we indeed observe a climatic feature here that is related to temperature variability, since an increase in temperature variability with timescale is generally expected (e.g., Pelletier, 1998; Huybers and Curry, 2006; Laepple and Huybers, 2014). Our findings thus underscore that single isotope records from the Antarctic Plateau are no reliable recorders of Holocene temperature variations, as already inferred from other studies (Karlöf et al., 2006; Münch et al., 2016b; Laepple et al., 2018), and that stacking of records is essential to overcome the inherent noise.

In contrast to Dronning Maud Land, the signal spectrum of the isotope records from the West Antarctic Ice Sheet exhibits virtually no increase in power spectral density with timescale above the 10 yr period (Fig. 6.3b). This is surprising since it either suggests a coherent white-noise signal of temperature variations over West Antarctica, or strong non-climatic effects affecting the WAIS isotope records. However, both possibilities are unexpected. First of all, the present-day spatial decorrelation lengths of annual-mean temperatures are similar for both Antarctic regions (Fig. 6.1) which also suggests a similar, or even stronger, coherence on the longer timescales covered by the firn-core data. To a first approximation, we would thus not assume a fundamentally different climate variability in West compared to East Antarctica in the Holocene. Secondly, ice cores in West Antarctica are usually thought to be more reliable recorders of local temperatures than their East Antarctic counterparts owing to the higher accumulation rates.

6.4.3 *Estimated signal-to-noise ratios*

As a direct result of the estimated signal and noise spectra we presented estimates for the timescale-dependency of the signal-to-noise ratios (Fig. 6.4), and of the representativity of firn-core-based reconstructions as a function of the temporal averaging period and the number of cores included in a stacked record. This representativity is here expressed as the correlation of a stacked record with the underlying common signal (Fig. 6.5).

For DML, the estimated signal-to-noise ratio, or equivalently, the representativity in terms of correlation, is consistent with previous findings. Graf et al. (2002) estimated the signal-to-noise ratio of a single isotope record at annual resolution, based on the intercore correlations of the same data set, to be $F = 0.14$, or, expressed in correlation, $r = 0.35$. The latter value is similar to what we find based on integrating the estimated signal-to-noise ratios (Fig. 6.5a), despite the high uncertainties on the high-frequency end of the spectra. This is of course expected since both estimates use the same data set, and the agreement thus only represents a confirmation of our model; however, similar values have been obtained using a larger set of cores from the same region that cover a shorter time period (Altnau et al., 2015). In addition, based on the analysis of the spatial and vertical variances in a two-dimensional sampling approach of the near-surface firn on a 1 km scale, Münch et al. (2016b) estimated signal-to-noise ratios for annual resolution of ~ 0.1–0.8. Our estimates for the here studied larger scales thus fall on the lower end of this estimate.

For longer timescales, the signal-to-noise ratios for DML show a steady increase (Fig. 6.4) due to the increase in signal power and the concurrent constancy of the noise level (Fig. 6.3a). This explains the general agreement of isotope records obtained from deep ice cores on glacial–interglacial timescales. Given that the signal power increases further with even longer timescales than studied here, and that the noise level stays constant at the same time, even single records will exhibit a high correlation with the underlying signal on periods above centennial scales (Fig. 6.5a).

For Greenland, signal-to-noise ratios have been estimated at annual resolution to be significantly higher as compared to DML, typically in the range of 1–3 (Fisher et al., 1985; Steen-Larsen et al., 2011). This is usually thought to reflect the higher accumulation rates in Greenland. However, while our results presented for WAIS show higher signal-to-noise ratios around decadal timescales (Fig. 6.4), in line with the higher accumulation rates (Table 6.1), the signal-to-noise ratios seem not to increase with timescale. If this finding is indeed a true feature and holds in future studies, this suggests that there is no simple scaling of the signal-to-noise ratios with accumulation rate but that additional effects are involved. Finally, our findings suggest a correlation with the common signal at WAIS of around 0.7–0.8 for the average over 10 cores studied at annual resolution (Fig. 6.5b). This is higher as the observed correlation of a stack of firn cores from the West Antarctic Ice Sheet with the temperature record from Byrd Station ($r = 0.48$; Steig et al., 2013). However, the record stack by Steig et al. (2013) is built from a variable number of firn cores depending on the time period, and the correlation is calculated only over the length of the Byrd temperature record, i.e. the last ~ 40 yr. In addition, the stack of Steig et al. (2013) was correlated directly with a temperature record, while our estimates refer to the correlation between a stack and the common isotope signal. This impedes a one-to-one comparison of both correlation results. Nevertheless, observed correlations to temperatures seem to be even lower than predicted here.

6.4.4 *What causes the difference between West and East Antarctica?*

Our study revealed significant differences in the timescale-dependencies of the signal and noise variability, and hence of the signal-to-noise ratio, between the East Antarctic Dronning Maud Land and the West Antarctic Ice Sheet. These are unexpected as, to a first approximation, one would expect similar climate signals in both regions over the studied timescales. Although we have not reached a definitive explanation for the discrepancies, there are some indications for an influence of different precipitation patterns.

Our model for the separation of signal and noise assumes the presence of a coherent signal across the region of the studied cores. However, the model does not make any assumptions on the nature of this signal. Although the present-day annual-mean temperature variations are coherent over both regions (Fig. 6.1) and therefore suggest a common temperature signal recorded by the firn cores, we cannot rule out the possibility of spatially coherent noise that additionally contributes to the estimated common signal. Precipitation intermittency is a known source for variability in isotope records (Persson et al., 2011). If the spatial separation of the cores is larger than the decorrelation length of the typical precipitation patterns but smaller than that of the temperature variations, the average isotope record will show reduced noise induced by precipitation weighting compared to single records, but will still record the full temperature signal.

However, there are indications that this is not the case for Dronning Maud Land. Reijmer and van den Broeke (2003) estimated the precipitation patterns for the region based on measurements of autonomic weather stations. They concluded that accumulation occurs in many small (1–2 cm) and few larger events ($\gtrsim 5$ cm) of snowfall, where the latter occur only a few times per year without clear seasonality but coherently over DML. This would suggest comparable decorrelation scales of both the temperature and precipitation fields in the region, at least for the large precipitation events. If this is true, our estimated DML signal might to some extent reflect the coherent precipitation weighting and not solely the temperature variations.

Our estimates of the signal-to-noise ratios at short timescales indeed point in this direction. If the effect of precipitation intermittency were spatially incoherent over the analysed spatial scales of the cores, we would expect a *higher* noise level in single records than estimated on a local (< 1 km) scale where the precipitation patterns can certainly be assumed coherent. However, the opposite seems to be the case since we observe signal-to-noise ratios on the spatial scale of the firn cores that fall on the lower end of the estimates for the local scale based on the study by Münch et al. (2016b). This might indicate that the effect of precipitation weighting is not averaged out by stacking the DML records but instead contributes to the overall common signal.

Following this interpretation, our results for the West Antarctic Ice Sheet might suggest different patterns of precipitation as compared to DML. There seems to be an increase in noise level on multidecadal timescales (Fig. 6.3b) which could be explained by variable precipitation intermittency between the cores for these time periods. However, this is speculative given the presented evidence and further studies are needed to constrain the role of precipitation intermittency across different regions of the Antarctic continent.

6.5 CONCLUSIONS

We presented a simple spectral method to separate the variations recorded by isotope records into the contributions from noise and from a common, i.e. spatially coherent, signal, and applied this to firn cores from the East Antarctic Dronning Maud Land (DML) and the West Antarctic Ice Sheet (WAIS). Using this method, we made a first attempt to estimate the isotopic signal-to-noise ratio as a function of timescale, which is of fundamental interest for the interpretation of isotope records obtained from ice cores. Although our results for DML provide evidence that the average firn-core isotope record exhibits a temperature signal consistent with expectations, the combination of our findings for both regions suggests an influence from precipitation intermittency on the estimated signal. We conclude that attempts to reconstruct the natural temperature variability should not only aim at averaging as many records as possible, but instead have to consider the spatial coherence of precipitation patterns in order to realise an optimal sampling strategy for averaging, or obtaining new, firn-core isotope records.

7

GLOBAL PATTERNS OF DECLINING TEMPERATURE VARIABILITY FROM THE LAST GLACIAL MAXIMUM TO THE HOLOCENE

Kira Rehfeld[1,2], Thomas Münch[1,3], Sze Ling Ho[4,1], and
Thomas Laepple[1]

[1] *Alfred Wegener Institute Helmholtz Centre for Polar and Marine Research, Telegrafenberg A43, 14473 Potsdam, Germany*
[2] *British Antarctic Survey, High Cross, Madingley Road, Cambridge, CB3 0ET, United Kingdom*
[3] *Institute of Physics and Astronomy, University of Potsdam, Karl-Liebknecht-Str. 24/25, 14476 Potsdam, Germany*
[4] *University of Bergen and Bjerknes Centre for Climate Research, Allégaten 41, 5007 Bergen, Norway*

This chapter is published in:
Nature, **554** (7692), 356–359, DOI: `10.1038/nature25454`,
2018.

ABSTRACT. Changes in climate variability are as important for society to address as are changes in mean climate (Katz and Brown, 1992). Contrasting temperature variability during the Last Glacial Maximum and the Holocene can provide insights into the relationship between the mean state of the climate and its variability (Ditlevsen et al., 1996; Shao and Ditlevsen, 2016). However, although glacial–interglacial changes in variability have been quantified for Greenland (Ditlevsen et al., 1996), a global view remains elusive. Here, we use a network of marine and terrestrial temperature proxies to show that temperature variability decreased globally by a factor of four as the climate warmed by 3–8 degrees Celsius from the Last Glacial Maximum (around 21 000 years ago) to the Holocene epoch (the past 11 500 years). This decrease had a clear zonal pattern, with little change in the tropics (by a factor of only 1.6–2.8) and greater change in the mid-latitudes of both hemispheres (by a factor of 3.3–14). By contrast, Greenland ice-core records show a reduction in temperature variability by a factor of 73, suggesting influences beyond local temperature or a decoupling of atmospheric and global surface temperature variability for Greenland. The overall pattern of reduced variability can be explained by changes in the meridional temperature gradient, a mechanism that points to further decreases in temperature variability in a warmer future.

There is scientific consensus that the mean global temperature has been rising over the instrumental era (IPCC, 2013). However, whether this warming has caused surface temperatures to become more (Hansen et al., 2012) or less (Rhines and Huybers, 2013; Huntingford et al., 2013) variable, and how this variability will change in a warmer future, remain topics of debate. Here we use palaeoclimate proxy data to quantify changes in temperature variability before and after the last major transition in global mean climate: the 3–8 °Cwarming (Shakun and Carlson, 2010) from the Last Glacial Maximum (LGM, around 21 000 years (21 kyr) ago) to the current warm period of the Holocene (Fig. 7.1). The magnitude of temperature change during this transition is in the same range as that projected for the coming centuries (IPCC, 2013).

The global spatial pattern of the mean LGM-to-Holocene temperature change has been established through numerous studies (Shakun and Carlson, 2010; Annan and Hargreaves, 2013; MARGO Project Members, 2009). However, except for some studies on changes in interannual climate variability in the tropics (Koutavas and Joanides, 2012), our current understanding of changes in variability is largely based on the stable oxygen isotope records of the high-resolution central Greenland ice cores (NGRIP members, 2004). The isotope records, which are interpreted as a proxy for temperature (Masson-Delmotte et al., 2005), show that the last glacial period appears to have been not only cold but also highly variable on decadal to millennial timescales (Ditlevsen et al., 1996; Shao and Ditlevsen, 2016). This finding is not limited to the magnitude of distinct events, such as the Heinrich stadials (that is, cold periods in Greenland) or the abrupt transitions into the Dansgaard–Oeschger interstadials; it also holds for the background variability during the LGM (Fig. 7.1b).

Consequently, glacial climate has been characterised as highly variable (Ditlevsen et al., 1996; Shao and Ditlevsen, 2016), whereas the Holocene is commonly described as a stable and quiescent period (Shao and Ditlevsen, 2016). The large reduction in variability was proposed to have supported human dispersal throughout Europe (Gamble et al., 2004) and cultural evolution (Richerson et al., 2001). However, the evidence for an exclusively stable Holocene climate—beyond that of Greenland ice-core records—is unclear, particularly because other proxy records for temperature in and outside of Greenland suggest considerable variability during the Holocene (Kobashi et al., 2011; Laepple and Huybers, 2014).

In this study, we derive a quantitative estimate for global and regional change in temperature variability between the LGM (27–19 kyr ago) and the Holocene (8–0 kyr ago) based on high-resolution palaeoclimate proxy records for temperature (Fig. 7.1a). These time periods represent rather stable boundary conditions with minimal changes in ice-sheet size and sea level. Furthermore, our LGM time window contains only one small Dansgaard–Oeschger event, thereby enabling us to focus our analysis on the glacial background state. We compile two global data sets* (Methods, Sect. A.1). The first ("joint") data set contains 28 records that cover both the LGM and the Holocene.

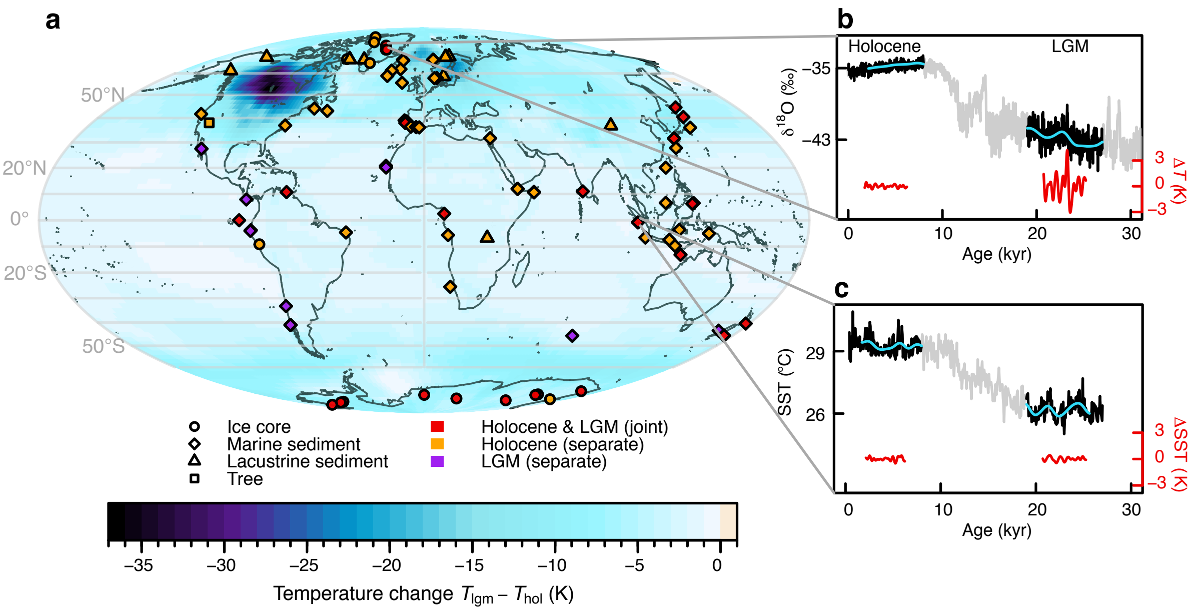

FIGURE 7.1. Proxy records for temperature. (**a**) Site locations (symbols) and mean LGM-to-Holocene temperature change ($T_{\mathrm{lgm}} - T_{\mathrm{hol}}$; background), estimated from climate model and proxy data (Annan and Hargreaves, 2013). The pre-industrial (AD 1850) temperature is used as a surrogate for the Holocene time slice because we are interested in only the first-order pattern of the deglaciation. (**b**) North Greenland Ice Core Project (NGRIP) ice-core δ^{18}O data for Greenland (NGRIP members, 2004; black, expressed in ‰ with respect to Vienna Standard Mean Ocean Water) with millennial trend (blue) and bandpass-filtered temperature (ΔT; 0.5–1.75 kyr^{-1}; red) for Holocene and LGM (grey lines in background show the full record). (**c**) Sea-surface temperature (SST) inferred from Mg/Ca ratios from tropical marine sediment record SO189-39KL (Mohtadi et al., 2014); colours as in (**b**).

We estimate the change in variability from the ratio of LGM to Holocene variance separately for each record and thus independently of calibration uncertainties, as long as the calibrations are constant over time. This is a reasonable assumption because state-dependent calibrations have been proposed only for Greenlandic ice cores (Jouzel et al., 1997) and we take this into account. Analysing variance ratios from single cores also minimises site-specific effects on the variance estimates, such as the ecological preferences of the organisms that record the climate signal or the extent of bioturbation, which affects marine proxies (Methods, Sect. A.6). The second ("separate") data set is more extensive, containing 88 records for the Holocene and 39 for the LGM. In this case, we first derive zonal mean estimates of temperature variability for each time slice and then form the ratio. All proxy types for which multiple calibrations exist were recalibrated using a single temperature relationship for each proxy type and region. For both the joint and the separate data set, we quantify the change in variability as the ratio of variance at timescales between 500 and 1750 years in the spectral domain using a method that is insensitive to changes in the temporal sampling. We correct the ratio for the effects of non-climate variability in the proxy records using independent estimates of the signal-to-noise ratio of the proxies (Methods, Sect. A.5).

All three Greenlandic ice-core records display large changes in variability, with an average LGM-to-Holocene variance ratio $R = V_{\mathrm{lgm}}/V_{\mathrm{hol}}$ of 73 (90 % confidence interval of 50–112; Fig. 7.2a). In contrast to this marked reduction, the area-weighted average change in variability for the rest of the globe is far lower: the separate estimate indicates a decrease in variability by a factor of 7.0 (90 % confidence interval, 2.2–16). The large uncertainty range is due to the combination of many different proxy records which are affected by potential site-specific effects such as differing seasonal responses. The magnitude of change is confirmed by the joint data set, which offers a more precise estimate of $R = 4.4$ (90 % confidence interval, 2.5–6.6) by circumventing these complications. Together, these data sets suggest a significantly lower ($p \leq 0.01$) change in variability outside of Greenland than is found in Greenlandic ice-core records. The discrepancy also cannot be reconciled by considering a potentially lower quality of marine-based temperature reconstructions (Methods, Sect. A.5.1). This observation suggests that Greenlandic ice-core records should not be used as a sole reference for climate variability, particularly concerning the amplitude of change.

The spatial pattern of variability change (Fig. 7.2b–d) shows a distinct latitude dependence (Fig. 7.3a). A small, yet statistically significant, change can be found in the tropics (20° S–20° N; $R = 2.1$; (90 % confidence interval, 1.6–2.8)). The mid-latitudes (20–50° S and 20–50° N) show a moderate decrease in variability from the glacial period to the Holocene by a factor of 5.4 (90 % confidence interval, 3.3–10) and 11 (90 % confidence interval, 8.0–14). The polar regions (50–90° S and 50–90° N) are represented by only Greenlandic and Antarctic ice-core records and reveal an asymmetric pattern: the Greenland change is the highest globally, whereas Antarctica displays only a small change ($R = 2.5$; 90 % confidence interval, 2.0–3.2), comparable to that in the tropical ocean. West Antarctic ice cores show a stronger variability change than do ice cores from East Antarctica (Fig. 7.2d), a finding that is similar to the west–east contrast in the response to anthropogenic forcing (Bromwich et al., 2013). The estimated pattern of variability change is similar for multicentennial and millennial timescales (Methods, Fig. A.1), which demonstrates that our finding is not limited to one specific frequency band. This result further suggests that the Dansgaard–Oeschger event included in the LGM time slice has only a minor influence.

The equator-to-pole surface air temperature gradient in the LGM was larger than in the Holocene, because the high latitudes have warmed more than the tropics since the LGM (MARGO Project Members, 2009; Figs. 7.1a, 7.2b). Furthermore, the land–sea contrast in mid- to high latitudes was stronger in the LGM because a relatively

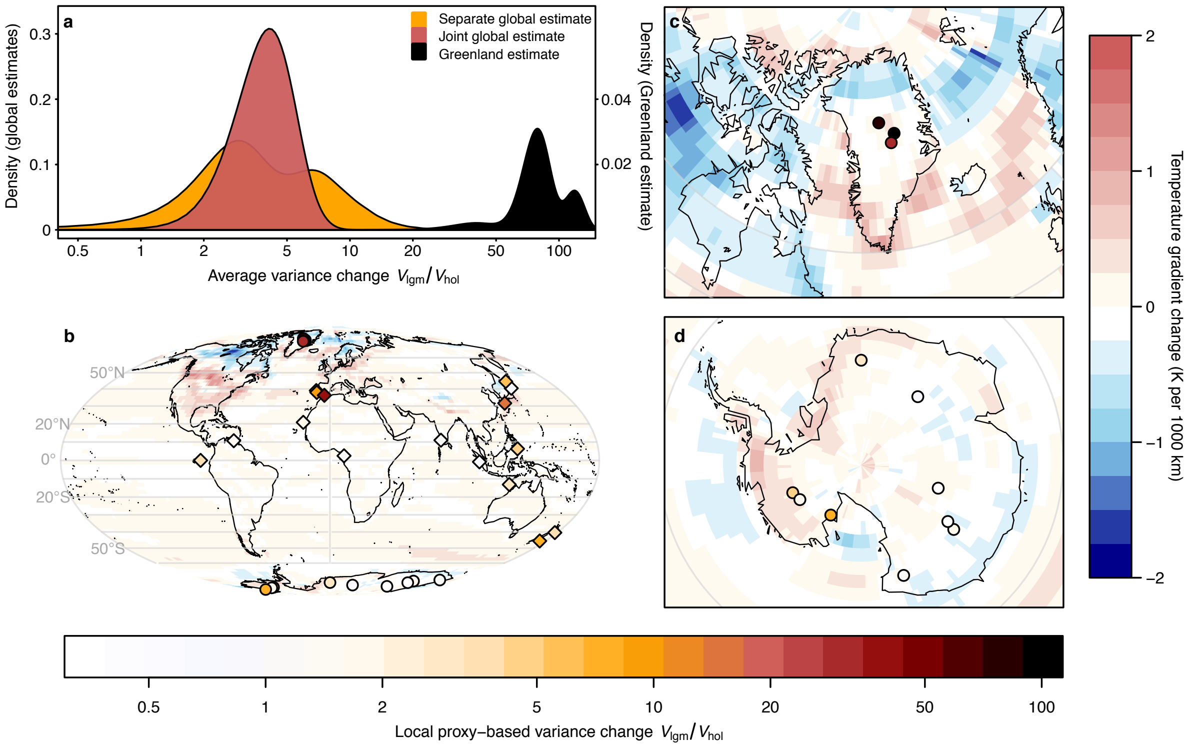

FIGURE 7.2. Global LGM-to-Holocene change in variability and temperature gradient. (**a**) Distribution of the globally averaged area-weighted LGM-to-Holocene variance ratio ($V_{\mathrm{lgm}}/V_{\mathrm{hol}}$; without Greenland; red denotes the joint data set, orange the separate data set) and the regional Greenland variance ratio (black). Note that for visibility the Greenland density estimates are on a separate y axis. (**b–d**) LGM-to-Holocene proxy-derived variance ratios (symbols, bottom colour scale) and modelled change in temperature gradient (Annan and Hargreaves, 2013; background, right colour scale; details in Methods, Sect. A.2) for the globe (**b**), Greenland (**c**) and Antarctica (**d**).

warm open ocean contrasted with the partly ice-covered land, and changing sea-ice cover affected both the meridional and zonal temperature gradients (de Vernal et al., 2006). Atmospheric temperature gradients are a primary driver of local temperature variability on synoptic timescales. Accordingly, changes in spatial gradients due to mean climate changes have been proposed to control changes in variability (Schneider et al., 2015; Holmes et al., 2016). Hence, steeper temperature gradients in the LGM may have led to increased synoptic variability. Describing climate variability as the linear response to stochastic weather forcing integrated by the slow components of the climate system, such as the ocean (Hasselmann, 1976), increased synoptic variability relates directly to an increase in variability on interannual to millennial timescales (Rypdal et al., 2015). Contrasting the change in the atmospheric equator-to-pole temperature gradient—as estimated from a combined model–data temperature reconstruction (Annan and Hargreaves, 2013)—with the estimated change in variability (Fig. 7.3b; Methods, Fig. A.2) indeed reveals a consistent pattern on a global scale (Spearman's rank correlation coefficient

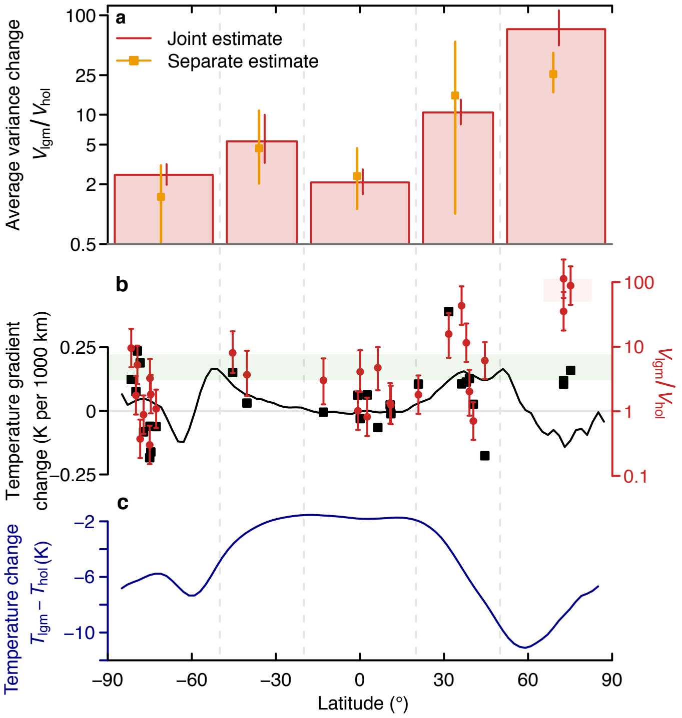

FIGURE 7.3. Latitudinal structure of LGM-to-Holocene variability and mean changes. (**a**) Zonal-mean change in variability from the proxy compilations (red bars denote the joint estimate, orange points the separate estimate). (**b**) Latitude dependence of the equator-to-pole change in temperature gradient. The five-point smoothed zonal-mean change in gradient (black line) is shown together with the change in gradient at the proxy locations (black squares), compared to the individual proxy estimates of the change in variability (red circles). Green and red shading denotes the 90 % confidence interval of the global-mean change in variance without Greenland and of the change in variance for Greenland, respectively. (**c**) Zonal-mean change in temperature (Annan and Hargreaves, 2013). All error bars are 90 % confidence intervals.

$r = 0.43$, $p = 0.03$, $n = 28$), although the high variability reconstructed for Greenland appears as an outlier (Fig. 7.3b). This relationship between temperature gradient and variability change also holds for the heterogeneous pattern of temperature variability change over Antarctic land surfaces (Fig. 7.2d), although the quality of the gradient estimates on this regional scale is unclear. In addition, a reconfiguration of the large-scale oceanic circulation could also drive changes in temperature variability. Perturbation experiments in climate models suggest that the Atlantic meridional overturning circulation (AMOC) may have been less stable in the LGM than in the Holocene (Sévellec and Fedorov, 2015), and the temperature response to a varying AMOC that modulates the oceanic poleward heat flux shows a first-order pattern (Sévellec and Fedorov, 2015) that is consistent with our estimated changes in variability (Fig. 7.3). However, there is no evidence that the imprint of AMOC modulations should be greater on Greenlandic air temperatures than on any other North Atlantic region.

The general meridional pattern is thus consistent with both synoptic atmospheric and oceanic contributions to the change in variability. However, neither contribution can explain the considerably stronger variability change found in the oxygen isotope records from Greenlandic ice cores, which is 18 times stronger than the global mean—a polar-to-global change in variance that is much larger than the observed polar amplification during the twentieth century (IPCC, 2013). In addition, the resultant asymmetry between Greenlandic and Antarctic variability change contrasts with the rather symmetric polar amplification that is simulated by climate models for past and future climate states (Masson-Delmotte et al., 2006). The specific discrepancy for the Greenlandic records thus points either to a decoupling of Greenlandic temperature variability from global surface temperature variability, for example owing to the altitude of the ice sheet representing close to mid-tropospheric atmospheric conditions, or to strong influences on the isotopic composition of Greenlandic ice cores beyond the local site temperature.

Sea-ice changes have been linked to temperature variability changes on interannual to decadal timescales (Huntingford et al., 2013), and may also contribute to the uniqueness of the Greenlandic variability estimates. The sea-ice extent during the glacial period was larger than at present (de Vernal et al., 2006), and the increased area favoured increased sea-ice variability on centennial timescales, a change that is corroborated by proxy-based sea-ice reconstructions (Table 7.1). A large sea-ice lid shields more ocean heat from the atmosphere, reduces the effective heat capacity at the surface and thus also renders local temperatures more volatile under the same forcing. Additionally, a larger sea-ice area can change more, which amplifies temperature variability on the Greenland ice sheet through atmospheric feedbacks (Li et al., 2005). Changes in sea-ice extent also influence the seasonality of snow accumulation on the central Greenland ice sheet (Rhines and Huybers, 2014), which can strongly affect the isotopic composition recorded in ice cores (Laepple et al., 2011). Furthermore, changes in the moisture pathways as an atmospheric response to the large Northern Hemisphere ice sheets could also have caused changes in isotope variability that are unrelated to local temperatures (Wunsch, 2006).

On the interannual to multidecadal scale, the surface temperature variability ratio in coupled model simulations from PMIP3 confirms the overall reduction in temperature variability from the LGM to the Holocene (Methods; Sect. A.2, Fig. A.3). The spatial pattern is similar, but the magnitude of change is smaller ($R = 1.28$; 90 % confidence interval, 1.25–1.30), suggesting either a difference in the partitioning

TABLE 7.1. North Atlantic sea-ice variability ratios. The variance ratios R are listed, based on sea-ice reconstructions from three North Atlantic records (two sites, one based on two different sea ice proxies).

Site	**Lat.** (° N)	**Lon.** (° E)	**Proxy**	***R*** (90 % CI)
MSM5-5-712-2[a]	78.9	6.8	PBIP25	2.1 (1.1–4.1)
MSM5-5-712-2[a]	78.9	6.8	IP25	11.2 (5.6–22.1)
JM11-FI-19PC[b]	62.8	−3.9	PBIP25	14.1 (5.8–35.8)

[a] Müller and Stein (2014). [b] Hoff et al. (2016).

of variability between fast and slow timescales, or that the models suppress long-term climate variability (Laepple and Huybers, 2014) and so do not display realistic variability changes. The tendency of coupled climate models to underestimate changes in the meridional temperature gradient (Masson-Delmotte et al., 2006) might also contribute to this discrepancy. To establish to what extent variability change is uniform across timescales, as predicted by linear energy balance models (Hasselmann, 1976; Rypdal et al., 2015), or is specific to certain timescales related to dynamic modes in the climate system, variability estimates at decadal to centennial scales are needed. Possibilities include annually laminated sediment records or a better understanding of non-climate effects on ice-core records to enable reliable high-resolution reconstructions. The PMIP3 climate model results also suggest that the temperature variability change in Greenland is not larger than elsewhere. Therefore, it is paramount to establish whether the Greenlandic variability change is indeed a change in local temperature variability or specific to the oxygen isotope proxy for temperature. The representativeness of Greenlandic isotope variability for Arctic and global temperature variability could be clarified using non-stable-water-isotope proxies for temperature in Greenland (Kobashi et al., 2011), more data from across the Arctic and climate modelling with embedded water-isotope tracers.

Our results have implications for the understanding of past and future climate variability. The reconstruction reveals that temperature variability decreased globally by a factor of four for a warming of 3–8 °C from the LGM to the Holocene. This decrease is small compared with the reduction by a factor of 73 estimated for Greenland and indicates that the change in variability recorded by Greenlandic ice cores is not representative of changes in variability across the globe. In terms of the magnitude of variability, these iconic data sets thus do not provide a reference for global climate changes as is often implicitly assumed. Consequently, we have to rethink the notion of an unstable glacial period and a very stable Holocene and the implications for societal evolution. Although a direct extrapolation from the glacial period to the future would not be prudent, it is reasonable to assume that the relationship between mean change and variability change holds, given our mechanistic understanding of the drivers and the direction of future changes in the temperature gradient. Our findings therefore add support to climate modelling studies that predict a reduction in winter temperature variability under global warming via reduced spatial gradients (Schneider et al., 2015; Holmes et al., 2016). Our results further suggest that this variability (which dominates annual-mean temperature variability), might also translate to a reduction in multidecadal and slower variability (Huntingford et al., 2013). More high-resolution records of glacial climate, continued quantification of recording and preserving processes of palaeoclimate signals, and an extension of similar analyses to other climate states will help to further constrain the mean-state dependence of climate variability.

The methods to this paper and the supplementary figures and tables are compiled in Appendix A.

8

GENERAL DISCUSSION AND CONCLUSIONS

This dissertation presents six research articles that contribute to an improved understanding of the mechanisms behind the spatial and temporal variability of isotope records from low-accumulation regions of the Antarctic Plateau. The scales covered by the studies mainly range from a seasonal and local (< 1 km) to a centennial and regional point of view, but are also extended to glacial–interglacial and global scales. In the following general discussion, we link the main results of the different articles to elucidate their overall relevance for the interpretation of isotope variations in terms of temperature variability.

8.1 SHORT-SCALE SPATIAL AND TEMPORAL VARIABILITY OF ANTARCTIC LOW-ACCUMULATION ISOTOPE DATA

8.1.1 *Local spatial variability*

The isotopic composition of firn at the EDML site on the Antarctic Plateau exhibits strong variability over the entire analysed horizontal scale ($\sim$ 1–500 m). It is shown that this variability is not purely random but has a spatial[1] structure, following an AR(1) process with a horizontal decorrelation length of $\sim$ 1.5 m (Chap. 3).

A physical understanding of our statistical model of the spatial variability is gained from studying the typical surface roughness observed on site. In a model for stratigraphic noise based on observations from Greenland (Fisher et al., 1985), the spatial variability is shown to arise from the undulations of the former snow surfaces that create spatially variable snow layer thicknesses. While according to this model a stronger effect can be expected for the lower accumulation rates in Antarctica compared to Greenland, we additionally argue here that the spatial variability at our study site is also significantly driven by the movement and mixing of snow at the surface. The local surface at the EDML site is shaped by the formation of dunes in strong wind events that exhibit height variations of the order of 10 cm, and typical horizontal extents of several metres (Birnbaum et al., 2010). This is confirmed by the surface height profiles obtained in the trench studies (e.g., Fig. 3.2a). Importantly, the observed dune formation processes do not change the regional accumulation but rather redistribute the surface snow on a 10-metre scale (Birnbaum et al., 2010). Thus, in combination with the steady

---

[1] To avoid misinterpretation, it is noted that the term *spatial* here always refers to a horizontal dimension, in contrast to the vertical direction in the firn.

surface winds (Reijmer and van den Broeke, 2003) that generate a more or less constant snow drift, the dune structures lead to typical spatial patterns where snow is either predominantly deposited, or eroded. This conclusion is supported by the similar horizontal correlation structure of the density profiles obtained from the same sites (Appendix B and Fig. B.5). Then, a snow layer will not be isotopically homogeneous but show a distinct spatial structure, and we suggest this to be the main driver for the short-scale coherence of the spatial isotope variations. This is supported by the high and structured variability observed locally for the isotopic composition of surface snow samples ($\sim$ 2–3 cm depth; Klein, 2014). This physical interpretation of the spatial variability would imply that the decorrelation structure and strength of the variability scale not only with the accumulation rate but also with the wind speed, since higher speeds presumably lead to a stronger and longer drift of the surface snow and a stronger erosion. For a test of this hypothesis, additional high-resolution two-dimensional samplings of the near-surface firn at other locations with markedly different environmental conditions are needed.

8.1.2 *Seasonal to interannual variability*

The seasonal to interannual isotope variability is dominated within the first few metres by a layering of the isotopic composition that is, as illustrated above, strongly spatially variable (Figs. 3.2 and 4.3). These layers have been interpreted to reflect the climatic seasonal cycle in temperature (Chap. 3) as suggested by their average separation, which is in agreement with the local accumulation of snow per year estimated independently from volcanic ash layers (Oerter et al., 2000) or counting of seasonal variations in impurity records (Sommer et al., 2000a). Furthermore, seasonal cycles in the isotopic composition of Antarctic precipitation have been observed at other sites (Fujita and Abe, 2006; Touzeau et al., 2016) and are assumed to be driven by local air temperatures. Moreover, after averaging a sufficient number of vertical isotope profiles to overcome the spatial variability, the isotope signal within the first 2 m reproduces over $\sim$ 500 m (Figs. 3.5 and 4.3). This is consistent with the assumption of a regional climatic signal, which is driven by the local seasonal cycle in temperature, as the origin of the isotope variations. This hypothesis is further supported by comparing the isotope signal with the average density and impurity profiles that have been obtained at the same sites and at the same time (Fig. B.6). Although the data sets are limited, they exhibit significant correlations (Appendix B), and the timing of the impurity relative to the isotope profiles is consistent with the known seasonality of the investigated impurities and the assumption that the isotopic composition follows the seasonal cycle in temperature.

A deeper understanding of the temporal variability, additionally applying to different sites on the Antarctic Plateau, is gained from studying the typical spacings of the isotope variations (Chap. 5). This shows that the effect of firn diffusion (Sect. 2.2.4), acting on a completely uncorrelated isotope signal (i.e. white noise) at the surface, creates typical average spacings of maxima and minima deeper in the firn which are proportional to the diffusion length (Eq. 5.2). Remarkably, the average diffusion length of the near-surface firn (first 4 m) is relatively constant across the Antarctic Plateau, which is caused by the competing influences of accumulation rate and local temperature, and corresponds to a typical average spacing of the extrema of around 20 cm (Fig. 5.3). Intriguingly, this stochastic value for a white noise input signal at the surface is for the EDML site about the same value as expected in the deterministic case from the annual accumulation rate of snow. Analysing the depth dependency of the typical spacing lengths provides further information here. If the input signal is not only white noise but additionally has a seasonal component, the strength of this seasonal component will determine that depth dependency (Fig. 5.6): For a seasonally dominated signal, the typical spacing of isotopic maxima and minima depicts the seasonal cycle and decreases with depth due to densification (Sect. 2.2.2). In contrast, for a noise-dominated input signal, the typical spacing mainly reflects a statistical property of the diffused noise and increases with depth as a result of the increase in diffusion length (Fig. 5.3). The corresponding analyses of snow-pit records reveal for nearly all studied sites an increase in typical spacing length with depth (Fig. 5.7), which can only be explained by invoking high noise levels of the input signal. An exception is South Pole for which indeed the seasonal component seems to dominate, as suggested from the constant or slightly decreasing typical spacing length.

These findings make a reassessment of the assumed seasonal cycle in the observed isotopic composition at the EDML site necessary. However, the inferred high noise level for EDML does not prevent the observation of the seasonal component. Within the first ~ 1 m where the diffusional smoothing is weak, the phase between the seasonal input and the noisy and diffused isotope signal in the firn is still preserved, even in the case of a high initial noise fraction (Fig. 5.6, right column; Fig. 5.7). This explains why the average separation of isotopic layers in the trench data set is close to the expected value from the seasonal cycle, and matches the layering of density and impurity profiles. In contrast, counting isotopic minima or maxima deeper in the firn will no longer reflect the original seasonal cycle (Fig. 5.7). This also holds more generally. At sites with lower accumulation rates, such as Vostok or EPICA Dome C, no unknown climatic cycles need to be invoked to explain the typical spacing of isotopic extrema of the order of 20–30 cm before testing against the diffusion effect on the inherent noise.

The previous discussions of temporal variability represent a static point of view since they looked at the variations at a single point in time. However, how does this picture evolve when the same profiles get buried deeper down in the firn? This question is essential for the interpretation of deep ice-core isotope data in terms of local temperatures. Any significant temporal change of the isotopic composition as compared to the original values in precipitation would influence the interpretation of the temperature reconstruction. Since both diffusion and densification do not lead to any net change of the isotopic composition over time, Chap. 4 studies whether additional processes cause temporal changes.

By comparing the average isotope profiles from the two trench studies obtained two years apart, no evidence is found for further processes affecting the temporal evolution of the isotope profiles. This conclusion is obtained by taking into account the influence of the high spatial variability, and of the temporal changes expected from densification and diffusion through their explicit modelling. The finding was unexpected since several studies suggest a significant change in isotopic composition after deposition of the snow (Town et al., 2008; Steen-Larsen et al., 2014; Ritter et al., 2016). Specifically, Town et al. (2008) infer strong isotopic enrichments of South Pole snow ($\sim 3\,‰$ change in mean, corresponding to a change in reconstructed temperature of nearly 4 °C (Masson-Delmotte et al., 2008)) from modelling the effects of wind-driven firn ventilation and diffusion of atmospheric vapour, which is assumed to lead to an exchange of isotopic composition between the firn and the atmosphere. However, despite the similar annual mean temperatures, accumulation rates and wind speeds between the South Pole and the EDML site, the observational data from EDML do not reproduce the model results. Several explanations of the discrepancy are possible. (1) The model of Town et al. (2008) overestimates the effects of ventilation and diffusive exchange. (2) The two sites are different with respect to other parameters not yet identified. (3) The trench-based analysis misses the effect since the direct surface layer ($\lesssim 10\,\mathrm{cm}$) had to be excluded due to the surface undulations, which prevent statistically solid inferences for this part of the record. The last possibility would imply that the ventilation effect is constrained to the very near surface, thus to rather short times after the deposition of the snow. To make progress in this field, a joint effort to study the temporal changes on short (seasonal) timescales across many different sites is needed, which takes into account the large spatial variability in order to separate the temporal from the spatial dimension.

The presented results underline the importance of firn diffusion for the apparent temporal variability of isotope records. The agreement of modelled and observed typical spacing lengths of the isotope variations support the current diffusion theory, which has been questioned recently (van der Wel et al., 2015a). The latter work argues that the classical diffusion theory (Johnsen et al., 2000) overestimates the diffusion length, and suggests this discrepancy to arise mainly from an imprecise parametrisation of the tortuosity in the upper firn column. Our results of Chap. 5 do not indicate such a discrepancy, which is supported by the match of the temporal differences observed between the average trench records when accounting for diffusion (Chap. 4). Extending the studies of Chap. 5 to deeper firn cores could thus provide an independent way to estimate diffusion lengths and by this test the theory. We note that strong gradients in temperature in the near-surface firn could influence the validity of the approximated equation for firn diffusion, as suggested by the scaling analysis in Sect. 2.2.4. This might be necessary to take into account for future assessments of modelled and observed diffusion results.

8.1.3 *On the relation of spatial and temporal variability*

The above analysis showed that the common regional trench isotope signal obtained from spatially averaging across a sufficient number of single profiles (e.g., Fig. 4.3c) may be partly indicative, at least for the first $\sim$ 1–2 m, of the climatic seasonal cycle in temperature. However, the signal is strongly distinct from the evolution of local surface air temperatures (Fig 4.1), which also cannot be explained by strong post-depositional effects related to atmosphere–firn vapour exchange processes (Chap. 4). Further insights into the nature of this average isotope signal can be gained from investigating the relationship of the spatial and temporal isotope variability discussed in the previous sections.

An indicator of the representativity of the regional average trench signal is obtained from the signal-to-noise variance ratio (F) on seasonal timescales, as determined by the average correlation of the single isotope profiles separated by much more ($\geq$ 10 m) than the decorrelation length of the spatial noise. We find an average value over all analysed snow trenches of roughly $F_{\text{trench}} = 1$, associated however with considerable uncertainty (Table 4.2). By contrast, a noise fraction ξ of $\sim$ 80 to $\lesssim$ 100 % is necessary to explain the typical spacings of seasonal-scale isotope variations at EDML (Chap. 5), corresponding to a signal-to-noise ratio of $(1-\xi)/\xi \approx$ 0–0.25, which is on average one order of magnitude below the first estimate. Given the poor agreement of trench and local temperature record, this apparent discrepancy can be reconciled by assuming that a large part of the regional average trench signal is due to coherent noise. Writing the trench signal as $S_{\text{trench}} = C + N_{\text{coh}}$ and the total noise as $N = N_{\text{coh}} + N_{\text{spat}}$, where C is the true climatic signal (i.e. the seasonal cycle), N_{coh} the coherent noise and N_{spat} the spatial variability, the variance ratio of true climatic to trench signal is

$$\frac{C}{S_{\text{trench}}} = 1 - \xi \left(1 + F_{\text{trench}}^{-1}\right) + F_{\text{trench}}^{-1} \lesssim 0.4. \tag{8.1}$$

Thus, this analysis suggests that a maximum of $\sim 40\,\%$ of the regional average trench isotope signal at the EDML site is climatically driven while the rest is presumably coherent noise.

One explanation for the source of the coherent noise is precipitation intermittency, besides the possibility of large-scale coherent fractionation processes during deposition (Steen-Larsen et al., 2011, 2014; and Chap. 4). Seasonal intermittency of precipitation has been shown to strongly impact the mean isotopic composition of Antarctic snow (Sime et al., 2009; Laepple et al., 2011), but it also induces variability due to variations from year to year (Persson et al., 2011) which represent temporal noise in relation to the temperature variations. Direct estimates of the seasonal accumulation in Antarctica are difficult (Bromwich, 1988; Reijmer and van den Broeke, 2003; Helsen et al., 2005). However, Reijmer and van den Broeke (2003) estimate for Dronning Maud Land (DML) based on measurements of autonomic weather stations (AWS), including the one at EDML, that accumulation occurs in many small (1–2 cm) and few larger events ($\gtrsim 5$ cm) of snowfall, where the latter occur only a few times per year without clear seasonality but coherently over large areas ($\sim 10^4\,\text{km}^2$). Despite the limitations of the AWS-derived accumulation, this adds support to the interpretation of the regional average trench isotope signal on seasonal timescales to be mainly driven by spatially coherent temporal noise.

This interpretation immediately poses the question why the noise levels as inferred from the typical spacing of isotope variations are different between the EDML site and the South Pole (Fig. 5.7), despite similar accumulation rates, temperatures and wind speeds. For the South Pole, Casey et al. (2014) estimate that around 50 % of the annual accumulation originates in storms, i.e. from single events similar to DML, but the rest in the form of clear-sky precipitation ("diamond dust"). The latter is a typical feature of the dry regions on the high Antarctic Plateau and represents a very continuous form of precipitation. This might lead to a better preservation of the seasonal signal in the isotopic composition of the snow, and consequently to higher signal-to-noise ratios than at the EDML site where diamond dust precipitation is rarely observed. A similar partition of the precipitation into event and diamond dust contributions is observed for Dome F and for other high-plateau sites, together with a strong seasonal cycle in the isotopic composition of the precipitation (Fujita and Abe, 2006; Touzeau et al., 2016). Here one could argue that the much lower accumulation rates at the high-plateau sites (roughly 3–4 times lower than at EDML and South Pole, Table 5.1) correlate with a higher wind-driven erosion and vertical mixing of the snow at the surface, causing a stronger corruption of the seasonal cycle and hence higher noise levels than for the South Pole. Overall, this would imply an influence of precipitation patterns on the total noise level of isotope records, but further studies are needed to validate this inference.

8.2 EXTENSION TO LONGER SCALES

8.2.1 *Spatial vs. temporal variability on interannual timescales*

For timescales longer than seasonal, the signal-to-noise ratio of isotope records will depend on the vertical covariance of the noise, and on the timescale-dependency of the climate signal. The temporal covariance of the noise related to precipitation variability can consist of (1) variations in annual amounts of snowfall, and (2) intermittent precipitation within a year as discussed above. The first case is typically assumed to show a "blue" spectrum with power concentrated at the high frequencies (Fisher et al., 1985); related noise will therefore be averaged out quickly for relatively short temporal averages. By contrast, the temporal covariance of precipitation intermittency is largely unknown. Some indication for autocorrelation is seen in the trench data (Chap. 3); however, the assessment of the vertical covariance is affected by the smoothing effect of diffusion.

In Chap. 3, signal-to-noise ratios for interannual timescales are derived from a data-based estimate of the annual signal variance and by assuming the two possible limiting cases of the vertical noise covariance: (a) white noise or (b) complete inter-dependence on the sub-annual timescale. While this analysis yields values $\left(F_{\text{trench}}^{(\text{annual})} \sim 0.1\text{–}0.8\right)$ which for the lower case (b) reproduce the signal-to-noise ratios estimated from an annually resolved firn-core array from DML (Graf et al., 2002), the results likely underestimate the total noise level given the possible influence of precipitation intermittency (Eq. 8.1). In addition, the estimation of the annual signal variance is uncertain due to the short data set. This suggests that the inferred interannual signal-to-noise ratios put a first constraint on the representativity of low-accumulation East-Antarctic firn cores, i.e. on their reliability in recording interannual temperature signals (Figs. 3.8 and 3.9), but that the true representativity on these timescales is likely even lower. A better estimate of the temporal noise covariance and the signal-to-noise ratio for longer temporal and spatial scales is thus needed.

8.2.2 *Holocene and longer timescales*

In order to extend the previous analysis, Chap. 6 studies the timescale-dependency of Antarctic isotope variations from decadal to centennial timescales. For this, a simple model working in the spectral domain is presented to separate the signal from the local noise in isotope records, based on a spatial network of cores and under the assumption that all cores record the same, i.e. a spatially coherent, signal. The model is applied to two different arrays of cores: one from DML in East Antarctica, including cores close to the EDML site at Kohnen Station, and one from the West Antarctic Ice Sheet (WAIS). By means of the spectral approach, the study directly allows the inference of the timescale-dependencies of the estimated signal and noise spectra, and consequently of the signal-to-noise ratio.

For DML, the obtained results are at first sight promising. The average spectrum of the isotope variations shows, after correction for the noise, an increase in spectral power towards longer timescales (Fig. 6.3a), which is expected since many temperature observations show similar spectra (e.g., Pelletier, 1998; Huybers and Curry, 2006; Laepple and Huybers, 2014). Some qualitative understanding of these findings can be gained from conceptual models of internal climate variability (e.g., Hasselmann, 1976; Rypdal et al., 2015; see also Sect. 2.3). The noise spectrum exhibits an essentially white character with no timescale-dependency for variations on multidecadal and longer periods (Fig. 6.3a). In consequence, the signal-to-noise ratio of the DML records increases with timescale (Fig. 6.4). This is an important result as climate reconstructions that reach far back in time typically have to rely on a few records. In general, estimates of the signal-to-noise ratio across timescales can help to correct the isotope-inferred variabilities for the noise contribution.

To a first approximation, the effect of diffusion will not affect the signal-to-noise ratio estimates (Chap. 6), which allows us to infer estimates for annually resolved records by integrating the signal-to-noise ratio spectrum (Eq. 6.5). The analysis confirms the values estimated previously from the same set of cores (Graf et al., 2002). This is a little surprising since time uncertainty affects the signal variability and thus the estimated signal-to-noise ratio on fast timescales (Chap. 6). The similar results we obtain compared to Graf et al. (2002) could thus indicate that the fast timescales originally contained only a small signal, and that the predominant part of the correlation is due to variations on longer timescales. The annual signal-to-noise ratio is also similar to the lower bound $\left(F_{\text{trench}}^{(\text{annual})} \sim 0.1\right)$ inferred from the trench data, as already stated above. This possibly is inconsistent with the assumption that the noise due to precipitation intermittency is decorrelated on the spatial scale ($\sim 10^2$ km) of the cores. Instead, it might suggest that the effect of precipitation intermittency is not only coherent on the spatial scale of the trenches (Eq. 8.1) but also on larger scales across DML (Chap. 6). One indication for this are the results by Reijmer and van den Broeke (2003). Thus, findings obtained on different scales could be explained by the same mechanism.

Comparing the results obtained for DML with those inferred for WAIS provides further insights into this topic. Both regions exhibit differences in the shape of the estimated signal and noise spectra above decadal timescales, and consequently in inferred signal-to-noise ratios (Figs. 6.3 and 6.4). To a first approximation, one would not expect the climate in the two regions to behave differently. Therefore, one might speculate that the differences arise from differences in precipitation patterns: while for DML the precipitation weighting acts coherently on spatial scales similar to the decorrelation length of temperature variations, for WAIS varying precipitation patterns between the individual core sites yield the lower signal-to-noise ratios towards centennial timescales. This would suggest that there is no simple scaling of the overall signal-to-noise ratio with accumulation rate. While estimates for interannual timescales from high-accumulation regions in Greenland (Fisher et al., 1985; Steen-Larsen et al., 2011) point in this direction, as they show considerably higher signal-to-noise ratios ($\sim$ 1–3) than at DML, the observed difference between DML and WAIS cannot be explained by the difference in accumulation rate. Instead, other factors seem to be important; e.g., wind speed as suggested from the studies on spatial variability, or the spatial patterns of precipitation weighting as speculated here. However, future work is needed to test the presented inferences.

In addition, this study provides implications for works similar to that presented in Chap. 7, both for the climatic interpretation of the results as well as for a deeper understanding of the isotopic variability.

The study in Chap. 7 quantifies the change in multicentennial to millennial-scale temperature variability between the Last Glacial Maximum (LGM) and the Holocene. The results suggest a global decrease in variability from the cold to the warm state of the order of 4, while isotope records from Greenland alone indicate a decrease by a factor of $\sim$ 70. The global results are interpreted to reflect the changes in the meridional temperature gradient. This is motivated by the fact that spatial temperature gradients are the main driver of synoptic-scale temperature variability, and, assuming a mechanism at play as suggested by conceptual models for the internal climate variability (Sect. 2.3), that these fast variations are integrated by the slow components of the climate system and thus cause variability also on longer timescales. Studies of temperature variability on intermediate scales would therefore provide an important test for the assumption of such a linear scaling of temperature variability, and the studies from DML and WAIS present a first approach for this kind of test.

In addition, the interpretation of the variability ratios between the LGM and the Holocene is strongly dependent on the noise present in the proxy records, since noise will bias low any ratio that is larger than 1 (Sect. A.5 and Fig. A.6a). Since the general timescale-dependencies of the signal-to-noise ratios are still unknown, simple assumptions had to be made to correct the estimated ratios for the effect of noise. Therefore, timescale-dependent estimates of the signal-to-noise ratio as presented in Chap. 6 are highly needed, not only for isotope records but for temperature proxy records in general.

Finally, a deeper understanding of the variability in isotope records is also needed to understand the drastic difference of the observed variability change between Greenland-based and Antarctic isotope records. At this stage, it is not fully understood if the difference indeed reflects a difference in temperature variability, or climate in general, or if we observe proxy-specific effects here.

8.3 CONCLUDING REMARKS AND OUTLOOK

This dissertation sheds light on the mechanisms that create the spatial and temporal variability in East Antarctic low-accumulation isotope records from Dronning Maud Land.

Specifically, it is shown that the total noise level of a single isotope record partitions into contributions from (1) spatial variability, following an autoregressive process on a metre scale, and (2) temporal variability, suggested to be driven by precipitation intermittency, and significantly affected by the effect of vapour diffusion in the firn. The overall results indicate that likely only a small portion of the total variability of single records from the studied region can be attributed to temperature variations. The inferred magnitude and spectral shape of the noise explains the low correlation of available Holocene decadal-scale isotope variations (Fig. 1.1c), and the corresponding power spectra (Fig. 1.2).

Future studies are needed across sites with different environmental conditions to test the inferences made for (1) the relationship between the local environmental parameters and the spatiotemporal variability and its spectral structure, and (2) the impact of post-depositional processes.

Finally, a first attempt is made to infer the timescale-dependency of the isotopic signal-to-noise ratio which is essential to interpret isotope records across different timescales. The results might indicate that the spatial averaging of records across a certain region to reduce the noise level possibly has to take into account the spatial coherence of precipitation patterns. Therefore, methods need to be established to decipher the role of precipitation intermittency for the variability of East Antarctic isotope records, and to correct for it.

BIBLIOGRAPHY

Alfred-Wegener-Institut Helmholtz-Zentrum für Polar- und Meeresforschung: Neumayer III and Kohnen Station in Antarctica operated by the Alfred Wegener Institute, Journal of large-scale research facilities, **2** (A85), DOI: 10.17815/jlsrf-2-152, 2016.

Alley, R. B.: Concerning the Deposition and Diagenesis of Strata in Polar Firn, J. Glaciol., **34** (118), 283–290, DOI: 10.1017/S0022143000007024, 1988.

Alley, R. B. and Joughin, I.: Modeling Ice-Sheet Flow, Science, **336** (6081), 551–552, DOI: 10.1126/science.1220530, 2012.

Altnau, S., Schlosser, E., Isaksson, E. and Divine, D.: Climatic signals from 76 shallow firn cores in Dronning Maud Land, East Antarctica, The Cryosphere, **9** (3), 925–944, DOI: 10.5194/tc-9-925-2015, 2015.

Anand, P., Elderfield, H. and Conte, M. H.: Calibration of Mg/Ca thermometry in planktonic foraminifera from a sediment trap time series, Paleoceanography, **18** (2), 1050, DOI: 10.1029/2002PA000846, 2003.

Annan, J. D. and Hargreaves, J. C.: A new global reconstruction of temperature changes at the Last Glacial Maximum, Clim. Past, **9** (1), 367–376, DOI: 10.5194/cp-9-367-2013, 2013.

Anschütz, H., Eisen, O., Oerter, H., Steinhage, D. and Scheinert, M.: Investigating small-scale variations of the recent accumulation rate in coastal Dronning Maud Land, East Antarctica, Ann. Glaciol., **46** (1), 14–21, 2007.

Arcone, S. A., Spikes, V. B. and Hamilton, G. S.: Phase structure of radar stratigraphic horizons within Antarctic firn, Ann. Glaciol., **41** (1), 10–16, 2005.

Arthern, R. J., Vaughan, D. G., Rankin, A. M., Mulvaney, R. and Thomas, E. R.: In situ measurements of Antarctic snow compaction compared with predictions of models, J. Geophys. Res., **115** (F3), F03011, DOI: 10.1029/2009JF001306, 2010.

Arthern, R. J., Corr, H. F. J., Gillet-Chaulet, F., Hawley, R. L. and Morris, E. M.: Inversion for the density-depth profile of polar firn using a stepped-frequency radar, J. Geophys. Res. Earth Surf., **118**, 1257–1263, DOI: 10.1002/jgrf.20089, 2013.

Baroni, M., Bard, E., Petit, J.-R., Magand, O. and Bourlès, D.: Volcanic and solar activity, and atmospheric circulation influences on cosmogenic ^{10}Be fallout at Vostok and Concordia (Antarctica) over the last 60 years, Geochim. Cosmochim. Acta, **75** (22), 7132–7145, DOI: 10.1016/j.gca.2011.09.002, 2011.

Beltrami, H. and Taylor, A. E.: Records of climatic change in the Canadian Arctic: towards calibrating oxygen isotope data with geothermal data, Glob. Planet. Change, **11** (3), 127–138, DOI: 10.1016/0921-8181(95)00006-2, 1995.

Benson, C. S.: Stratigraphic Studies in the Snow at Byrd Station, Antarctica, Compared with Similar Studies in Greenland, in: *Antarctic Snow and Ice Studies II*, ed. by A. Crary, Antarctic Research Series, pp. 333–353, American Geophysical Union, Washington, D. C., 1971.

Berger, W. H. and Heath, G. R.: Vertical mixing in pelagic sediments, J. Mar. Res., **26** (2), 134–143, 1968.

Bigler, M., Svensson, A., Kettner, E., Vallelonga, P., Nielsen, M. E. and Steffensen, J. P.: Optimization of High-Resolution Continuous Flow Analysis for Transient Climate Signals in Ice Cores, Environ. Sci. Technol., **45** (10), 4483–4489, DOI: 10.1021/es200118j, 2011.

Birnbaum, G., Freitag, J., Brauner, R., König-Langlo, G., Schulz, E., Kipfstuhl, S., Oerter, H., Reijmer, C. H., Schlosser, E., Faria, S. H., Ries, H., Loose, B., Herber, A., Duda, M. G., Powers, J. G., Manning, K. W. and van den Broeke, M. R.: Strong-wind events and their influence on the formation of snow dunes: observations from Kohnen station, Dronning Maud Land, Antarctica, J. Glaciol., **56** (199), 891–902, 2010.

Bloomfield, P.: *Fourier Analysis of Time Series: An Introduction*, vol. 159, Wiley Series in Probability and Statistics – Applied Probability and Statistics Section, Wiley, New York, 1976.

Bromwich, D. H.: Snowfall in High Southern Latitudes, Rev. Geophys., **26** (1), 149–168, DOI: 10.1029/RG026i001p00149, 1988.

Bromwich, D. H., Nicolas, J. P., Monaghan, A. J., Lazzara, M. A., Keller, L. M., Weidner, G. A. and Wilson, A. B.: Central West Antarctica among the most rapidly warming regions on Earth, Nat. Geosci., **6** (2), 139–145, DOI: 10.1038/ngeo1671, 2013.

Buizert, C., Cuffey, K. M., Severinghaus, J. P., Baggenstos, D., Fudge, T. J., Steig, E. J., Markle, B. R., Winstrup, M., Rhodes, R. H., Brook, E. J., Sowers, T. A., Clow, G. D., Cheng, H., Edwards, R. L., Sigl, M., McConnell, J. R. and Taylor, K. C.: The WAIS Divide deep ice core WD2014 chronology – Part 1: Methane synchronization (68–31 ka BP) and the gas age–ice age difference, Clim. Past, **11** (2), 153–173, DOI: 10.5194/cp-11-153-2015, 2015.

Casado, M., Landais, A., Picard, G., Münch, T., Laepple, T., Stenni, B., Dreossi, G., Ekaykin, A., Arnaud, L., Genthon, C., Touzeau, A., Masson-Delmotte, V. and Jouzel, J.: Archival of the water stable isotope signal in East Antarctic ice cores, The Cryosphere Discuss., DOI: 10.5194/tc-2016-263, 2016.

Casado, M., Landais, A., Picard, G., Münch, T., Laepple, T., Stenni, B., Dreossi, G., Ekaykin, A., Arnaud, L., Genthon, C., Touzeau, A., Masson-Delmotte, V. and Jouzel, J.: Archival processes of the water stable isotope signal in East Antarctic ice cores, The Cryosphere Discuss., DOI: 10.5194/tc-2017-243, 2017.

Casey, K. A., Fudge, T. J., Neumann, T. A., Steig, E. J., Cavitte, M. G. P. and Blankenship, D. D.: The 1500 m South Pole ice core: recovering a 40 ka environmental record, Ann. Glaciol., **55** (68), 137–146, DOI: 10.3189/2014AoG68A016, 2014.

Chatfield, C.: *The Analysis of Time Series: An Introduction*, 6th ed., Chapman & Hall/CRC, Boca Raton, Florida, 2004.

Craig, H. and Gordon, L. I.: Deuterium and oxygen 18 variations in the ocean and the marine atmosphere, in: *Stable Isotopes in Oceanographic Studies and Paleotemperatures*, ed. by E. Tongiorgi, Proceedings Spoleto 1965, pp. 9–130, V. Lishi e F., Pisa, 1965.

Crowley, T. J.: Causes of Climate Change Over the Past 1000 Years, Science, **289** (5477), 270–277, DOI: 10.1126/science.289.5477.270, 2000.

Cuffey, K. M., Alley, R. B., Grootes, P. M., Bolzan, J. M. and Anandakrishnan, S.: Calibration of the δ^{18}O isotopic paleothermometer for central Greenland, using borehole temperatures, Journal of Glaciology, **40** (135), 341–349, DOI: 10.3189/S0022143000007425, 1994.

Cuffey, K. M., Clow, G. D., Alley, R. B., Stuiver, M., Waddington, E. D. and Saltus, R. W.: Large Arctic Temperature Change at the Wisconsin-Holocene Glacial Transition, Science, **270** (5235), 455–458, DOI: 10.1126/science.270.5235.455, 1995.

Cuffey, K. M. and Clow, G. D.: Temperature, accumulation, and ice sheet elevation in central Greenland through the last deglacial transition, J. Geophys. Res., **102** (C12), 26383–26396, DOI: 10.1029/96JC03981, 1997.

Cuffey, K. M. and Steig, E. J.: Isotopic diffusion in polar firn: implications for interpretation of seasonal climate parameters in ice-core records, with emphasis on central Greenland, J. Glaciol., **44** (147), 273–284, DOI: 10.1017/S0022143000002616, 1998.

Dansgaard, W.: Stable isotopes in precipitation, Tellus, **16** (4), 436–468, DOI: 10.3402/tellusa.v16i4.8993, 1964.

Dansgaard, W. and Johnsen, S. J.: A flow model and a time scale for the ice core from Camp Century, Greenland, J. Glaciol., **8** (53), 215–223, DOI: 10.3189/S0022143000031208, 1969.

Dansgaard, W., Johnsen, S. J., Clausen, H. B., Dahl-Jensen, D., Gundestrup, N. S., Hammer, C. U., Hvidberg, C. S., Steffensen, J. P., Sveinbjörnsdottir, A. E., Jouzel, J. and Bond, G.: Evidence for general instability of past climate from a 250-kyr ice-core record, Nature, **364** (6434), 218–220, DOI: 10.1038/364218a0, 1993.

Dee, D. P., Uppala, S. M., Simmons, A. J., Berrisford, P., Poli, P., Kobayashi, S., Andrae, U., Balmaseda, M. A., Balsamo, G., Bauer, P., Bechtold, P., Beljaars, A. C. M., van de Berg, L., Bidlot, J., Bormann, N., Delsol, C., Dragani, R., Fuentes, M., Geer, A. J., Haimberger, L., Healy, S. B., Hersbach, H., Hólm, E. V., Isaksen, L., Kållberg, P., Köhler, M., Matricardi, M., McNally, A. P., Monge-Sanz, B. M., Morcrette, J.-J., Park, B.-K., Peubey, C., de Rosnay, P., Tavolato, C., Thépaut, J.-N. and Vitart, F.: The ERA-Interim reanalysis: configuration and performance of the data assimilation system, Q. J. R. Meteorol. Soc., **137** (656), 553–597, DOI: 10.1002/qj.828, 2011.

Dee, S., Emile-Geay, J., Evans, M. N., Allam, A., Steig, E. J. and Thompson, D. M.: PRYSM: An open-source framework for PRoxY System Modeling, with applications to oxygen-isotope systems, J. Adv. Model. Earth Syst., **7** (3), 1220–1247, DOI: 10.1002/2015MS000447, 2015.

Denoth, A.: Snow dielectric measurements, Adv. Space Res., **9** (1), 233–243, DOI: 10.1016/0273-1177(89)90491-2, 1989.

Dethloff, K., Dorn, W., Rinke, A., Fraedrich, K., Junge, M., Roeckner, E., Gayler, V., Cubash, U. and Christensen, J. H.: The impact of Greenland's deglaciation on the Arctic circulation, Geophys. Res. Lett., **31** (19), L19201, DOI: 10.1029/2004GL020714, 2004.

de Vernal, A., Rosell-Melé, A., Kucera, M., Hillaire-Marcel, C., Eynaud, F., Weinelt, M., Dokken, T. and Kageyama, M.: Comparing proxies for the reconstruction of LGM sea-surface conditions in the northern North Atlantic, Quat. Sci. Rev., **25** (21–22), 2820–2834, DOI: 10.1016/j.quascirev.2006.06.006, 2006.

Ditlevsen, P. D., Svensmark, H. and Johnsen, S.: Contrasting atmospheric and climate dynamics of the last-glacial and Holocene periods, Nature, **379** (6568), 810–812, DOI: 10.1038/379810a0, 1996.

Eisen, O., Frezzotti, M., Genthon, C., Isaksson, E., Magand, O., van den Broeke, M. R., Dixon, D. A., Ekaykin, A., Holmlund, P., Kameda, T., Karlöf, L., Kaspari, S., Lipenkov, V. Y., Oerter, H., Takahashi, S. and

Vaughan, D. G.: Ground-based measurements of spatial and temporal variability of snow accumulation in East Antarctica, Rev. Geophys., **46** (2), RG2001, DOI: 10.1029/2006RG000218, 2008.

Ekaykin, A. A., Lipenkov, V. Y., Barkov, N. I., Petit, J. R. and Masson-Delmotte, V.: Spatial and temporal variability in isotope composition of recent snow in the vicinity of Vostok station, Antarctica: implications for ice-core record interpretation, Ann. Glaciol., **35** (1), 181–186, DOI: 10.3189/172756402781816726, 2002.

Ekaykin, A. A., Kozachek, A. V., Lipenkov, V. Y. and Shibaev, Y. A.: Multiple climate shifts in the Southern Hemisphere over the past three centuries based on central Antarctic snow pits and core studies, Ann. Glaciol., **55** (66), 259–266, 2014.

Ekaykin, A., Eberlein, L., Lipenkov, V., Popov, S., Scheinert, M., Schröder, L. and Turkeev, A.: Non-climatic signal in ice core records: lessons from Antarctic megadunes, The Cryosphere, **10** (3), 1217–1227, DOI: 10.5194/tc-10-1217-2016, 2016.

EPICA community members: Eight glacial cycles from an Antarctic ice core, Nature, **429** (6992), 623–628, DOI: 10.1038/nature02599, 2004.

EPICA community members: One-to-one coupling of glacial climate variability in Greenland and Antarctica, Nature, **444** (7116), 195–198, DOI: 10.1038/nature05301, 2006.

Etheridge, D. M., Pearman, G. I. and Fraser, P. J.: Changes in tropospheric methane between 1841 and 1978 from a high accumulation-rate Antarctic ice core, Tellus B, **44** (4), 282–294, DOI: 10.3402/tellusb.v44i4.15456, 1992.

Fernandoy, F., Meyer, H., Oerter, H., Wilhelms, F., Graf, W. and Schwander, J.: Temporal and spatial variation of stable-isotope ratios and accumulation rates in the hinterland of Neumayer station, East Antarctica, J. Glaciol., **56** (198), 673–687, DOI: 10.3189/002214310793146296, 2010.

Fisher, D. A., Koerner, R. M., Paterson, W. S. B., Dansgaard, W., Gundestrup, N. and Reeh, N.: Effect of wind scouring on climatic records from ice-core oxygen-isotope profiles, Nature, **301** (5897), 205–209, DOI: 10.1038/301205a0, 1983.

Fisher, D. A., Reeh, N. and Clausen, H. B.: Stratigraphic Noise in Time Series Derived from Ice Cores, Ann. Glaciol., **7** (1), 76–83, DOI: 10.1017/S0260305500005942, 1985.

Frankignoul, C. and Hasselmann, K.: Stochastic climate models, Part II Application to sea-surface temperature anomalies and thermocline variability, Tellus, **29** (4), 289–305, DOI: 10.3402/tellusa.v29i4.11362, 1977.

Freitag, J., Kipfstuhl, S. and Laepple, T.: Core-scale radioscopic imaging: a new method reveals density–calcium link in Antarctic firn, J. Glaciol., **59** (218), 1009–1014, DOI: 10.3189/2013JoG13J028, 2013a.

Freitag, J., Kipfstuhl, S., Laepple, T. and Wilhelms, F.: Impurity-controlled densification: a new model for stratified polar firn, J. Glaciol., **59** (218), 1163–1169, DOI: 10.3189/2013JoG13J042, 2013b.

Frezzotti, M., Gandolfi, S., La Marca, F. and Urbini, S.: Snow dunes and glazed surfaces in Antarctica: new field and remote-sensing data, Ann. Glaciol., **34** (1), 81–88, DOI: 10.3189/172756402781817851, 2002.

Fujita, K. and Abe, O.: Stable isotopes in daily precipitation at Dome Fuji, East Antarctica, Geophys. Res. Lett., **33** (L18503), DOI: 10.1029/2006GL026936, 2006.

Fujita, S., Hirabayashi, M., Goto-Azuma, K., Dallmayr, R., Satow, K., Zheng, J. and Dahl-Jensen, D.: Densification of layered firn of the ice sheet at NEEM, Greenland, J. Glaciol., **60** (223), 905–921, DOI: 10.3189/2014JoG14J006, 2014.

Gamble, C., Davies, W., Pettitt, P. and Richards, M.: Climate change and evolving human diversity in Europe during the last glacial, Phil. Trans. R. Soc. Lond. B Biol. Sci., **359** (1442), 243–254, DOI: 10.1098/rstb.2003.1396, 2004.

Gerland, S., Oerter, H., Kipfstuhl, J., Wilhelms, F., Miller, H. and Miners, W. D.: Density log of a 181 m long ice core from Berkner Island, Antarctica, Annals of Glaciology, **29** (1), 215–219, 1999.

Gfeller, G., Fischer, H., Bigler, M., Schüpbach, S., Leuenberger, D. and Mini, O.: Representativeness and seasonality of major ion records derived from NEEM firn cores, The Cryosphere, **8** (5), 1855–1870, DOI: 10.5194/tc-8-1855-2014, 2014.

Gkinis, V., Popp, T. J., Blunier, T., Bigler, M., Schüpbach, S., Kettner, E. and Johnsen, S. J.: Water isotopic ratios from a continuously melted ice core sample, Atmos. Meas. Tech., **4** (11), 2531–2542, DOI: 10.5194/amt-4-2531-2011, 2011.

Gkinis, V., Simonsen, S. B., Buchardt, S. L., White, J. W. C. and Vinther, B. M.: Water isotope diffusion rates from the NorthGRIP ice core for the last 16,000 years – Glaciological and paleoclimatic implications, Earth Planet. Sci. Lett., **405**, 132–141, DOI: 10.1016/j.epsl.2014.08.022, 2014.

Glen, J. W. and Paren, J. G.: The electrical properties of snow and ice, J. Glaciol., **15** (73), 15–38, DOI: 10.1017/S0022143000034249, 1975.

Göktas, F., Fischer, H., Oerter, H., Weller, R., Sommer, S. and Miller, H.: A glacio-chemical characterization of the new EPICA deep-drilling site on Amundsenisen, Dronning Maud Land, Antarctica, Ann. Glaciol., **35** (1), 347–354, 2002.

Gonfiantini, R.: Standards for stable isotope measurements in natural compounds, Nature, **271** (5645), 534–536, DOI: 10.1038/271534a0, 1978.

Goujon, C., Barnola, J.-M. and Ritz, C.: Modeling the densification of polar firn including heat diffusion: Application to close-off characteristics and gas isotopic fractionation for Antarctica and Greenland sites, J. Geophys. Res., **108** (D24), 4792, DOI: 10.1029/2002JD003319, 2003.

Gow, A. J.: On the accumulation and seasonal stratification of snow at the South Pole, J. Glaciol., **5** (40), 467–477, DOI: 10.1017/S002214300001844X, 1965.

Graf, W., Oerter, H., Reinwarth, O., Stichler, W., Wilhelms, F., Miller, H. and Mulvaney, R.: Stable-isotope records from Dronning Maud Land, Antarctica, Ann. Glaciol., **35** (1), 195–201, 2002.

Gregory, S., Albert, M. and Baker, I.: Impact of physical properties and accumulation rate on pore close-off in layered firn, The Cryosphere, **8**, 91–105, DOI: 10.5194/tc-8-91-2014, 2014.

Gupta, P., Noone, D., Galewsky, J., Sweeney, C. and Vaughn, B. H.: Demonstration of high-precision continuous measurements of water vapor isotopologues in laboratory and remote field deployments using wavelength-scanned cavity ring-down spectroscopy (WS-CRDS) technology, Rapid Commun. Mass Spectrom., **23** (16), 2534–2542, DOI: 10.1002/rcm.4100, 2009.

Haam, E. and Huybers, P.: A test for the presence of covariance between time-uncertain series of data with application to the Dongge Cave speleothem and atmospheric radiocarbon records, Paleoceanography, **25** (2), PA2209, DOI: `10.1029/2008PA001713`, 2010.

Hachikubo, A., Hashimoto, S., Nakawo, M. and Nishimura, K.: Isotopic mass fractionation of snow due to depth hoar formation, Polar Meteorol. Glaciol., **14**, 1–7, 2000.

Hansen, J., Sato, M. and Ruedy, R.: Perception of climate change, Proc. Natl. Acad. Sci. U.S.A., **109** (37), E2415–E2423, DOI: `10.1073/pnas.1205276109`, 2012.

Harper, J. T. and Bradford, J. H.: Snow stratigraphy over a uniform depositional surface: spatial variability and measurement tools, Cold Reg. Sci. Technol., **37** (3), 289–298, DOI: `10.1016/S0165-232X(03)00071-5`, 2003.

Hasselmann, K.: Stochastic climate models Part I. Theory, Tellus, **28** (6), 473–485, DOI: `10.3402/tellusa.v28i6.11316`, 1976.

Helsen, M. M., van de Wal, R. S. W., van den Broeke, M. R., van As, D., Meijer, H. A. J. and Reijmer, C. H.: Oxygen isotope variability in snow from western Dronning Maud Land, Antarctica and its relation to temperature, Tellus B, **57** (5), 423–435, DOI: `10.3402/tellusb.v57i5.16563`, 2005.

Helsen, M. M., van de Wal, R. S. W., van den Broeke, M. R., Masson-Delmotte, V., Meijer, H. A. J., Scheele, M. P. and Werner, M.: Modeling the isotopic composition of Antarctic snow using backward trajectories: Simulation of snow pit records, J. Geophys. Res. Atmos., **111** (D15109), DOI: `10.1029/2005JD006524`, 2006.

Herron, M. M. and Langway Jr., C. C.: Firn Densification: An Empirical Model, J. Glaciol., **25** (93), 373–385, DOI: `10.3189/S0022143000015239`, 1980.

Hilbrecht, H., *Extant Planktic Foraminifera and the Physical Environment in the Atlantic and Indian Oceans: An atlas based on CLIMAP and Levitus (1982) data*, Mitteilungen aus dem Geologischen Institut der Eidgen. Technischen Hochschule und der Universität Zürich, Neue Folge, No. 300, p. 93, Zürich, 1996.

Ho, S. L. and Laepple, T.: Flat meridional temperature gradient in the early Eocene in the subsurface rather than surface ocean, Nature Geosci., **9** (8), 606–610, DOI: `10.1038/ngeo2763`, 2016.

Hoff, U., Rasmussen, T. L., Stein, R., Ezat, M. M. and Fahl, K.: Sea ice and millennial-scale climate variability in the Nordic seas 90 kyr ago to present, Nat. Commun., **7**, 12247, DOI: `10.1038/ncomms12247`, 2016.

Hoffman, P. F., Kaufman, A. J., Halverson, G. P. and Schrag, D. P.: A Neoproterozoic Snowball Earth, Science, **281** (5381), 1342–1346, DOI: `10.1126/science.281.5381.1342`, 1998.

Holmes, C. R., Woollings, T., Hawkins, E. and de Vries, H.: Robust Future Changes in Temperature Variability under Greenhouse Gas Forcing and the Relationship with Thermal Advection, J. Climate, **29** (6), 2221–2236, DOI: `10.1175/JCLI-D-14-00735.1`, 2016.

Hörhold, M. W., Kipfstuhl, S., Wilhelms, F., Freitag, J. and Frenzel, A.: The densification of layered polar firn, J. Geophys. Res., **116** (F01001), DOI: `10.1029/2009JF001630`, 2011.

Hörhold, M., Laepple, T., Freitag, J., Bigler, M., Fischer, H. and Kipfstuhl, S.: On the impact of impurities on the densification of polar firn, Earth Planet. Sci. Lett., **325–326**, 93–99, DOI: `10.1016/j.epsl.2011.12.022`, 2012.

Hoshina, Y., Fujita, K., Nakazawa, F., Iizuka, Y., Miyake, T., Hirabayashi, M., Kuramoto, T., Fujita, S. and Motoyama, H.: Effect of accumulation rate on water stable isotopes of near-surface snow in inland Antarctica, J. Geophys. Res. Atmos., **119** (1), 274–283, DOI: `10.1002/2013JD020771`, 2014.

Hoshina, Y., Fujita, K., Iizuka, Y. and Motoyama, H.: Inconsistent relationships between major ions and water stable isotopes in Antarctic snow under different accumulation environments, Polar Sci., **10** (1), 1–10, DOI: `10.1016/j.polar.2015.12.003`, 2016.

Huntingford, C., Jones, P. D., Livina, V. N., Lenton, T. M. and Cox, P. M.: No increase in global temperature variability despite changing regional patterns, Nature, **500** (7462), 327–330, DOI: `10.1038/nature12310`, 2013.

Huybers, P. and Curry, W.: Links between annual, Milankovitch and continuum temperature variability, Nature, **441** (7091), 329–332, DOI: `10.1038/nature04745`, 2006.

Imbrie, J. and Imbrie, J. Z.: Modeling the Climatic Response to Orbital Variations, Science, **207** (4434), 943–953, DOI: `10.1126/science.207.4434.943`, 1980.

IPCC, 2013: *Climate Change 2013: The Physical Science Basis. Contribution of Working Group I to the Fifth Assessment Report of the Intergovernmental Panel on Climate Change*, ed. by T. F. Stocker, D. Qin, G.-K. Plattner, M. Tignor, S. K. Allen, J. Boschung, A. Nauels, Y. Xia, B. Bex and B. M. Midgley, Cambridge University Press, Cambridge, United Kingdom and New York, NY, USA, 2013.

Johnsen, S. J.: Stable isotope homogenization of polar firn and ice, in: *Isotopes and Impurities in Snow and Ice, no. 118*, Proceedings of the Grenoble Symposium 1975, pp. 210–219, IAHS-AISH Publication, Grenoble, France, 1977.

Johnsen, S. J., Dansgaard, W. and White, J. W. C.: The origin of Arctic precipitation under present and glacial conditions, Tellus B, **41** (4), 452–468, DOI: `10.3402/tellusb.v41i4.15100`, 1989.

Johnsen, S. J., Dahl-Jensen, D., Dansgaard, W. and Gundestrup, N.: Greenland palaeotemperatures derived from GRIP bore hole temperature and ice core isotope profiles, Tellus B, **47** (5), 624–629, DOI: `10.3402/tellusb.v47i5.16077`, 1995.

Johnsen, S. J., Clausen, H. B., Dansgaard, W., Gundestrup, N. S., Hammer, C. U., Andersen, U., Andersen, K. K., Hvidberg, C. S., Dahl-Jensen, D., Steffensen, J. P., Shoji, H., Sveinbjörnsdóttir, Á. E., White, J., Jouzel, J. and Fisher, D.: The δ^{18}O record along the Greenland Ice Core Project deep ice core and the problem of possible Eemian climatic instability, J. Geophys. Res., **102** (C12), 26397–26410, DOI: `10.1029/97JC00167`, 1997.

Johnsen, S. J., Clausen, H. B., Cuffey, K. M., Hoffmann, G., Schwander, J. and Creyts, T.: Diffusion of stable isotopes in polar firn and ice: the isotope effect in firn diffusion, in: *Physics of Ice Core Records*, ed. by T. Hondoh, vol. 159, pp. 121–140, Hokkaido University Press, Sapporo, Japan, 2000.

Johnsen, S. J., Dahl-Jensen, D., Gundestrup, N., Steffensen, J. P., Clausen, H. B., Miller, H., Masson-Delmotte, V., Sveinbjörnsdottir, A. E. and White, J.: Oxygen isotope and palaeotemperature records from six Greenland ice-core stations: Camp Century, Dye-3, GRIP, GISP2, Renland and NorthGRIP, J. Quat. Sci., **16** (4), 299–307, DOI: `10.1002/jqs.622`, 2001.

Jones, T. R., White, J. W. C. and Popp, T.: Siple Dome shallow ice cores: a study in coastal dome microclimatology, Clim. Past, **10** (3), 1253–1267, DOI: 10.5194/cp-10-1253-2014, 2014.

Jouzel, J., Merlivat, L., Petit, J. R. and Lorius, C.: Climatic Information Over the Last Century Deduced From a Detailed Isotopic Record in the South Pole Snow, J. Geophys. Res., **88** (C4), 2693–2703, DOI: 10.1029/JC088iC04p02693, 1983.

Jouzel, J. and Merlivat, L.: Deuterium and Oxygen 18 in Precipitation: Modeling of the Isotopic Effects During Snow Formation, J. Geophys. Res., **89** (D7), 11749–11757, DOI: 10.1029/JD089iD07p11749, 1984.

Jouzel, J., Alley, R. B., Cuffey, K. M., Dansgaard, W., Grootes, P., Hoffmann, G., Johnsen, S. J., Koster, R. D., Peel, D., Shuman, C. A., Stievenard, M., Stuiver, M. and White, J.: Validity of the temperature reconstruction from water isotopes in ice cores, J. Geophys. Res., **102** (C12), 26471–26487, DOI: 10.1029/97JC01283, 1997.

Jouzel, J., Vimeux, F., Caillon, N., Delaygue, G., Hoffmann, G., Masson-Delmotte, V. and Parrenin, F.: Magnitude of isotope/temperature scaling for interpretation of central Antarctic ice cores, J. Geophys. Res., **108** (D12), 4361, DOI: 10.1029/2002JD002677, 2003.

Jouzel, J., Masson-Delmotte, V., Cattani, O., Dreyfus, G., Falourd, S., Hoffmann, G., Minster, B., Nouet, J., Barnola, J. M., Chappellaz, J., Fischer, H., Gallet, J. C., Johnsen, S., Leuenberger, M., Loulergue, L., Luethi, D., Oerter, H., Parrenin, F., Raisbeck, G., Raynaud, D., Schilt, A., Schwander, J., Selmo, E., Souchez, R., Spahni, R., Stauffer, B., Steffensen, J. P., Stenni, B., Stocker, T. F., Tison, J. L., Werner, M. and Wolff, E. W.: Orbital and Millennial Antarctic Climate Variability over the Past 800,000 Years, Science, **317** (5839), 793–796, DOI: 10.1126/science.1141038, 2007.

Kameda, T., Motoyama, H., Fujita, S. and Takahashi, S.: Temporal and spatial variability of surface mass balance at Dome Fuji, East Antarctica, by the stake method from 1995 to 2006, J. Glaciol., **54** (184), 107–116, DOI: 10.3189/002214308784409062, 2008.

Karlöf, L., Winebrenner, D. P. and Percival, D. B.: How representative is a time series derived from a firn core? A study at a low-accumulation site on the Antarctic plateau, J. Geophys. Res., **111** (F04001), DOI: 10.1029/2006JF000552, 2006.

Kaspari, S., Mayewski, P. A., Dixon, D. A., Spikes, V. B., Sneed, S. B., Handley, M. J. and Hamilton, G. S.: Climate variability in West Antarctica derived from annual accumulation-rate records from ITASE firn/ice cores, Ann. Glaciol., **39** (1), 585–594, DOI: 10.3189/172756404781814447, 2004.

Katz, R. W. and Brown, B. G.: Extreme events in a changing climate: Variability is more important than averages, Clim. Change, **21** (3), 289–302, DOI: 10.1007/BF00139728, 1992.

Kerstel, E. R. T., van Trigt, R., Dam, N., Reuss, J. and Meijer, H. A. J.: Simultaneous Determination of the ^{2}H/^{1}H, ^{17}O/^{16}O, and ^{18}O/^{16}O Isotope Abundance Ratios in Water by Means of Laser Spectrometry, Anal. Chem., **71** (23), 5297–5303, DOI: 10.1021/ac990621e, 1999.

Kindler, P., Guillevic, M., Baumgartner, M., Schwander, J., Landais, A. and Leuenberger, M.: Temperature reconstruction from 10 to 120 kyr b2k from the NGRIP ice core, Clim. Past, **10** (2), 887–902, DOI: 10.5194/cp-10-887-2014, 2014.

Kirchner, J. W.: Aliasing in $1/f^{\alpha}$ noise spectra: Origins, consequences, and remedies, Phys. Rev. E, **71** (6), 066110, DOI: 10.1103/PhysRevE.71.066110, 2005.

Klein, K.: *Variability in dry Antarctic firn—Investigations on spatially distributed snow and firn samples from Dronning Maud Land, Antarctica*, PhD thesis, Universität Bremen, Bremen, 2014.

Kobashi, T., Kawamura, K., Severinghaus, J. P., Barnola, J.-M., Nakaegawa, T., Vinther, B. M., Johnsen, S. J. and Box, J. E.: High variability of Greenland surface temperature over the past 4000 years estimated from trapped air in an ice core, Geophys. Res. Lett., **38** (21), L21501, DOI: 10.1029/2011GL049444, 2011.

Koutavas, A. and Joanides, S.: El Niño–Southern Oscillation extrema in the Holocene and Last Glacial Maximum, Paleoceanography, **27** (4), PA4208, DOI: 10.1029/2012PA002378, 2012.

Kreutz, K. J., Mayewski, P. A., Twickler, M. S., Whitlow, S. I., White, J. W. C., Shuman, C. A., Raymond, C. F., Conway, H. and McConnell, J. R.: Seasonal variations of glaciochemical, isotopic and stratigraphic properties in Siple Dome (Antarctica) surface snow, Ann. Glaciol., **29** (1), 38–44, 1999.

Küttel, M., Steig, E. J., Ding, Q., Monaghan, A. J. and Battisti, D. S.: Seasonal climate information preserved in West Antarctic ice core water isotopes: relationships to temperature, large-scale circulation, and sea ice, Clim. Dyn., **39** (7–8), 1841–1857, DOI: 10.1007/s00382-012-1460-7, 2012.

Laepple, T., Werner, M. and Lohmann, G.: Synchronicity of Antarctic temperatures and local solar insolation on orbital timescales, Nature, **471** (7336), 91–94, DOI: 10.1038/nature09825, 2011.

Laepple, T. and Huybers, P.: Reconciling discrepancies between Uk37 and Mg/Ca reconstructions of Holocene marine temperature variability, Earth Planet. Sci. Lett., **375**, 418–429, DOI: 10.1016/j.epsl.2013.06.006, 2013.

Laepple, T. and Huybers, P.: Ocean surface temperature variability: Large model–data differences at decadal and longer periods, Proc. Natl. Acad. Sci. U.S.A., **111** (47), 16682–16687, DOI: 10.1073/pnas.1412077111, 2014.

Laepple, T., Hörhold, M., Münch, T., Freitag, J., Wegner, A. and Kipfstuhl, S.: Layering of surface snow and firn at Kohnen Station, Antarctica: Noise or seasonal signal?, J. Geophys. Res. Earth Surf., **121** (10), 1849–1860, DOI: 10.1002/2016JF003919, 2016.

Laepple, T., Münch, T., Casado, M., Hoerhold, M., Landais, A. and Kipfstuhl, S.: On the similarity and apparent cycles of isotopic variations in East Antarctic snow pits, The Cryosphere, **12** (1), 169–187, DOI: 10.5194/tc-12-169-2018, 2018.

Laine, V.: Antarctic ice sheet and sea ice regional albedo and temperature change, 1981–2000, from AVHRR Polar Pathfinder data, Remote Sens. Environ., **112** (3), 646–667, DOI: 10.1016/j.rse.2007.06.005, 2008.

Landais, A., Barnola, J.-M., Kawamura, K., Caillon, N., Delmotte, M., Van Ommen, T., Dreyfus, G., Jouzel, J., Masson-Delmotte, V., Minster, B., Freitag, J., Leuenberger, M., Schwander, J., Huber, C., Etheridge, D. and Morgan, V.: Firn-air δ^{15}N in modern polar sites and glacial–interglacial ice: a model-data mismatch during glacial periods in Antarctica?, Quat. Sci. Rev., **25** (1–2), 49–62, DOI: 10.1016/j.quascirev.2005.06.007, 2006.

Latif, M.: *Klimawandel und Klimadynamik [Climate Change and Climate Dynamics]*, 1. Aufl., Verlag Eugen Ulmer, Stuttgart, 2009.

Lefebvre, E., Arnaud, L., Ekaykin, A. A., Lipenkov, V. Y., Picard, G. and Petit, J.-R.: Snow temperature measurements at Vostok station from an autonomous recording system (TAUTO): preliminary results from the first year operation, Ice and Snow, **52** (4), 138–145, DOI: 10.15356/2076-6734-2012-4-138-145, 2012.

Legrand, M. and Mayewski, P.: Glaciochemistry of polar ice cores: A review, Rev. Geophys., **35** (3), 219–243, DOI: 10.1029/96RG03527, 1997.

Li, C., Battisti, D. S., Schrag, D. P. and Tziperman, E.: Abrupt climate shifts in Greenland due to displacements of the sea ice edge, Geophys. Res. Lett., **32** (19), L19702, DOI: 10.1029/2005GL023492, 2005.

Li, J. and Zwally, H. J.: Modeled seasonal variations of firn density induced by steady-state surface air-temperature cycle, Ann. Glaciol., **34**, 299–302, 2002.

Libois, Q., Picard, G., Arnaud, L., Morin, S. and Brun, E.: Modeling the impact of snow drift on the decameter-scale variability of snow properties on the Antarctic Plateau, J. Geophys. Res. Atmos., **119**, 11, 662–11, 681, DOI: 10.1002/2014JD022361, 2014.

Ligtenberg, S. R. M., Helsen, M. M. and van den Broeke, M. R.: An improved semi-empirical model for the densification of Antarctic firn, The Cryosphere, **5** (4), 809–819, DOI: 10.5194/tc-5-809-2011, 2011.

Lindgren, G.: *Stationary Stochastic Processes: Theory and Applications*, 1st ed., Chapman & Hall/CRC Texts in Statistical Science, CRC Press, Boca Raton, FL, 2012.

Lisiecki, L. E. and Raymo, M. E.: A Pliocene-Pleistocene stack of 57 globally distributed benthic δ^{18}O records, Paleoceanography, **20** (1), PA1003, DOI: 10.1029/2004PA001071, 2005.

Liu, Z., Otto-Bliesner, B. L., He, F., Brady, E. C., Tomas, R., Clark, P. U., Carlson, A. E., Lynch-Stieglitz, J., Curry, W., Brook, E., Erickson, D., Jacob, R., Kutzbach, J. and Cheng, J.: Transient Simulation of Last Deglaciation with a New Mechanism for Bølling-Allerød Warming, Science, **325** (5938), 310–314, DOI: 10.1126/science.1171041, 2009.

Looyenga, H.: Dielectric constants of heterogeneous mixtures, Physica, **31** (3), 401–406, DOI: 10.1016/0031-8914(65)90045-5, 1965.

Lorius, C., Merlivat, L. and Hagemann, R.: Variation in the Mean Deuterium Content of Precipitations in Antarctica, J. Geophys. Res., **74** (28), 7027–7031, DOI: 10.1029/JC074i028p07027, 1969.

Lovejoy, S., Schertzer, D. and Varon, D.: Do GCMs predict the climate ... or macroweather?, Earth Syst. Dynam., **4** (2), 439–454, DOI: 10.5194/esd-4-439-2013, 2013.

Majoube, M.: Fractionnement en 18O entre la glace et la vapeur d'eau [Fractionation in O18 between ice and water vapour], J. Chim. Phys., **68**, 625–636, DOI: 10.1051/jcp/1971680625, 1971a.

Majoube, M.: Fractionnement en oxygène 18 et en deutérium entre l'eau et sa vapeur [Oxygen-18 and deuterium fractionation between water and vapour], J. Chim. Phys., **68**, 1423–1436, DOI: 10.1051/jcp/1971681423, 1971b.

Maraun, D. and Kurths, J.: Cross wavelet analysis: significance testing and pitfalls, Nonlin. Processes Geophys., **11** (4), 505–514, DOI: 10.5194/npg-11-505-2004, 2004.

Marcott, S. A., Shakun, J. D., Clark, P. U. and Mix, A. C.: A Reconstruction of Regional and Global Temperature for the Past 11,300 Years, Science, **339** (6124), 1198–1201, DOI: 10.1126/science.1228026, 2013.

MARGO Project Members: Constraints on the magnitude and patterns of ocean cooling at the Last Glacial Maximum, Nature Geosci., **2** (2), 127–132, DOI: 10.1038/ngeo411, 2009.

Martinerie, P., Raynaud, D., Etheridge, D. M., Barnola, J.-M. and Mazaudier, D.: Physical and climatic parameters which influence the air content in polar ice, Earth Planet. Sci. Lett., **112** (1–4), 1–13, DOI: 10.1016/0012-821X(92)90002-D, 1992.

Masson-Delmotte, V., Delmotte, M., Morgan, V., Etheridge, D., van Ommen, T., Tartarin, S. and Hoffmann, G.: Recent southern Indian Ocean climate variability inferred from a Law Dome ice core: new insights for the interpretation of coastal Antarctic isotopic records, Clim. Dyn., **21** (2), 153–166, DOI: 10.1007/s00382-003-0321-9, 2003.

Masson-Delmotte, V., Jouzel, J., Landais, A., Stievenard, M., Johnsen, S. J., White, J. W. C., Werner, M., Sveinbjornsdottir, A. and Fuhrer, K.: GRIP Deuterium Excess Reveals Rapid and Orbital-Scale Changes in Greenland Moisture Origin, Science, **309** (5731), 118–121, DOI: 10.1126/science.1108575, 2005.

Masson-Delmotte, V., Kageyama, M., Braconnot, P., Charbit, S., Krinner, G., Ritz, C., Guilyardi, E., Jouzel, J., Abe-Ouchi, A., Crucifix, M., Gladstone, R. M., Hewitt, C. D., Kitoh, A., LeGrande, A. N., Marti, O., Merkel, U., Motoi, T., Ohgaito, R., Otto-Bliesner, B., Peltier, W. R., Ross, I., Valdes, P. J., Vettoretti, G., Weber, S. L., Wolk, F. and Yu, Y.: Past and future polar amplification of climate change: climate model intercomparisons and ice-core constraints, Clim. Dyn., **26** (5), 513–529, DOI: 10.1007/s00382-005-0081-9, 2006.

Masson-Delmotte, V., Hou, S., Ekaykin, A., Jouzel, J., Aristarain, A., Bernardo, R. T., Bromwich, D., Cattani, O., Delmotte, M., Falourd, S., Frezzotti, M., Gallée, H., Genoni, L., Isaksson, E., Landais, A., Helsen, M. M., Hoffmann, G., Lopez, J., Morgan, V., Motoyama, H., Noone, D., Oerter, H., Petit, J. R., Royer, A., Uemura, R., Schmidt, G. A., Schlosser, E., Simões, J. C., Steig, E. J., Stenni, B., Stievenard, M., van den Broeke, M. R., van de Wal, R. S. W., van de Berg, W. J., Vimeux, F. and White, J. W. C.: A Review of Antarctic Surface Snow Isotopic Composition: Observations, Atmospheric Circulation, and Isotopic Modeling, J. Climate, **21** (13), 3359–3387, DOI: 10.1175/2007JCLI2139.1, 2008.

Masson-Delmotte, V., Steen-Larsen, H. C., Ortega, P., Swingedouw, D., Popp, T., Vinther, B. M., Oerter, H., Sveinbjornsdottir, A. E., Gudlaugsdottir, H., Box, J. E., Falourd, S., Fettweis, X., Gallée, H., Garnier, E., Gkinis, V., Jouzel, J., Landais, A., Minster, B., Paradis, N., Orsi, A., Risi, C., Werner, M. and White, J. W. C.: Recent changes in north-west Greenland climate documented by NEEM shallow ice core data and simulations, and implications for past-temperature reconstructions, The Cryosphere, **9** (4), 1481–1504, DOI: 10.5194/tc-9-1481-2015, 2015.

Mayewski, P. A., Frezzotti, M., Bertler, N., van Ommen, T., Hamilton, G., Jacka, T. H., Welch, B., Frey, M., Qin, D., Ren, J., Simões, J., Fily, M., Oerter, H., Nishio, F., Isaksson, E., Mulvaney, R., Holmund, P., Lipenkov, V. and Goodwin, I.: The International Trans-Antarctic Scientific Expedition (ITASE): An Overview, Ann. Glaciol., **41** (1), 180–185, DOI: 10.3189/172756405781813159, 2005.

McMorrow, A. J., Curran, M. A. J., Van Ommen, T. D., Morgan, V. I. and Allison, I.: Features of meteorological events preserved in a high-resolution Law Dome (East Antarctica) snow pit, Ann. Glaciol., **35** (1), 463–470, 2002.

Merlivat, L.: Molecular diffusivities of $H_2^{16}O$, $HD^{16}O$, and $H_2^{18}O$ in gases, J. Chem. Phys., **69** (6), 2864–2871, DOI: 10.1063/1.436884, 1978.

Milanković, M.: *Kanon der Erdbestrahlung und seine Anwendung auf das Eiszeitenproblem [Canon of Earth solar insolation and its application to the ice-age problem]*, vol. 133, Königlich Serbische Akademie, Beograd, 1941.

Mitchell, L. E., Buizert, C., Brook, E. J., Breton, D. J., Fegyveresi, J., Baggenstos, D., Orsi, A., Severinghaus, J., Alley, R. B., Albert, M., Rhodes, R. H., McConnell, J. R., Sigl, M., Maselli, O., Gregory, S. and Ahn, J.: Observing and modeling the influence of layering on bubble trapping in polar firn, J. Geophys. Res. Atmos., **120**, 2558–2574, DOI: 10.1002/2014JD022766, 2015.

Mix, A. C.: The oxygen-isotope record of glaciation, in: *North America and adjacent oceans during the last deglaciation*, ed. by W. F. Ruddiman and H. E. Wright Jr., vol. K-3, The Geology of North America, pp. 111–135, Geological Society of America, Boulder, Colorado, 1987.

Mohtadi, M., Prange, M., Oppo, D. W., De Pol-Holz, R., Merkel, U., Zhang, X., Steinke, S. and Lückge, A.: North Atlantic forcing of tropical Indian Ocean climate, Nature, **509** (7498), 76–80, DOI: 10.1038/nature13196, 2014.

Morgan, V. I.: An oxygen isotope — climate record from the Law Dome, Antarctica, Clim. Change, **7** (4), 415–426, DOI: 10.1007/BF00139056, 1985.

Moser, H. and Stichler, W.: Deuterium and oxygen-18 contents as an index of the properties of snow covers, in: *Snow Mechanics, 114*, Proceedings of the Grindelwald Symposium, pp. 122–135, IAHS-AISH Publication, 1974.

Mosley-Thompson, E., Kruss, P. D., Thompson, L. G., Pourchet, M. and Grootes, P.: Snow stratigraphic record at South Pole: potential for paleoclimatic reconstruction, Ann. Glaciol., **7**, 26–33, DOI: 10.1017/S0260305500005863, 1985.

Mosley-Thompson, E., McConnell, J. R., Bales, R. C., Li, Z., Lin, P.-N., Steffen, K., Thompson, L. G., Edwards, R. and Bathke, D.: Local to regional-scale variability of annual net accumulation on the Greenland ice sheet from PARCA cores, J. Geophys. Res., **106** (D24), 33839–33851, DOI: 10.1029/2001JD900067, 2001.

Müller, J. and Stein, R.: High-resolution record of late glacial and deglacial sea ice changes in Fram Strait corroborates ice–ocean interactions during abrupt climate shifts, Earth Planet. Sci. Lett., **403**, 446–455, DOI: 10.1016/j.epsl.2014.07.016, 2014.

Müller, P. J., Kirst, G., Ruhland, G., von Storch, I. and Rosell-Melé, A.: Calibration of the alkenone paleotemperature index $U_{37}^{K'}$ based on core-tops from the eastern South Atlantic and the global ocean (60°N-60°S), Geochim. Cosmochim. Acta, **62** (10), 1757–1772, DOI: 10.1016/S0016-7037(98)00097-0, 1998.

Münch, T., Kipfstuhl, S., Freitag, J., Meyer, H. and Laepple, T.: Oxygen isotopes from two snow trenches from Kohnen Station, Dronning Maud Land, Antarctica from the 2012/13 field season, DOI: 10.1594/PANGAEA.861675, 2016a.

Münch, T., Kipfstuhl, S., Freitag, J., Meyer, H. and Laepple, T.: Regional climate signal vs. local noise: a two-dimensional view of water isotopes in Antarctic firn at Kohnen Station, Dronning Maud Land, Clim. Past, **12** (7), 1565–1581, DOI: 10.5194/cp-12-1565-2016, 2016b.

Münch, T., Kipfstuhl, S., Freitag, J., Meyer, H. and Laepple, T.: Constraints on post-depositional isotope modifications in East Antarctic firn from analysing temporal changes of isotope profiles, The Cryosphere, **11** (5), 2175–2188, DOI: 10.5194/tc-11-2175-2017, 2017a.

Münch, T., Kipfstuhl, S., Freitag, J., Meyer, H. and Laepple, T.: Stable water isotopes measured along two snow trenches sampled at Kohnen Station, Dronning Maud Land, Antarctica in the 2014/15 field season, DOI: 10.1594/PANGAEA.876639, 2017b.

Nassar, R., Bernath, P. F., Boone, C. D., Gettelman, A., McLeod, S. D. and Rinsland, C. P.: Variability in HDO/H_2O abundance ratios in the tropical tropopause layer, J. Geophys. Res., **112** (D21), D21305, DOI: 10.1029/2007JD008417, 2007.

NEEM community members: Eemian interglacial reconstructed from a Greenland folded ice core, Nature, **493** (7433), 489–494, DOI: 10.1038/nature11789, 2013.

Neumann, T. A. and Waddington, E. D.: Effects of firn ventilation on isotopic exchange, J. Glaciol., **50** (169), 183–194, 2004.

NGRIP members: High-resolution record of Northern Hemisphere climate extending into the last interglacial period, Nature, **431** (7005), 147–151, DOI: 10.1038/nature02805, 2004.

Nicholls, K. W., Makinson, K. and Robinson, A. V.: Ocean circulation beneath the Ronne ice shelf, Nature, **354** (6350), 221–223, DOI: 10.1038/354221a0, 1991.

Nicolas, J. P. and Bromwich, D. H.: New Reconstruction of Antarctic Near-Surface Temperatures: Multidecadal Trends and Reliability of Global Reanalyses, J. Clim., **27** (21), 8070–8093, DOI: 10.1175/JCLI-D-13-00733.1, 2014.

North, G. R., Wang, J. and Genton, M. G.: Correlation Models for Temperature Fields, J. Climate, **24** (22), 5850–5862, DOI: 10.1175/2011JCLI4199.1, 2011.

Oerlemans, J.: *Minimal Glacier Models*, 2nd print (with some revisions), Igitur, Utrecht Publishing & Archiving Services, Universiteitsbibliotheek Utrecht, Utrecht, 2011.

Oerter, H., Wilhelms, F., Jung-Rothenhäusler, F., Göktas, F., Miller, H., Graf, W. and Sommer, S.: Accumulation rates in Dronning Maud Land, Antarctica, as revealed by dielectric-profiling measurements of shallow firn cores, Ann. Glaciol., **30** (1), 27–34, 2000.

Oerter, H., Graf, W., Meyer, H. and Wilhelms, F.: The EPICA ice core from Dronning Maud Land: first results from stable-isotope measurements, Ann. Glaciol., **39** (1), 307–312, 2004.

Palais, J. M.: *Snow stratigraphic investigations at Dome C, East Antarctica: A study of depositional and diagenetic processes*, Institute of Polar Studies Report No. 78, Institute of Polar Studies, The Ohio State University, 1984.

Parish, T. R. and Cassano, J. J.: The Role of Katabatic Winds on the Antarctic Surface Wind Regime, Mon. Wea. Rev., **131** (2), 317–333, DOI: 10.1175/1520-0493(2003)131<0317:TROKWO>2.0.CO;2, 2003.

Paterson, W. S. B.: *Physics of Glaciers*, 3rd ed., reprinted with corrections 1998, 2001, 2002, Butterworth-Heinemann, Oxford, Burlington, MA, 1994.

Pelletier, J. D.: The power spectral density of atmospheric temperature from time scales of 10^{-2} to 10^6 yr, Earth Planet. Sci. Lett., **158** (3–4), 157–164, DOI: 10.1016/S0012-821X(98)00051-X, 1998.

Percival, D. B. and Walden, A. T.: *Spectral Analysis for Physical Applications: Multitaper and Conventional Univariate Techniques*, Cambridge University Press, Cambridge, UK, 1993.

Persson, A., Langen, P. L., Ditlevsen, P. and Vinther, B. M.: The influence of precipitation weighting on interannual variability of stable water isotopes in Greenland, J. Geophys. Res., **116** (D20120), DOI: 10.1029/2010JD015517, 2011.

Petit, J. R., Jouzel, J., Pourchet, M. and Merlivat, L.: A Detailed Study of Snow Accumulation and Stable Isotope Content in Dome C (Antarctica), J. Geophys. Res., **87** (C6), 4301–4308, DOI: 10.1029/JC087iC06p04301, 1982.

Petit, J. R., Jouzel, J., Raynaud, D., Barkov, N. I., Barnola, J.-M., Basile, I., Bender, M., Chappellaz, J., Davis, M., Delaygue, G., Delmotte, M., Kotlyakov, V. M., Legrand, M., Lipenkov, V. Y., Lorius, C., Pépin, L., Ritz, C., Saltzman, E. and Stievenard, M.: Climate and atmospheric history of the past 420,000 years from the Vostok ice core, Antarctica, Nature, **399** (6735), 429–436, DOI: 10.1038/20859, 1999.

Pol, K., Masson-Delmotte, V., Cattani, O., Debret, M., Falourd, S., Jouzel, J., Landais, A., Minster, B., Mudelsee, M., Schulz, M. and Stenni, B.: Climate variability features of the last interglacial in the East Antarctic EPICA Dome C ice core, Geophys. Res. Lett., **41** (11), 4004–4012, DOI: 10.1002/2014GL059561, 2014.

Proksch, M., Löwe, H. and Schneebeli, M.: Density, specific surface area, and correlation length of snow measured by high-resolution penetrometry, J. Geophys. Res. Earth Surf., **120**, 346–362, DOI: 10.1002/2014JF003266, 2015.

R Core Team: R: A Language and Environment for Statistical Computing, R Foundation for Statistical Computing, Vienna, Austria, URL: https://www.R-project.org/, 2016.

Rasmussen, S. O., Seierstad, I. K., Andersen, K. K., Bigler, M., Dahl-Jensen, D. and Johnsen, S. J.: Synchronization of the NGRIP, GRIP, and GISP2 ice cores across MIS 2 and palaeoclimatic implications, Quat. Sci. Rev., **27** (1–2), 18–28, DOI: 10.1016/j.quascirev.2007.01.016, 2008.

Raynaud, D., Jouzel, J., Barnola, J. M., Chappellaz, J., Delmas, R. J. and Lorius, C.: The Ice Record of Greenhouse Gases, Science, **259** (5097), 926–934, DOI: 10.1126/science.259.5097.926, 1993.

Rehfeld, K., Marwan, N., Heitzig, J. and Kurths, J.: Comparison of correlation analysis techniques for irregularly sampled time series, Nonlin. Processes Geophys., **18** (3), 389–404, DOI: 10.5194/npg-18-389-2011, 2011.

Rehfeld, K., Münch, T., Ho, S. L. and Laepple, T.: Global patterns of declining temperature variability from the Last Glacial Maximum to the Holocene, Nature, **554** (7692), 356–359, DOI: 10.1038/nature25454, 2018.

Reijmer, C. H. and van den Broeke, M. R.: Temporal and spatial variability of the surface mass balance in Dronning Maud Land, Antarctica, as derived from automatic weather stations, J. Glaciol., **49** (167), 512–520, 2003.

Rhines, A. and Huybers, P.: Estimation of spectral power laws in time uncertain series of data with application to the Greenland Ice Sheet Project 2 δ^{18}O record, J. Geophys. Res., **116** (D1), D01103, DOI: 10.1029/2010JD014764, 2011.

Rhines, A. and Huybers, P.: Frequent summer temperature extremes reflect changes in the mean, not the variance, Proc. Natl. Acad. Sci. U.S.A., **110** (7), E546, DOI: 10.1073/pnas.1218748110, 2013.

Rhines, A. and Huybers, P. J.: Sea Ice and Dynamical Controls on Preindustrial and Last Glacial Maximum Accumulation in Central Greenland, J. Clim., **27** (23), 8902–8917, DOI: 10.1175/JCLI-D-14-00075.1, 2014.

Rice, S. O.: Mathematical analysis of random noise, Bell Syst. Tech. J., **23** (3), 282–332, DOI: 10.1002/j.1538-7305.1944.tb00874.x, 1944.

Rice, S. O.: Mathematical analysis of random noise, Bell Syst. Tech. J., **24** (1), 46–156, DOI: 10.1002/j.1538-7305.1945.tb00453.x, 1945.

Richerson, P. J., Boyd, R. and Bettinger, R. L.: Was Agriculture Impossible during the Pleistocene but Mandatory during the Holocene? A Climate Change Hypothesis, Am. Antiq., **66** (3), 387–411, DOI: 10.2307/2694241, 2001.

Ritter, F., Steen-Larsen, H. C., Werner, M., Masson-Delmotte, V., Orsi, A., Behrens, M., Birnbaum, G., Freitag, J., Risi, C. and Kipfstuhl, S.: Isotopic exchange on the diurnal scale between near-surface snow and lower atmospheric water vapor at Kohnen station, East Antarctica, The Cryosphere, **10** (4), 1647–1663, DOI: 10.5194/tc-10-1647-2016, 2016.

Rotschky, G., Rack, W., Dierking, W. and Oerter, H.: Retrieving Snowpack Properties and Accumulation Estimates From a Combination of SAR and Scatterometer Measurements, IEEE Tgrans. Geosc. Remote Sens., **44** (4), 943–956, DOI: 10.1109/TGRS.2005.862524, 2006.

Rott, H., Sturm, K. and Miller, H.: Active and passive microwave signatures of Antarctic firn by means of field measurements and satellite data, Ann. Glaciol., **17** (1), 337–343, DOI: 10.1017/S0260305500013070, 1993.

Ruddiman, W. F.: *Earth's Climate: Past and Future*, 2nd edition, 4th printing, W. H. Freeman and Company, New York, NY, Basingstoke, Engand, 2008.

Rypdal, K., Rypdal, M. and Fredriksen, H.-B.: Spatiotemporal Long-Range Persistence in Earth's Temperature Field: Analysis of Stochastic–Diffusive Energy Balance Models, J. Climate, **28** (21), 8379–8395, DOI: 10.1175/JCLI-D-15-0183.1, 2015.

Schneider, T., Bischoff, T. and Płotka, H.: Physics of Changes in Synoptic Midlatitude Temperature Variability, J. Climate, **28** (6), 2312–2331, DOI: 10.1175/JCLI-D-14-00632.1, 2015.

Schwander, J., Sowers, T., Barnola, J.-M., Blunier, T., Fuchs, A. and Malaizé, B.: Age scale of the air in the summit ice: Implication for glacial-interglacial temperature change, J. Geophys. Res., **102** (D16), 19483–19493, DOI: 10.1029/97JD01309, 1997.

Sévellec, F. and Fedorov, A. V.: Unstable AMOC during glacial intervals and millennial variability: The role of mean sea ice extent, Earth Planet. Sci. Lett., **429**, 60–68, DOI: 10.1016/j.epsl.2015.07.022, 2015.

Shackleton, N. J. and Imbrie, J.: The δ^{18}O spectrum of oceanic deep water over a five-decade band, Clim. Change, **16** (2), 217–230, DOI: 10.1007/BF00134658, 1990.

Shakun, J. D. and Carlson, A. E.: A global perspective on Last Glacial Maximum to Holocene climate change, Quat. Sci. Rev., **29** (15–16), 1801–1816, DOI: 10.1016/j.quascirev.2010.03.016, 2010.

Shao, Z.-G. and Ditlevsen, P. D.: Contrasting scaling properties of interglacial and glacial climates, Nat Commun, **7**, 10951, DOI: 10.1038/ncomms10951, 2016.

Shuman, C. A., Alley, R. B., Anandakrishnan, S., White, J. W. C., Grootes, P. M. and Stearns, C. R.: Temperature and accumulation at the Greenland Summit: Comparison of high-resolution isotope profiles and satellite passive microwave brightness temperature trends, J. Geophys. Res., **100** (D5), 9165–9177, DOI: 10.1029/95JD00560, 1995.

Sime, L. C., Marshall, G. J., Mulvaney, R. and Thomas, E. R.: Interpreting temperature information from ice cores along the Antarctic Peninsula: ERA40 analysis, Geophys. Res. Lett., **36** (L18801), DOI: 10.1029/2009GL038982, 2009.

Sime, L. C., Lang, N., Thomas, E. R., Benton, A. K. and Mulvaney, R.: On high-resolution sampling of short ice cores: Dating and temperature information recovery from Antarctic Peninsula virtual cores, J. Geophys. Res., **116** (D20117), DOI: 10.1029/2011JD015894, 2011.

Simonsen, S. B., Johnsen, S. J., Popp, T. J., Vinther, B. M., Gkinis, V. and Steen-Larsen, H. C.: Past surface temperatures at the NorthGRIP drill site from the difference in firn diffusion of water isotopes, Clim. Past, **7** (4), 1327–1335, DOI: 10.5194/cp-7-1327-2011, 2011.

Sjolte, J., Hoffmann, G., Johnsen, S. J., Vinther, B. M., Masson-Delmotte, V. and Sturm, C.: Modeling the water isotopes in Greenland precipitation 1959–2001 with the meso-scale model REMO-iso, J. Geophys. Res., **116** (D18), D18105, DOI: 10.1029/2010JD015287, 2011.

Sokratov, S. A. and Golubev, V. N.: Snow isotopic content change by sublimation, J. Glaciol., **55** (193), 823–828, 2009.

Sommer, S., Appenzeller, C., Röthlisberger, R., Hutterli, M. A., Stauffer, B., Wagenbach, D., Oerter, H., Wilhelms, F., Miller, H. and Mulvaney, R.: Glacio-chemical study spanning the past 2 kyr on three ice cores from Dronning Maud Land, Antarctica: 1. Annually resolved accumulation rates, J. Geophys. Res., **105** (D24), 29411–29421, DOI: 10.1029/2000JD900449, 2000a.

Sommer, S., Wagenbach, D., Mulvaney, R. and Fischer, H.: Glacio-chemical study spanning the past 2 kyr on three ice cores from Dronning Maud Land, Antarctica: 2. Seasonally resolved chemical records, J. Geophys. Res., **105** (D24), 29423–29433, DOI: 10.1029/2000JD900450, 2000b.

Steen-Larsen, H. C., Masson-Delmotte, V., Sjolte, J., Johnsen, S. J., Vinther, B. M., Bréon, F.-M., Clausen, H. B., Dahl-Jensen, D., Falourd, S., Fettweis, X., Gallée, H., Jouzel, J., Kageyama, M., Lerche, H., Minster, B., Picard, G., Punge, H. J., Risi, C., Salas, D., Schwander, J., Steffen, K., Sveinbjörnsdóttir, A. E., Svensson, A. and White, J.: Understanding the climatic signal in the water stable isotope records from the NEEM shallow firn/ice cores in northwest Greenland, J. Geophys. Res., **116** (D6), D06108, DOI: 10.1029/2010JD014311, 2011.

Steen-Larsen, H. C., Masson-Delmotte, V., Hirabayashi, M., Winkler, R., Satow, K., Prié, F., Bayou, N., Brun, E., Cuffey, K. M., Dahl-Jensen, D., Dumont, M., Guillevic, M., Kipfstuhl, S., Landais, A., Popp, T., Risi, C., Steffen, K., Stenni, B. and Sveinbjörnsdottír, A. E.: What controls the isotopic composition of Greenland surface snow?, Clim. Past, **10** (1), 377–392, DOI: 10.5194/cp-10-377-2014, 2014.

Steig, E. J., Mayewski, P. A., Dixon, D. A., Kaspari, S. D., Frey, M. M., Schneider, D. P., Arcone, S. A., Hamilton, G. S., Spikes, V. B., Albert, M., Meese, D., Gow, A. J., Shuman, C. A., White, J. W. C., Sneed, S., Flaherty, J. and Wumkes, M.: High-resolution ice cores from US ITASE (West Antarctica): development and validation of chronologies and determination of precision and accuracy, Ann. Glaciol., **41** (1), 77–84, DOI: `10.3189/172756405781813311`, 2005.

Steig, E. J., Schneider, D. P., Rutherford, S. D., Mann, M. E., Comiso, J. C. and Shindell, D. T.: Warming of the Antarctic ice-sheet surface since the 1957 International Geophysical Year, Nature, **457** (7228), 459–462, DOI: `10.1038/nature07669`, 2009.

Steig, E. J., Ding, Q., White, J. W. C., Küttel, M., Rupper, S. B., Neumann, T. A., Neff, P. D., Gallant, A. J. E., Mayewski, P. A., Taylor, K. C., Hoffmann, G., Dixon, D. A., Schoenemann, S. W., Markle, B. R., Fudge, T. J., Schneider, D. P., Schauer, A. J., Teel, R. P., Vaughn, B. H., Burgener, L., Williams, J. and Korotkikh, E.: Recent climate and ice-sheet changes in West Antarctica compared with the past 2,000 years, Nat. Geosci., **6** (5), 372–375, DOI: `10.1038/ngeo1778`, 2013.

Stenni, B., Scarchilli, C., Masson-Delmotte, V., Schlosser, E., Ciardini, V., Dreossi, G., Grigioni, P., Bonazza, M., Cagnati, A., Karlicek, D., Risi, C., Udisti, R. and Valt, M.: Three-year monitoring of stable isotopes of precipitation at Concordia Station, East Antarctica, The Cryosphere, **10** (5), 2415–2428, DOI: `10.5194/tc-10-2415-2016`, 2016.

Stenni, B., Curran, M. A. J., Abram, N. J., Orsi, A., Goursaud, S., Masson-Delmotte, V., Neukom, R., Goosse, H., Divine, D., van Ommen, T., Steig, E. J., Dixon, D. A., Thomas, E. R., Bertler, N. A. N., Isaksson, E., Ekaykin, A., Werner, M. and Frezzotti, M.: Antarctic climate variability on regional and continental scales over the last 2000 years, Clim. Past, **13** (11), 1609–1634, DOI: `10.5194/cp-13-1609-2017`, 2017.

Stichler, W., Schotterer, U., Fröhlich, K., Ginot, P., Kull, C., Gäggeler, H. and Pouyaud, B.: Influence of sublimation on stable isotope records recovered from high-altitude glaciers in the tropical Andes, J. Geophys. Res., **106** (D19), 22613–22620, DOI: `10.1029/2001JD900179`, 2001.

Svensson, A., Fujita, S., Bigler, M., Braun, M., Dallmayr, R., Gkinis, V., Goto-Azuma, K., Hirabayashi, M., Kawamura, K., Kipfstuhl, S., Kjær, H. A., Popp, T., Simonsen, M., Steffensen, J. P., Vallelonga, P. and Vinther, B. M.: On the occurrence of annual layers in Dome Fuji ice core early Holocene ice, Clim. Past, **11** (9), 1127–1137, DOI: `10.5194/cp-11-1127-2015`, 2015.

Thompson, L. G., Mosley-Thompson, E., Davis, M. E., Lin, P.-N., Henderson, K. A., Cole-Dai, J., Bolzan, J. F. and Liu, K.-b.: Late Glacial Stage and Holocene Tropical Ice Core Records from Huascarán, Peru, Science, **269** (5220), 46–50, DOI: `10.1126/science.269.5220.46`, 1995.

Touzeau, A., Landais, A., Stenni, B., Uemura, R., Fukui, K., Fujita, S., Guilbaud, S., Ekaykin, A., Casado, M., Barkan, E., Luz, B., Magand, O., Teste, G., Le Meur, E., Baroni, M., Savarino, J., Bourgeois, I. and Risi, C.: Acquisition of isotopic composition for surface snow in East Antarctica and the links to climatic parameters, The Cryosphere, **10** (2), 837–852, DOI: `10.5194/tc-10-837-2016`, 2016.

Town, M. S., Warren, S. G., Walden, V. P. and Waddington, E. D.: Effect of atmospheric water vapor on modification of stable isotopes in near-surface snow on ice sheets, J. Geophys. Res., **113** (D24303), DOI: `10.1029/2008JD009852`, 2008.

Uemura, R., Masson-Delmotte, V., Jouzel, J., Landais, A., Motoyama, H. and Stenni, B.: Ranges of moisture-source temperature estimated from Antarctic ice cores stable isotope records over glacial–interglacial cycles, Clim. Past, **8** (3), 1109–1125, DOI: `10.5194/cp-8-1109-2012`, 2012.

van der Wel, L. G., Streurman, H. J., Isaksson, E., Helsen, M. M., van de Wal, R. S. W., Martma, T., Pohjola, V. A., Moore, J. C. and Meijer, H. A. J.: Using high-resolution tritium profiles to quantify the effects of melt on two Spitsbergen ice cores, J. Glaciol., **57** (206), 1087–1097, DOI: `10.3189/002214311798843368`, 2011.

van der Wel, L. G.: *Analyses of water isotope diffusion in firn: Contributions to a better palaeoclimatic interpretation of ice cores*, PhD thesis, University of Groningen, Groningen, The Netherlands, 2012.

van der Wel, L. G., Been, H. A., van de Wal, R. S. W., Smeets, C. J. P. P. and Meijer, H. A. J.: Constraints on the δ^2H diffusion rate in firn from field measurements at Summit, Greenland, The Cryosphere, **9** (3), 1089–1103, DOI: `10.5194/tc-9-1089-2015`, 2015a.

van der Wel, G., Fischer, H., Oerter, H., Meyer, H. and Meijer, H. A. J.: Estimation and calibration of the water isotope differential diffusion length in ice core records, The Cryosphere, **9** (4), 1601–1616, DOI: `10.5194/tc-9-1601-2015`, 2015b.

van Geldern, R. and Barth, J. A.: Optimization of instrument setup and post-run corrections for oxygen and hydrogen stable isotope measurements of water by isotope ratio infrared spectroscopy (IRIS), Limnol. Oceanogr. Methods, **10**, 1024–1036, DOI: `10.4319/lom.2012.10.1024`, 2012.

van Ommen, T. D. and Morgan, V.: Calibrating the ice core paleothermometer using seasonality, J. Geophys. Res., **102** (D8), 9351–9357, DOI: `10.1029/96JD04014`, 1997.

Vimeux, F., Masson, V., Delaygue, G., Jouzel, J., Petit, J. R. and Stievenard, M.: A 420,000 year deuterium excess record from East Antarctica: Information on past changes in the origin of precipitation at Vostok, J. Geophys. Res., **106** (D23), 31863–31873, DOI: `10.1029/2001JD900076`, 2001.

Vinther, B. M., Buchardt, S. L., Clausen, H. B., Dahl-Jensen, D., Johnsen, S. J., Fisher, D. A., Koerner, R. M., Raynaud, D., Lipenkov, V., Andersen, K. K., Blunier, T., Rasmussen, S. O., Steffensen, J. P. and Svensson, A. M.: Holocene thinning of the Greenland ice sheet, Nature, **461** (7262), 385–388, DOI: `10.1038/nature08355`, 2009.

Waddington, E. D., Steig, E. J. and Neumann, T. A.: Using characteristic times to assess whether stable isotopes in polar snow can be reversibly deposited, Ann. Glaciol., **35** (1), 118–124, 2002.

WAIS Divide Project Members: Onset of deglacial warming in West Antarctica driven by local orbital forcing, Nature, **500** (7463), 440–444, DOI: `10.1038/nature12376`, 2013.

Weller, R. and Wagenbach, D.: Year-round chemical aerosol records in continental Antarctica obtained by automatic samplings, Tellus B, **59** (4), 755–765, DOI: `10.1111/j.1600-0889.2007.00293.x`, 2007.

Werner, M., Mikolajewicz, U., Heimann, M. and Hoffmann, G.: Borehole versus isotope temperatures on Greenland: Seasonality does matter, Geophys. Res. Lett., **27** (5), 723–726, DOI: `10.1029/1999GL006075`, 2000.

Werner, M., Langebroek, P. M., Carlsen, T., Herold, M. and Lohmann, G.: Stable water isotopes in the ECHAM5 general circulation model: Toward high-resolution isotope modeling on a global scale, J. Geophys. Res., **116** (D15), D15109, DOI: `10.1029/2011JD015681`, 2011.

Whillans, I. M. and Grootes, P. M.: Isotopic diffusion in cold snow and firn, J. Geophys. Res., **90** (D2), 3910–3918, DOI: `10.1029/JD090iD02p03910`, 1985.

Whitlow, S., Mayewski, P. A. and Dibb, J. E.: A comparison of major chemical species seasonal concentration and accumulation at the South Pole and summit, Greenland, Atmos. Environ., **26A** (11), 2045–2054, DOI: `10.1016/0960-1686(92)90089-4`, 1992.

Wigley, T. M. L., Briffa, K. R. and Jones, P. D.: On the Average Value of Correlated Time Series, with Applications in Dendroclimatology and Hydrometeorology, J. Climate Appl. Meteor., **23** (2), 201–213, DOI: `10.1175/1520-0450(1984)023<0201:OTAVOC>2.0.CO;2`, 1984.

Wilhelms, F.: Leitfähigkeits-und Dichtemessung an Eisbohrkernen [Measuring the conductivity and density of ice cores], Ber. Polarforsch., **191**, 1996.

Wilhelms, F., Kipfstuhl, J., Miller, H., Heinloth, K. and Firestone, J.: Precise dielectric profiling of ice cores: a new device with improved guarding and its theory, J. Glaciol., **44** (146), 171–174, DOI: `10.1017/S002214300000246X`, 1998.

Winebrenner, D. P., Arthern, R. J. and Shuman, C. A.: Mapping Greenland accumulation rates using observations of thermal emission at 4.5-cm wavelength, J. Geophys. Res., **106** (D24), 33919–33934, DOI: `10.1029/2001JD900235`, 2001.

Wunsch, C.: The spectral description of climate change including the 100 ky energy, Clim. Dyn., **20** (4), 353–363, DOI: `10.1007/s00382-002-0279-z`, 2003.

Wunsch, C.: Abrupt climate change: An alternative view, Quat. Res., **65** (2), 191–203, DOI: `10.1016/j.yqres.2005.10.006`, 2006.

Xu, X.: *Methods in Hypothesis Testing, Markov Chain Monte Carlo and Neuroimaging Data Analysis*, PhD thesis, Harvard University, Cambridge, Massachusetts, 2013.

Yoshimura, K.: Stable Water Isotopes in Climatology, Meteorology, and Hydrology: A Review, J. Meteor. Soc. Japan, **93** (5), 513–533, DOI: `10.2151/jmsj.2015-036`, 2015.

Zachos, J., Pagani, M., Sloan, L., Thomas, E. and Billups, K.: Trends, Rhythms, and Aberrations in Global Climate 65 Ma to Present, Science, **292** (5517), 686–693, DOI: `10.1126/science.1059412`, 2001.

Zwally, H. J. and Li, J.: Seasonal and interannual variations of firn densification and ice-sheet surface elevation at the Greenland summit, J. Glaciol., **48** (161), 199–207, DOI: `10.3189/172756502781831403`, 2002.

A

METHODS TO: GLOBAL PATTERNS OF DECLINING TEMPERATURE VARIABILITY FROM LAST GLACIAL MAXIMUM TO HOLOCENE

A.1 PROXY DATA FOR VARIABILITY ESTIMATES

For the variability analyses we collected all available proxy records for temperature that fulfilled the following sampling criteria. To be included, a record had to (1) be associated with an established, published calibration to temperature and (2) cover at least 4 kyr in the interval of the Holocene (8–0 kyr ago) and/or the LGM (27–19 kyr ago) at (3) a mean sampling frequency of $1/225\,\text{yr}^{-1}$ or higher. Our definition for the LGM time slice, based on previously published starting (Rasmussen et al., 2008) and end (MARGO Project Members, 2009) times, covers the coldest part of the last glacial period[∨] with the most stable boundary conditions while maintaining the same period duration as for the Holocene section. All proxy time series which fulfil the sampling criteria for both time intervals are included in our primary "joint" data set[⋆]. All time series which fulfil the criteria for only one of the two intervals are included only for this period ("separate" data set). This data set consequently also includes all records from the joint data set. All selected records are listed in Supplementary Information[1] along with the time intervals for which they were included. Table (A.1) summarises the individual variance ratio estimates for the joint data set.

A.2 MODEL-BASED ESTIMATES FOR THE TEMPERATURE GRADIENT AND VARIABILITY CHANGE

Changes in temperature gradient between the LGM and the Holocene were estimated on the basis of an LGM-to-pre-industrial temperature anomaly (Annan and Hargreaves, 2013), based on proxy and model data from the Paleoclimate Modelling Intercomparison Project Phase 2 (PMIP2). The equator-to-pole temperature gradient change was calculated from the temperature anomaly differences between adjacent gridboxes in the poleward direction (north relative to south), divided by the meridional gridbox extent (222 km) and normalised to 1000 km. The model-based LGM-to-Holocene variability change estimate was derived from surface (2 m) air temperature output for the LGM and pre-industrial simulations available through PMIP Phase 3

---

[1] Supplementary Information to this paper are available in the published online version (DOI: `10.1038/nature25454`).

Table A.1. Individual variability ratio estimates for all records from the joint data set. The estimate used throughout this paper is the noise-corrected variance ratio R_{est} (first data column). R_{calib} (lower/upper) denotes the results for the variance ratios when using the calibration parameters with the lower/upper limits of the calibration uncertainty for the LGM and the upper/lower calibration uncertainty limits for the Holocene. Data columns four and five give the 5 % and 95 % quantiles of the estimate used (R_{est}). Data column six gives the raw, uncorrected ratio (R_{raw}). Numbers (first column) refer to the list of records given in Supplementary Information. For ODP976-4 and ODP1240, no calibration uncertainty estimate is available.

No.	**Record**	R_{est}	R_{calib} (upper)	R_{calib} (lower)	R_{est} (5 %)	R_{est} (95 %)	R_{raw}
3	NGRIP	88.6	28.8	103.8	44.7	175.8	53.6
4	GISP2	35.5	11.7	42	17.9	70.4	21.7
5	GRIP	113.4	36.8	132.6	57.1	224.9	68.4
30	MD01-2412	6.1	3.2	4	3.2	11.8	3.6
34	PC-6	0.7	0.8	1	0.4	1.4	0.9
35	MD03-2699	2	1.3	1.7	0.9	4.4	1.5
38	MD01-2444	11.6	5.6	7.1	5.8	22.9	6.3
42	ODP976-4	43.5			21.9	86.2	22.2
47	MD98-2195	15.8	7.4	9.5	6.8	33.1	8.4
52	ODP658C-Zhao	1.8	1.2	1.6	0.9	3.6	1.4
60	SK237-GC04	1.3	1	1.3	0.6	2.5	1.1
62	ODP1240	4.1			2	8.8	2.6
63	PL07-39PC	1.3	1	1.3	0.6	2.7	1.2
67	MD98-2181	4.7	2.5	3.3	2.1	9.9	2.9
68	MD03-2707	0.8	0.8	1	0.4	1.6	0.9
69	SO189-39KL	1	0.9	1.2	0.5	2	1
81	MD01-2378	3	1.8	2.3	1.3	6.6	2
84	MD97-2121	3.7	2.1	2.7	1.7	8.7	2.4
88	MD97-2120	8.1	4	5.1	3.9	17.4	4.5
90	Talos Dome	1.1	0.5	2.4	0.6	2.2	1
91	Dome C	1.9	0.6	3.2	0.9	3.7	1.4
92	EPICA DML	3.3	0.9	4.8	1.6	6.5	2.1
93	EPICA Dome C	0.3	0.3	1.5	0.2	0.6	0.7
94	Dome F	0.9	0.4	2.1	0.4	1.8	0.9
96	Vostok	0.4	0.3	1.5	0.2	0.7	0.7
97	WAIS Divide	5.3	1.4	7	2.7	10.4	3.1
98	Byrd	1.8	0.6	3.1	0.9	3.5	1.4
99	Siple Dome	9.6	2.4	11.9	4.8	19	5.3

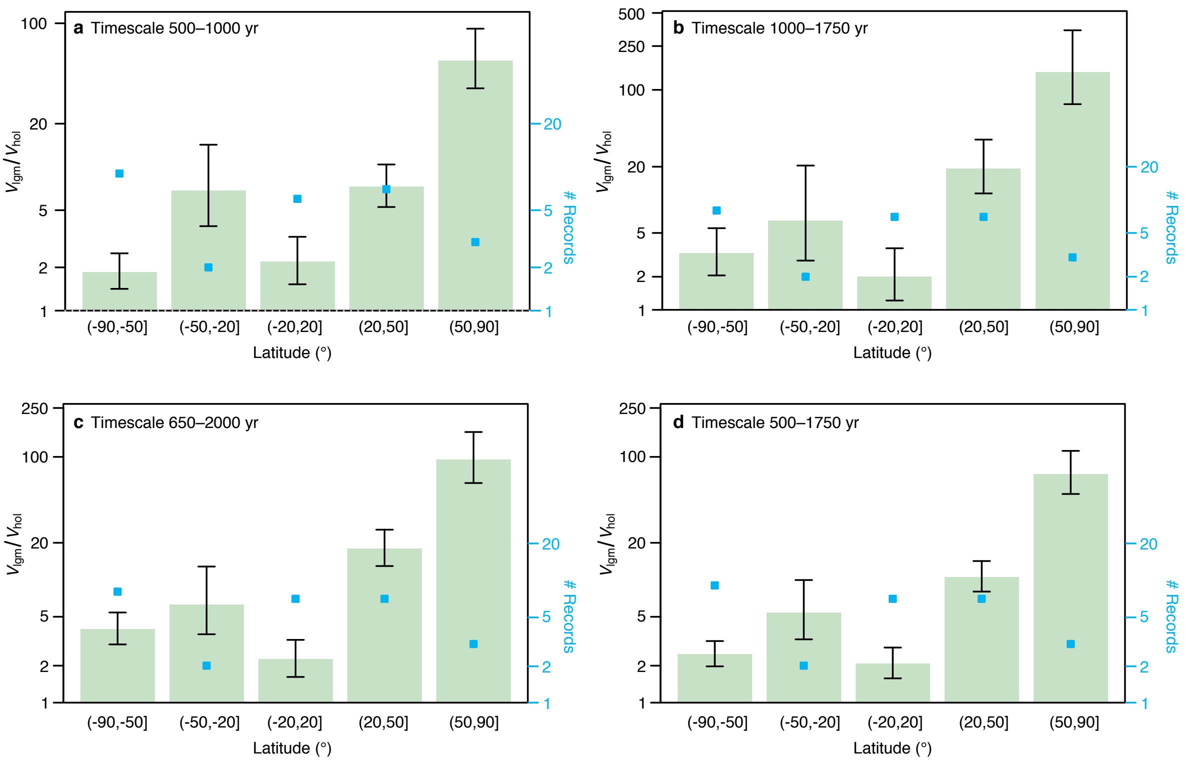

Figure A.1. Zonal variability change pattern for different timescales and length requirements. (**a**–**d**) Results for the estimated zonal-mean variance ratios based on the joint data set are shown as a function of the timescale considered and the minimum number of data points in the time period: 500–1000-year timescale with a minimum of 25 data points (**a**); 1000–1750-year timescale with a minimum of 25 data points (**b**); 650–2000-year timescale with a minimum of 20 data points (**c**); and 500–1750-year timescale with a minimum of 25 data points (**d**), which corresponds to the results shown in the main text. The number of records for each zonal-mean ratio is indicated by blue points. The total number of records varies depending on the timescale constraints. Error bars denote the 90 % confidence intervals of the zonal mean.

(PMIP3-CMIP5) archives. Model simulations were included from the CCSM4, CNRM-CM5, FGOALS-g2, GISS-E2-R, IPSL-CM5A-LR, MIROC-ESM, MPI-ESM-P and MRI-CGCM3 models. For each model, the last 100 years of the archived simulations were used to estimate temperature variance fields. The fields of the ratio of variances were then re-gridded to a common T63 resolution to form the model-mean ratio of variances (Fig. A.3). We use the pre-industrial model results as a reasonable surrogate for the Holocene time slice because we are interested in the first-order patterns of the gradient and variability changes, which are governed by the deglaciation.

A.3 TEMPERATURE RECALIBRATION OF PROXY RECORDS

Marine and ice-core records were recalibrated using a single temperature relationship for each proxy type and region to minimise the

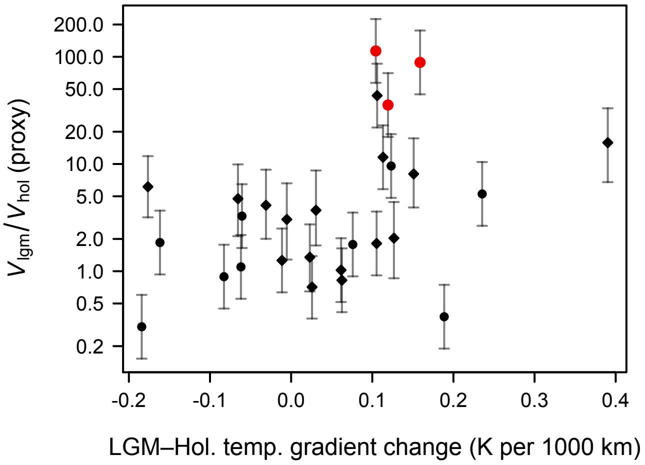

Figure A.2. Temperature gradient versus variability change. Scatter plot of the model-based equator-to-pole temperature gradient change at the proxy locations versus the variability change estimated from the proxy records. Filled circles correspond to ice-core records (red, Greenland; black, other) and filled diamonds to marine records. Error bars denote the 90 % confidence interval of the estimated variance ratios. The data have a Spearman's rank correlation coefficient of 0.43 ($p \leq 0.03$, $n = 28$) when including the Greenland ice cores and of 0.35 ($p \leq 0.09$, $n = 25$) when excluding them.

calibration-dependent uncertainty for variability estimates based on the separate data set. Terrestrial records based on lacustrine sediments, pollen and tree data were not recalibrated owing to the lack of a suitable global calibration for these proxy types.

A.3.1 *Recalibration of ice-core records*

For the calibration of ice-core stable isotope data to temperature (isotope-to-temperature slope in °C per ‰) two distinct methods exist: based on either the relationship of observed present-day spatial gradients in surface snow isotopic composition and temperature (spatial slope) or temporal gradients observed at a single site (temporal slope).

For Greenland, temporal slopes appear to lie consistently above the spatial slope, depending on the timescale, probably owing to changes in moisture origin and seasonality of precipitation (Jouzel et al., 1997). For the Holocene temporal slope we used a borehole temperature calibration (Vinther et al., 2009) of 2.1 °C per ‰, with an estimated uncertainty of ±0.4 °C per ‰ based on the slopes reported by other studies (Shuman et al., 1995; Beltrami and Taylor, 1995; Cuffey et al., 1994; Cuffey and Clow, 1997; Johnsen et al., 1997; Sjolte et al., 2011). The LGM temporal slope is a factor of 1–2 greater than the Holocene slope (Johnsen et al., 1995; Johnsen et al., 1997; Cuffey et al., 1995;

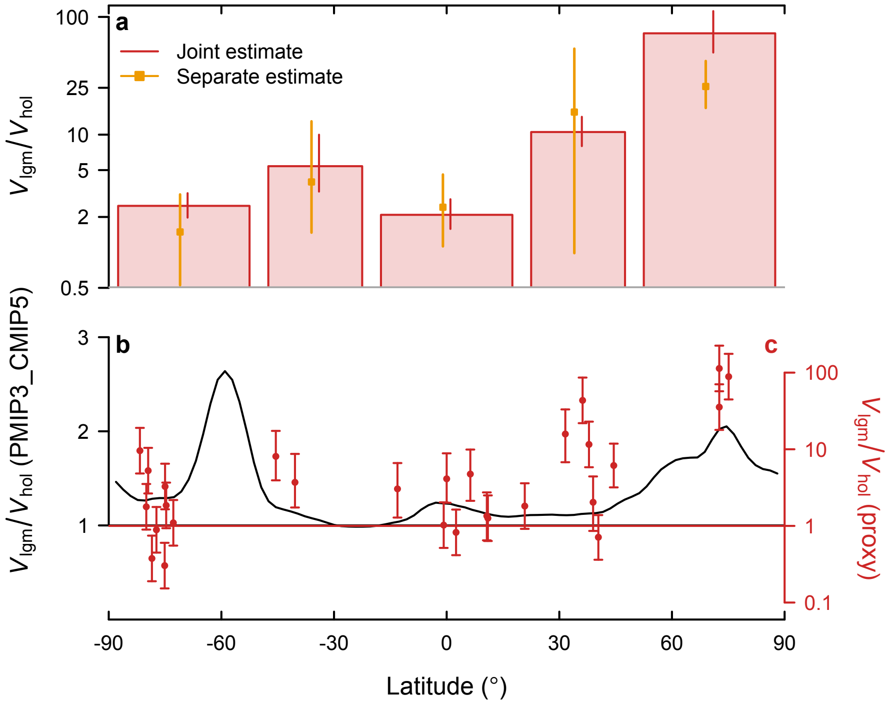

FIGURE A.3. Proxy- versus model-based variability change. (**a**) Zonal-mean LGM-to-Holocene variability change from the proxy compilations (red bars denote the joint estimate, orange points the separate estimate). (**b**) Interannual to multidecadal zonal-mean variability change based on the PMIP3-CMIP5 simulations for the LGM and the pre-industrial period. (**c**) Individual variability change at the proxy locations from the joint data set. Error bars in (**a**) show the 90 % confidence interval of the mean, error bars in (**c**) the 90 % confidence interval of the individual variance ratios.

Cuffey and Clow, 1997; Kindler et al., 2014); as a best guess we used a factor of 1.5.

For Antarctica, direct estimations of temporal slopes are difficult. However, the difference between spatial and temporal slopes as well as the timescale dependence of the latter is expected to be small (Jouzel et al., 2003). Here, we adopted reported spatial slopes (Masson-Delmotte et al., 2008) of 1.25 °C per ‰ for δ^{18}O and 0.16 °C per ‰ for δ^{2}H, with an uncertainty of 20 % for recalibrating the Antarctic ice-core data.

For tropical ice cores, we adopted a constant calibration slope for δ^{18}O of 1.49 °C per ‰ (Thompson et al., 1995).

A.3.2 *Recalibration of marine records*

Marine proxy records were recalibrated if the proxy type occurred more than once in our data collection and a suitable global calibration existed. Most of the Mg/Ca records in our compilation are based on planktic foraminifera *Globigerinoides ruber*, converted to temperatures using the calibration (Anand et al., 2003) $\mathrm{Mg/Ca} = b \cdot \exp(a \cdot \mathrm{SST})$, with $a = 0.09\,\mathrm{mmol\,mol^{-1}\,°C^{-1}}$, $b = 0.38\,\mathrm{mmol\,mol^{-1}}$, standard errors $s_a = 0.003\,\mathrm{mmol\,mol^{-1}\,°C^{-1}}$, $s_b = 0.02\,\mathrm{mmol\,mol^{-1}}$. For consistency, we recalibrated other *G. ruber* Mg/Ca records to the same calibration even though it is established using sediment trap samples and hence not a global calibration. For species other than *G. ruber*, that is, *Globigerina bulloides* (two records from different regions) and *Neogloboquadrina pachyderma* (left-coiling; one record), we kept the Mg/Ca records as published. Similarly, temperature records based on the transfer function of diatom, radiolarian and foraminifera assemblages were kept as published. All $\mathrm{U}^{\mathrm{K}'}_{37}$-based records were recalibrated using the calibration (Müller et al., 1998) $\mathrm{U}^{\mathrm{K}'}_{37} = a \cdot \mathrm{SST} + b$, with $a = 0.033\,°\mathrm{C}^{-1}$, $b = 0.044$, $s_a = 0.001\,°\mathrm{C}^{-1}$ and $s_b = 0.016$. All TEX_{86} and $\mathrm{TEX}^{\mathrm{H}}_{86}$ records were recalibrated to the subsurface $\mathrm{TEX}^{\mathrm{H}}_{86}$ calibration (Ho and Laepple, 2016) $T = a \cdot \mathrm{TEX}^{\mathrm{H}}_{86} + b$, with $a = 40.8\,°\mathrm{C}$, $b = 22.3\,°\mathrm{C}$, $s_a = 4.37\,°\mathrm{C}$ and $s_b = 2.19\,°\mathrm{C}$, because marine surface and subsurface temperature variability are on average similar (Ho and Laepple, 2016).

A.4 TIMESCALE-DEPENDENT VARIANCE AND VARIANCE RATIO ESTIMATION

The records were interpolated onto a regular time axis given by their individual mean sampling frequency in the LGM or the Holocene, following a previously reported procedure (Laepple and Huybers, 2014). To minimise aliasing, data were first linearly interpolated to ten times the target resolution, low-pass filtered using a finite response filter with a cut-off frequency of 1.2 divided by the target time step, and then resampled at the target resolution. Linear interpolation of a process that has been unevenly sampled reduces the variance near the Nyquist frequency, but the sampling rate of our records relative to the timescale of the variance estimates is high enough to minimise this effect (Fig. A.4). Timescale-dependent variance estimates were obtained by integrating the raw periodogram (Chatfield, 2004) in the frequency band (f_1, f_2) using $f_1 = 1/500\,\mathrm{yr}^{-1}$ and $f_2 = 1/1750\,\mathrm{yr}^{-1}$ to capture multicentennial- to millennial-scale temperature variability. All spectra are shown in Fig. (A.4). Tests with surrogate records on the original time axes demonstrate that our estimates are largely unbiased (Fig. A.5). Furthermore, our results are robust to changes of the sampling criteria (Fig. A.1).

Confidence intervals for the variance estimates were derived from the χ^2 distribution with d degrees of freedom, in which d is given by twice the number of spectral power estimates in the frequency band (f_1, f_2). Confidence intervals for variance ratios were derived accordingly from the F distribution with the degrees of freedom of the variance estimates.

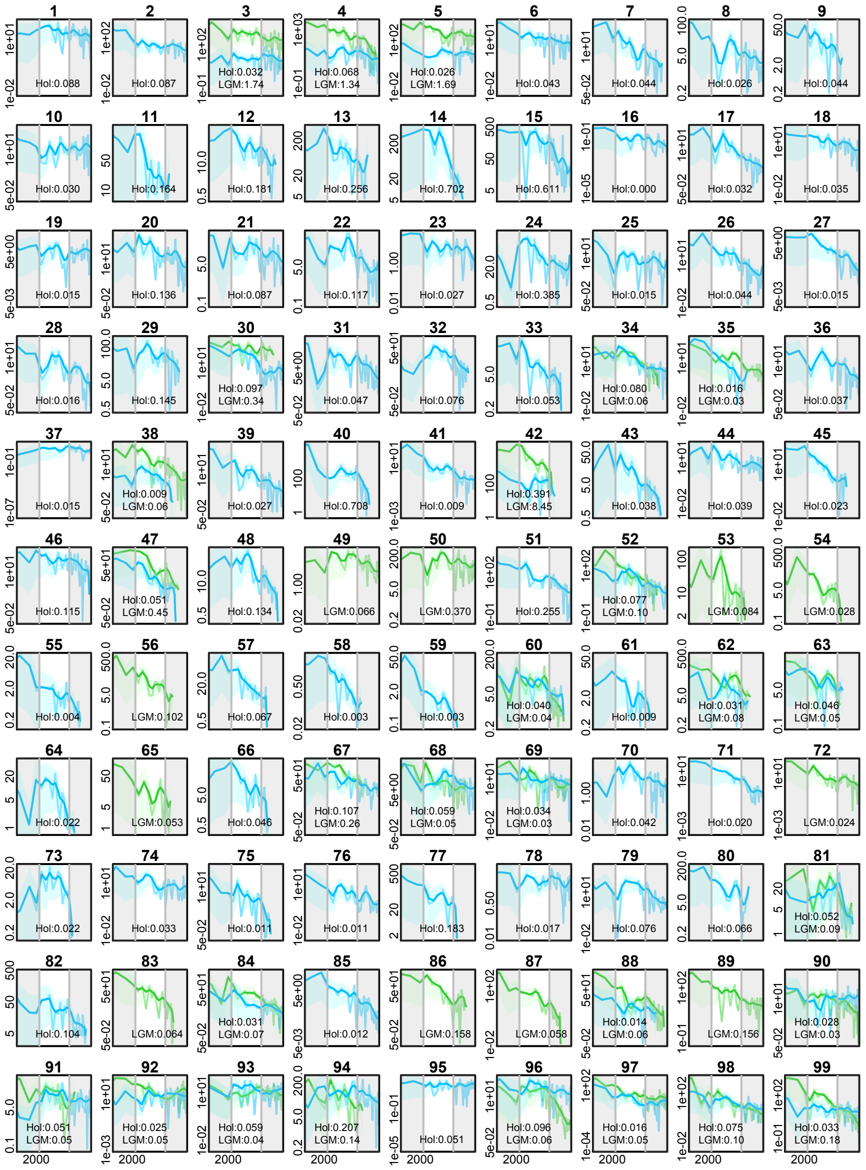

FIGURE A.4. Raw periodograms of all records. Thin blue lines show the spectra of the Holocene time slice; thin green lines show the spectra of the LGM time slice. Logarithmically smoothed spectra are given as thick lines with 90 % confidence intervals as shading. Grey areas indicate the frequency response outside the bandwidth used for the timescale-dependent variance ratio estimate. *x*-axis scaling is in periods in years; *y*-axis scaling denotes power spectral density. Text insets give the time-slice variances for the LGM and the Holocene ("Hol") in K^2; variance ratios for the records from the joint data set are listed in Table (A.1).

For the joint data set, zonally averaged variance ratios were derived from the bias-corrected individual ratio estimates as

$$\overline{R} = \frac{1}{N}\sum_{i=1}^{N}\frac{d_{\mathrm{hol},i}-2}{d_{\mathrm{hol},i}}R_i, \qquad \text{(A.1)}$$

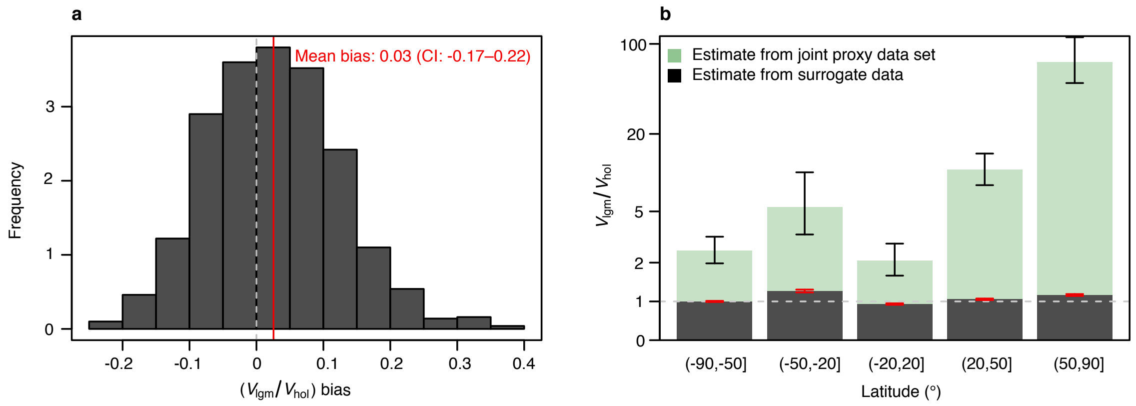

FIGURE A.5. Surrogate tests for the magnitude of variance change. The magnitude of potential biases in the variance ratio estimates were derived using 1000 realisations of power-law noise (slope $\beta = 1$) of constant variance on the original time axes of the records. Analyses for variability quantification were performed as for the primary analyses described in the text*. (**a**) Histogram of the bias of the variance ratio estimated from the surrogate data. The mean of the distribution (red line) is not significantly different from zero (CI, confidence interval). (**b**) Estimated zonal-mean ratios from the surrogate data. The individual surrogate zonal-mean ratios (black bars) are all close to 1 and show no latitudinal pattern, in contrast to the zonal-mean ratios from the proxy data (joint data set, green bars). Error bars show the 90 % confidence interval for the proxy data and ±2 times the standard error of the zonal mean for the surrogate data ($n = 1000$).

in which $R_i = V_{\mathrm{lgm},i}/V_{\mathrm{hol},i}$ is the noise-corrected variance ratio of the ith record. For the separate data set, zonally averaged variance ratios were derived from the ratio of the zonal-mean variances with subsequent noise correction.

For both data sets, global-mean variance ratios were derived from the area-weighted zonal means. To obtain the ratio distributions (Fig. 7.2a) we sample 50 000 times with replacement from the proxy estimates (joint, ratios; separate, variances). For each realisation, we form the zonal-mean estimates of the variance change (for the joint data set), or of the mean Holocene and LGM variance and then take the ratio (for the separate data set). We then form the area-weighted global mean for the variance change. Confidence intervals for the global-mean estimate are derived as quantiles from the realisations. The ratio distribution for Greenland is estimated using the same method but considering only the three Greenlandic ice cores. Kernel density estimates are shown (Fig. 7.2a) using a Gaussian smoothing kernel with a bandwidth of 1/10 of the mean ratio, so 0.4 for the global mean and 7 for Greenland.

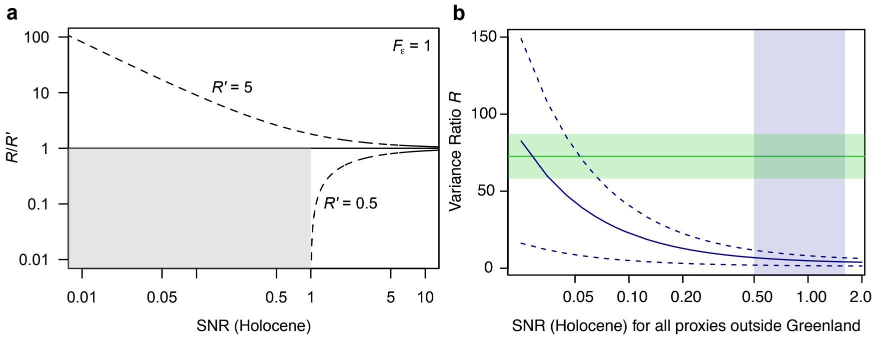

FIGURE A.6. Effect of the Holocene signal-to-noise ratio (SNR)$^\vee$ of proxy records on the noise correction of the variance ratios estimated. (**a**) Noise correction as a function of SNR*. The ratio of the true variance ratio to the estimated one, R/R', is displayed for $R' = 0.5$ and $R' = 5$ (dashed lines) for a noise variance ratio of $F_\varepsilon = 1$. The shaded area denotes the region where for $R' = 0.5$, no $R/R' \geq 0$ exists. (**b**) Test for the comparability of marine and Greenland ice-core variance ratios as a function of the SNR. The expected value of R for the mean over all records of the joint data set below 70° N is shown under the assumption of a wide range of SNR (solid blue line), with uncertainty (dashed lines) of ±2 s.e.m. ($n = 25$). Within the realistic range of Holocene SNR (shaded blue area, based on the published estimates listed in Table A.2), the noise-corrected global variance ratio (excluding Greenland) ranges from 1.7 to 11.4, which cannot be brought into agreement with the mean variance ratio of the Greenland ice cores (horizontal green line; shading denotes full uncertainty including the range of Greenland SNR (Table A.2) used in the noise correction).

A.5 NOISE CORRECTION

We determine the effect of noise on the estimated variance ratio R' between two climate periods,

$$R' := \frac{\mathrm{var}\left(X_1\right)}{\mathrm{var}\left(X_0\right)}\,. \tag{A.2}$$

Here, X_1 and X_0 are the proxy time series of the investigated (LGM) and reference (Holocene) climate periods, respectively. Each proxy time series contains noise. Assuming additive noise, and that the climate signal and noise are uncorrelated on each timescale covered, we can split the variances in Eq. (A.2) into contributions from the signal S and the noise ε,

$$\begin{aligned} R' &= \frac{\mathrm{var}\left(S_1\right) + \mathrm{var}\left(\varepsilon_1\right)}{\mathrm{var}\left(S_0\right) + \mathrm{var}\left(\varepsilon_0\right)} \\ &= \frac{\mathrm{var}\left(S_1\right)}{\mathrm{var}\left(S_0\right)\left[1 + \mathrm{SNR}^{-1}\right]} + \frac{\mathrm{var}\left(\varepsilon_1\right)}{\mathrm{var}\left(S_0\right)\left[1 + \mathrm{SNR}^{-1}\right]}\,, \end{aligned} \tag{A.3}$$

in which we have introduced the reference-period signal-to-noise variance ratio, $\mathrm{SNR} = \mathrm{var}\left(S_0\right)/\mathrm{var}\left(\varepsilon_0\right)$. Identifying the true climate variance ratio, $R = \mathrm{var}(S_1)/\mathrm{var}(S_0)$, and denoting the noise variance ratio by $F_\varepsilon = \mathrm{var}(\varepsilon_1)/\mathrm{var}(\varepsilon_0)$, we obtain

$$R' = \frac{\mathrm{SNR}}{1+\mathrm{SNR}} R + \frac{F_\varepsilon}{1+\mathrm{SNR}} . \tag{A.4}$$

Solving for R yields

$$R = R' \frac{1+\mathrm{SNR}}{\mathrm{SNR}} - \frac{F_\varepsilon}{\mathrm{SNR}} . \tag{A.5}$$

Because R cannot be negative, the parameters must always satisfy the condition $F_\varepsilon/(1+\mathrm{SNR}) \leq R'$. For any $R' \geq F_\varepsilon$, the effect of noise dampens the true ratio ($R \geq R'$; Fig. A.6a).

To correct for the effect of noise on the LGM-to-Holocene variance ratio, we apply Eq. (A.5) both to every individual variance ratio estimated for the joint data set and to the zonal-mean variance ratios derived from the separate data set. A reasonable assumption is that the noise level is independent of the climate period ($F_\varepsilon = 1$), which we adopt for all analyses. For the joint data set, we assume a $\mathrm{SNR}^\star$ of 1.5 for the Greenland records and of 1 for all other records. To correct the zonal-mean variance ratios derived from the separate data set, we adopt a SNR of 1.

A.5.1 *Testing the effect of the noise correction on the variability change difference*

The SNR is a considerable source of uncertainty for the noise correction. SNR can be estimated, among other approaches, by direct forward modelling of the proxy (Laepple and Huybers, 2014) or by correlation of nearby records (Fisher et al., 1985; Steen-Larsen et al., 2011; Laepple and Huybers, 2014; Münch et al., 2017a). An overview of SNR for the regions and proxies of interest is given in Table (A.2). We tested the effect of the noise correction on the difference between the Greenland ice-core-based variance ratio estimates and those from the proxy records outside Greenland. To bring the variance ratios into agreement, the SNR of proxies outside Greenland would have to be less than 0.05 (Fig. A.6b), which is one order of magnitude below published estimates for marine proxy (Laepple and Huybers, 2014) and Antarctic isotope records (Münch et al., 2017a). It is therefore unlikely that the observed variability difference can be attributed to Greenland ice cores being better recorders (that is, having a higher SNR) than marine sediment or Antarctic ice-core records.

A.6 POTENTIAL EFFECT OF ECOLOGICAL ADAPTION AND BIOTURBATIONAL MIXING ON MARINE VARIANCE RATIOS

Variability derived from biological proxies, that is, recorded by marine organisms, are possibly muted relative to the actual environ-

TABLE A.2. Overview of published proxy signal-to-noise ratio estimates for the Holocene. Greenlandic and Antarctic estimates refer to δ^{18}O. CI, confidence interval.

Domain	**Estimate** (CI)	**Method**	**Timescale**
Central Greenland[a] (Milcent & Crete)	1.25 (±0.6)	correlation	interannual
Central Greenland[b] (NEEM)	2.7	correlation	interannual
Marine Mg/Ca[c] (global)	0.5	forward model	centennial
Marine UK'37[c] (global)	1.6	forward model	centennial
East Antarctica[d] (EDML)	1.0 (±0.5)	correlation	seasonal

[a] Fisher et al. (1985). [b] Steen-Larsen et al. (2011). [c] Laepple and Huybers (2014).
[d] Münch et al. (2017a).

mental changes owing to the tendency of organisms to adapt and seek their ecological niche (for example, of a certain temperature or nutrient range; Mix, 1987. Our results are based on the ratio of variability and not on absolute variability estimates. Therefore, for ecological adaptation to affect our results, LGM variability needs to be muted to a much larger extent than that for the Holocene. In the simple conceptual ecological model (Mix, 1987), given the same temperature preference, larger variability would result in a stronger damping. However, the largest part of the variability seen by marine organisms is the seasonal and vertical temperature range in the depth habitat. This spread is controlled by insolation and stratification and not primarily by the climate state. The interannual to millennial variability, which we find to be larger in the LGM, contributes only a small fraction to the total variability and so should not be a primary control of the damping strength affecting the proxy records. Our oceanic temperature variability estimates for the joint data set (containing both Holocene and LGM) are based on alkenone-based $U^{K'}_{37}$ (eight sites) and the Mg/Ca of planktic foraminifera *G. ruber* (seven sites), the latter from tropical sites. Unlike planktic foraminifera, which have a preferred temperature niche, the known major producers of alkenones such as the coccolithophore *Emiliana huxleyi* occur throughout the global ocean from the tropics to the polar waters. Their abundance is mostly controlled by nutrient and light availability, which do not always co-vary with temperature. Most of our *G. ruber* Mg/Ca records are from the tropics, with Holocene temperatures (such as 29 °C at SO189-39KL; Fig. 7.1c) close to the warm end of their temperature niche (15–29 °C; Hilbrecht, 1996), whereas LGM temperatures (such as 26 °C at SO189-39KL; Fig. 7.1c) are closer to the mean of the range. Therefore, if there is ecological adaptation, it is more likely to occur near the extremes (that is, the Holocene) rather than in the middle of the range. This would result in an amplified variance ratio between the Holocene and the LGM.

Bioturbational mixing in marine sediments reduces the absolute variability preserved in marine sediments (Berger and Heath, 1968). However, here we focus our analysis on variability changes and thus largely circumvent this problem, because both the glacial and the Holocene part of the core are affected by bioturbation. Bioturbation can be approximated as a linear filter (Berger and Heath, 1968) and so the ratio of variances is not affected as long as the sedimentation rate and bioturbation strength that define the filter are similar in both time periods or do not change systematically between climate states. Our data set shows no evidence of a systematic change in sedimentation rate with 7 of the 16 marine cores in our joint data set showing higher and 9 lower sedimentation rates in the Holocene (with a statistically non-significant* change in mean sedimentation rate of 20 %). The changes also show no detectable latitudinal dependency. There is also no evidence of a systematic change in largely unconstrained bioturbation strength between the time periods in the manuscripts that describe the data sets.

Despite not being effects of climate, the ecological preference of the organisms that record the climate signal and bioturbational mixing of the sediment can affect variability estimates and may thus add to site-specific variability changes. But the aforementioned arguments demonstrate that their effect is expected to be very small compared to the orders of magnitude difference between tropics and mid-latitudes and between marine cores and ice cores.

A.7 TESTING THE EFFECT OF THE PROXY SAMPLING LOCATIONS ON ZONAL-MEAN VARIANCE ESTIMATES

The proxy locations are not randomly distributed in space, which could lead to sampling biases. To test for a potential sampling bias we analyse the 2-metre temperature field of the past 7000 years from the coupled atmosphere ocean TraCE-21K simulation (Liu et al., 2009). The time period is chosen to focus on the continuum of climate variability and to minimise the effect of the deglaciation. The temperature variance field for centennial and longer timescales is derived by estimating the variance at every grid point after applying a low-pass finite response filter with a cut-off frequency of $1/100\,\mathrm{yr}^{-1}$.

We sample the variance field at the actual proxy locations and average the results into the same latitude bands as for the proxy-based variance ratio estimates. To estimate the expected distribution of mean values from unbiased locations, we sample N random locations

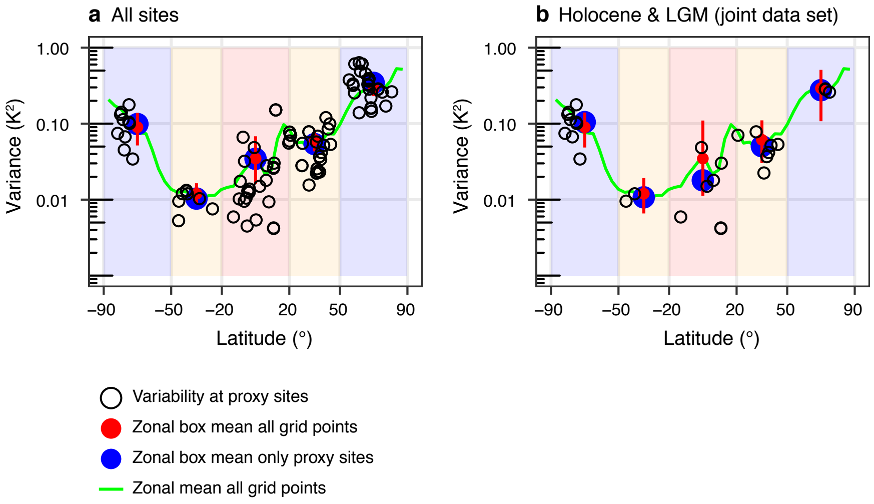

FIGURE A.7. Representativeness of the proxy data locations. The centennial temperature variability in the TraCE-21K simulation, sampled at the proxy locations (black circles), the zonal-mean variability (green line) and the mean of the variability in the zonal box, either formed only from the variance at the proxy sites (blue) or formed using all grid points (red), are shown. The red vertical lines show the 90 % quantiles from the mean of *N* random samples of the variance field, where *N* is the number of proxy sites in the zonal box. (**a**) Results when sampling from the proxy locations of the separate data set. (**b**) Results when sampling from the joint data set. In all cases the mean of the proxy sites is inside the distribution of random samples, which demonstrates that under the assumption of this variance field the proxy estimates are unbiased.

at each latitude band, where *N* corresponds to the number of actual records in each band. We form the mean of this random sample and repeat the procedure 10 000 times, from which we report the 90 % quantiles. The results (Fig. A.7) show that the mean values from the actual proxy locations are always inside the expected distribution. This result holds when using the full data set and when restricting the analysis to the records that cover both the LGM and the Holocene.

B

LAYERING OF SURFACE SNOW AND FIRN AT KOHNEN STATION, ANTARCTICA: NOISE OR SEASONAL SIGNAL?

Thomas Laepple[1], Maria Hörhold[2,3], Thomas Münch[1,4],
Johannes Freitag[5], Anna Wegner[5], and Sepp Kipfstuhl[5]

[1] *Alfred Wegener Institute Helmholtz Centre for Polar and Marine Research, Telegrafenberg A43, 14473 Potsdam, Germany*
[2] *Institute of Environmental Physics, University of Bremen, Otto-Hahn-Allee 1, 28359 Bremen, Germany*
[3] *Now at Alfred Wegener Institute Helmholtz Centre for Polar and Marine Research, Am Alten Hafen 26, 27568 Bremerhaven, Germany*
[4] *Institute of Physics and Astronomy, University of Potsdam, Karl-Liebknecht-Str. 24/25, 14476 Potsdam, Germany*
[5] *Alfred Wegener Institute Helmholtz Centre for Polar and Marine Research, Am Alten Hafen 26, 27568 Bremerhaven, Germany*

This chapter is published in:
Journal of Geophysical Research: Earth Surface, **121** (10), 1849–1860, DOI: 10.1002/2016JF003919, 2016.

ABSTRACT. The density of firn is an important property for monitoring and modelling the ice sheets as well as to model the pore close-off and thus to interpret ice-core-based greenhouse gas records. One feature, which is still under⋆ debate, is the potential existence of an annual cycle of firn density in low-accumulation regions. Several studies describe or assume seasonally successive density layers, horizontally evenly distributed, as seen in radar data. On the other hand, high-resolution density measurements on firn cores in Antarctica and Greenland show no clear seasonal cycle in the top few metres. A major caveat of most existing snow-pit and firn-core-based studies is that they represent one vertical profile from a laterally heterogeneous density field. To overcome this, we created an extensive data set of horizontal and vertical density data at Kohnen Station, Dronning Maud Land, on the Antarctic Plateau⋆. We drilled and analysed three 90 m long firn cores as well as 143 1 m long⋆ vertical profiles from two elongated snow trenches to obtain a two-dimensional view of the density variations. The analysis of the 45 m wide and 1 m deep density fields reveals a seasonal cycle in density. However, the seasonality is overprinted by strong stratigraphic noise, making it invisible when analysing single firn cores. Our density data set extends the view from the local ice-core perspective to a 100-metre⋆ scale and thus supports linking spatially integrating methods such as radar and seismic studies to ice and firn cores.

B.1 INTRODUCTION

Density, as a physical property of polar firn, is important for many topics of polar research. The determination of the ice sheet mass balance by either modelling or monitoring of the ice sheets with ground-penetrating radar or with satellite laser altimetry is strongly related to firn density (Rott et al., 1993; Li and Zwally, 2002; Rotschky et al., 2006). The evolution of the firn density further determines the air enclosure in ice at the firn–ice transition (Martinerie et al., 1992; Schwander et al., 1997).

Polar firn is characterised by layering, each layer generated by a single deposition event and associated with different physical properties. The resulting vertical density variability caused by this layering is responsible for the depth and time when air trapped in the firn and ice is sealed off from the exchange with the atmosphere, thereby determining the age difference between air bubbles in ice cores and their surrounding ice (Landais et al., 2006; Mitchell et al., 2015). It was previously demonstrated that the layering changes with depth, showing a seasonal cyclicity in depths below 20–30 m that is highly correlated with seasonally varying impurity concentration (Hörhold et al., 2012; Freitag et al., 2013a). It has been speculated since then that impurities, featuring a seasonal cycle in their concentration, reshape the layering by changing the mechanical properties of the snow and the firn and thus influence the densification of single layers (Hörhold et al., 2012; Freitag et al., 2013a; Fujita et al., 2014; Gregory et al., 2014).

The horizontal and vertical density variabilities at the surface of ice sheets are unclear. On one hand, radar images suggest an image of layers that undulate at a kilometre scale but are nevertheless continuous (Arcone et al., 2005; Anschütz et al., 2007; Arthern et al., 2013). Thus, the firn column on top of the ice sheets is often understood as a sequence of successive layers (Gow, 1965; Palais, 1984; Kreutz et al., 1999). Accumulation rates extracted from ground-penetrating radar or satellite images are one example for this concept of successive horizontally distributed annual layers (Winebrenner et al., 2001; Anschütz et al., 2007; Eisen et al., 2008; Arthern et al., 2013). The concept of annual layer deposition is furthermore supported by measurements of impurity concentrations or stable water isotopes, which exhibit a seasonal cycle in the atmosphere prior to deposition. These properties show a seasonal cycle within the snow and firn at many polar sites (Gow, 1965; Benson, 1971; Palais, 1984; Alley, 1988; Göktas et al., 2002; Svensson et al., 2015), suggesting homogenous formation of successive layers throughout each year. On the other hand, especially in low-accumulation regions, considerable horizontal variability is observed (Libois et al., 2014). This is reflected by the different stratification found in nearby snow pits (Fisher et al., 1985; Karlöf et al., 2006). Fur-

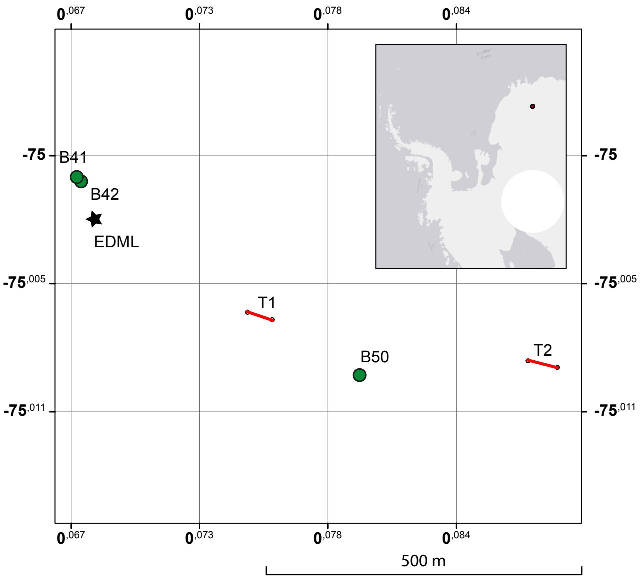

FIGURE B.1. Map of the firn-core and snow trench positions. Firn-core sites are shown as green-filled circles, trenches as red lines. The drilling site of the EPICA Dronning Maud Land (EDML) ice core is shown as black star.

ther, high-resolution density analysis of firn-core material (Hörhold et al., 2012; Freitag et al., 2013a) did not reveal a seasonal cycle in the surface firn density, suggesting that re-deposition and wind scouring dominate over the successive deposition of seasonal layers.

In this manuscript, we reconcile the previous findings of a lack in seasonality in the top metres of firn cores with the observed large-scale seasonal layering of the firn. Analysing density on vertical and horizontal scales from the centimetre to the 100-metre scale, we demonstrate that the question of layering and seasonality depends on the analysed spatial scale.

B.2 MATERIALS AND METHODS

In austral summer 2012/2013, close to the European Project for Ice Coring in Antarctica (EPICA) Dronning Maud Land drilling* site (EDML), firn cores and trenches were sampled and analysed for density (Fig. B.1). The site is characterised by a mean temperature of 44.5 °C and a mean accumulation rate of $62–73\,\mathrm{kg\,m^{-2}\,yr^{-1}}$ depending on the age interval used in the accumulation estimate (Oerter et al., 2004; Klein, 2014). The isotope data of the trenches are described in Münch et al. (2016b).

Table B.1. Summary of the Snow Trenches Analysed in this Study.

Trench Name	Position (NW end)	Bearing	Length Sampled	No. of profiles
T1	75.00641° S 0.074978° E	140° N	45.6 m	62
T2	75.00849° S 0.08693° E	130° N	49.1 m	81

B.2.1 *Density Profiles From Firn Cores*

Four firn cores of at least 90 m length were drilled in the close vicinity of the EDML site* and analysed for density variations. We include three of the cores in this study (Fig. B.1) as the core quality of the first core of the season (B40) was considerably lower than for the remaining cores. The firn cores were transported in 1 m pieces to the cold laboratory at the Alfred-Wegener-Institute (AWI) in Bremerhaven, Germany. Density of the firn cores was measured at a 0.5 mm resolution using high-resolution X-ray Computer Tomography* (CT) (Freitag et al., 2013a).

B.2.2 *2-D Density Profiles From Shallow Firn Trenches*

To study the horizontal density structure, close to the firn-core positions, two 1.2 m deep, 1.2 m wide, and around 45 m long trenches named T1 and T2 were excavated by using a snow blower (Table B.1). Each trench was directed perpendicularly to the local snow-dune direction. In contrast to other studies, the vertical zero position for each trench was not set to the snow surface, but an absolute height reference was defined as a horizontal line between the highest points of the surface level of each trench. This was established by using short bamboo poles every 60 cm, aligned by a spirit level and a laser device. Unfortunately, due to technical problems, no absolute height reference between the two trenches could be established. A coarse measurement based on stacked laser level measurements showed that the vertical difference between the trenches is less than 20 cm.

Every 60 cm, 1 m long firn cores were taken by carefully pushing a glass fibre liner with 98 mm diameter vertically into the firn at ∼ 5–10 cm distance to the trench wall. The full liners were carefully recovered by digging them out. During the process of pushing the liners into the snow, care was taken that the snow inside the liner did not get compressed. Liners with more than 1 cm compression, visible as a reduction of the snow level at the top relative to its surroundings, were remeasured by moving the position 15 cm perpendicularly to the trench wall. In some cases, the replicate measurements again showed compression, and thus, no data could be obtained for this position. The vertical distance from the top of the liner to the absolute reference was recorded with an accuracy of 1 cm. The snow-filled liners were carefully transported to the EDML processing trench.

B.2.3 *Dielectric Profiling and Density Estimates*

The dielectric stratigraphy was measured in the processing trench applying the dielectric profiling (DEP) technique using the device described in Wilhelms et al. (1998). Measurements were performed at 250 kHz frequency in 5 mm increments. The effective resolution is limited by the finite width of the 1 cm wide electrode and was found to be around 2 cm based on analysing the air to ice transition at the top of the core. The top and bottom 4 cm of the DEP measurements are affected by edge effects due to the air to ice transition. Sometimes, a loss of snow at the top or bottom of the liner in the packing or transporting phase could not be completely avoided. The maximum-recorded loss was 4 cm at the top and 1 cm at the bottom. We therefore only analyse the part from 8 to 95 cm depth. For each measurement, the cable stray capacitance was subtracted and the capacitance record was divided by the free air capacitance, to derive the relative permittivity $\varepsilon^{\vee}$. To convert the DEP measurements into density, we use the real-valued Looyenga mixing model (Looyenga, 1965).

$$\rho = \rho_{\text{ice}} \frac{\varepsilon^{1/3} - 1}{\varepsilon_{\text{ice}}^{1/3} - 1} \tag{B.1}$$

where $\rho_{\text{ice}} = 920\,\text{kg}\,\text{m}^{-3}$ is the density of pure ice and $\varepsilon_{\text{ice}} = 3.17$ is the relative permittivity of ice at frequencies above 100 kHz (Glen and Paren, 1975). This mixing model is a good approximation in the top metres of the firn, and a comparison to gamma-ray-based density measurements showed deviations of less than 5 % in the top 40 m of a firn core (Wilhelms, 1996).

B.2.4 *Comparison of DEP-Derived Density and CT Density*

It is known that effects other than density also influence the dielectric stratigraphy including strong impurity changes or changes in the snow structure (Denoth, 1989). Further, CT-derived densities have a true resolution of 0.5 mm, whereas DEP-derived densities are always integrated over a width of several millimetres and are more sensitive to core breaks.

As we use both density measurement techniques in our study, we tested comparability of the methods by comparing the CT- and DEP-derived density for the firn core B41 (Fig. B.2). We analysed the top 10 m for they cover a similar density range (250–550 kg m^{-3}) as found

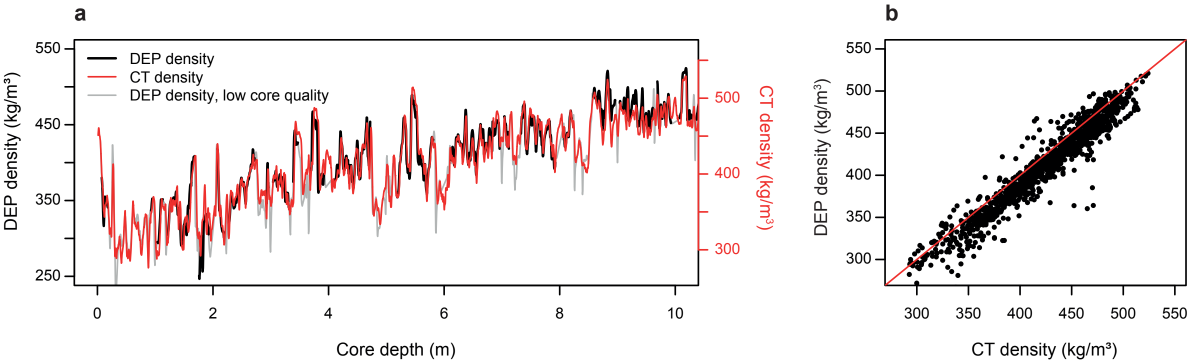

FIGURE B.2. Comparison of CT- and DEP-derived density of the top 10 m of B41. (**a**) Comparison of the depth series. The grey lines$^{\vee}$ show the areas in which a low core quality was noted during the DEP measurements. Both axes have the same scaling. (**b**) Scatterplot of DEP versus CT density. The 1:1 line is shown in red. Points with low core quality (= grey in **a**) are not included in the analysis.

in the trench. CT-derived densities were smoothed over 25 mm by using a 50-point running mean filter to result in a comparable resolution. In the remaining manuscript, we will always use the 25 mm running mean smoothed CT data except for the spectral analysis, which is performed on the raw data.

Both methods show a strong agreement in variations on the centimetre to metre scale ($r^2 = 0.91$). A small offset (12 kg m^{-3} difference in the 0–10 m mean density) between the CT and DEP density is observed, with the DEP showing a smaller density than the CT, but this does not affect our results as we only rely on relative density variations in this study.

The main deviations occur at core breaks and at the boundary of the 1 m pieces. By integrating over several centimetre, the DEP device is more sensitive to small geometrical deviations from core catchers and breaks than the CT measurements. As the trench DEP measurements were performed by using firn inside liners, the firn/snow is better preserved, and we expect a higher quality of the DEP-derived density of the trenches compared to the firn-core results shown here.

B.2.5 *Ion Measurements*

Within trench T2, discrete sampling at core positions 0.3, 10, 29.8, and 40 m (distance along the trench) was conducted. The snow surface was cleaned by removing the outermost layers. The snow was sampled in 3 cm increments and collected in Whirlpak plastic bags by using a precleaned Teflon spatula. The samples were closed carefully and sealed again for transportation back to Germany. During sampling protective Tyvek cloths were worn to avoid contamination. Samples were shipped in cool containers to Bremerhaven, Germany, and kept frozen until analysis.

The analyses of the samples were carried out in the ion chromatography laboratory facilities at AWI by using DIONEX IC-S 2100. Blanks were checked regularly and typically showed below 0.6 ppb for Na^+ and below the detection limit for methyl sulphonate (MSA). The ions of Na^+ and MSA are presented here. Ca^{2+} measurements suffer from contamination and are thus not included in the analysis. Because impurity concentrations are always positive but show an asymmetry towards large values (e.g., Bigler et al., 2011), we use the logarithm of the ion concentration in all cases.

B.3 RESULTS

B.3.1 *2-D Density Data From the Trenches*

The large number (160) of density profiles analysed from the two trenches allows creating a two-dimensional image of the horizontal and vertical density variations (Fig. B.3). The density distribution in both trenches shows a high vertical and horizontal variability with very similar magnitudes in both dimensions ($sd_{\text{vertical}} = 20.7\,\text{kg}\,\text{m}^{-3}$ and $sd_{\text{horizontal}} = 19.7\,\text{kg}\,\text{m}^{-3}$).

Roughly four layers can be identified as alternations of high- and low-density regions. Interestingly, as previously found while analysing the isotope data from trench T1 (Münch et al., 2016b), the density layers below 30 cm seem to be on average horizontal and do not follow the actual snow surface. Indicative for this behaviour is the smaller horizontal variability below 30 cm when all profiles are aligned to an absolute height ($sd = 17.8\,\text{kg}\,\text{m}^{-3}$) compared to the horizontal variability relative to the snow surface ($sd = 20.1\,\text{kg}\,\text{m}^{-3}$). Therefore, in the remainder of this study, we use and display the profiles relative to an absolute height reference and not to the snow surface.

The layers show undulations of several centimetres, similar in magnitude to the surface undulations that were present during the time of the sampling. Some density variations could be explained by vertically compressing or stretching the same density profile. However, in addition, other features are visible. Prominent are high-density anomalies (400–420 $\text{kg}\,\text{m}^{-3}$) with a horizontal extension of 2–5 m, which are especially frequent in the 20–70 cm firn depth range.

B.3.2 *Correlation Structure of Trench and Firn-Core Data*

To visualise the density variability and representativity of single profiles, we show four arbitrarily picked density profiles from the trenches T1 and T2 together with the density profiles of the top 5 m from the firn cores (Fig. B.4). This mimics the results we would have obtained in a classical study analysing single snow pits or firn cores. The first metre does not show an increase in density. Furthermore, no clear

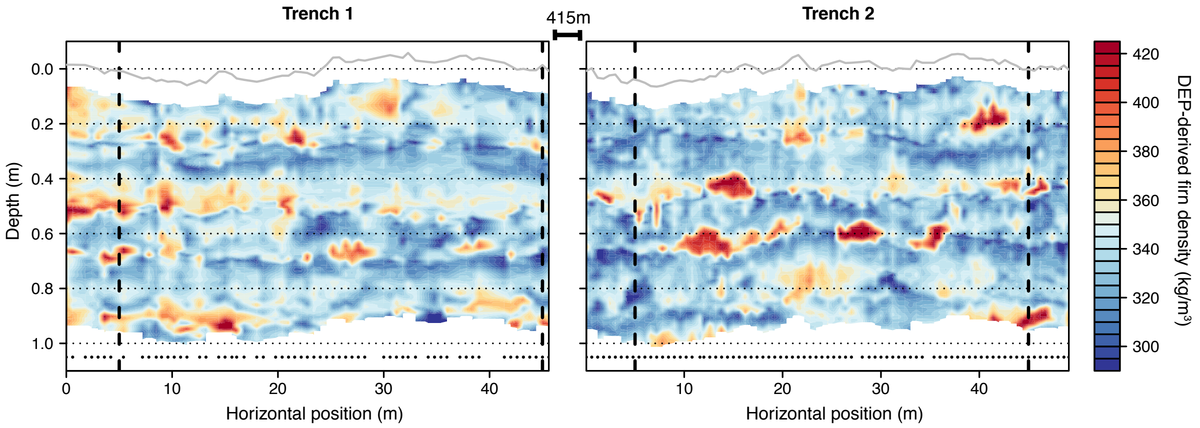

FIGURE B.3. 2-D (vertical and horizontal) structure of the DEP-derived density variations of both trenches. The depth is relative to an imaginary horizontal surface, which was arbitrarily set to 0 at the mean actual snow surface. The actual snow surface is shown as a$^{\vee}$ grey line. The removal of areas affected by edge effects in the DEP measurements lead to the missing areas below the snow surface. Dots at the bottom of each panel depict where a profile was taken. The vertical dashed lines indicate the positions of the profiles shown in Fig. B.4. For displaying reasons, we limit the colour scale to the 99 % quantile range of the density variations.

seasonal cycle is visible in the uppermost metre. Interestingly, all shown density profiles are uncorrelated to each other ($r < 0.2$ for all possible correlation pairs), demonstrating that the density profile of a single core is not representative for a larger region, at least on the vertical centimetre to metre scale shown here.

Similar results are obtained from analysing all profiles by correlating all the possible pairs of individual profiles from trench T1 with individual profiles from T2. This results in a mean correlation of 0.0. Allowing for a shift in the depth of ±12 cm for every single profile, and thus for potential undulations of the present snow surface, increases the mean correlation to 0.31. However, this is roughly what is expected by chance ($r = 0.28$ using surrogate data with the same autocorrelation structure as the sample autocorrelation of the real data) since allowing for shifts always leads to spurious positive correlations.

While these horizontally separated profiles are uncorrelated, a different picture is obtained for nearby profiles. Estimating the correlation for different separation distances (Fig. B.5) shows that nearby (< 1 m distance) firn profiles are highly correlated ($r = 0.65$), but this correlation drops to ~ 0.13 for separation distances larger than 10 m.

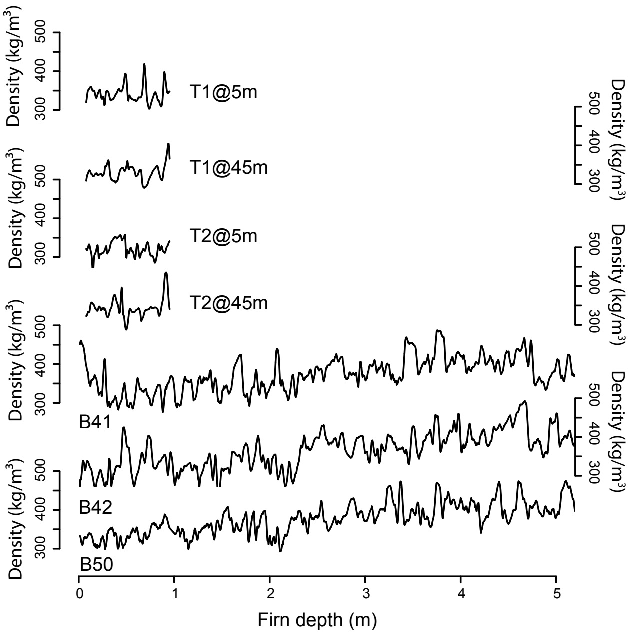

FIGURE B.4. Examples of vertical density profiles from the trench and firn-core data. Profiles from trench T1 at the horizontal positions 5 and 45 m, from T2 at 5 and 45 m, and the top 5 m from firn cores B41, B42, and B50 are shown. There is no significant correlation between any of the profiles ($r < 0.2$ using detrended data).

B.3.3 *Mean Profiles and Comparison to Water Isotopes and Ion Concentrations*

To reduce the local variability, we average all profiles inside each trench to obtain a mean density profile for each of the two trenches (Fig. B.6a). Interestingly, whereas single profiles between both trenches are uncorrelated, the mean profiles are highly reproducible ($r = 0.83$) when allowing for a 6 cm depth shift, which is well inside the relative vertical alignment uncertainty of both trenches. This demonstrates that the profiles contain a signal representative at least over a 500-metre* scale.

To learn about the timing of the density variations, we additionally show the mean $\delta^{18}O$ profiles based on 38 profiles in trench T1 and four profiles in trench T2 (Fig. B.6b and Fig. B.6c, Münch et al., 2016b). In both trenches, $\delta^{18}O$ and density variations show a weak but significant positive correlation ($r = 0.34$ and 0.31). High $\delta^{18}O$ values correspond to higher densities and vice versa. However, there are also considerable differences between both parameters, especially below 60 cm where the density shows a minimum not represented in $\delta^{18}O$. Both trenches suggest a slight (depth) lag between $\delta^{18}O$ and density with $\delta^{18}O$ leading by 2 cm (T1) and 3 cm (T2). Such a difference would correspond to 1–2 months in time assuming equal

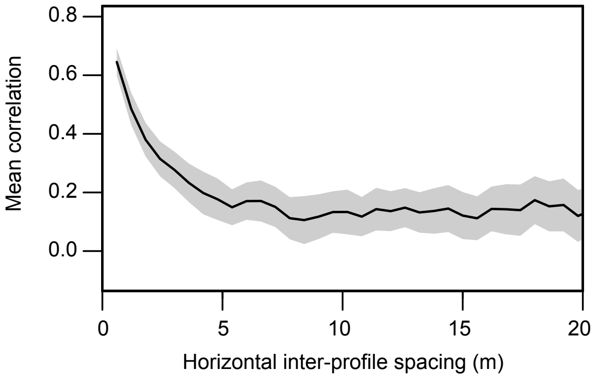

Figure B.5. Dependency of the density profile correlation on the horizontal separation distance between profiles. The mean correlation values of both trenches are shown. Nearby density profiles are highly correlated, but this correlation decreases strongly in the first 5 m. Shading indicates the estimation uncertainty (2 sd).

accumulation over the year, but the shortness of the time series does not allow reliable estimate of the potential time lag.

In trench T2, we additionally show the mean ion-concentration profiles of MSA and Na^+, obtained from averaging over the four available profiles (Fig. B.6c). Both ion profiles show a pronounced cyclicity and are anticorrelated to each other with peaks in MSA concentration corresponding to troughs in Na^+ concentration and vice versa (Table B.2). The peaks in $\delta^{18}O$ are in phase with the ascending flanks in the MSA profile and with the descending flanks of Na^+ concentration or almost within the trough. The peaks in the density profile are in phase with the peaks in MSA and the troughs in Na^+.

B.3.4 *Spectral Analysis of the Vertical Firn-Core Density Evolution*

The four layers in the trench density data set (Fig. B.3), the reproducible density variations in the mean profiles, and the correlation with the $\delta^{18}O$ profile (Fig. B.6) that is usually interpreted as a temperature signal suggest that the density variations contain a seasonal signal. This is further supported by the observation that the layer thickness of around 20 cm (Fig. B.3) agrees with the annual accumulation rate at the site.

In a first view, this seems to contradict earlier findings (Hörhold et al., 2012; Freitag et al., 2013a) where it was shown that high-resolution density data in the top metres of the firn do not show any clear seasonality as diagnosed by analysing the depth variability in the spectral domain. As these previous studies have been obtained at different sites and with different data sets, we repeat the wavelet analysis by using the same methods as described in Hörhold et al. (2012) for the CT density data of all three firn cores. To be able to investigate

TABLE B.2. Correlation, Signal-to-Noise Ratio (SNR) and Relative Phasing of the Different Parameters.[a]

	Mean Correlation r ($\geq$ 10 m Distance)	SNR ($r/(1-r)$)	Lag to Density in cm ($\sim$ months)
Density	0.13	0.15	
δ^{18}O	0.53	1.1	-3 cm (-2 months)
MSA	0.30	0.43	-1 cm (-1 month)
Na^{+}	0.31	0.45	$+9$ cm$/-10$ cm ($+5/-6$ months)

[a] Correlations for density (this study) and δ^{18}O (Münch et al., 2016b) are the mean values of both trenches, whereas MSA and Na^{+} (this study) were only measured in Trench 2. Lags were determined by cross correlation with negative values indicating a lead relative to density. For Na^{+}, the maximum cross correlation for negative and positive lags is the same inside uncertainty; therefore, both values are given.

variations in respect to time as the seasonal cycle, the depth scale is converted into water equivalent depth (w.eq.) and averaged to 5 mm w.eq. resolution. Low-frequency variations in the density records were removed by using a finite impulse response high-pass filter (Bloomfield, 1976; cut-off frequency of 0.5 (m w.eq.)$^{-1}$). The wavelet sample spectrum was estimated by using the Morley wavelet (sowas package; Maraun and Kurths, 2004) to analyse the depth-dependent behaviour of the density in the frequency domain. Local significance was again tested against a red-noise null hypothesis. The mean wavelet for all three cores is shown (Fig. B.7), but similar results are obtained with any of the three cores. We note that this mean wavelet spectrum is a different quantity to that obtained by stacking the three cores first and then calculating the wavelet.

The result of the wavelet analysis (Fig. B.7a) is very similar to the ones previously obtained from other Antarctic and Greenlandic cores (Hörhold et al., 2012), showing a broad continuum of variability at the surface, a decrease in variability with a minimum around 10–20 m w.eq. and statistically significant patches of energy (black contours in Fig. B.7a) appearing at depth close to the frequency of the modern accumulation rate range.

To complement the results of the wavelet analysis, we estimate the power spectra of the density variability of the firn cores at different depths (Fig. B.7b) using the multitaper technique. Local significance was tested against a red-noise null hypothesis. The spectrum of the upper 10 m w.eq. of the core shows a variability continuum from the millimetre scale up to 0.3 m w.eq. length scale with increasing energy towards longer variations and no clear, statistically significant signal at the indicated present-day accumulation rate. In contrast, the two other depth intervals show a distinct signal at the frequency of the accumulation rate. This in good agreement with former findings, where wavelet analysis revealed no distinct frequencies at the surface but the* development of a significant peak at the frequency of the$^\vee$ accumulation rate with depth. We note that the statistically non-significant local maximum at the low-frequency end of the spectrum (2–3 $(\mathrm{m\,w.eq.})^{-1}$) might be an artefact of the core processing as 1 m pieces correspond to ~ 0.34 m w.eq. at the surface and more deeper in the core. Therefore, we can summarise that using spectral analysis, no clear seasonal cycle can be detected in the near surface firn (upper 10 m w.eq.) when analysing single cores.

b.4 discussion

We present an extensive high-resolution density data set characterising the near-surface density variability in an Antarctic low-accumulation region. In the following, we will discuss potential mechanisms for the build-up of the layered snow column, its link to the layered structure of compacted firn, and the representativeness of single firn-core measurements.

b.4.1 *Spatial Variability of Density in the Upper Snow Column*

The re-deposition due to interaction with wind is one of the reasons for the high lateral density variability of surface snow (Fisher et al., 1985; Birnbaum et al., 2010; Libois et al., 2014). Our site is located within a region of light katabatic winds leading to a moderate mean snow density of 340 $\mathrm{kg\,m^{-3}}$ (Ligtenberg et al., 2011). Here, snow is deposited in snowfields of several metre length with sporadic formations of barchan-type dunes of high density during strong wind events (Birnbaum et al., 2010). Below the surface, patches of high snow density in the trench (Fig. B.3) suggest that these dunes have been buried and are a main cause for the lateral density variability. This confirms recent findings of a nearby 2-D density profile (Proksch et al., 2015).

While an earlier study investigating five shallow firn cores from the same region found that the dune horizons were randomly located within the cores (Birnbaum et al., 2010), our data show that the high-density regions are parts of continuous layers and thus cause at least part of the stratification. Both results are consistent given that the firn cores presented in Birnbaum et al. (2010) were spaced more than 50 m from each other, and thus, continuous layers would not have been detectable.

Wind scouring can create a pronounced surface roughness on a daily timescale with an amplitude sometimes exceeding the annual

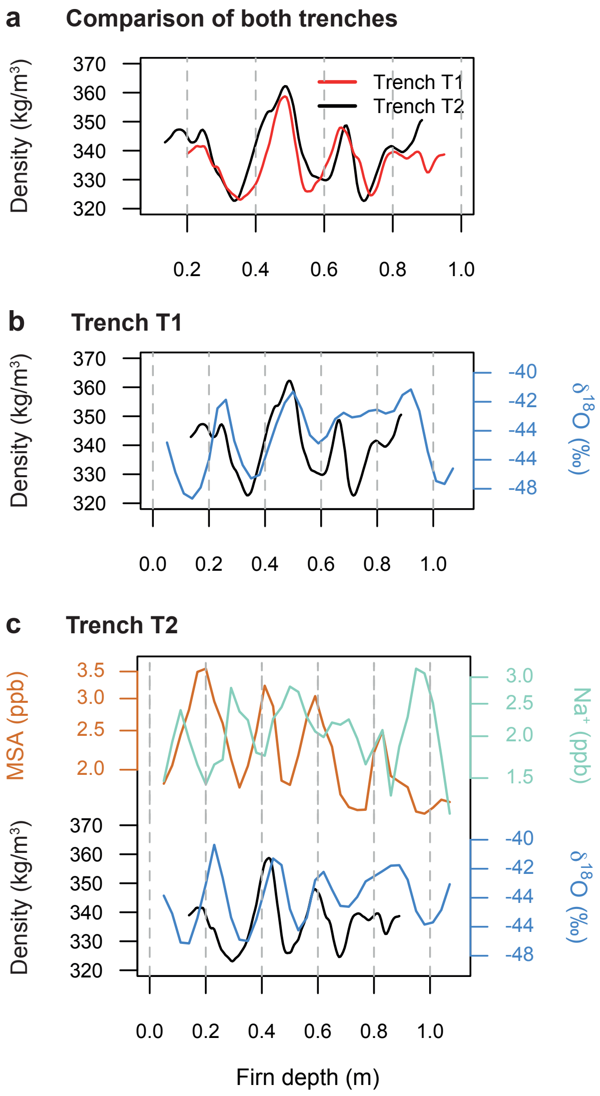

FIGURE B.6. Mean density*, mean isotope, and mean impurity profiles. (**a**) Mean density profiles of Trench T1 and T2 (T2 shifted by$^\vee$ 6 cm) are highly correlated ($r = 0.84$). (**b** and **c**) Comparison of mean density and mean δ^{18}O profiles. In (**c**), in addition, the mean impurity profiles are shown. The impurity concentration axes are on a logarithmic scale in parts per billion (ppb)$^\vee$.

accumulation rate (Gow, 1965; Libois et al., 2014). In our case, the surface undulations have peak-to-trough variations of 12 cm for trench T1 and 13 cm for T2 (Fig. B.3). This represents a snapshot during the time of sampling and is less than the annual accumulation of about 20 cm of snow.

These undulation do not grow larger with time as evidenced by the fact that the surface looks similar from year to year. Earlier studies described dunes and sastrugi to be worn down by sublimation-deflation over the summer (Gow, 1965; Benson, 1971; Palais, 1984;

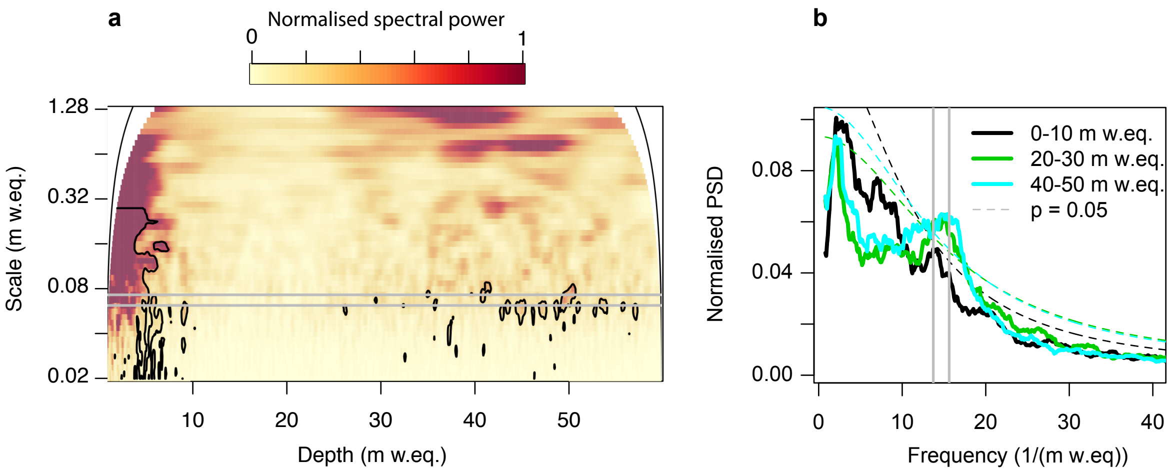

FIGURE B.7. Spectral analysis of the depth dependency of density variability. (**a**) Mean wavelet spectrum of the firn-core density variations. The black contour lines enclose the regions with significant concentrations of spectral power. (**b**) Mean power spectra of density variations at three depth intervals. Significance levels are shown as dashed lines. The approximate range of annual layer thickness is shown as horizontal grey lines in (**a**) and vertical grey lines in (**b**). Significance ($p = 0.05$) in (**a**) and (**b**) tested assuming a first-order autoregressive (AR(1)) model.

Mosley-Thompson et al., 1985). Alternatively, a negative relationship between the actual height anomaly and the accumulation must exist: troughs get more accumulation than peaks. Both mechanisms could explain our finding that the layering at depth is on average horizontal and does not follow the modern snow surface (Fig. B.3). Thus, the metre to decametre surface undulations seem to be a seasonal phenomenon, which get "reset" every year.

B.4.2 *Representativeness of Single Vertical Density Profiles*

The large lateral variability of density at our study site (Fig. B.3) is also reflected in the poor correlation between different vertical density profiles and different firn cores. This is a typical finding for low-accumulation sites (Palais, 1984; Jones et al., 2014) and also applies to other parameters such as oxygen isotopes (Karlöf et al., 2006; Münch et al., 2016b). The results are in strong contrast to Antarctic high-accumulation sites, e.g., at Law Dome in which single profiles seem to be representative over an area of multiple kilometres (McMorrow et al., 2002).

Going beyond showing the limitations of single profiles and firn cores, we could demonstrate the existence of a common signal across horizontal scales of at least 500 m as reflected in the strong correlation of the mean profiles from each trench. The strong increase in correlation, when analysing averages across multiple profiles, shows that the horizontal scale of the depositional noise is considerably smaller than the length of the trenches yet larger than our lateral sample spacing. This is reflected in a lateral decorrelation length (Fig. B.5) of less than 5 m. For future studies, this result suggests that in this region point measurements such as snow stakes or firn cores should be placed at least 5 m from each other in order to avoid recording the same local depositional noise. It is important to note that our analysis was performed perpendicularly to the dune direction. Since the dunes are likely to determine the lateral scale of the local signal/depositional noise, the decorrelation length, and thus the optimal spacing to determine a representative signal, has to be larger in the dune direction because of the larger dimensions of dunes in wind direction.

The other approach to increase the representativeness of the signal is to vertically average the data. The effectiveness of this approach depends on the vertical correlation of the noise. Our finding that the surface undulations seem to be lost further down in the firn column is promising, but a more detailed analysis of the vertical correlation structure of the signal and the noise is needed in order to quantify the effects of vertical smoothing on the representativeness of the signal.

B.4.3 *Seasonal Cycle in Snow Density*

The most prominent feature in our data set is the horizontal layering of the density variations. The spacing of the layers of 15–25 cm, in line with a typical annual layer thickness of 20 cm (62–73 kg m^{-2} accumulation per year/mean density of 340 kg m^{-3}) suggests that these are seasonal phenomena. This is supported by the similarity to the signal in the water isotopes, which is usually interpreted as being driven by the seasonal cycle in temperature (Fig. B.6).

The ion concentrations of MSA and Na$^+$ are known to exhibit a seasonal cycle in the atmosphere over Kohnen Station (Weller and Wagenbach, 2007), as well as a pronounced seasonal cycle in surface snow pits, firn-core measurements (Göktas et al., 2002), and in the deeper firn (Sommer et al., 2000b). The timing of MSA peaks is in late summer to fall, for Na$^+$ in winter to spring (Göktas et al., 2002; Weller and Wagenbach, 2007). This seasonality is consistent with the observed phase relationships between density, impurities, and isotopes (Fig. B.6 and Table B.2), and it thus strongly supports that the average density profile shows a seasonal signal with maximum density around summer and minimum density around winter. We note that from previous published data from Antarctic and Greenlandic sites (Benson, 1971; Etheridge et al., 1992; Gerland et al., 1999) no clear definition of a relationship between season and high or low density can be drawn. Therefore, the representativity of our finding for other Antarctic sites is unclear.

In contrast to the clear seasonality in the average density profile, the seasonal cycle of density in single cores is weak and often not detectable (Fig. B.4 and Fig. B.7). This can be attributed to two reasons. First, the signal (approximated by the mean profile) is small relative to the total variability. Estimating the signal-to-noise ratio (SNR) from the correlation across profiles as $r/(1-r)$ (Fisher et al., 1985), only considering profiles separated by more than the decorrelation length of the noise ($\geq 10\,\mathrm{m}$)[1], results in a SNR of 0.15 (Table B.2). Second, the accumulation rate shows considerable interannual (Oerter et al., 2000) and interdecadal (Klein, 2014) variability. This distributes the energy across frequencies and thus inhibits the detection of the seasonal cycle even when analysing longer density profiles. In contrast, given that the average accumulation rate over a region is uniform, averaging over space overcomes this problem and explains why horizontally integrating sensing techniques such as radar (but also the eye visually tracking horizons in snow pits) see annual horizons (Winebrenner et al., 2001; Anschütz et al., 2007; Eisen et al., 2008; Arthern et al., 2013).

The most obvious reasons for seasonality in the density signal are seasonal variations of temperature, wind, and radiation. They can affect the precipitation/deposition, on the one hand, and post-depositional effects like snow metamorphism caused by temperature gradients or other destructive processes induced by radiation or wind, on the other hand (Alley, 1988; Harper and Bradford, 2003). However, very different observations are published regarding the time and season of low- or high-density snow deposition/formation, delivering an overall heterogeneous picture of snow seasonality on top of the ice sheets (Gow, 1965; Palais, 1984; Alley, 1988; Li and Zwally, 2002; Birnbaum et al., 2010; Fujita et al., 2014). Given the contradicting evidences from the literature and the limited number of years covered by our data set, we refrain from proposing a mechanistic understanding of the seasonal variations in density in this study. Nevertheless, we hope that our empirical finding of summer related to high density will foster new investigations on the seasonality of surface firn.

B.4.4 *Density Layering in Firn and Impurities*

The density layering in deep firn is the result of a densification process acting on the layered snow with an increase in mean density by almost a factor of three in the top 100 m (Freitag et al., 2013b). Our new data set proposes the existence of an annual cycle in density already in the top metre. However, the relative contribution of the seasonality to the total variability is small ($< 20\,\%$), which therefore does not allow the detection of the seasonal cycle in single cores. In contrast, analysing the firn deeper than 30 m below the surface shows

---

[1] The original publication erroneously states that profiles separated by more than 5 m have been used. In fact, the calculations were made for profile separations of at least 10 m, as it is also correctly stated in the heading of Table B.2.

a stronger seasonal signal (relative to the total variability) (Fig. B.7), confirming earlier findings (Hörhold et al., 2012; Freitag et al., 2013a).

To explain the stronger seasonal cycle in the deeper firn, two scenarios seem possible. First, the deep seasonal cycle might be an amplified version of the surface seasonal cycle of an earlier time. Therefore, a driver with the same seasonal phasing or a selective densification mechanism would need to be invoked, which damps all variability but the seasonal cycle. Physical or microstructural properties of layers can be thought to be generated directly at the surface during deposition and favouring high densification rates in low-density layers and low densification rates in high-density layers (Hörhold et al., 2012; Fujita et al., 2014).

Second, the deep seasonal cycle might originate from processes independent of⋆ the surface seasonal cycle in density. For this hypothesis, another driver with a seasonal cycle, potentially with a different phasing than the surface density seasonality, would be needed. It was proposed earlier that impurity concentrations might be this driver (Hörhold et al., 2012; Freitag et al., 2013a). In this case the original properties of layers deposited at the surface are overprinted by post-depositional metamorphism depending on their impurity load. Such an impurity effect on density is highly debated, and the chemical species responsible for such an effect is not clear. At the Kohnen site the Ca^{2+} ion concentration develops a strong correlation with density with depth, which suggests impurities with a comparable seasonal cycle as the Ca^{2+} concentration to be involved (Freitag et al., 2013a). At other sites no correlation between Ca^{2+} and density was found (Buizert et al., 2015) or other species are discussed with respect to processes actually transferring the impurity load into a densification rate (Fujita et al., 2014).

While the trench data are too limited to reach a definite conclusion, the available evidence from the phasing of impurities (Fig. B.6 and Table B.2) argues for the second hypothesis. Earlier studies showed an in-phase relationship of Na^{+} with Ca^{2+} (Sommer et al., 2000a) as well as strong correlation of Ca^{2+} with density at greater depths at the Kohnen site (Freitag et al., 2013a). In the trench mean density profile, Na^{+} is out of phase with the density signal (Table B.2), thus in contrast to the in-phase relationship expected at greater depths, suggesting a depth-dependent change of the density layering. This hypothesis is also consistent with the finding that the impurities in our data set show a stronger seasonality than the density at the surface (Table B.2).

The observed seasonal cycles in isotopes, density, and impurities indicate that depositional and post-depositional processes at the surface are not strong enough to destroy the subannual order of buried snow layers at Kohnen. This allows for the possibility that seasonal properties are preserved that later lead to a lateral homogenisation of density. We speculate that such layering in the deep firn could efficiently prevent the diffusive exchange of trapped air between adjacent layers near the bubble close-off.

B.5 CONCLUSIONS

An extensive density data set from two trenches and three firn cores near Kohnen Station, Antarctica, allowed a detailed investigation of the lateral and vertical density variability in a low-accumulation region. We find that the density variations of single firn profiles are not representative on seasonal to interannual timescales. However, averaging across multiple density profiles reveals a signal, at least representative on a 500-metre scale. The analysis of oxygen isotopes and impurities, as well as the spacing of density layering, suggests that the average density signal is dominated by a seasonal cycle with summer related to higher densities.

It follows that at least in our study region, the contribution of the seasonal cycle to the total variability is strongly depending on the analysed horizontal scale. In single snow pits or firn cores, stratigraphic noise dominates the variability and the seasonal cycle only explains a small part of the total variability. This masks the seasonal cycle and explains why previous firn-core studies reported a lack of a seasonal signal in Antarctic surface snow. Averaging over a larger region, for example, by averaging across many firn cores or using horizontally integrating techniques such as radar data, damps the stratigraphic noise and thus reveals the seasonal cycle. For measurements sensitive to the layering of the top metres of firn such as$^{\vee}$ microwave remote sensing or high-resolution radar altimetry, the lateral variability has to be taken into account when comparing these spatially integrating observations to firn cores.

Our findings of a seasonal cycle with maximum density in summer raise new questions on the genesis of physical properties at the surface of polar ice sheets and their fate with depth. While our data set is too limited to draw definitive conclusions, it suggests that the seasonal cycle in density at the surface and the seasonal cycle in density at depth might be decoupled. This emphasises the need to detangle the interaction of isotopic composition, density, and impurities from the very beginning of the depositional and post-depositional processes in order to understand their linkage with depth and its meaning for the pore close-off.

ACKNOWLEDGEMENTS – DANKSAGUNG

This dissertation would not have been written without the help, support and creativity of many people. You made this work possible!

I thank all my co-authors and colleagues who contributed to the individual articles. Special thanks go to Sepp Kipfstuhl for taking me to Antarctica, and for digging in the snow even in the blistering cold. I warmly thank Christoph Manthey, and the other staff of the isotope laboratories at the AWI in Bremerhaven and Potsdam, for their support of the measurements. I thank all scientists who made their work and data available so that I could take benefit of it. For further acknowledgements, I kindly refer to the individual acknowledgements of the published versions of the articles.

Special thanks go to the supervisors and mentors of this work. I thank Jürgen Kurths for serving as the second supervisor, and for the many helpful comments and the support of this project; and I thank Peter Ditlevsen for serving as the external examiner. Big thanks go to Johannes Freitag for mentoring this dissertation, for discussions, the jokes, the always nice atmosphere when I visited Bremerhaven, and for proofreading of the manuscript. I further thank Hanno Meyer for his support and help.

I thank all members of the working group ECUS/SPACE for the great time I had in the last couple of years; thank you Kira, Ling, Maria, Torben, Andrew, Alexandra, and Igor! Special thanks go to Andrew for the valuable help in improving the language of my writing, the support in questions regarding R, the proofreading and the scientific discussions; and also to Torben for the discussions on climate variability and further comments on and proofreading of this thesis.

I am grateful for the financial support by POLMAR which allowed me to take part in the Karthaus Summer School.

I also want to thank my colleagues and friends from AWI Potsdam, who made my PhD time so enjoyable, especially during the PhD Days on Helgoland, on Sylt and in Potsdam – big thanks to Matthias, George, Samuel, Kati, Berit, Daniel, Erik, Markus, Stefan and Ingmar!

Finally, I am deeply grateful to Thomas Laepple. He had the initial idea for this project, decided that I would be the right guy to conduct it, and helped and supported me during the entire time of the last couple of years – thank you very much, Thom! You significantly improved my scientific way of thinking!

Nun möchte ich allen Menschen danken, die mir im Privaten ermöglicht und mich dabei unterstützt haben, dieses Projekt durchzuführen und diese Arbeit fertigzustellen.

Ich danke Swen, David, Alex, Yori, René und Luise, Falko, Christopher, Max, Andreas, Tini, Steffen, Philipp, Joe, Achmed, Håkan och Monica, und Geisi, Niklas, Bruchi und Nils, dafür, mich während meines Studiums und in den letzten Jahren begleitet zu haben. Es war eine tolle Zeit zusammen, lasst uns so weitermachen! Und ich danke Euch, René, Nico, Marco, Micha und Basti, für die Musik. (Es tut mir aufrichtig leid, wenn ich jemanden vergessen haben sollte – ich schreibe diese Zeilen kurz vor Drucklegung. . .).

Vielen Dank auch an Ulla und Christian, und Frau Eckhardt, für die Ideen, die Hilfe und die Umsetzung bei der Gestaltung des Titelblatts.

Meiner Familie und Ulla gebührt schlussendlich mein größter Dank.

Michael und Annette mit Bene, Hannes und Jesse: Es ist einfach schön, dass es Euch gibt!

Ich danke meinen Eltern für ihre uneingeschränkte und bedingungslose Unterstützung meines Studiums, für ihre Liebe, die Hilfe zu allen Zeiten, und für den sicheren Hafen – wie Michael es so schön beschrieben hat –, den Ihr mir und uns immer offen gehalten habt, dort vor Anker zu gehen. Ich danke Euch für die kritische Weltsicht, die Ihr mir beigebracht habt, auch wenn diese das Leben nicht immer einfacher macht.

Ulla, ich kann in diesem Moment wohl nicht mehr vernünftig in Worte fassen, wie dankbar ich Dir bin. Danke für alles, für die gemeinsame Zeit, für Nora, unsere Urlaube, das Baltikum, den Wein und das Bier, die Konzertbesuche, und für die riesige und unschätzbare Hilfe in den letzten Wochen und Monaten! Wenn Du mir nicht so sehr den Rücken freigehalten hättest, würde ich heute nicht hier sitzen und diese Dissertation in den Druck geben – Danke!

EIDESSTATTLICHE ERKLÄRUNG

Hiermit versichere ich, Thomas Münch, dass ich die vorliegende Dissertation mit dem Titel: "Interpretation of Temperature Signals from Ice Cores: Insights into the spatial and temporal variability of water isotopes in Antarctica" selbständig verfasst und keine anderen als die angegebenen Quellen und Hilfsmittel verwendet habe. Alle Ausführungen, die anderen Schriften wörtlich oder inhaltlich entnommenen wurden, sind als solche kenntlich gemacht.

Ich habe diese kumulative Dissertation am Alfred-Wegener-Institut Helmholtz-Zentrum für Polar- und Meeresforschung in Potsdam erarbeitet und in englischer Sprache angefertigt.

Diese Dissertation wird erstmalig und ausschließlich an der Universität Potsdam eingereicht. Die dem Promotionsverfahren zugrundeliegende Promotionsordnung vom 18.09.2013 ist mir bekannt.

Potsdam, den 29. November 2017

Thomas Münch